CONSTRAINTS ON THE NEUTRON EQUATION OF STATE USING THE DIFFERENCE IN ^{54}Ni-^{54}Fe MIRROR PAIR CHARGE RADII

By

Skyy Venancio Pineda

A DISSERTATION

Submitted to
Michigan State University
in partial fulfillment of the requirements
for the degree of

Chemistry – Doctor of Philosophy

2022

ABSTRACT

Just like the ideal gas law is used to characterize a 'perfect' gas, equations of state can be used to describe nuclear matter. Two such equations of state include the symmetric matter equation of state and the neutron matter equation of state. While symmetric matter is well known, neutron matter is not, especially when extrapolating to higher densities. The nuclear matter equation of state is of interest because a greater understanding of it is required to predict properties of both super-heavy nuclei and neutron stars. There is ongoing debate about whether the neutron equation of state is 'soft' or 'stiff', where a 'stiff' equation of state implies the pressure in the nucleus increases rapidly with increasing density and consequently implies a larger neutron star radius. A way to constrain this neutron equation of state is through the slope of the symmetry energy (the L parameter), where the symmetry energy is the difference between the symmetric and neutron matter equations of state. Conceptually, L is proportional to the pressure of pure neutron matter at a specific density, and can also be thought of as a restoration force ('spring constant') between protons and neutrons when they are dislocated in the nucleus.

The complication is that L is not a physical observable and cannot be directly measured in the laboratory. However, it has been shown that the neutron skin thickness ($\Delta R_{\rm np}$) of neutron-rich nuclei are correlated to L. By measuring the neutron skin we can therefor place constraints on the L parameter and ultimately the neutron equation of state. Many experimental and theoretical techniques have been used to constrain L. It is noted that all of them are model-dependent in some way. Even though many of these analyses agree within 1σ, they each have tendencies toward either the 'soft' or the 'stiff' nuclear equation of state. Results from the PREX and CREX experiments, highly regarded benchmarks for the neutron skin value, also show tension between their results, highlighting that discretion is needed when addressing the model-dependent components in these analyses. This model-dependence brings about the need for increased systematic measurements of the L parameter to add to the discussion on constraints on L.

The difference in charge radii ($\Delta R_{\rm ch}$) is a new, purely electromagnetic probe to deduce the neutron skin and constrain L. Assuming perfect charge symmetry, the distribution of the protons is equal to the distribution of the neutrons in the mirror nucleus. By taking the difference in charge radii, the neutron skin can be obtained. In reality, however, the charge symmetry is broken by the Coulomb interaction that pushes protons out relative to neutrons, leading to a weaker correlation between $\Delta R_{\rm np}$ and $\Delta R_{\rm ch}$. However, even with this Coulomb disruption, $\Delta R_{\rm ch}$ shows tighter correlation to L than that of $\Delta R_{\rm np}$. It was also shown that $\Delta R_{\rm ch}$ is correlated to $|N-Z| \times L$. Due to this correlation, ideally a mirror pair would be chosen with a high $|N-Z|$ to provide a tighter constraint, where the maximum possible is $|N-Z| = 6$ for the ^{22}Si-^{22}O pair. The present ^{54}Ni-^{54}Fe mirror pair has a rather low $|N-Z| = 2$, and therefor requires a highly sensitive

technique to be able to provide good enough results to place constraints on L, otherwise too large of an uncertainty would void any meaningful discussion.

Isotope shift measurements using bunched beam collinear laser spectroscopy of ^{54}Ni ($I^{\pi} = 0^{+}$, $t_{1/2} =$ 114 ms) and other nickel isotopes were performed at the BEam COoling and LAser spectroscopy (BECOLA) facility at the National Superconducting Cyclotron Laboratory (NSCL) at Michigan State University. These precise measurements were used to extract the charge radius for ^{54}Ni for the first time to be $R(^{54}\text{Ni}) = 3.737 \pm 0.003$ fm. Using the already known ^{54}Fe charge radius from literature, the difference in charge radii between the mirror pairs was taken in order to obtain $\Delta R_{\text{ch}} = 0.049 \pm 0.004$ fm. Based on the correlation between L and ΔR_{ch} calculated by density functional theory using the Skyrme energy density functional, the present $\Delta R_{\text{ch}}(A = 54)$ set a constraint on the L parameter as $21 \leq L \leq 88$ MeV. The model takes into account corrections for the quadrupole deformation, which was evaluated through the β_2 deformation parameter obtained by the reduced $E2$ transition probability $B(E2, \uparrow)$ for ^{54}Ni. These constraints on L from BECOLA are in good agreement with the GW170817 neutron star merger, whose results also favor the 'soft' neutron equation of state, providing an link between a new terrestrial-based experimental method and an astrophysical observation. These results are different from the PREX results, which favor the 'stiff' EOS. To add to the systematics, the same method using parity violating electron scattering to measure the electroweak form factor was used with the CREX experiment. Using the ΔR_{ch} method has also enabled constraints on the neutron skin for ^{48}Ca which agree with the CREX results. The tension between CREX and PREX stems from the model-dependent step during the analyses demonstrated by a reevaluation of the PREX results which resulted in a smaller neutron skin and L value consistent with GW170817, BECOLA, and CREX.

A global trend analysis evaluated the relationship between ΔR_{ch} and L. The results concluded that while there was correlation between the observable and the L parameter, it could not place stringent constrains on the neutron equation of state within the model, hearkening back to model-dependence playing a critical role in the determination of L.

Dedicated to my parents Susan and Miguel

ACKNOWLEDGEMENTS

Firstly, I would like to thank my advisor Kei Minamisono for his patience and guidance throughout my graduate career at BECOLA. He helped me to become a better scientist, while his kindness and support were essential in the completion of this degree. This gratitude is extended to my committee members Sean Liddick, Alex Brown, Gregory Severin, whose invested time and and input allowed me to progress through the PhD program. Thanks to Chandana Sumithrarachchi, who provided high quality beams from the gas stopper to BECOLA. On that note I would like to thank of the people who made my thesis experiment possible, especially during the COVID-19 pandemic. I appreciate all of the cooperation during the declared of state of emergency. I thank Witold Nazarewicz for his time and input with the model-dependence discussion. I thank Yuan Liu for taking the time to teach me new laser alignment and servicing techniques.

Thank you to the Post-doc Kristian König for his helpful explanations and knowledge about the lasers. I appreciate all of the support from graduate students at BECOLA, and the help from Andrew Miller, Jeremy Lantis, and Robert Powel aided my transition into the group when I was just starting out. Building and flying drones with Andrew was always fun. Post-COVID, I would like to thank Brooke Rickey for her help during a deficiency of students in the group due to the pandemic, and for the opportunity to be a teacher to her as the senior graduate student, which provided me another learning opportunity. Alex Brinson and the MIT collaboration also helped in the lab, I would like to thank them as well. Although there is a long list of undergraduate students who came and went from BECOLA, I would like to thank Adam Dockery for his support and his continuing efforts in the group.

I extend my thanks to my professors in the Augustana University Chemistry Department, who were critical in inspiring me to choose this career path. My undergraduate advisor Andrew Klose and my organic chemistry professor Jetty Duffy encouraged me and took the time to introduce me to areas of science that sparked my interest. Undergraduate research with Andrew Klose opened the door to laser spectroscopy and he is a large factor in why I chose BECOLA for my graduate research. Jetty Duffy, apart from fostering my affinity for organic chemistry, made me feel at home when I first got to the United States from Guatemala. The initial pressures, complications, and sickness during those first critical months alone in a foreign country were blunted by her care and made things more bearable.

There are a few teachers from Inter-American School who were essential to my success in college, and they are Sean Manchester, Michael Smith, and Kristen Moser. Their dedication and kindness for children in a third world country like Guatemala made my PhD possible. This goes for Michael Smith especially, and his passion for science added fuel to mine. I would have chosen him as my advisor if they existed for high school, although unofficially, we could say he was my advisor. Laurel McMarlin and David Fox also deserve

recognition because their philosophies and wisdom had a positive impact on my journey.

I would like to thank all of the professors I had the opportunity to learn from at my *alma mater* Augustana University (formerly Augustana College) and Michigan State University.

I would like to thank my parents, Susan Potter and Miguel Pineda, for their unconditional love, support, and emphasis on the importance of education and music. I would not be here today if it were not for their good parenting and the many sacrifices they made to ensure I succeeded in life. Apart from academics, had I not trained in classical guitar for those many years under their encouragement, I would not have composed the piece which won a competitive music scholarship in the United States. This is the scholarship which started my journey into science by allowing me to study ACS Biochemistry at Augustana University. The music, apart from feeding my soul, opened up many scientific doors along the way that I had not anticipated. I would like to thank my grandfather Rajendra Patel, whose wisdom kept me on the right path in life and in my career. I am happy to say I have completed his wish in becoming a doctor, which is the best way I could commemorate him after his passing midway through my doctoral program. My grandmother, Florence Patel, also deserved recognition as her 'never-give-up' mentality and advice guided me through my life and career as well. I thank all of my family members in the United States and abroad who supported me during my education. Agradezco mucho el apoyo de mi familia en Guatemala. En parte quiero también dedicar esta tésis a mi abuelita Leonor Barrios (de Pineda), quien como mi abuelo Rajendra Patel falleció durante la pandemia. Siempre fue un gusto explicar lo que estaba aprendiendo e investigando a ella, y su interés en la ciencia me animó más.

Thank you to Annie Nunan, as her support was critical in my journey through university.

Thank you to the friends I made during graduate school, especially Akash Saxena and Cristhian Gonzales, who made East Lansing a much more interesting place. Quiero también agradecer a mis amigos en Guatemala que me ayudaron aguantar la pandemia con llamadas, especialmente durante la cuarentena donde estaba aislado por meses. Específicamente quiero agradecer a Jose Pablo Velasquez por distraerme con zombis y chela los fines de semana durante ese periodo de COVID. Agradezco a Hugo Bethancourt por ser un apoyo constante a lo largo de mi carrera universitaria. There are so many others I would like to thank and my sincerest apologies for leaving anyone out.

Many thanks are extended to the many people along the way that led me to this point. Thank you for your support.

Doy muchas gracias a las muchas personas a lo largo del camino que me llevaron a este punto. Gracias por tu apoyo.

TABLE OF CONTENTS

LIST OF ABBREVIATIONS

AIC ..... **A**kaike-**I**nformation **C**riterion

AOM ..... **A**cousto-**O**ptic **M**odulator

ASCII ..... **A**merican **S**tandard **C**ode for **I**nformation **I**nterchange

BCS ..... **B**ardeen-**C**ooper-**S**chrieffer

BECOLA ..... **BE**am **CO**ol[ing][er] and **LA**ser Spectroscopy Facility

BECOLA-RISE ..... **BECOLA**-**R**esonance **I**onization **S**pectroscopy **E**xperiment

BIC ..... **B**ayesian-**I**nformation **C**riterion

BiFi ..... **Bi**refringent **Fi**lter

BOB ..... **B**eam **O**bservation **B**ox

CCD ..... **C**harge-**C**oupled **D**evice

CEC ..... **C**harge **E**xchange **C**ell

CLS ..... **C**ollinear **L**aser **S**pectroscopy

CM ..... **C**enter of **M**ass

COD ..... **C**oefficient **O**f **D**etermination

CODATA ..... **C**ommittee on **DATA** of the International Science Council

CODF ..... **CO**variant **D**ensity **F**unctional

CPC ..... **C**ompound **P**arabolic **C**oncentrator

CREX ..... **C**a (calcium) **R**adius **EX**periment

DAQ ..... **D**igital **A**c**Q**uisition system

DC ..... **D**irect **C**urrent

DVM ..... **D**igital **V**olt **M**eter

EDF ..... **E**nergy **D**ensity **F**unctional

EOM ..... **E**lectro-**O**ptic **M**odulator

EOS ..... **E**quation **O**f **S**tate

FHG ..... **F**ourth **H**armonic **G**eneration

FNS ..... **F**inite **N**uclear **S**ize

FRIB ..... **F**acility for **R**are **I**sotope **B**eams

FSR ..... **F**ree **S**pectral **R**ange

FWHM ..... **F**ull **W**idth at **H**alf **M**aximum

GW170817 ..... **G**ravitational **W**ave 170817

HFB ..... **H**artree-**F**ock-**Bogoliubov**

HF+EFA ..... **H**artree-**F**ock+**E**qual **F**illing **A**pproximation

HV ..... **H**igh **V**oltage

IMSRG ..... **I**n-**M**edium **S**imilarity **R**enormalization **G**roup

IS ..... **I**so**S**calar

ISOL ..... **I**sotope **S**eparation **O**n-**L**ine

IUPAC ..... **I**nternational **U**nion of **P**ure and **A**pplied **C**hemistry

IV ..... **I**so**V**ector

LMFIT ..... Non-linear **L**east-squares **M**inimization and Curve **FIT**ting for Python

LPC ..... **L**aser **P**ower **C**ontroller

MIT ..... **M**assachusetts **I**nstitute of **T**echnology

MS ..... **M**ean **S**quare

MSU ..... **M**ichigan **S**tate **U**niversity

NIR ..... **N**ear-**I**nfra**R**ed

NIST ..... **N**ational **I**nstitute of **S**tandards and **T**echnology

NMS ..... **N**ormal **M**ass **S**hift

NSCL ..... **N**ational **S**uperconducting **C**yclotron **L**aboratory

ORNL ..... **O**ak **R**idge **N**ational **L**aboratory

PAC ..... **P**rogram **A**dvisory **C**ommittee

PIG ..... **P**enning **I**onization **G**auge

PMT ..... **P**hoto**M**ultiplier **T**ube

PREX ..... **P**b (lead) **R**adius **EX**periment

RF ..... **R**adio **F**requency

RFQ ..... **R**adio **F**requency **Q**uadrupole

RMS ..... **R**oot **M**ean **S**quare

SHG ..... **S**econd **H**armonic **G**eneration

SMS ..... **S**pecific **M**ass **S**hift

SNR ..... **S**ignal to **N**oise **R**atio

Ti:Sa ..... **Ti**tanium:**Sa**pphire laser

Nd-YAG ..... **N**eodymium-**d**oped **Y**ttrium **A**luminum **G**arnet laser

1 Introduction

1.1 Nuclear Equations of State and the Symmetry Energy

An equation of state is an equation that relates state variables, such as pressure P, volume V, and temperature T, in order to describe a substance. The general form of an equation of state is

$$P = f(T, V, n) \tag{1}$$

where n is the number of moles, showing that if T, V, and n are specified then the pressure has a fixed value. Although each substance has its own equation of state, their explicit forms are known for only a few specific cases [1]. A well known example taught in General and Physical Chemistry is the 'Perfect Gas' equation of state,

$$PV = nRT \tag{2}$$

where n is the number of moles in the gas and R is the universal gas constant where $R = 8.31$ J/mol K. In physics this same equation is usually expressed using density instead of moles [2], where Eq. 2 becomes

$$P = \rho k_B T \tag{3}$$

where k_B is Boltzmann's constant and ρ is the density. This conversion starts by substituting $n = \frac{N}{N_A}$:

$$PV = nRT = \frac{N}{N_A} RT = N \frac{R}{N_A} T \tag{4}$$

where N is the number of molecules and N_A is Avogadro's number. Since Boltzmann's constant is defined as

$$k_B = \frac{R}{N_A} = 1.38 \times 10^{-23} \text{J/K} \tag{5}$$

and density in this case is the number of molecules per unit volume

$$\rho = \frac{N}{V}, \tag{6}$$

making those substitutions (Eq. 5, Eq. 6) into Eq.4 yields Eq. 3. Using this ideal gas equation the average translational kinetic energy of a monatomic gas for a given volume can be expressed as

$$\frac{E}{V} = \frac{3}{2} \frac{N}{V} k_B T = \frac{3}{2} \rho k_B T \tag{7}$$

where the appearances of energy E and density ρ begin to show some resemblance to the nuclear matter equation of state.

The symmetry energy [3] is defined as the difference between pure neutron matter (neutron matter EOS) and symmetric matter (symmetric matter EOS), which is matter with equal numbers of protons and neutrons, as shown in Eq. 8, and represents the symmetry of the nuclear system shown in the cartoon model (Fig. 1). The values in brackets in Eq. 8 are representative of the equations of state, with $\left[\frac{E}{A}\right]$ for symmetric matter and $\left[\frac{E}{N}\right]$ for neutron matter.

$$E_{\text{sym}} = \left[\frac{E}{A}\right](\rho) - \left[\frac{E}{N}\right](\rho) \tag{8}$$

In the liquid drop model, the symmetry energy term determines how the binding energy decreases as the system moves away from stability (equal numbers of protons and neutrons) [4], or in other words, it measures the change in binding energy of the system as the neutron and proton ratio is changed at a fixed value of the total number of particles [3]. The symmetric matter EOS can take a negative value because the pairing between nucleons causes a bound state, while pure neutron matter is unbound and continues upward in energy. Therefor the symmetry energy can be thought of as the energy gained due to the symmetry of the system.

By taking a Taylor expansion (Eq. 9) of E_{sym} around the nuclear saturation density (where the density $\rho = \rho_0 = 0.16$ nucleons $\cdot\, \text{fm}^{-3}$) it is possible to extract the slope parameter (L) of the symmetry energy, a parameter that, because it comes from the symmetry energy, links neutron matter and symmetric matter together. Although typically referred as a 'slope' in the literature, L is expressed only in terms of MeV. This is because it is the slope at a specific density (saturation density $\rho = \rho_0$), so instead of being expressed in units of MeV/fm^3 it is only shown in MeV. In Eq. 9, J is the symmetry energy at saturation density (which has a strong correlation to the slope parameter), L is the slope of the symmetry energy, K_{sym} is the incompressibility.

$$E_{\text{sym}}(\rho) = J + L\left[\frac{\rho - \rho_0}{3\rho_0}\right] + \frac{K_{\text{sym}}}{2}\left[\frac{(\rho - \rho_0)^2}{3\rho_0}\right] + \cdots \tag{9}$$

By constraining the L parameter one is thereby able to constrain the neutron equation of state. Learning about the neutron EOS is important due to its relevance to the neutron skin and the structure of heavy elements, as well as astrophysical applications such as the radii of neutron stars and gravitational wave signals due to neutron star mergers [5, 6, 7].

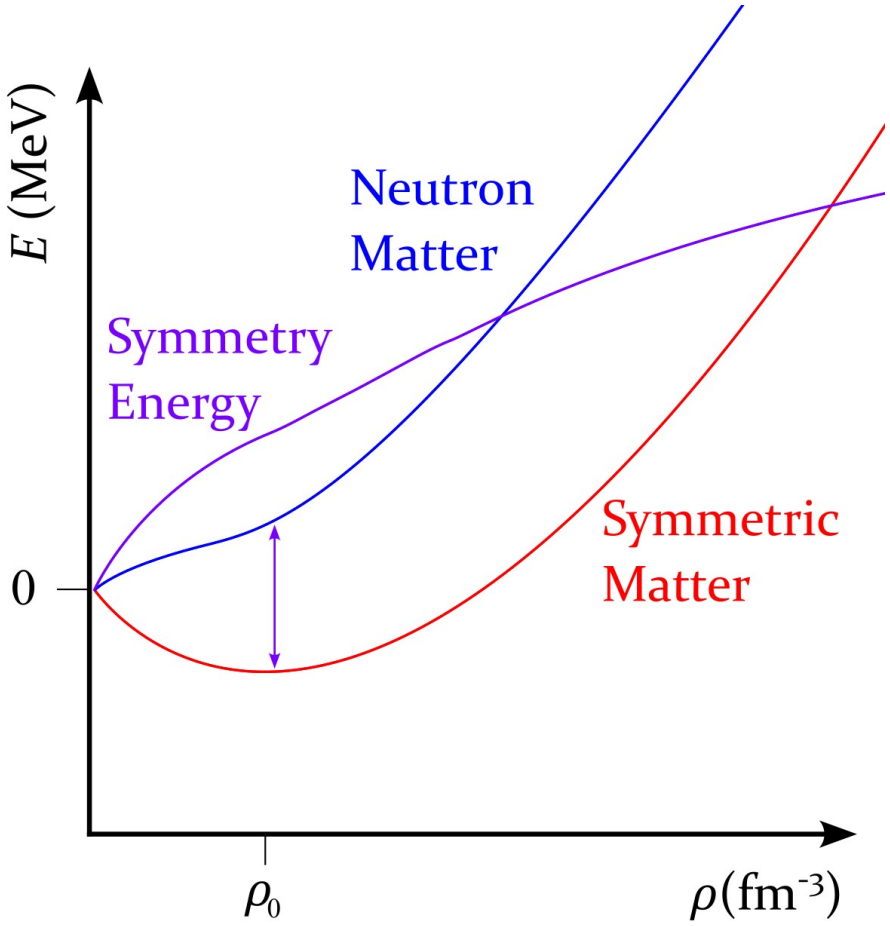

Figure 1: Symmetry energy conceptual model. The difference between neutron matter and symmetric matter (the purple double-sided arrow). Because neutron matter is not bound, the energy increases. Symmetric matter reaches a low point and the saturation density, indicating the most bound state. Nuclei with similar numbers of protons and neutrons are typically the most stable. As the ratio between the number of protons and neutrons in the nucleus becomes more extreme (as the asymmetry parameter deviates from zero and increases) (the asymmetry parameter becomes larger) and you change the symmetry of the system, the condition changes from bound (negative energy) to, in the most extreme case, pure neutron matter which is completely unbound. For interpretation of the references to color in this and all other figures, the reader is referred to the electronic version of this thesis.

While the symmetric matter portion of the symmetry energy has been constrained relatively well, different parameterizations of Skyrme energy density functionals show large variations in the stiffness of the neutron matter EOS (Fig. 2), especially when extrapolating to higher nuclear densities [8]. The link to the neutron matter equation of state is to constrain the slope of the symmetry energy. By placing constraints on the slope L, we are able to determine the softness or stiffness of the neutron EOS. A soft equation of state rises slowly along the y-axis while a stiff equation of state has a steeper slope.

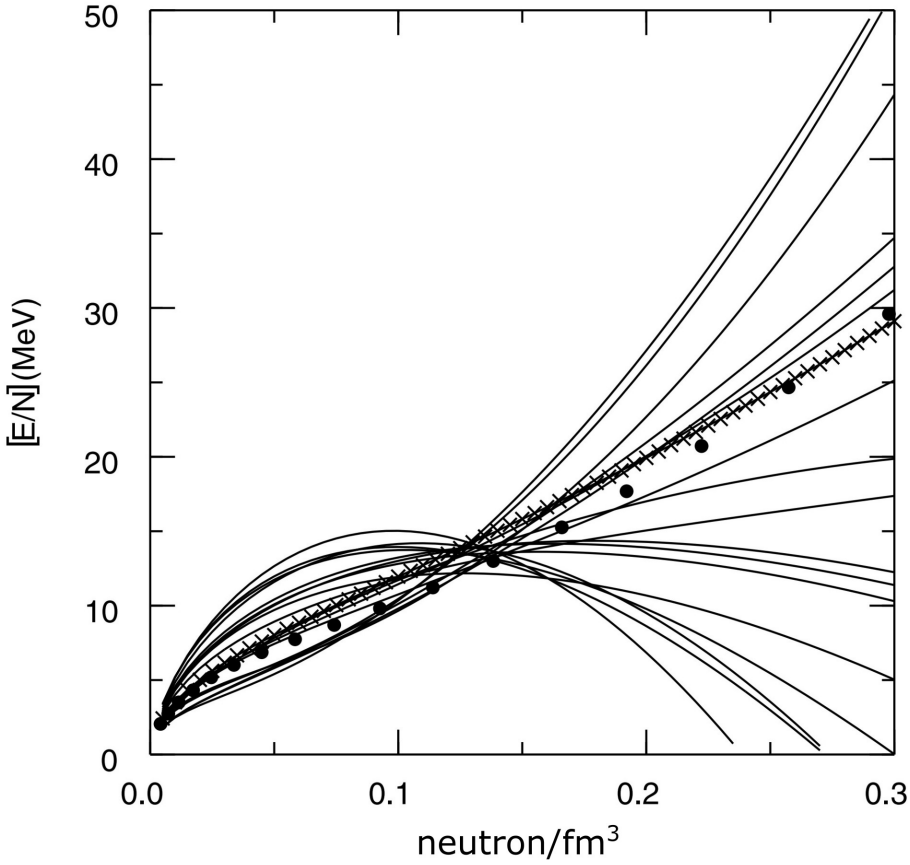

Figure 2: The neutron EOS for 18 Skyrme EDF parameter sets taken from Ref. [8].

1.2 Methods in Constraining the Nuclear Equation of State

Although L is a fundamental parameter in the EOS, it is not a physical observable and therefore correlations between physical observables have been sought after. The neutron skin $\Delta R_{\rm np}$ is defined as the difference in the root-mean-square radii of neutrons and protons in the nucleus [9]. Because nuclear matter saturates, there is a limit to how densely the neutrons can be packed into the nuclear volume. When this density limit (saturation) is reached, the distribution of neutrons seeps out of the nuclear volume relative to the protons, observed as the neutron skin. It has been shown that the neutron skin in neutron-rich nuclei is correlated to the slope (L) of the symmetry energy term in the nuclear equation of state (EOS) [8, 10]. The usefulness of $\Delta R_{\rm np}$ lies in its strong dependence on the isovector density ($\rho_1 = \rho_n - \rho_p$) and weaker dependence on the isoscalar (total) density ($\rho_0 = \rho_n + \rho_p$) [11]. An isovector indicator (quantity) is useful because it is strongly correlated to J and L parameters of the symmetry energy, which are considered isovector nuclear matter properties [12].

To avoid confusion on this key term which is used heavily in the literature, the word 'isovector' describes the difference between the nuclear densities and is connected to the symmetry energy-where the symmetry energy is the difference between symmetric and nuclear matter and is therefor an 'isovector' quantity. Isovector indicators are important because they describe the nucleus in a way that separates its neutron and proton components.

Thus far there have been many means [13] to provide constraints on this L parameter, however, a few in particular are more promising isovector indicators [14]: parity violation in electron scattering ($A_{\rm PV}$) and $\Delta R_{\rm np}$ in ^{208}Pb [15, 16, 17], and electric dipole polarizability $\alpha_{\rm D}$ [11, 18, 19, 20]. Astronomical observations have also been capable of constraining L via astrophysical results from neutron star mergers [21, 22, 7, 23, 24]. A brief summary of these analyses are provided below. Even with model-independent experimental observables, there is always some model-dependent step to constrain the L parameter. This model-dependence increases the importance on having different experimental observables and methods to add to the systematics of L.

1.2.1 Measuring the Parity Violating Amplitude with Electron Scattering

The Pb (lead) Radius EXperiment (PREX) provides a direct electromagnetic probe of neutron densities via parity violating electron scattering. When electrons interact with nuclei, they can do so by exchanging photons and Z^0 bosons. The Z^0 boson typically couples to neutrons because the neutron weak charge $Q_W^{\rm n} = -1$ is much larger than the proton weak charge $Q_W^{\rm p} \approx 0.075$, and the direct output of the PREX experiment was the value of the asymmetry $A_{\rm PV}$ at a single scattering angle [15]. Because there is a linear

correlation between $R_{\rm np}$ and $A_{\rm PV}$, both the neutron rms radius and $R_{\rm np}$ can be extracted. While $A_{\rm PV}$ is a model-independent quantity, the analysis which determines the $\Delta R_{\rm np}$ and places constraints on L still depends significantly on theory. Results from Ref. [25] give $L = 106 \pm 37\,{\rm MeV}$ and are shown in Fig. 3. A strong correlation between L and $\Delta R_{\rm np}^{208}$ can be seen on the left-hand panel. The slope of the symmetry energy as a function of $\Delta R_{\rm np}^{208}$ is shown in the left panel of Fig. 3, showing a strong correlation at ρ_0 and an even stronger correlation at $\rho = (2/3)\rho_0 \approx 0.1\,{\rm fm}^{-3}$. The Calcium Radius EXperiment (CREX) used a similar method using the ^{48}Ca nucleus (Sec. 6.3.2). It is also noted that while there are other measurements that measure the neutron skin by hadronic scattering, the analysis of these experiments also depends on models for the strong interaction [26, 27, 28].

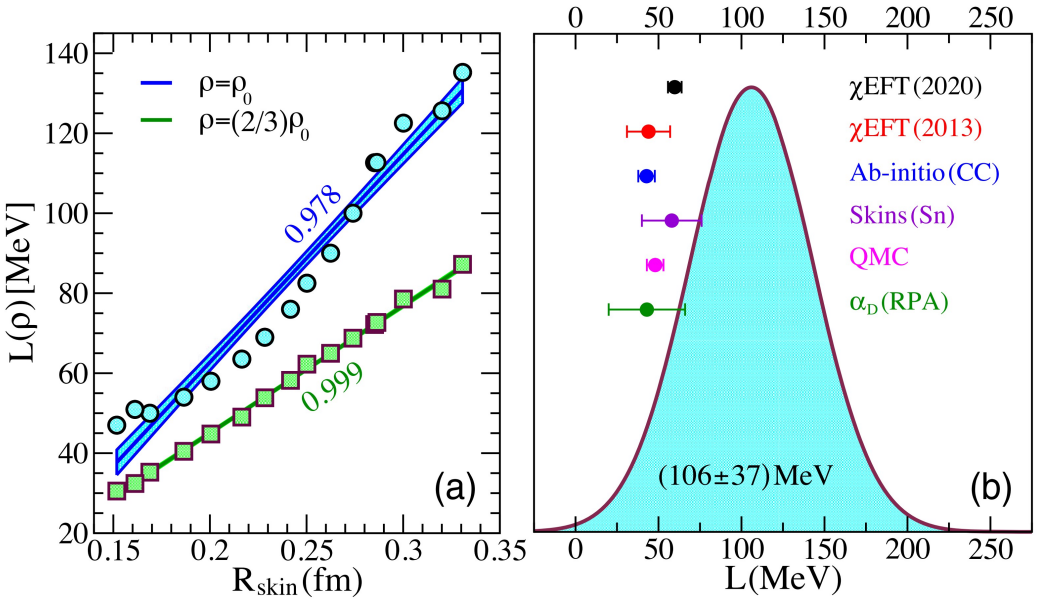

Figure 3: Constraints on L from Ref. [25]. The left panel of the figure shows the correlation between the slope of the symmetry energy and the neutron skin of ^{208}Pb. A strong correlation is exhibited between the two, with an even stronger correlation at $\rho = (2/3)\rho_0$. In the right panel the Gaussian probability distribution for L is inferred by combining the linear correlation in the left figure at the nuclear sturation density $\rho = \rho_0$ with the PREX-2 limit. The six theoretical points are constraints on L obtained by using different theoretical approaches. Notice there is a tendency for the theoretical approaches to favor smaller L compared to the result obtained with PREX-2 data.

1.2.2 Electric Dipole Polarizability Experiments

The nuclear electric dipole polarizability $\alpha_{\rm D}$ is a displacement of protons and neutrons in a nucleus under an external electric dipole (E1) field (Fig. 4). It can be obtained as a sum-rule of E1 transition moments weighted by the reciprocal of transitions energies [29], and is correlated to the neutron skin [11] since the symmetry energy acts as the restoring force of isovector oscillation [18]. Correlation between $\Delta R_{\rm np}$ and $\alpha_{\rm D}$ is shown in Fig. 5, where there is a high correlation coefficient of $c_{AB} = 0.98$ between the neutron skin of ^{208}Pb and $\alpha_{\rm D}$ [11]. Since the dipole polarizability is sensitive to the neutron distribution [11, 30], these measurements have been performed on ^{208}Pb [31, 32], ^{68}Ni [20] (radioactive), ^{120}Sn [33], and ^{48}Ca [34] and each placed their constraints on L [30]. A comparison between these three isotopes can be found in Ref. [35] where they give $20 \leq L \leq 66$ MeV. These results, however, are model-dependent and checking consistency with other systems and experimental techniques is critical. A table with various L results from Ref. [36] using this experimental technique is shown in Tab. 1. The correlation between $\alpha_{\rm D} J$ and L is shown in Fig. 6.

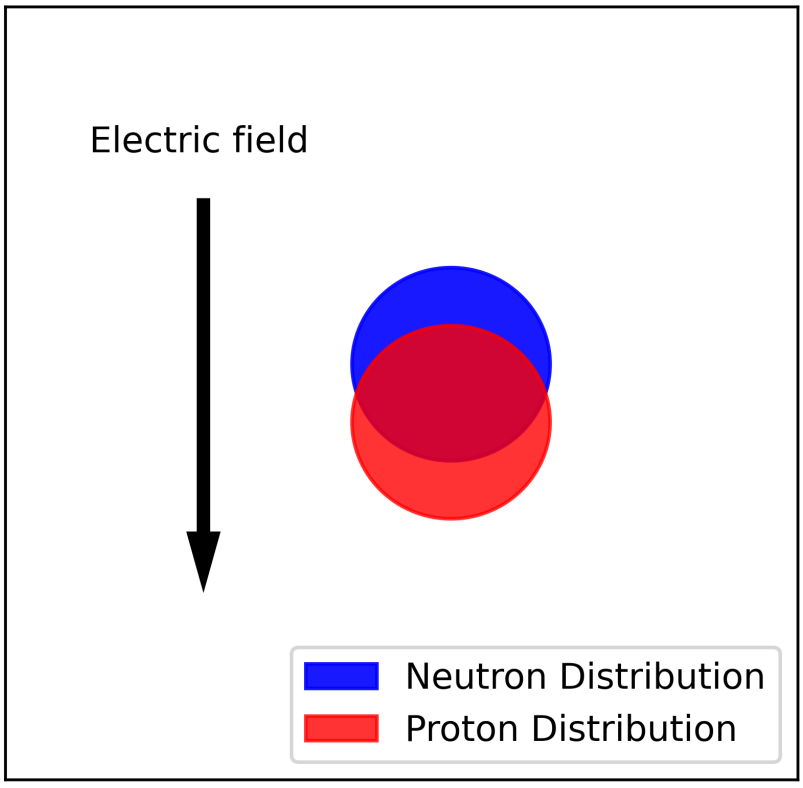

Figure 4: Cartoon example demonstrating electric dipole polarizability. The distribution of protons are separated from the distribution of the neutrons in a nucleus, and L acts as a restoring force (spring constant) of the nucleus.

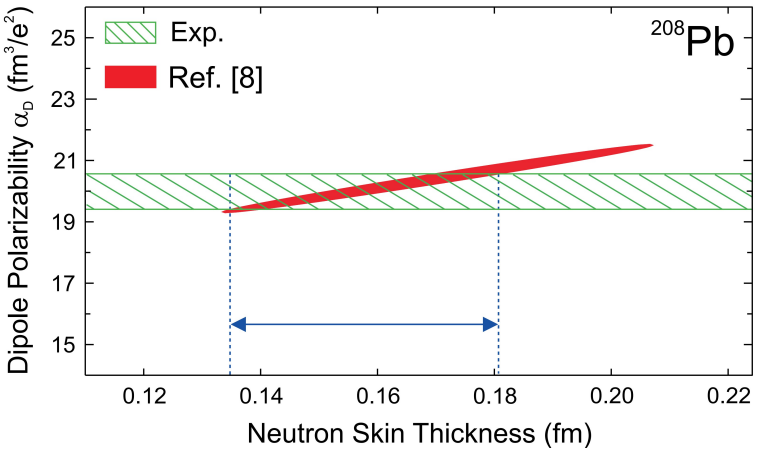

Figure 5: Extraction of the neutron skin in ^{208}Pb based on the correlation between $\Delta R_{\rm np}$ and $\alpha_{\rm D}$ taken from Ref. [31]. The red covariance ellipsoid relating to the neutron skin for ^{208}Pb was taken from Ref. [11] (labeled Ref. [8]).

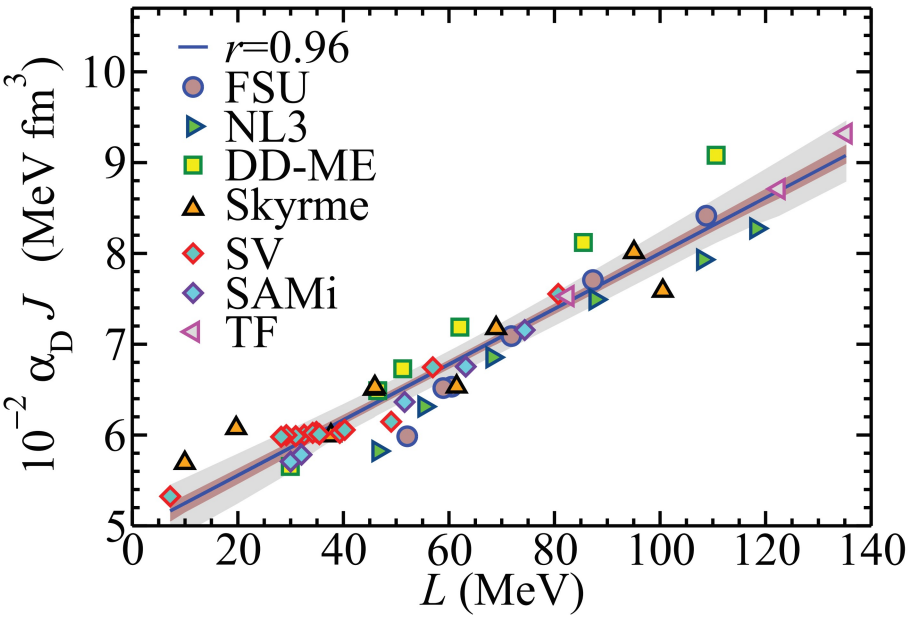

Figure 6: Dipole polarizability in ^{208}Pb times the symmetry energy at saturation as a function of the slope parameter L, resulting in a correlation of $r = 0.96$ taken from Ref. [32].

Isotope	L MeV
^{208}Pb	38 ± 31
^{48}Ca	16 ± 42
^{112}Sn	13 ± 35
^{114}Sn	11 ± 36
^{116}Sn	12 ± 33
^{118}Sn	18 ± 41
^{120}Sn	18 ± 33
^{124}Sn	8 ± 30
^{68}Ni	33 ± 40

Table 1: Constraints on L from $\alpha_{\rm D}$ experiments taken from Ref. [36].

1.2.3 The GW170817 Neutron Star Merger

The GW170817 binary neutron star merger has also placed constraints on L and used tidal deformability as a probe of the neutron star radius [23, 7]. Tidal deformability is a measure of how much a stellar body is deformed by tidal forces, where the body is stretched towards the center of mass of another body due to a difference in strength in a gravitational field. The neutron EOS is particularly relevant to astrophysical observations such as the neutron star merger because it determines the neutron star radius and affects the gravitational-wave emission during the merger, among other characteristics [7]. Results from Ref. [7] display the L dependence of different parameters of the neutron star merger: mass-radius curves from the polytropic approximation, the apsidal constant k_2 as a function of stellar compactness $C = Gm/Rc^2$, and the tidal deformability Λ as a function of L. A common trend to see among these results is that as L gets larger, the radius of the star increases, becomes less compact, and is easier to deform.

Although various analyses on the GW170817 data have placed constraints on the neutron EOS, one in particular introduced a new framework to reduce the theoretical parameter space. The authors show that the gravitational-wave data depends strongly on the slope of the symmetry energy, and by reducing the parameters $(L, K_{\rm sym}, Q_{\rm sym}, ...)$ to just L is sufficient to reproduce a wide range of EOS. It was found that tidal deformability is very sensitive to L and constraints agree with soft EOS, implying a smaller, more compact neutron star. From Ref. [7], $11 \leq L \leq 65\,\text{MeV}$.

1.2.4 Difference in Mirror Pair Charge Radii

Another purely electromagnetic probe [9, 37] uses the difference in mirror pair charge radii $\Delta R_{\rm ch}$ to deduce the neutron skin thickness, whereby constraints on the slope L of the symmetry energy can be placed. The mirror nucleus of an isotope ${}^{A}X$ has the same number of nucleons, but has numbers of neutrons and protons flipped relative to ${}^{A}X$. When assuming perfect charge symmetry, the radius of the distribution of protons in one nucleus is equal to the distribution of neutrons in its mirror (Fig. 7). Therefor by taking the difference between the proton distributions, the neutron skin is extracted as shown in Eq. 10, where A is the total number of nucleons, N is the total number of neutrons, and Z is the total number of protons in the respective nuclei. X and Y designate their respective elements.

$$\Delta R_{\rm ch} = R_{\rm ch}\left({}^{A}_{Z}X_{N}\right) - R_{\rm ch}\left({}^{A}_{N}Y_{Z}\right) = \Delta R_{\rm np} \tag{10}$$

In nature, perfect charge symmetry is disrupted by Coulomb repulsion. However, although the Coulomb interaction pushes out the density of the protons relative to the neutrons (which results in some scatter in

the points on Figs. 8,9), this correlation between $R_{\rm ch}$ and L is still present. By looking at Fig. 8, $\Delta R_{\rm np}$ is affected more by the Coulomb repulsion than $\Delta R_{\rm ch}$ since the theoretical neutron skin results have a wider spread than those using the difference in mirror-pair charge radii.

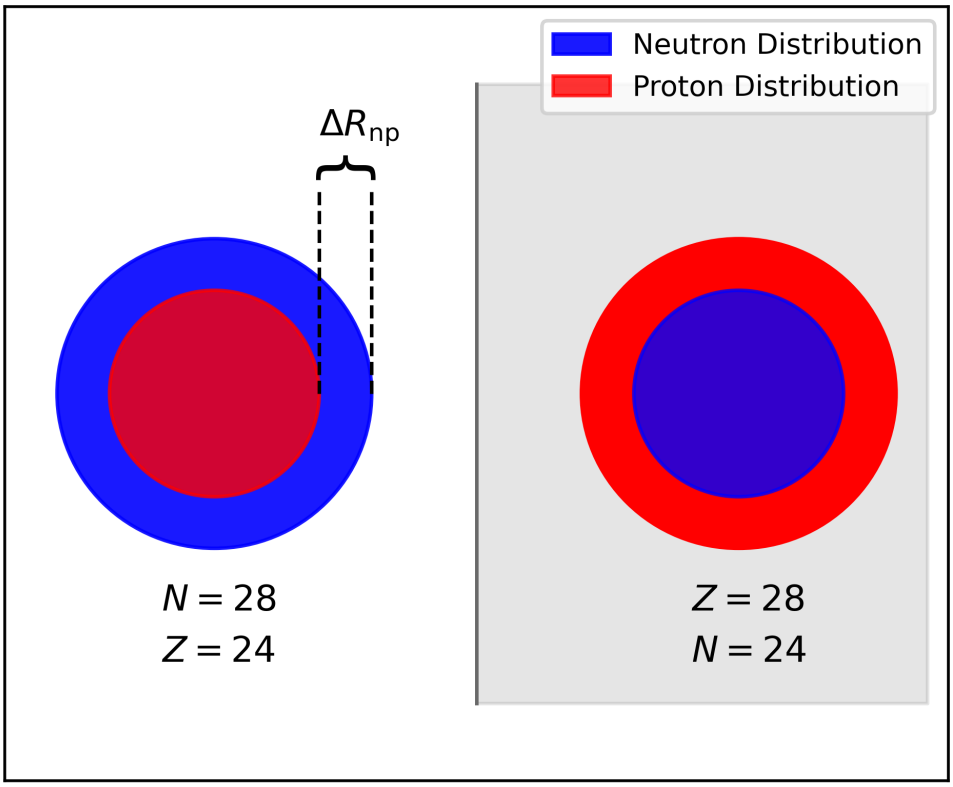

Figure 7: A visual representation of a nucleus (left) and its mirror pair (right) displaying perfect charge symmetry, with neutron and proton distributions shown in blue and red, respectively. The dividing line and grey shading are symbolic of a mirror in order to aid with the concept of mirror pair radii. As one passes from one side of the mirror to the other, the number of protons and neutrons is inverted. Taking the difference between the proton distributions (charge radii) or the mirror pair will result in the neutron skin $\Delta R_{\rm np}$.

In the analysis from Ref. [9], theoretical radii calculated using the Skyrme interaction with different constraints on the neutron skin for ^{208}Pb show a correlation between L and the difference in mirror pair charge radii $\Delta R_{\rm ch}$ for a range of neutron skin thicknesses. Looking at Fig. 8 on the top panel the neutron skin as a function of L is shown. There is a clear correlation where as the neutron skin becomes thicker, the value of L increases. Looking at the bottom panel on the same figure, the same correlation can be seen with the difference in mirror pair charge radii.

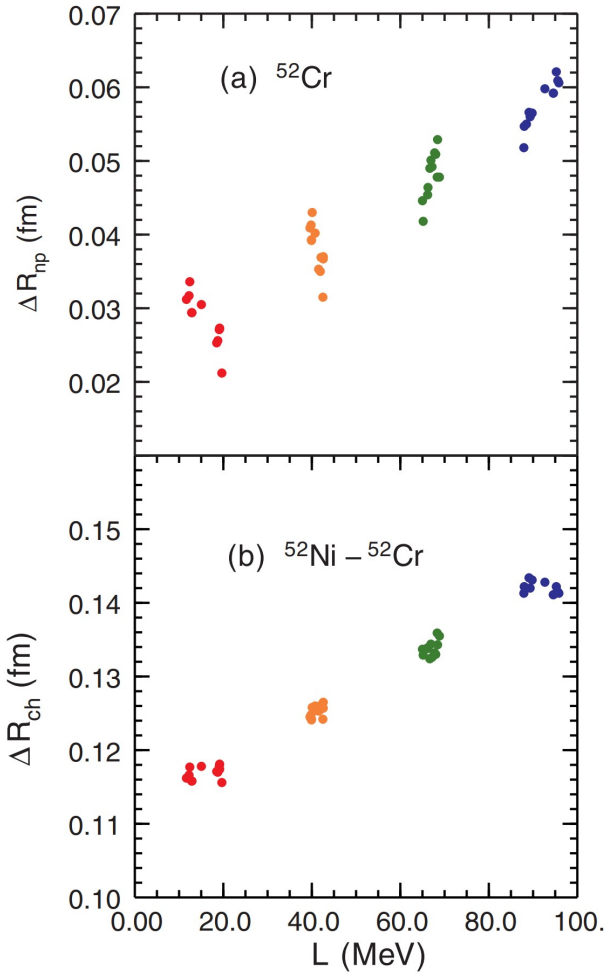

Figure 8: Skyrme results from Ref. [9] for the difference in mirror pair charge radii and the neutron skin for the $A = 52$ pair. The colors correspond to constraints placed on the neutron skin (which are based on the neutron skin of ^{208}Pb), with red=0.12 fm, orange=0.16 fm, green=0.20 fm, and blue=0.24 fm.

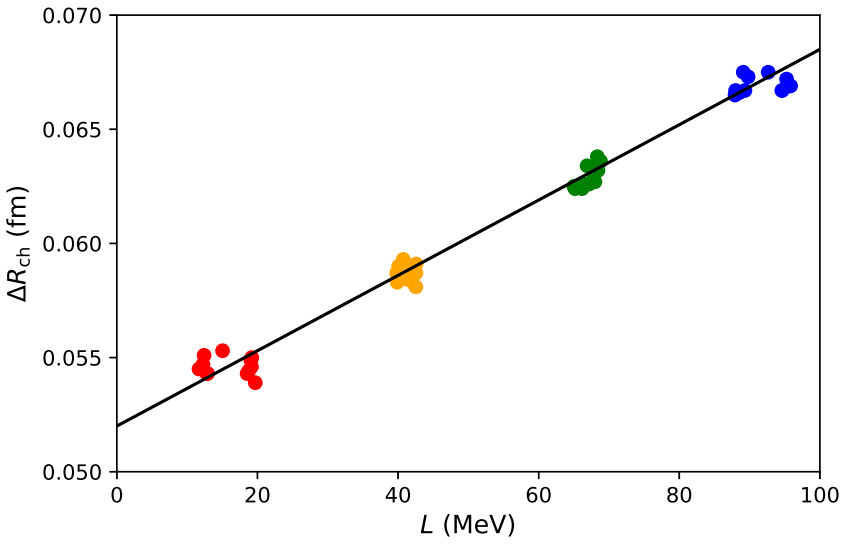

Figure 9: Skyrme results for the difference in mirror pair charge radii for the ^{54}Ni-^{54}Fe pair. The colors correspond to constraints placed on the neutron skin (which are based on the neutron skin of ^{208}Pb), with red=0.12 fm, orange=0.16 fm, green=0.20 fm, and blue=0.24 fm. The black line is to guide the eye for this correlation.

The conclusion of this analysis was that $\Delta R_{\rm ch}$ is correlated with $|N-Z|L$, so as $|N-Z|$ increases, so does the sensitivity to L. This sensitivity corresponds to the slope of the correlation line in Fig. 9 and emphasized in Fig. 10: as its slope gets steeper, the constraints on L become narrower.

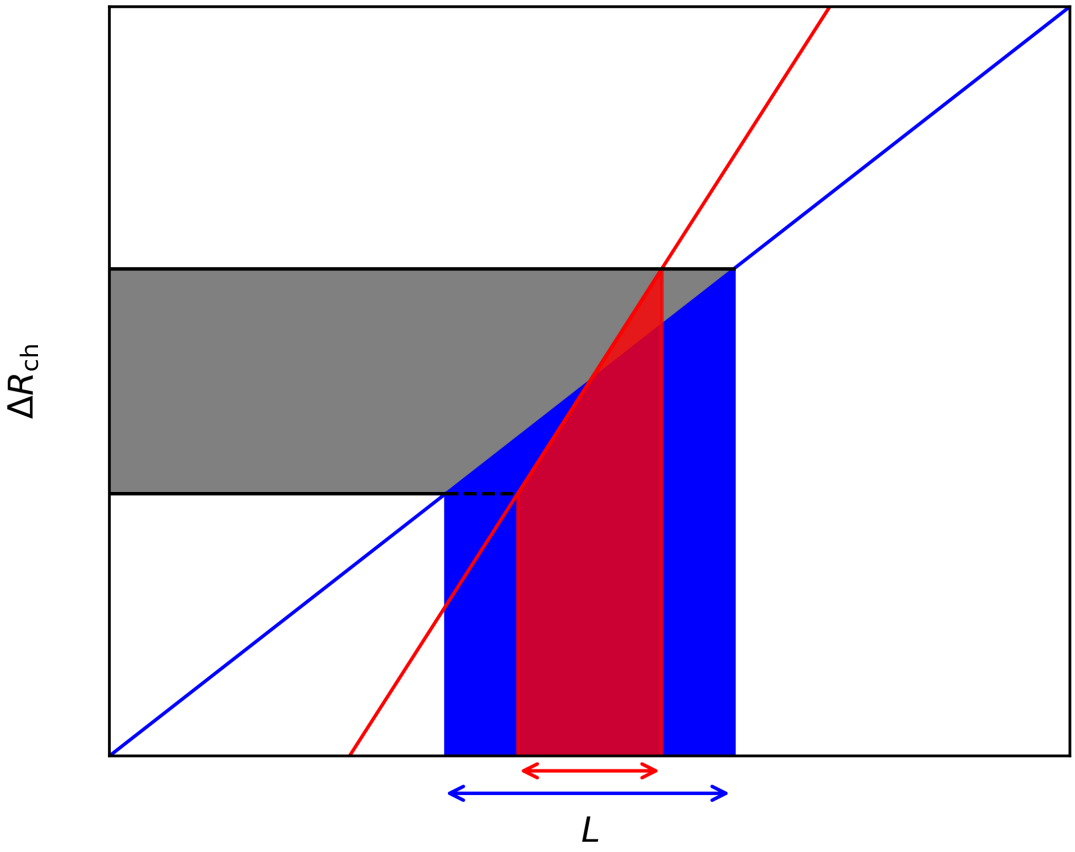

Figure 10: Correlation lines for smaller $N-Z$ (blue) and larger $N-Z$ (red). This plot demonstrates the effect on the constraints on L with the same $\Delta R_{\rm ch}$, with larger $N-Z$ (red) placing tighter constraints and vice-versa. The double sided arrows show the magnitude of the constraint for each slope.

Note that even the model-independent experimental observables *still* rely on theory to place constraints on the L parameter and the neutron EOS. Adding to the systematics of L, especially by using new techniques such as the difference in mirror pair charge radii, enriches this ongoing discussion in the pursuit to reduce the uncertainty in this parameter. The difference in mirror-pair charge radii adds another observable to contribute to the systematics of L.

1.2.5 Other Techniques Used to Determine L

Although electromagnetic experiments are the primary focus in this thesis, there are various other techniques and analyses that have placed constraints on the symmetry energy. A compilation can be found in Refs. [38,

39] and Fig. 11 shows their results plotted side-by-side. It is interesting to note that an average $L \approx 59\,\mathrm{MeV}$ [38] was obtained, which leans towards a soft neutron equation of state. A recent analysis from this year extracts an $L = 54 \pm 6\,\mathrm{MeV}$ from a combined result of different observables [40]. The authors point out that most experimental observables actually probe the symmetry energy at different densities far from ρ_0, making the extracted values for L imprecise. By focusing on the densities those observables actually probe, a more detailed picture of the density dependence of the symmetry energy was obtained from $0.25\rho_0$ to $2.0\rho_0$. From this range they were able to extrapolate values at ρ_0.

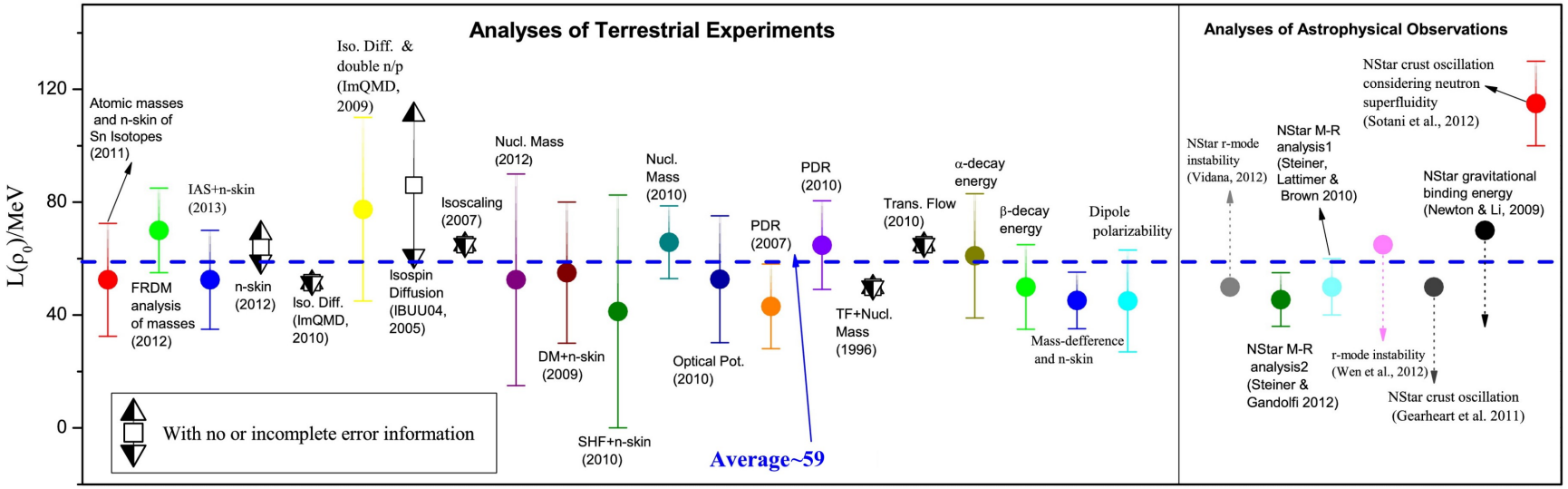

Figure 11: Constraints on L from terrestrial and astrophysical analyses taken from Ref. [38].

1.3 Systematics of Nuclear Charge Radii

The CLS technique measures the differential mean-squared (ms) charge radius, allowing for the extraction of the root-mean-squared (rms) charge radius. The rms charge radius is expressed as

$$\langle r^2 \rangle = \frac{1}{Ze} \int r^2 \rho(r) d\tau \tag{11}$$

The density distributions of ^{54}Ni were calculated using density functional theory (DFT) and the Skyrme interaction (Sec. 5.1), shown in Fig. 12 for both neutron and proton densities, and the rms (charge and matter) radii were obtained. Notice how the density of the nucleus does not surpass a density of $\rho = \rho_0$, where $\rho_0 = 0.16\,\text{nucleons/fm}^3$. This is due to the nuclear saturation density at $\rho = \rho_0$.

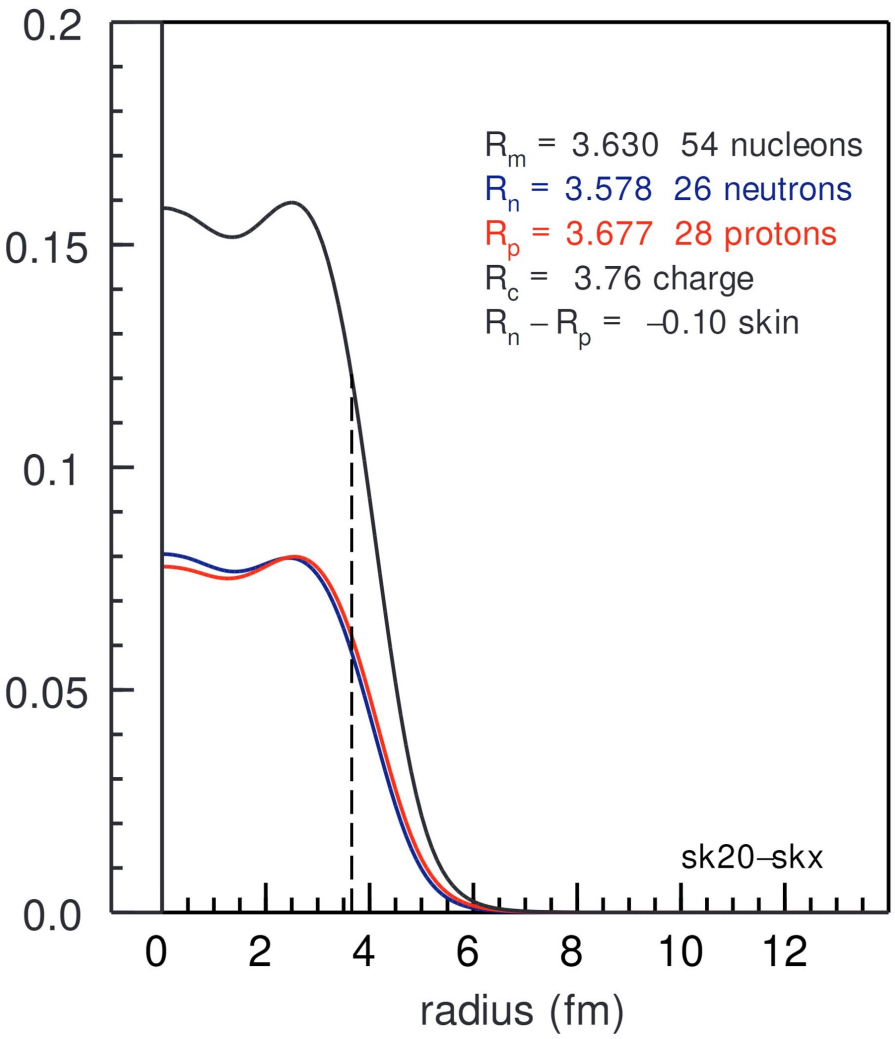

Figure 12: Nuclear densities for ^{54}Ni calculated using Skyrme via NuShellX program [41]. R_m is the matter radius, R_n is the radius of the distribution of neutrons, R_p is the radius of the distribution of protons, R_c is the charge radius, and $R_\mathrm{n} - R_\mathrm{p}$ is the neutron skin. The laser is only sensitive to the outside of the nuclear density before saturation (ρ_0). On the plot this would be the area under the curve after the dashed vertical line, which indicates the rms radius.

While a large portion of the nuclear chart has been studied using laser spectroscopy, there are still many areas left to explore. In Fig. 13 isotopes probed with laser spectroscopy are shown in red, stable isotopes are shown in black, and unexplored regions are shown in grey. From the chart it is clear that while spectroscopic studies span its entire length, there are gaps for isotopes in certain mass regions all throughout the chart of the nuclides. Three examples of uncharted and interesting nuclear phenomena able to be studied with laser spectroscopy are described in Sec. K.2. This effort to obtain vast amounts of systematics of charge radii is motivated by its considerable importance to nuclear physics, detailed in the rest of this section.

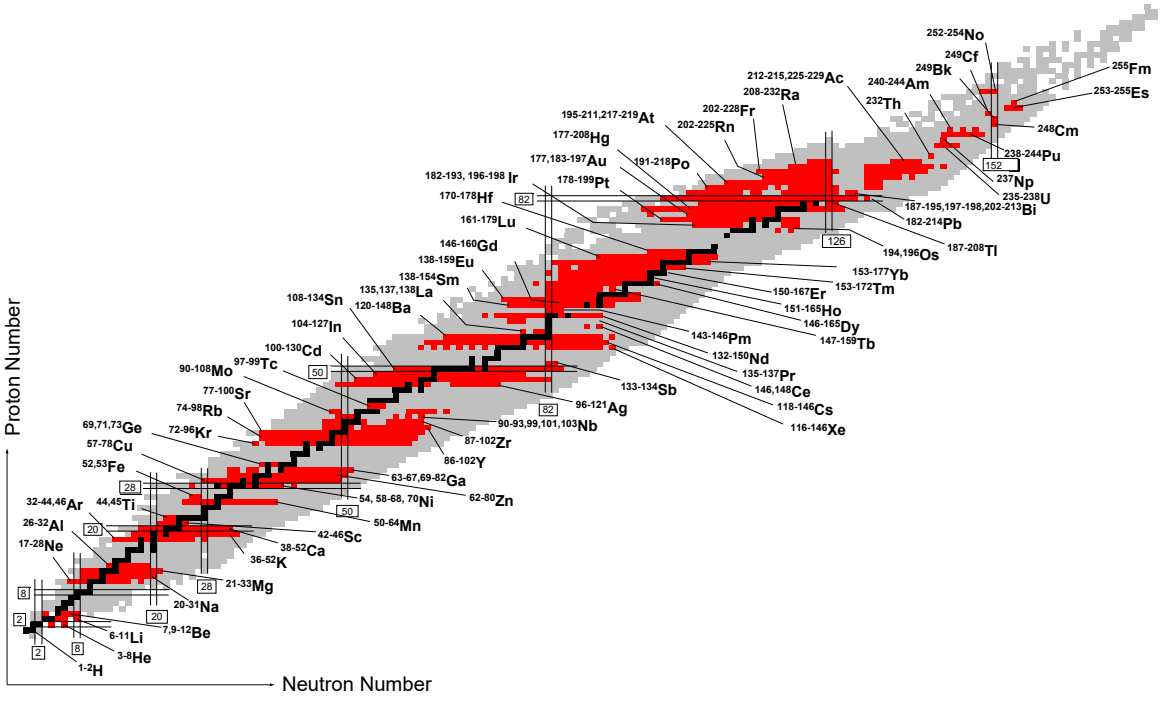

Figure 13: Chart of the nuclides from Ref. [42], where red shows all that have been studied using laser spectroscopy. Grey areas have yet to be studied, and black are the stable isotopes.

The nuclear charge radius is one of the most fundamental properties of nucleus which serves as an essential aid to theoretical nuclear models [43]. Systematic measurements of charge radii for isotopic chains display a characteristic kink structure at all neutron and proton shell closures (except at the neutron number $N = 20$ [44]), an effect aggrandized in doubly magic nuclei. Due to the spherical nature of magic nuclei at these proton and neutron shell closures, any addition or subtraction of nucleons naively results in a deformation of the nucleus, causing the root-mean-squared (rms) charge radius to increase and resulting in a kink structure when plotted against the neutron number seen in Fig. 14. Systematic measurements for the extraction of charge radii have been performed on many isotonic and isotopic chains around the 'traditional' magic numbers (8, 20, 28, 50, and 126) to characterize their structural evolution, including the appearance of non-traditional magic numbers at extreme ratios between protons and neutrons and in the region of light nuclei [45]. The evolution of shell structure has been studied extensively [46], however, the origin of the kink is still under debate [47, 48, 49, 50, 51].

The systematics of charge radii from Ca and Ni are shown in Fig. 14. Apart from the kink structure with minima at neutron shell closures, odd-even staggering can be seen throughout the chains and is pronounced in Ca between the $N = 20$ and $N = 28$ shell closures. This odd-event staggering aspect of charge radii chains results from binding energies of nucleonic pairs as the shells are filled [52] and is well reproduced using the Fayans model [53]. The mean-squared charge radius of an odd-N nucleus is usually smaller than for its even-N neighbors. The staggering effect is expressed by

$$\gamma_A = \frac{2\Delta\langle r^2\rangle_{A-1,A}}{\Delta\langle r^2\rangle_{A-1,A+1}} \tag{12}$$

where $\Delta\langle r^2\rangle_{A-1,A} = \langle r^2\rangle_A - \langle r^2\rangle_{A-1}$ with A being the atomic number of an odd-N nucleus [54]. For typical odd-even staggering, $\gamma_A < 1$.

Nuclei with extreme proton to neutron ratios may become increasingly weakly bound, as with the neutron-deficient Ca isotopes in Fig. 14. Along each chain of charge radii, the ratio between protons and neutrons is varied, which influences the binding energy of the nucleus. Nuclear binding energy is defined as the energy required to break up a given nucleus into its constituent parts of N and Z [4]. For nuclei with extreme ratios of protons to neutrons (Z/N), limits on configurations of protons or neutrons are defined by the proton and neutron driplines, respectively. At the driplines, the nucleus is no longer bound and the particles move into the continuum. Taking into account the driplines puts a limit to the maximum number of isotopes that can form a systematic chain of charge radii for each element, meaning that only certain isotopes can be used to study specific shell closures. Not only does this weak binding make certain neutron-deficient isotopes difficult to produce and study at rare isotope facilities due to their short half-lives, but they challenge nuclear

theory's ability to reproduce experimental results. Some theoretical models suffer from continuum effects, yielding unphysical calculations [44]. There are other interesting features in the systematic chains of charge radii: apart from what has already been discussed, the Ca chain, for example, exhibits a sharp increase at $N = 28$, like other elements in Fig. 14, but an extremely weak kink at $N = 20$. The parabolic shape between the two neutron shell closures shows local minima at $N = 20$ and $N = 28$, which is naively expected, with larger radii (deformed) in between. However, when crossing the $N = 20$ shell closure the kink is dissolved, constantly decreasing. More experiments across the $N = 20$ shell closure for these elements will provide a more complete picture as to how the closure evolves with heavier elements (See Appx. K.3 for an update). What's more, the kink structure at $N = 28$ with the Ni chain is similar to that of Ca–an unexpected result considering the 'soft' nature of ^{56}Ni (see Appx. K.1).

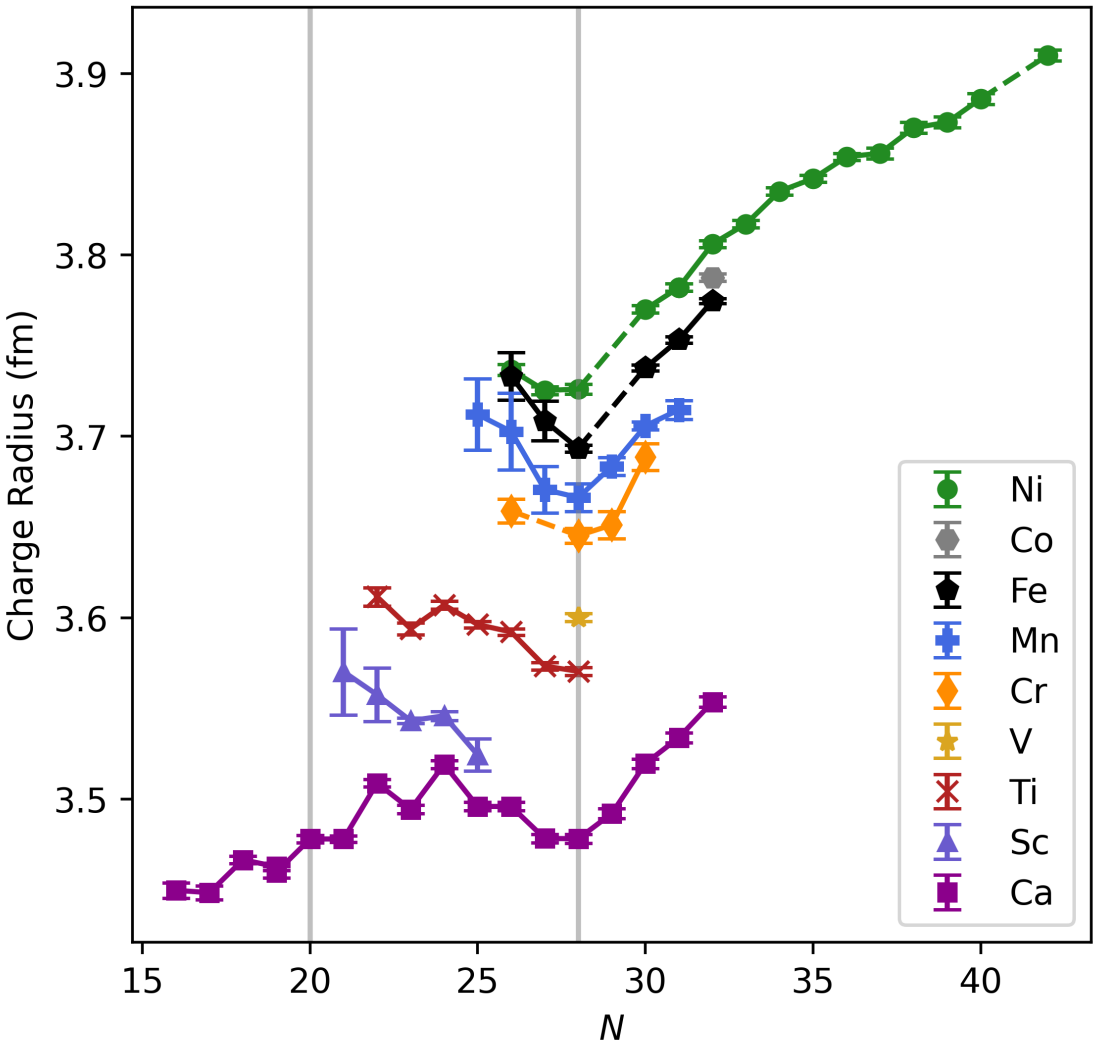

Figure 14: Charge radii from Refs. [55, 56, 57, 45, 58, 59, 44, 60, 51].

1.4 Laser Spectroscopy

1.4.1 Laser Spectroscopy at the BECOLA Facility

Laser spectroscopy is an extremely sensitive method that has been used to study large portions of the chart of the nuclides. A general picture of all the nuclides that have been studied using this method (Fig. 13) can be found in Refs. [61, 62, 63, 42], although this chart is constantly being updated due to the frequency of spectroscopic studies. At BECOLA, laser spectroscopy has been used to study various isotopes [64, 65, 66, 67, 68, 58, 69, 44, 63, 60, 51] across the chart of the nuclides, with many of the radioactive isotopes being neutron-deficient as seen in Fig. 15. Neutron deficient nuclei are not possible to study at every radioactive isotope facility due to their short lifetimes. However, this is overcome at the National Superconducting Cyclotron Laboratory (NSCL) with in flight production and separation providing an unique opportunity to achieve beam rates acceptable for laser spectroscopy. This extremely sensitive

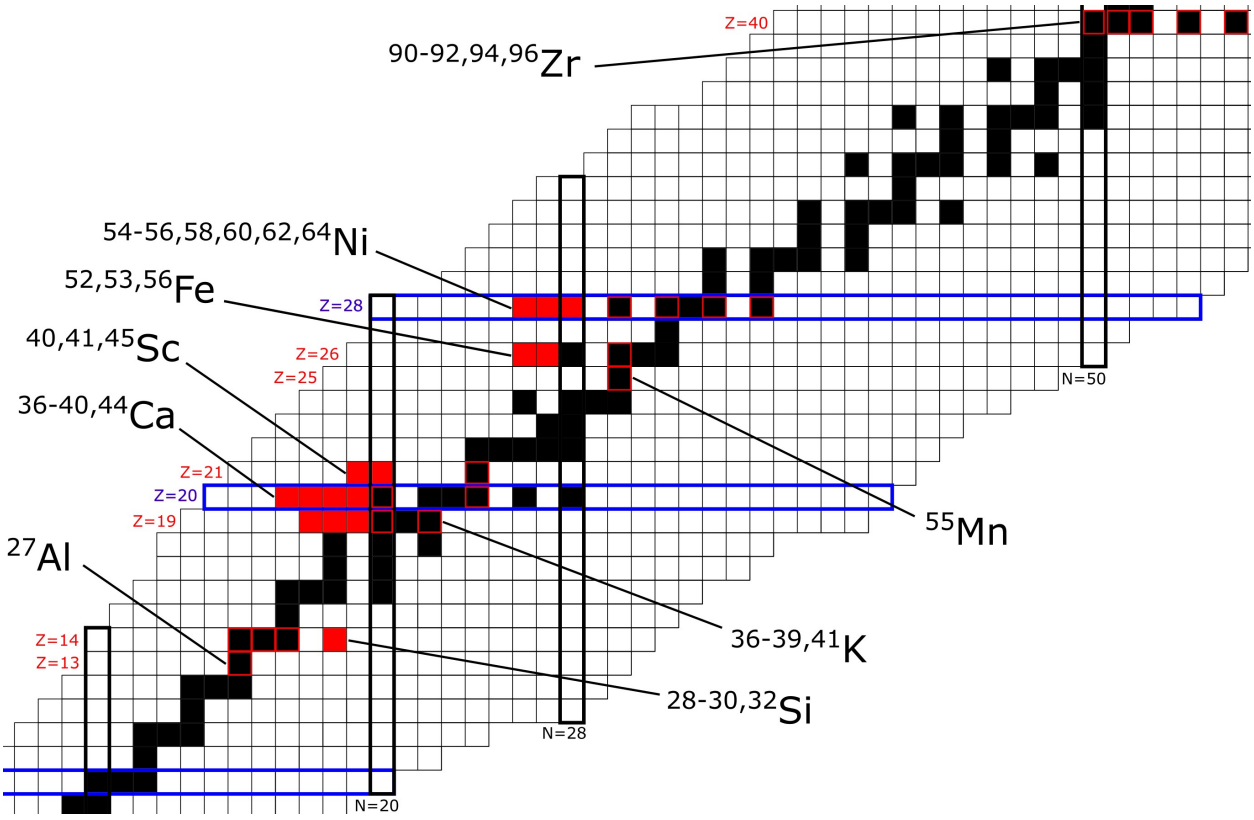

Figure 15: Chart of the nuclides showing the isotopes studied at BECOLA filled or highlighted in red and stable isotopes filled in black.

precision measurement overcomes three major issues [70]:

1. a small amount of material available requires high resolution/high sensitivity

2. short half-lives require online experiments and require lengthy procedures for sample preparations

3. the radioactivity may cause severe background problems

In a typical laser spectroscopy experiment at BECOLA, ions are trapped and released as beam bunches that are collinearly overlapped with a laser beam. These beam bunches pass through a charge exchange cell, which donates electrons to form neutral atoms ready for spectroscopy. Laser resonant fluorescence photons are then captured in the photon detection region with photomultiplier tubes, and the hyperfine spectrum can be analyzed to extract information on nuclear structure. Narrow linewidth continuous-wave lasers, such as those used at BECOLA, are typically restricted to the optical (visible, 400–700 nm) and infrared (700–1000 nm) regime, which can limit the transitions available for spectroscopy since many ion lines lie mostly in the ultraviolet [71]. Therefor, a charge exchange cell filled with an alkali vapor can donate electrons to ions of interest, making spectroscopic transitions accessible in the optical regime.

1.4.2 Bunched Beam Collinear Laser Spectroscopy

Collinear Laser Spectroscopy (CLS) is a high resolution method first proposed in 1976 to produce a resolution of a few MHz at optical frequencies and a sensitivity sufficient for experiments on short-lived isotopes [72]. High resolution in CLS is due to the post acceleration (at BECOLA 30 keV) which is called the velocity bunching phenomenon (kinematical compression). Bunched ion beams are used because ions with a large initial velocity spend less time in the accelerating field and gain less velocity than the initially slower ions, in consequence, lesser velocity spread and higher resolution. Less velocity spread means that probing the fast ion beam with a monochromatic laser beam results in spectra with virtually no Doppler-broadening. This effect of higher kinetic energy ion beam to the velocity spread is shown below in Fig. 16. The Doppler width [70], which ideally would match the laser line-width and the natural line-width, can be expressed through the equation

$$\delta\nu = \nu_0 \frac{\Delta E}{\sqrt{2eUmc^2}} \tag{13}$$

where ν_0 is the laser frequency used to excite the atoms, ΔE is the fluctuation of kinetic energy (velocity spread), eU is the beam energy in eV, m is the mass, and c is the speed of light.

The linewidth obtainable in practice will depend upon the angular divergence $\Delta\theta$ representing the spread of effective acceleration directions about the beam axis (z-axis). The angular divergence of a laser beam is much smaller than typical ion beam divergence, and may be neglected [72]. The distribution of z-components of the accelerated ions leads to a width

$$\Delta\omega_1 \simeq \omega_0 \frac{v_0}{c} \frac{(\Delta\theta)^2}{4R} \tag{14}$$

and the components of the thermal velocity perpendicular to the acceleration directions contribute by

$$\Delta\omega_2 \simeq \omega_0 \frac{v_0}{c} \Delta\theta. \tag{15}$$

where ω_0 is the unshifted frequency, $v_0 \simeq \frac{2kT}{m}^{1/2}$, and $R = \frac{1}{2}(kT/eU)^{1/2}$.

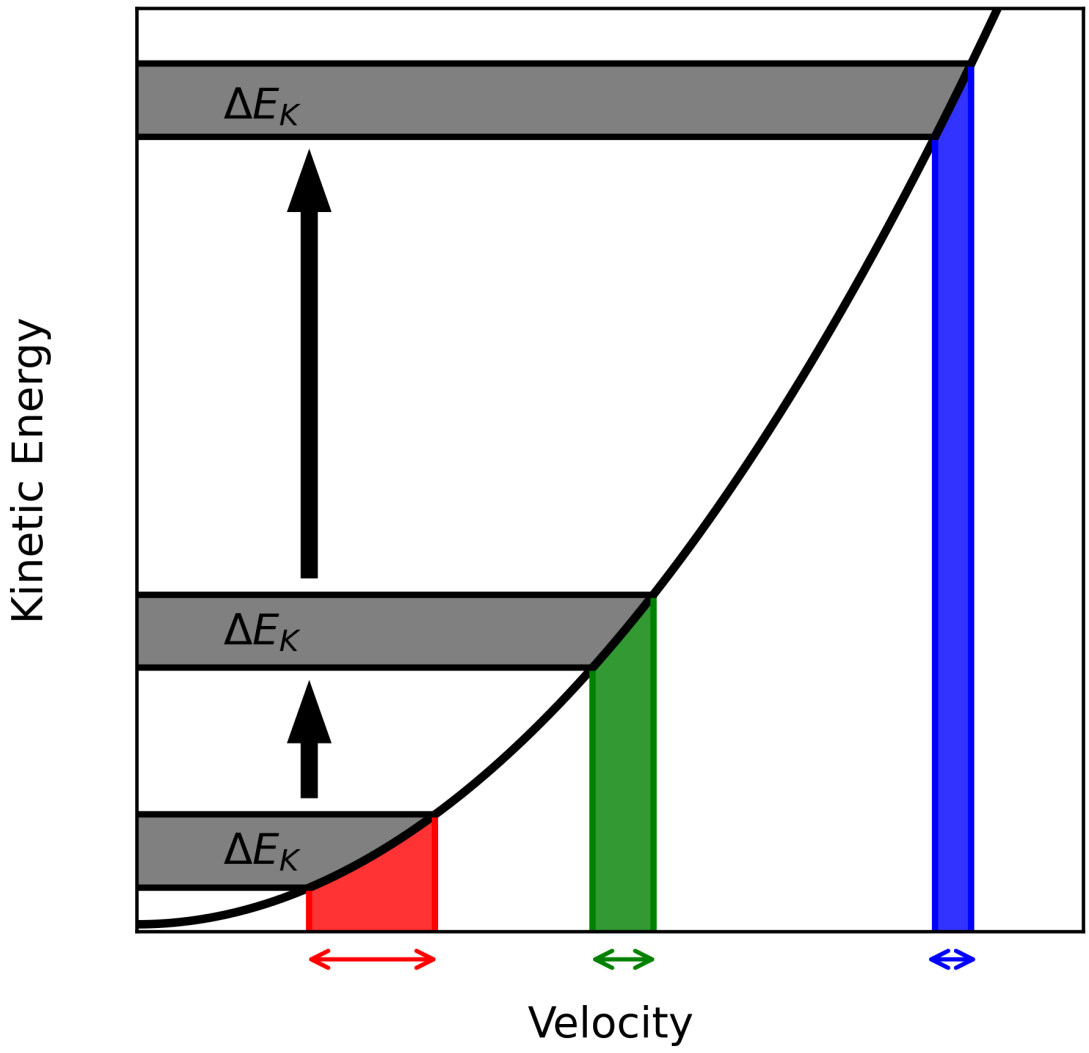

Figure 16: Velocity spread (red, green, and blue shaded regions) for the same kinetic energy difference at different velocities (grey regions). As one moved upwards in kinetic energy, the velocity spread (and thereby Doppler-broadening) becomes smaller for the same difference in kinetic energy ΔE_K (shown by the magnitude of the double sided arrows), resulting in resonance spectra that are nearly free of Doppler-broadening.

Using a bunched beam has another advantage: high sensitivity and increased signal to noise ratio. Stray laser light inside of the beamline can enter photomultiplier tubes, decreasing the signal to noise ratio [73]. By performing a bunched beam coincidence measurement, and selecting the data only when the ion bunch is at the photon detection region, one can cut out unwanted background during the measurement. A typical width for an ion bunch is 1 μs (Fig. 45), which reduces the laser background by a factor of 10^6 for a 1 s bunching cycle without losing the amount of signal observed [74]. Fig. 17 demonstrates how the width of the time cut selection influences the spectrum, where the larger cut results in poor quality. The coincidence measurement is powerful enough to detect very low rates down to tens of ions per second at BECOLA.

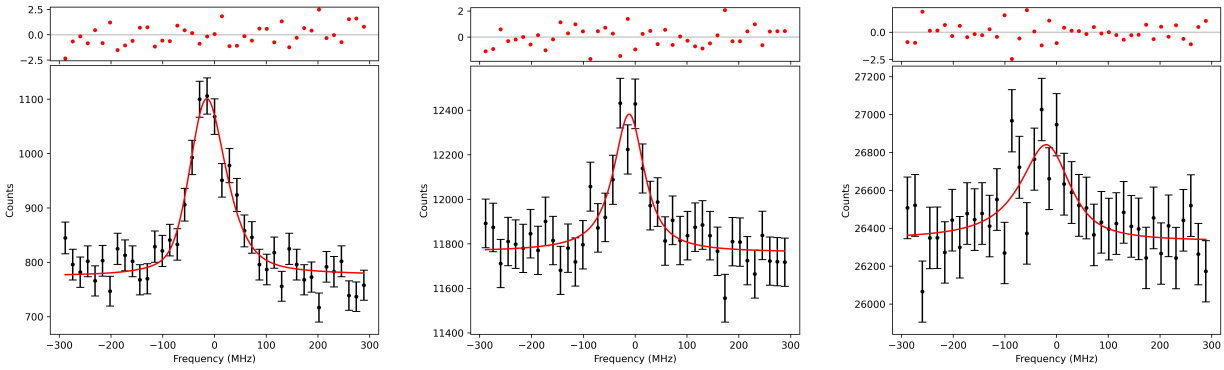

Figure 17: Spectra for stable ^{64}Ni from PMT0, with time cuts of 1 μs (left), 6 μs (middle), and 48 μs (right). The SNR is reduced by approximately 50% with the 6 μs time cut compared to the 1 μs spectrum. The 48 μs time cut is essentially no cut at all considering the total measurement time is 49 μs, showing the signal being overcome by noise and is of poor quality.

1.4.3 Doppler Tuning

By setting the laser to a specific frequency and applying a scanning potential (which changes the speed of the ions), one is able to scan a range that passes over the resonant frequency to effectively scan the laser frequency. The Doppler-shifted frequency ν_x attained via CLS is

$$\nu_x = \nu_0 \gamma \left(1 \pm \beta\right) \tag{16}$$

where β is the ion velocity in units of c, ν_0 is the laser frequency in the laboratory frame, and γ is the Lorentz term which is a function of velocity

$$\gamma = \frac{1}{\sqrt{1-\beta^2}} \tag{17}$$

Notice the '$\pm$' sign in Eq. 16. For the collinear case, where the ions travel in the same direction as the laser photons, $x = \mathrm{c}$ and β is added to 1. In the anti-collinear case, $x = \mathrm{a}$ and β is subtracted. The ion velocity β is shown below where q is the charge of the ion, eU is the electric potential energy in volts, and m is the mass of the ions in units of $\frac{eV}{c^2}$.

$$\beta = \sqrt{1 - \frac{1}{q^2\left(\frac{eU}{m}\right)^2 + 2q\left(\frac{eU}{m}\right) + 1}} \tag{18}$$

Conceptually, ν_x is the laser frequency experienced by the ions/atoms as they are accelerated through the CLS beamline. By applying different potentials the kinetic energy and velocity of the ions are also changed. A common alternative to the Doppler-shifted laser frequency (Eq. 16) may also be expressed as

$$f_{\mathrm{obs}} = f\sqrt{\frac{1-\beta}{1+\beta}} \tag{19}$$

where f is the stable frequency of the laser and f_{obs} is the Doppler-shifted frequency observed by the collinear particles as the move away from the source. Each voltage step changes the value of ν_x, which essentially scans the laser frequency. Detailed in Sec. 3.2, singly-ionized Ni ions were accelerated at a potential of $\sim 29\,850\,\mathrm{V}$ and scanned with a $\sim 40\,\mathrm{V}$ range. Each $1\,\mathrm{V}$ step translates to a frequency shift of approximately $15\,\mathrm{MHz}$ per volt, which is called the differential Doppler-shift and can be calculated using Eq. 20 where ν_0 is the rest-frame frequency.

$$\frac{\partial \nu_{\mathrm{c/a}}}{\partial E_{\mathrm{kin}}} \approx \frac{\nu_0}{\sqrt{2eUmc^2}} \tag{20}$$

A resonance peak, with a typical linewidth of $\sim 100\,\mathrm{MHz}$ [75], can be observed. The width of the peak can be affected by various types of broadening (Doppler, collisional, power, etc.) [76]. At BECOLA, ions are accelerated at 30 keV resulting in high resolution spectra that would otherwise contain too much Doppler-

broadening if measured a lower acceleration voltages and larger velocity spreads.

Because there is a slow drift of the high voltage (which determines the beam energy) and the exact voltage at which beam bunches are released is difficult to measure, the uncertainty in the high voltage has the largest contribution to the resonance centroid measurement. A 1 V deviation of the beam energy can shift the resonance frequency by approximately 15 MHz, a significant change relative to the uncertainty in resonance frequency centroid which, depending on the measurement, is typically in the 1 MHz to 500 kHz range. Therefor it is important to have a way to calibrate the beam energy precisely.

1.4.4 Voltage Calibration via Rest-frame Frequency Determination

Although the impacts from systematic uncertainties largely cancel in isotope shift measurements due to their constant offset, the beam energy uncertainty remains as the largest contribution [77]. By performing a series of collinear/anti-collinear measurements, the relative accuracy of the beam determination can be improved by an order of magnitude to the 10^{-5} level, in contrast to a typical measurement of the acceleration potential or measurement of a well known isotope shift from literature where the accuracy is limited. In CLS measurements, a high voltage is applied to an ion bunch which defines the beam energy. This voltage can be measured using a high voltage divider, where the accuracy depends on the voltage divider ratio (typically 10^{-4} relative accuracy), contact voltages, potential gradients, and field penetrations in the ion source, which results in an uncertainty of approximately $\pm 3 - 5$ eV. The rest-frame frequency is approximately two orders of magnitude more sensitive to an energy change than the isotope shift, and therefor is a better reference for the determination of the beam energy. While many rest-frame frequencies in the literature are known to a few 100 MHz [75], collinear/anti-collinear measurements can reduce that uncertainty significantly [77]. The general equation for the rest-frame frequency is shown in Eq. 21, where ν_0 is the rest-frame frequency, ν_c is the collinear frequency, and ν_a is the anti-collinear frequency.

$$\nu_{\mathrm{c}} \cdot \nu_{\mathrm{a}} = \nu_0^2 \gamma \left(1 + \beta\right) \left(1 - \beta\right) = \nu_0^2 \tag{21}$$

The sensitivity of the transition frequency to the beam energy is given by Eq. 22 where m is the mass, U is the acceleration potential and e is the electric charge.

$$\frac{\partial \nu_{\mathrm{c/a}}}{\partial E_{\mathrm{kin}}} = \frac{2\nu_0}{mc^2} \frac{\nu_{\mathrm{c/a}}^2}{\nu_{\mathrm{c/a}}^2 - \nu_0^2} \approx \frac{\nu_0}{\sqrt{2eUmc^2}} \tag{22}$$

Because a 1 eV change leads to a Doppler shift of the resonance frequency of $\sim 5 - 30$ MHz (which is on the order of the natural linewidth), precise determination of the beam energy is possible. Once the rest-

frame frequency is determined, it can be used to calibrate the beam energy. The rest-frame frequency was determined using data from alternating sets of collinear/anticollinear measurements of reference isotope ^{60}Ni, following the procedure in Sec. 4.4. Alternative methods are found in Appx. H.

2 Hyperfine Interactions

2.1 Atomic Transitions

A transition, in the context of laser spectroscopy, is the ability to excite an electron between two energy levels. In the 1900 Max Planck suggested that each mode of the radiation field can only emit or absorb energy in discrete amounts, building the foundation for quantum mechanics [76]. In a simple two-level system, there are three possibilities: stimulated absorption, stimulated emission, and spontaneous emission (Fig. 18).

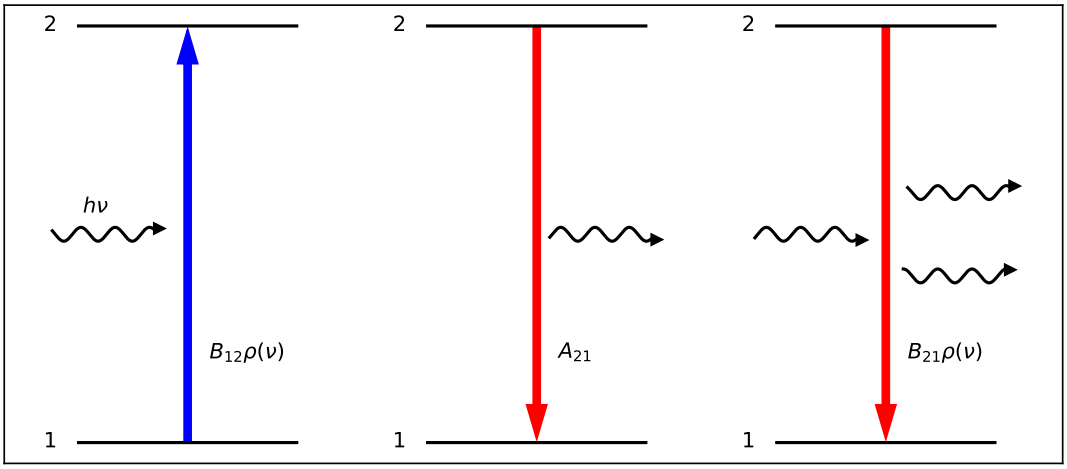

Figure 18: Atomic stimulated absorption (left), spontaneous emission (middle), and stimulated emission(right) of an electron.

The probability the atom or molecule will absorb a photon (dP/dt) is proportional to the number of photons of energy $h\nu$ per unit volume and can be expressed in terms of the spectral energy density $\rho(\nu)$ of the radiation field as

$$\frac{d\mathcal{P}}{dt} = B_{12}\rho(\nu) \tag{23}$$

B_{12} is the einstein coefficient of induced absorption and it depends on the electronic structure of the atom. The probability per second that a photon is spontaneously emitted is

$$\frac{d\mathcal{P}_{21}^{\text{spon}}}{dt} = A_{21} \tag{24}$$

When choosing a transition for spectroscopy, transitions with large A_{21} are preferred because they are easier to measure due to their high probability of excitation and short lifetimes, in some cases allowing an atom to experience multiple excitations in the detection region, improving signal of the measurement. The photoexcitation process is primarily governed by the probability per second for excitation of an atom in a photon flux $N(\nu)\,(\text{cm}^{-2}\text{sec}^{-1}\text{Hz}^{-1})$ is

$$P = \int_0^\infty N(\nu)\sigma(\nu)\,d\nu \tag{25}$$

with the cross section for absorption of a photon of frequency ν

$$\sigma(\nu) = \frac{\lambda^2}{8\pi}\frac{2a+1}{2g+1}\frac{\Gamma\Gamma_\gamma}{(\nu-\nu_0)^2+\frac{\Gamma^2}{4}} \tag{26}$$

where Γ is the sum of the total widths of the upper and lower level, Γ_γ is the partial width for radiative transitions to the lower level, λ is the wavelength at resonance, a and g are the angular momenta of the upper and lower level, respectively, and ν_0 is the resonance frequency. When applying laser excitation to fast ion beams at some angle θ, one has to integrate P over the dwell time of the atoms in the interaction region in order to obtain the excitation probability per beam atom. Additional factors also need to be taken account, such as the Doppler-broadening, the beam divergence, and the frequency change which each atom experiences when passing through laser radiation. These additional factors reduce the excitation probability by factors of the order of $10^2 - 10^4$ depending on each particular experiment [71].

One can use the atomic cross section to measure the strength of an atomic transition. This cross section, as a function of frequency, can be integrated across the entire line width to give the so-called transition

strength

$$T_{\mathrm{S}} \equiv \sigma\left(\omega\right) d\omega = \frac{3\gamma_{\mathrm{rad}}\lambda^2}{4} \tag{27}$$

which is the direct measure of the strength of the transition and is entirely independent of the lineshape. Measuring the integrated absorption cross section across the full linewidth of the atomic transition is one way of determining the radiative decay rate, or Einstein A coefficient, for that transition [78]. The lifetime of a transition due to spontaneous decay is

$$\tau = \frac{1}{A_{21}} \tag{28}$$

The transition used for ^{54}Ni experiment, with $A_{21} = 1.002 \times 10^8$ Hz [79], had a natural linewdith of 100 MHz and a lifetime is 10 ns. When choosing a transition for spectroscopy, it is favorable to choose transitions with larger Einstein coefficients because their lifetimes are shorter and it does not take long to emit photons after excitation. The branching ratio for the upper energy level back down to the ground state was calculated using two databases, NIST [75] and Kurucz [79]. The branching ratio was calculated using

$$r_{\mathrm{b}} = \frac{A_{21}^{\mathrm{m}}}{A_{21}^{\mathrm{m}} + \sum A_{21}^{\mathrm{o}}} \tag{29}$$

where r_{b} is the percentage of photons that decay back to the same ground state, A_{21}^{m} is the einstein coefficient for the main transition of interest, A_{21}^{o} is some other transition that does not decay back down some other state. In the case of the $3d^9 4p\,^3P_2 \rightarrow 3d^9 4s\,^3D_3$ transition in nickel $r_{\mathrm{b}} = 91.3\%$ (Fig. 19).

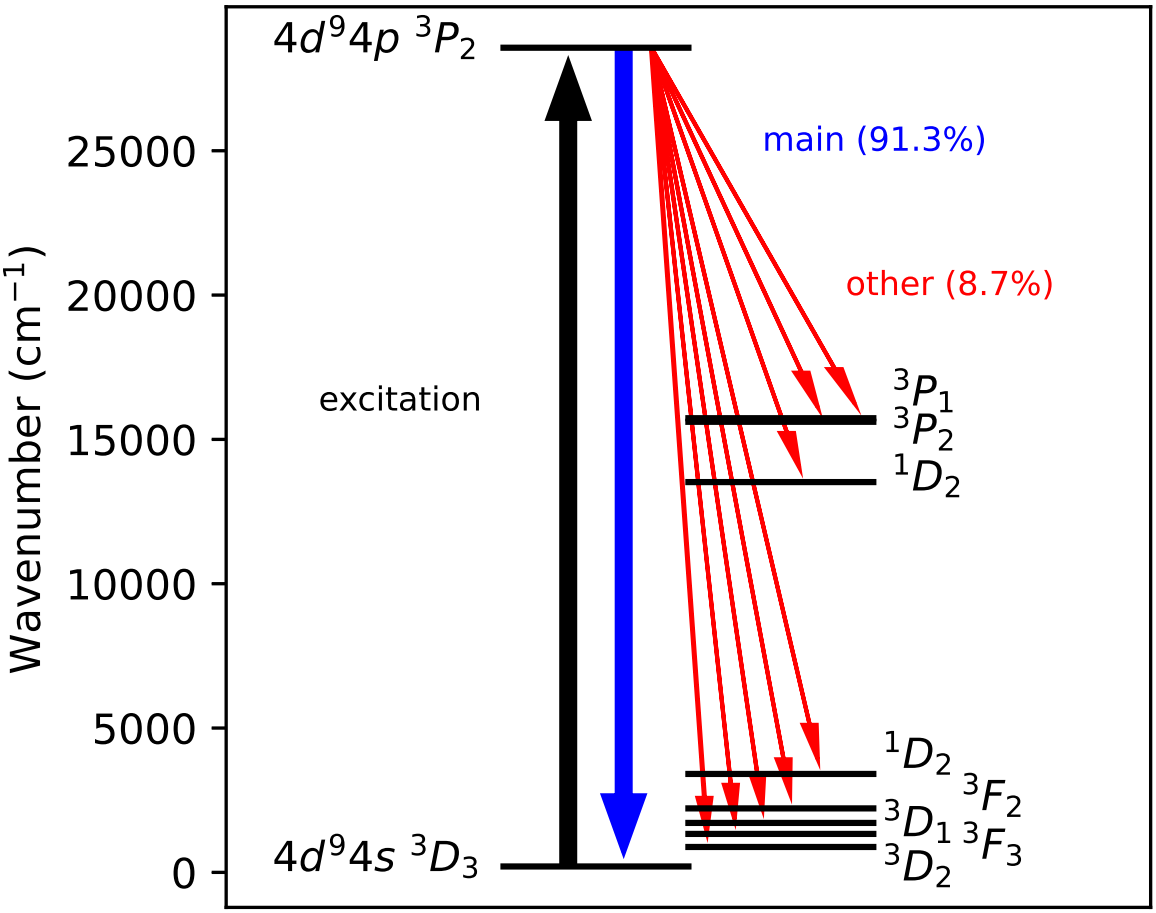

Figure 19: Partial electronic energy levels for the $3d^9 4s\,^3D_3 \rightarrow 3d^9 4p\,^3P_2$ transition in Ni I. The primary decay is at 352.4526 nm (91.3%). Decays to other states (8.7%) are shown in red with the majority at 361.0462 nm (6.57%) for $^3D_2$, and others $< 1\%$. The $^3P_1$ and $^3P_2$ states are very close together which is why they appear as a single thicker black line in the figure.

2.2 Hyperfine Transition

In an atomic transition, the fine structure is described as a coupling of the orbital angular momentum of the electrons L and the spin of the electrons S, which results in the fine structure. When we consider the spin of the nucleus the fine-level further splits resulting in the hyperfine structure [80]. The hyperfine (hf) levels are given by

$$\Delta E = \frac{K}{2} A^{\mathrm{hf}} + \frac{3K(K+1) - 4I(I+1)J(J+1)}{8I(2I-1)J(2J-1)} B^{\mathrm{hf}} \tag{30}$$

where A^{hf} and B^{hf} are the magnetic and quadrupole hf coupling constants, respectively, $K = F\,(F+1) - I\,(I+1) - J\,(J+1)$, I is the nuclear spin, J is the total angular momentum of the atom, and $F = I + J$. The total angular momentum $J = L + S$, where L is the total orbital angular momentum and S is the total spin of the electrons.

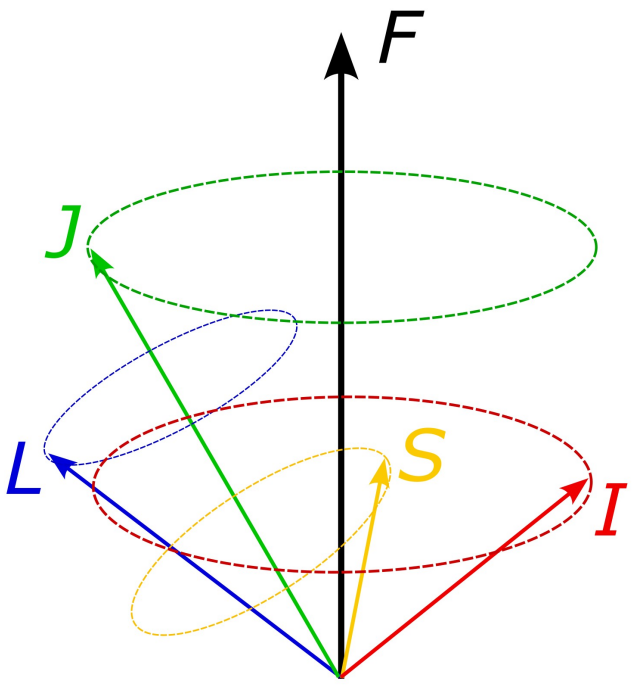

Figure 20: A visualization for the addition of angular momentum vectors to produce the hyperfine structure. The dashed lines indicate the precession of each vector (L, S around J and J, I around F). The addition of the total spin S of the electrons with the total orbital angular momentum L results in the total angular momentum J of the atom (and the fine structure). To get to hyperfine structure, we take into account the spin of the nucleus I and add the resulting vector to J, giving the hyperfine structure F.

The A^{hf} constant is defined as

$$A^{\mathrm{hf}} = \frac{\mu B_0}{IJ} \tag{31}$$

where μ is the magnetic dipole spectroscopic moment and B_0 is the magnetic field generated by the orbital electrons at the nucleus. The B^{hf} constant is defined as

$$B^{\mathrm{hf}} = eQV_{zz} \tag{32}$$

where Q is the spectroscopic quadrupole moment of the nucleus, e is the elementary charge and V_{zz} is the electric-field gradient produced at the nucleus by the orbital electrons. Because $I = 0$ for even nickel isotopes, only one resonance peak is observed and both A^{hf} and B^{hf} are equal to 0. For completeness, a sample hyperfine splitting tree for a nonzero nucleus can be found in Appx. E.2.

The relative linestrength factors for hyperfine transitions can be characterized using dipole matrix elements [81]. The dipole matrix element for a transition between ground (g) and exited (e) states is

$$\langle F_{\mathrm{g}}, m_{F_{\mathrm{g}}} | er_q | F_{\mathrm{e}}, m_{F_{\mathrm{e}}} \rangle. \tag{33}$$

This matrix element can be calculated by factoring out the angular dependence and writing the matrix element as a product of Wigner $3-j$ (parentheses) and $6-j$ (curly braces) symbols and a reduced matrix element (Eq. 34). F, I, J, L, S, and m_F are the angular momentum quantum numbers, and q is the integer change in m_F during the transition and takes the values $q = (-1, 0, 1)$.

$$\begin{aligned}\langle F_{\mathrm{g}}, m_{F_{\mathrm{g}}} | er_q | F_{\mathrm{e}}, m_{F_{\mathrm{e}}} \rangle = (-1)^{2F_{\mathrm{e}}+I+J_{\mathrm{g}}+J_{\mathrm{e}}+L_{\mathrm{g}}+S+m_{F_{\mathrm{g}}}+1} \langle L_{\mathrm{g}} || er || L_{\mathrm{e}} \rangle \\ \times \sqrt{(2F_{\mathrm{g}}+1)(2F_{\mathrm{e}}+1)(2J_{\mathrm{g}}+1)(2J_{\mathrm{e}}+1)(2L_{\mathrm{g}}+1)} \\ \times \begin{pmatrix} F_{\mathrm{e}} & 1 & F_{\mathrm{g}} \\ m_{F_{\mathrm{e}}} & -q & -m_{F_{\mathrm{e}}} \end{pmatrix} \begin{Bmatrix} J_{\mathrm{g}} & J_{\mathrm{e}} & 1 \\ F_{\mathrm{e}} & F_{\mathrm{g}} & I \end{Bmatrix} \begin{Bmatrix} L_{\mathrm{g}} & L_{\mathrm{e}} & 1 \\ J_{\mathrm{e}} & J_{\mathrm{g}} & S \end{Bmatrix}\end{aligned} \tag{34}$$

The $3-j$ symbol is non-zero for $m_{F_{\mathrm{e}}} = m_{F_{\mathrm{g}}} + q$ according to the normal definition of q. $\langle L_{\mathrm{g}} || er || L_{\mathrm{e}} \rangle$ is the reduced matrix element, and can be expressed in terms of wavelength of the transition and the decay rate of the excited state. By calculating the Wigner coefficients and prefactors, Eq. 34 reduces to

$$\langle F_{\mathrm{g}}, m_{F_{\mathrm{g}}} | er_q | F_{\mathrm{e}}, m_{F_{\mathrm{e}}} \rangle = c_{m_F} \langle L_{\mathrm{g}} || er || L_{\mathrm{e}} \rangle \equiv c_{m_F} d \tag{35}$$

where c_{m_F} is a coefficient that determines the transition strength and is dependent on the initial and final

states of the particular transition. The strength of the transition is proportional to the square of the transition matrix element (Eq. 36).

$$T_{\text{strength}} = c_{m_F}^2 d^2 \tag{36}$$

A comprehensive review of transition strengths, A-factors, and absorption cross sections can be found in Ref. [82].

2.3 Isotope Shift in the Hyperfine Structure

Hyperfine spectra can have different centroid values depending on the isotope being measured. The isotope shift (Fig. 21) is the difference in the centroid frequencies of hyperfine spectra between two isotopes. It is a phenomenon that presents itself due to two effects: the displaced center of gravity and change in nuclear motion due to different numbers of neutrons (mass shift, K) and the different finite size of the nucleus (field shift, F) [57, 83].

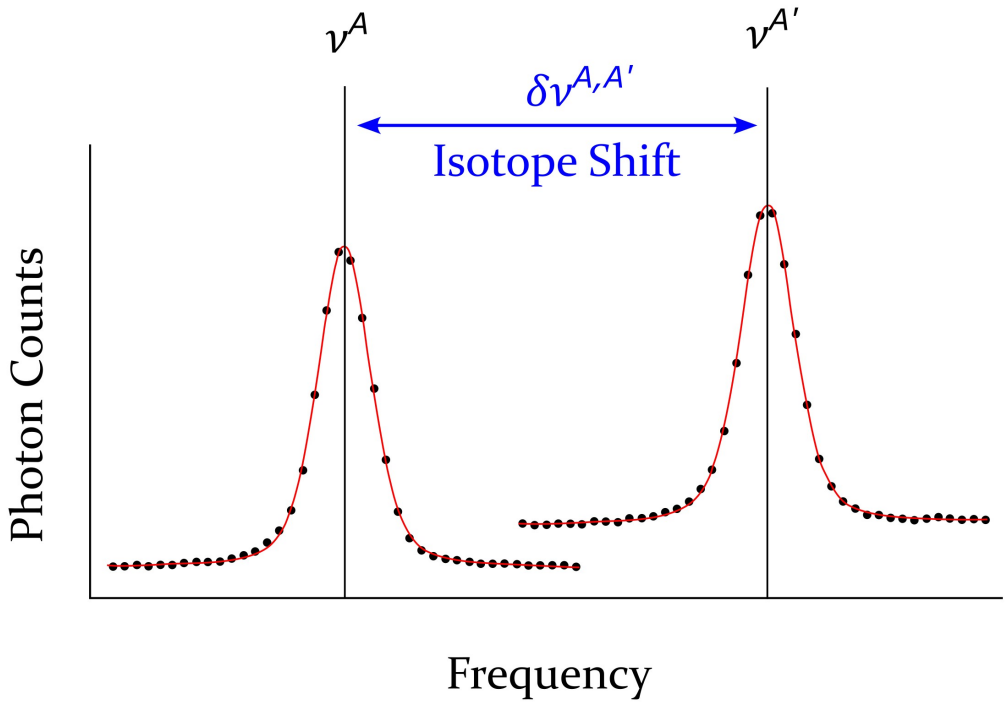

Figure 21: Isotope shift cartoon showing the shift in the center frequency of the hyperfine transition between isotope A and isotope A' of the same element.

The mass shift (Fig. 22) is connected to the change of the kinetic energy of the nuclear motion in the center-of-mass (CM) frame when additional neutrons are added to the nucleus, and it can be visually represented in Fig. 22. Because the total energy of the nuclear motion includes the total electron momenta, if one of the electrons is excited into a different state the nuclear motion must adapt to the new electron momenta and the kinetic energy might change [84]. The isotope shift is caused by the difference of this energy due to the different masses of the two isotopes, and is summarized in Eq. 37, where NMS and SMS stand for the normal mass shift and specific mass shift, respectively.

$$\delta\nu_{\mathrm{MS}}^{AA'} = \frac{M_A - M_{A'}}{M_A M_{A'}} \left(K_{\mathrm{NMS}} + K_{\mathrm{SMS}}\right) \tag{37}$$

The normal mass shift arises from the change in the $\overrightarrow{p}^2$ term in the nuclear motion (Eq. 38), while the specific mass shift is caused by the change of the electron correlation terms $\overrightarrow{p}_i \cdot \overrightarrow{p}_j$. This equation is the total energy of the nuclear motion for a specific electronic state.

$$E_{\mathrm{kin,nuc}} = \frac{\overrightarrow{P}^2_{\mathrm{nuc}}}{2M_{\mathrm{nuc}}} = \frac{\left(\sum \overrightarrow{p}_i\right)^2}{2M_{\mathrm{nuc}}} \left(\sum_i \overrightarrow{p}_i^2 + \sum_{i \neq j} \overrightarrow{p}_i \cdot \overrightarrow{p}_j\right) \tag{38}$$

The normal mass shift can be evaluated by replacing the electron mass m_e with the reduced mass of the system in $K_{\mathrm{NMS}} = m_e \nu$, while the specific mass shift is challenging to calculate since it has no analytical solution and must be calculated numerically by solving electron-correlation integrals [84].

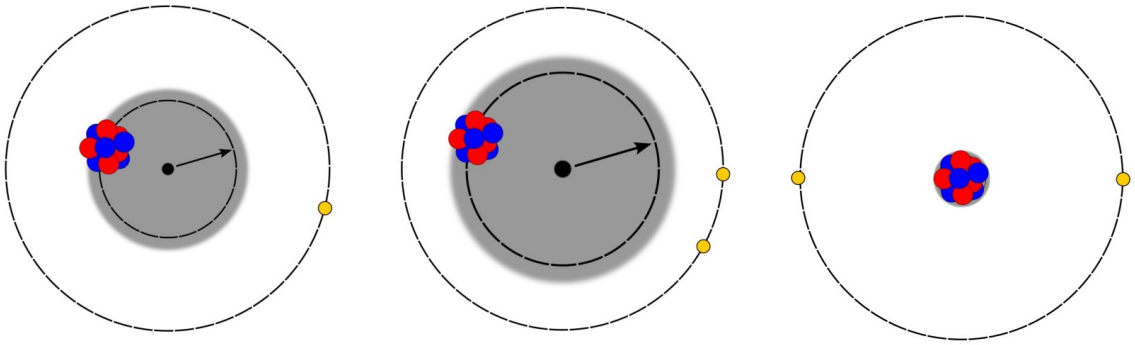

Figure 22: Mass shift principle. The difference in the center of mass to the nucleus is shown by the shaded grey area and the arrow pointing to the precession of the nucleus from the center of mass.

The other component in the isotope shift is related to finite size of the nucleus, where the electronic levels that have wave functions with a finite probability density inside the nuclear volume, $|\psi(0)|^2 \neq 0$, increase in energy since the electron is less strongly bound in this region. In other words, the field shift (Fig. 23) is the change of the electron density at the nucleus [57]. The contribution of the finite nuclear size effect to the total binding energy of an atomic level (Eq. 39) is proportional to the electron density at the nucleus (Fig. 24) and the nuclear mean-square charge radius (Eq. 40), where $\rho_c(r)$ is the nuclear charge density normalized to the charge of the nucleus ($\int \rho_c(r)\, dV = Ze$) [84].

$$E_{\mathrm{FNS}} = \frac{Ze^2}{6\epsilon_0} = \langle r_c^2 \rangle |\psi(0)|^2 \tag{39}$$

$$\langle r_c^2 \rangle = \frac{1}{Ze} \int \rho_c(r)\, r^2\, dV \tag{40}$$

The E_{FNS} is only accessible for hydrogenic atoms (one-electron systems). Laser spectroscopy is used as a probe to determine the energy difference between two atomic states with very high accuracy. The contribution of the FNS effect to the transition frequency (Eq. 41) arises from the difference of the electron density at the nucleus $|\psi(0)|^2$ between the initial (i) and the final (f) state of the transition, with $\left(\Delta|\psi(0)|^2\right)_{i\to f} = |\psi_f(0)|^2 - |\psi_i(0)|^2$.

$$\delta\nu_{\mathrm{FNS}\, i\to f} = \frac{Ze^2}{6h\epsilon_0} \langle r_c^2 \rangle \left(\Delta|\psi(0)|^2\right)_{i\to f} \tag{41}$$

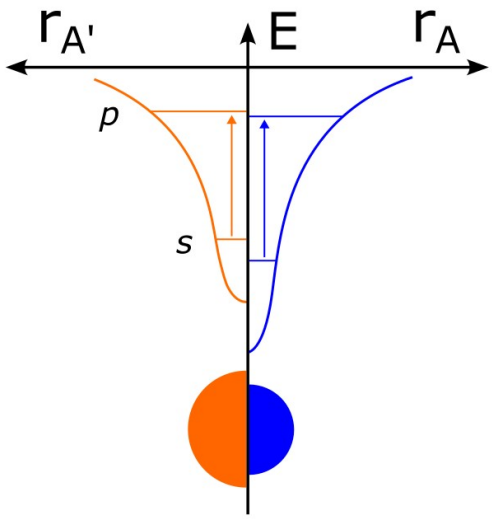

Figure 23: Field shift principle. There is a larger effect for electrons in the s orbital because the probability that they stay more time in the nucleus is higher. The p electrons are also effected by this shift, although the effect is not as strong as for the s orbital electrons.

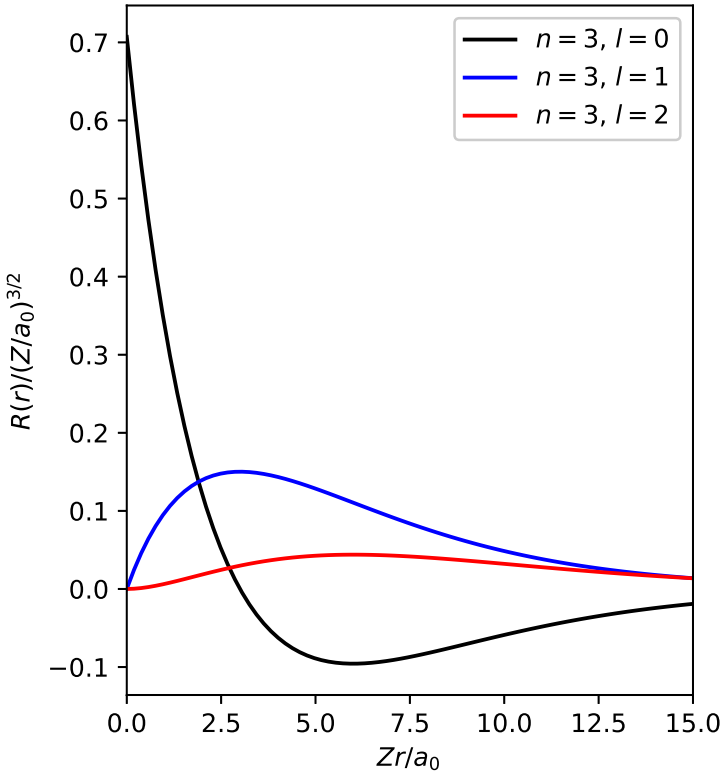

Figure 24: Radial wavefunctions of a hydrogenic atom for $l = 0, 1, 2$. The s-orbitals are affected by the field shift much greater than the p-orbitals because they have increased probability of being inside of the nucleus.

2.4 The King-plot

Both K and F, the atomic factors, can be extracted using a "King-plot" or "King-fit" analysis. Explained in the previous section (Sec. 2.3), the isotope shift (Eq. 42) is the difference in the center frequencies of two hyperfine transitions

$$\delta\nu^{A,A'} = \nu^{A} - \nu^{A'} = K\mu^{A,A'} + F\,\delta\langle r^2\rangle^{A,A'} \tag{42}$$

where A is the isotope of interest, A' is the reference isotope, ν is the resonance frequency, K is the mass shift, F is the field shift, $\delta\langle r^2\rangle^{A,A'}$ is the differential mean squared charge radius, and $\mu^{A,A'}$ is the mass coefficient (Eq. 43), where m_e is the mass of the electron.

$$\mu^{A,A'} = \frac{m_A - m_{A'}}{(m_A + m_e)\,(m_{A'} + m_e)} \tag{43}$$

Equation 42 can also be written

$$\delta\nu^{A,A'} = \nu^{A} - \nu^{A'} = K\mu^{A,A'} + F\Lambda^{A,A'} \tag{44}$$

where $\Lambda^{A,A'}$ is the nuclear parameter

$$\Lambda^{A,A'} = \delta\langle r^2\rangle^{A,A'} + \frac{C_2}{C_1}\delta\langle r^4\rangle^{A,A'} + \frac{C_3}{C_1}\delta\langle r^6\rangle^{A,A'} + \cdots \tag{45}$$

with Seltzer coefficients C and the differential mean-square charge radius $\delta\langle r^2\rangle^{A,A'}$. For low- and medium-mass elements, such as nickel, higher order contributions within the nuclear parameter are small and therefor $\Lambda^{A,A'} \approx \delta\langle r^2\rangle^{A,A'}$. This approximation causes a relative deviation of $< 0.05\%$ when the differential mean-squared charge radius is extracted from the King-plot [83].

The King-plot analysis starts with the rearrangement of the isotope shift equation (Eq. 42), where the the field shift and mass shift constants become the slope and y intercept of a linear function $y = mx + b$.

$$\underbrace{\frac{\delta\nu^{A,A'}}{\mu^{A,A'}}}_{y} = \underbrace{F}_{m}\,\underbrace{\frac{\delta\langle r^2\rangle^{A,A'}}{\mu^{A,A'}}}_{x} + \underbrace{K}_{b} \tag{46}$$

Measured isotope shifts are placed into the y term, while differential mean squared charge radii from literature are placed in the x term. The resulting plot can be fit using a linear fit to extract the slope (F) and the y intercept (K). However, the correlation between the x and y parameters is very high and increases the uncertainty in the atomic factors. To mitigate the uncertainty, an extra term, α, is used to offset and shift

the center of the abscissa to reduce the correlation between K and F using Eq. 47. When the α term is used in this modified isotope shift equation, the mass shift constant loses its physical meaning and is therefore denoted K_α. By reducing the correlation, the uncertainty in the K factor is reduced leading to an overall smaller uncertainty in the charge radius (Eq. 101). The linear regression was performed according to Ref. [85], using least-squares-adjusted points for both x and y values in the regression. The regression procedure is listed in Appx. J.

$$\frac{\delta\nu^{A,A'}}{\mu^{A,A'}} = F\left(\frac{\delta\langle r^2\rangle^{A,A'}}{\mu^{A,A'}} - \alpha\right) + K_\alpha \tag{47}$$

2.5 Evaluation of Model-independent Charge Radii

A combination of muonic X-ray spectroscopy and electron scattering measurements taken from Ref. [57] allows for the extraction of model-independent charge radii. The aim of using this analysis technique is to combine the knowledge about all electromagnetic interactions of electrons or muons with nuclei in order to achieve highly accurate values of nuclear charge radii – ensuring an absolute calibration of the optical results and increasing the reliability of the final results [57]. These four electromagnetic methods are optical and K X-ray isotope shifts, determination of transition energies in muonic atoms, and elastic electron scattering experiments, which are sensitive to different properties of the nuclear ground-state charge distributions. A combination of the data from different experimental methods generally yields more detailed and accurate knowledge of the nuclear radii that is available from any single method alone. A flow chart for the combined analysis is shown in (Fig. **??**).

The first of these experimental techniques, optical spectroscopy, is detailed in Sec. 2.2. The electrons in outer shells of atoms and ions serve as a probe to nuclear structure. The transitions between the energy levels are the observable, and isotope shift measurements are used to characterize small energy shifts for different isotopes of a certain optical transition [57]. K X-ray spectroscopy, named for X-rays emitted when an electron falls from an upper electronic shell to the K_1 shell, has the same origin as with optical transitions (field shift and mass shift). The 'K' used here describes atomic orbitals in IUPAC X-ray notation, with e.g. $\mathrm{K}_1 = 1S_{1/2}$ [86].

In general, spectroscopy using muons enhances spectroscopic effects due to its larger mass and proximity to the nucleus, as seen with studies used to measure the proton rms radius r_p [87, 88, 89]. The energy shift for transition energies is given by

$$\delta E_{if} = 4\pi \int \delta\rho_\mathrm{N}(r) \underbrace{\left[V_\mu^i(r) - V_\mu^f(r)\right]}_{\text{potential difference}} r r^2\, dr \tag{48}$$

where $V_\mu^i(r)$ and $V_\mu^f(r)$ are the potentials generated by the bound muon in the initial and final states, respectively, and $\delta\rho_{\rm N}(r)$ is the variation of the spherical charge distribution of the nucleus. When $\rho_{\rm N}(r)$ is large, the potential difference can be well approximated by an analytical expression by Barrett [90]. By using this expression, the Barrett radial moment may be deduced model-independently from the experimental transition energy E_{if} to give

$$\langle r^k e^{-\alpha r}\rangle = \frac{4\pi}{Ze}\int \rho_{\rm N}(r)\, r^k e^{-\alpha r} r^2\, dr \tag{49}$$

where k and α depend on Z and the specific transition. From this Barrett radial moment a Barrett equivalent radius $R_{k\alpha}$ can be deduced using

$$3\,[R_{k\alpha}]^{-3} = \int_0^{R_{k\alpha}} r^k e^{-\alpha r}\, dr = \langle r^k e^{-\alpha r}\rangle \tag{50}$$

where $R_{k\alpha}$ is the radius of a sphere with constant charge density.

In electron scattering measurements, electrons are scattered off of a target at angle θ to get the cross section of radii. The measured quantity is the differential cross section

$$\frac{d\sigma(E,\theta)}{d\Omega} \tag{51}$$

where E is the energy of the electron traveling at angle θ. In order to extract the model-independent charge radii $\langle r^n\rangle^{\frac{1}{n}}$ from the tabulated values in Fricke, the Barrett equivalent radius is weighted by the ratio of radial moments, V_n, given by electron scattering (Eq. 52). V_n factors are calculated from the charge distribution $\rho_N(r)$ which is extracted from electron scattering measurements and determined from the Fourier-Bessel method [91]. Electron scattering adds the unique possibility to determine the radial dependence of the charge distribution, whereas all other electromagnetic techniques deliver only integral quantities of $\rho_N(r)$ [57]. Charge distribution from electron scattering data has a smaller accuracy of rms radii compared to the accuracy of Barrett radii. However, the ratio (V_n) of the Barrett radius ($R_{k\alpha}$) to the different radial moments ($\langle r^n\rangle^{\frac{1}{n}}$) calculated from elastic electron scattering is almost one order of magnitude more precise than the radii from electron scattering. The V_2 are extracted using Eq. 52, since radial moments such as $R^{\rm e}_{k\alpha}$ and $\langle r^2\rangle_{\rm e}^{1/2}$ can be calculated from $\rho_N(r)$. The uncertainties in V_n have not been published and therefor they are treated without error as explained in Ref. [57].

$$V_2^e = \frac{R^{\rm e}_{k\alpha}}{\langle r^2\rangle_{\rm e}^{1/2}} \tag{52}$$

For the combined analysis, Eq. 53 is used to extract the model-independent charge radii. Notice the subscripts

beneath each variable, which are from different experimental techniques.

$$\langle r^n \rangle_{\circ\mu e}^{-\frac{1}{n}} = \frac{R_{k\alpha}^{\mu}}{V_n^{e}} \tag{53}$$

The experimental uncertainty for the Barrett radius combines the statistical and energy-calibration contributions, while the theoretical Barrett radius uncertainty originates from the calculation of the nuclear polarization correction, which is estimated to be less than 30% of the total nuclear polarization value. Ref. [57] points out that the uncertainty of relative Barrett-radii measurements is smaller and in that case the energy-calibration contribution cancels. The experimental error between neighboring isotopes is determined mainly by statistics and to a minor part by the subtraction of the background from the spectrum. The related differences for Barrett radii $\delta R_{k\alpha}^{\mu}$, show two errors: the first is statistical and the second is due to nuclear polarization uncertainty [92]. This error was estimated to be 10% of the larger one of the nuclear polarization values of the two isotopes. For deformed nuclei, 30% of the larger error of the two isotopes is assumed. Fricke and Heilig list values for the Barrett radii differences Eq. 54 and their corresponding uncertainties $\sigma_{\delta R_{k\alpha}^{AA'}}$ [57].

$$\delta R_{k\alpha}^{AA'} = R_{k\alpha}^{A} - R_{k\alpha}^{A'} \tag{54}$$

Equation 53 is produced by combining the muonic radius with the factor from electron scattering. The electron scattering result connects the slightly different radii from different experimental methods with almost no loss of accuracy. An example calculation to extract the model-independent rms charge radii from Fricke is shown in Tab. 2, where the calculated values are on the right side of the dividing vertical line. Looking at the table the $\langle r^2 \rangle$ is deduced by using Eq. 53, while $\sigma_{\langle r^2 \rangle}$ was obtained by adding $\sigma R_{k\alpha\,\mathrm{exp}}$ and $\sigma R_{k\alpha\,\mathrm{theo}}$ in quadrature (Eq. 99) and dividing by V_2.

Table 2: Example extraction of a Ni model-independent rms charge radius from Ref. [57].

$R_{k\alpha}$ (fm)	$\sigma R_{k\alpha\,\mathrm{exp}}$	$\sigma R_{k\alpha\,\mathrm{theo}}$	V_2	$\langle r^2 \rangle$ (fm)	$\sigma_{\langle r^2 \rangle}$ (fm)
4.8865	0.0007	0.002	1.28394	3.8059	0.0017

With the rms charge radii, the differential ms charge radii was calculated using

$$\begin{aligned}\delta\langle r^2\rangle^{A,A'} &= \langle r^2\rangle^{A} - \langle r^2\rangle^{A'} \\ &= \left(\frac{R^A_{k\alpha}}{V_2^A}\right)^2 - \left(\frac{R^{A'}_{k\alpha}}{V_2^{A'}}\right)^2 \\ &= \underbrace{\left(\frac{R^A_{k\alpha}}{V_2^A} - \frac{R^{A'}_{k\alpha}}{V_2^{A'}}\right)}_{\textbf{term I}} \cdot \underbrace{\left(\frac{R^A_{k\alpha}}{V_2^A} + \frac{R^{A'}_{k\alpha}}{V_2^{A'}}\right)}_{\textbf{term II}}\end{aligned} \tag{55}$$

This equation (Eq. 55) is shown split into two terms because it plays into how the uncertainty is calculated. If **term I** is isolated, it can be approximated by $\delta R^{AA'}_{k\alpha}/V_2$ because V is treated without error and the relative difference between V_2^A and $V_2^{A'}$ is usually below one part per million. This then results in an equation (Eq. 56) for the uncertainty of the differential mean square charge radius where $\sigma_{\delta R^{AA'}_{k\alpha}}$ can be found in Ref. [57]. The uncertainties in **term II** can be neglected since they are multiplied by **term I**, which is much smaller, and leads to a suppression by two order of magnitude.

$$\delta\langle r^2\rangle^{A,A'} \approx \left(\frac{\sigma_{\delta R^{AA'}_{k\alpha}}}{V_2^{A'}}\right) \cdot \left(\frac{R^A_{k\alpha}}{V_2^A} + \frac{R^{A'}_{k\alpha}}{V_2^{A'}}\right) \tag{56}$$

3 Experimental Detail

3.1 Exotic Isotope Beam Production at the NSCL

This experiment took place at the National Superconducting Cyclotron Laboratory (NSCL) [93, 94] at Michigan State University (Fig. 25). The primary nickel beam was produced from an Electron-Cyclotron Resonance (ECR) ion source. A ^{54}Ni ($I^{\pi} = 0^{+}$, $t_{1/2} = 114\,\text{ms}$) [95] beam was produced by projectile fragmentation of a ^{58}Ni primary beam at 160 MeV/nucleon on a 775 mg/cm^2 ^{9}Be target using the coupled cyclotrons. Fragmentation products were filtered using the A1900 fragment separator [96] and thermalized in the gas stopper [97, 98]. Singly-charged ^{54}Ni ions were transported at 30 keV to the BEam COoling and LAser spectroscopy (BECOLA) facility [64, 66]. An overhead view of the gas stopper and the BECOLA facility is shown in Fig. 26. The use of the gas-stopper cell was in order to obtain a good quality beam low-energy precision experiments at BECOLA. Decelerating the beam electrostatically is not practical for two reasons[99]:

1. the voltage necessary to slow the beam down are impractically large
2. the ability to efficiently transport a decelerated beam becomes challenging without a cooling mechanism since the transverse emittance scales reciprocally with beam momentum.

In flight production and separation at the NSCL is advantageous because it allows for the study of isotopes with shorter half lives, as opposed to Isotope Separation On-Line (ISOL) facilities where isotopes take a longer time to diffuse out of a thick target, resulting in isotopic losses. Also, the fragmentation reaction at NSCL is free from chemistry, while, with ISOL, some elements are difficult to extract from the target due to their chemistry. Due to the in-flight advantage, BECOLA can explore the neutron-deficient regions of the chart of the nuclides.

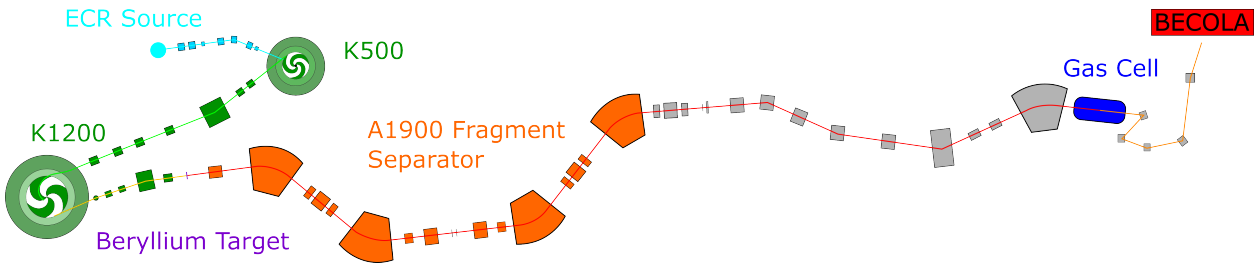

Figure 25: Overview of the coupled cyclotrons and the ion beam path from creation to the BECOLA facility.

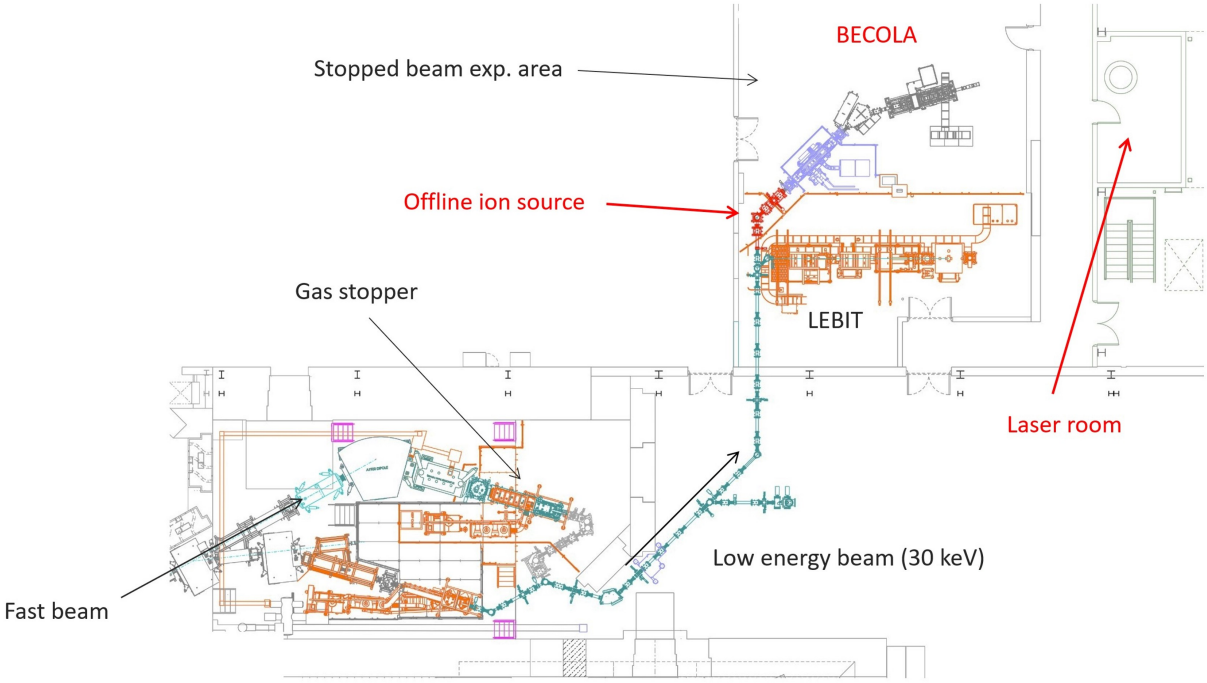

Figure 26: Overhead view of gas stopper area and BECOLA. A fast beam from the coupled cyclotrons is slowed to 30 keV and sent to the BECOLA facility. The cooler buncher and CLS beamline are shown, as well as the laser room where the lasers are maintained. Laser light must be transported safely from the laser room to the beamline for experiments.

The on-line ^{54}Ni experiment was approved for 197 hours with 176 hours of on-target time (Fig. 27). It is of interest to know how many ions are being measured during the experiment. In order to determine the ion counts achieved at BECOLA, the upstream ion beam current directly from the cyclotron (Fig. 27) and at the beginning of the BECOLA facility (Fig. 28) were studied. A Faraday cup reading is not a particle count but an electric current. The charge state of the ^{58}Ni primary beam was 27+ and using the conversion factor $\frac{570\,\text{enA}}{20\,\text{pnA}}$, the cyclotron current can be converted from enA to pnA. At Faraday cup D1173, which is right before entering the BECOLA facility (Fig. 26), β particles from ^{54}Ni were measured in counts/second and corrected in the solid angle of the detector. As shown by Fig. 28, the intensity of the counts at the entrace to the BECOLA facility corresponds to the intensities in the coupled cyclotron beam current. When normalizing the D1173 counts using the values from the coupled cyclotrons, there were 13 ± 3 counts/s per pnA of the primary beam.

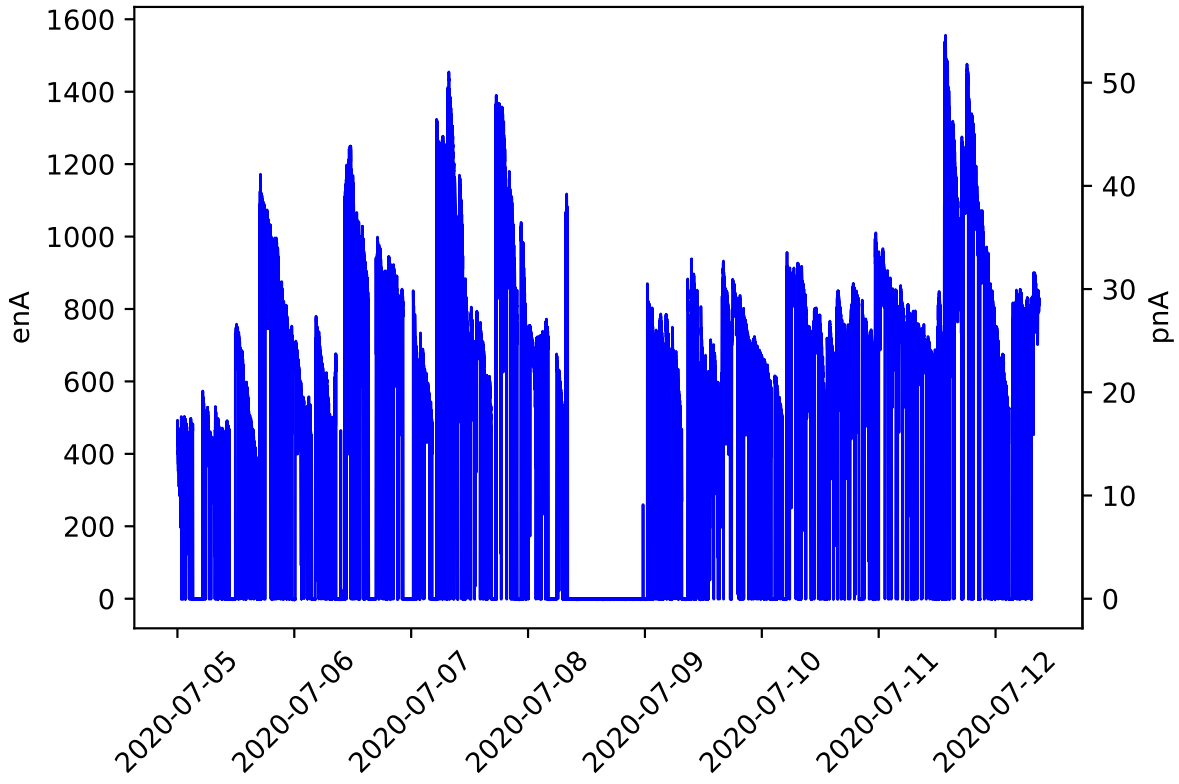

Figure 27: Beam current from the coupled cyclotrons during the entire on-line experiment. The average current during the entire experiment was 573 ± 379 enA (20 ± 13 pnA). Excluding times when the beam current was 0, the average beam current when beam was present was 752 ± 230 enA (26 ± 8 pnA).

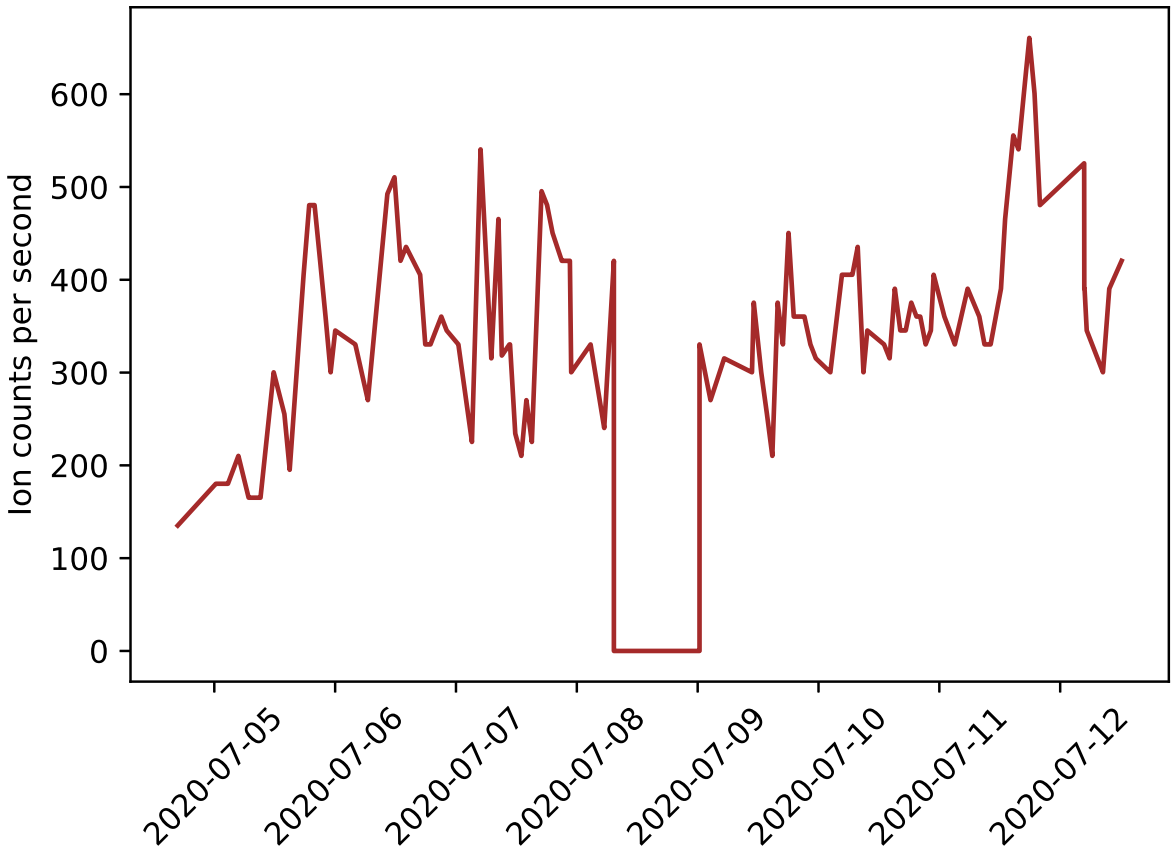

Figure 28: The average counts per second at D1173 were 359 ± 98 counts/second during the experiment

Due to the cross section, lifetime losses in the RFQ cooler buncher, charge exchange efficiency, and population fractionalization of Ni electronic states, the actual number of ^{54}Ni atoms transported to the photon detection region were much lower than that at D1173. These efficiencies are then taken into account to find the total amount of ^{54}Ni atoms that enter the photon detection region for spectroscopy. The number of atoms per second at the photon detection region during the online experiment was

$$N_{\text{ion}} = 359 \times \eta_{\text{lifetime}} \times \eta_{\text{CEC}} \times \eta_{\text{frac}} \approx 13 \text{ atom/s} \tag{57}$$

where the lifetime loss in the cooler buncher is given by $\eta_{\text{lifetime}} = 50\%$, the charge exchange cell efficiency by $\eta_{\text{CEC}} = 50\%$, and the population fraction at the correct electronic state by $\eta_{\text{frac}} = 15\%$ [68]. From the cyclotron to D1173, there were 13 ± 3 cps/pnA.

3.2 Collinear Laser Spectroscopy at BECOLA

At BECOLA (Figs. 29,30), ion beams are trapped and cooled through the RFQ cooler buncher. After the bunched ions cross the 30 degree bend they are collinearly overlapped with laser light. A charge exchange cell neutralized ions to atoms with sodium vapor, and a scanning potential applied to the cell Doppler-shifts the ions over the resonant frequency, effectively scanning over the resonance frequency. Laser-induced fluorescence is then observed at the photon detection region.

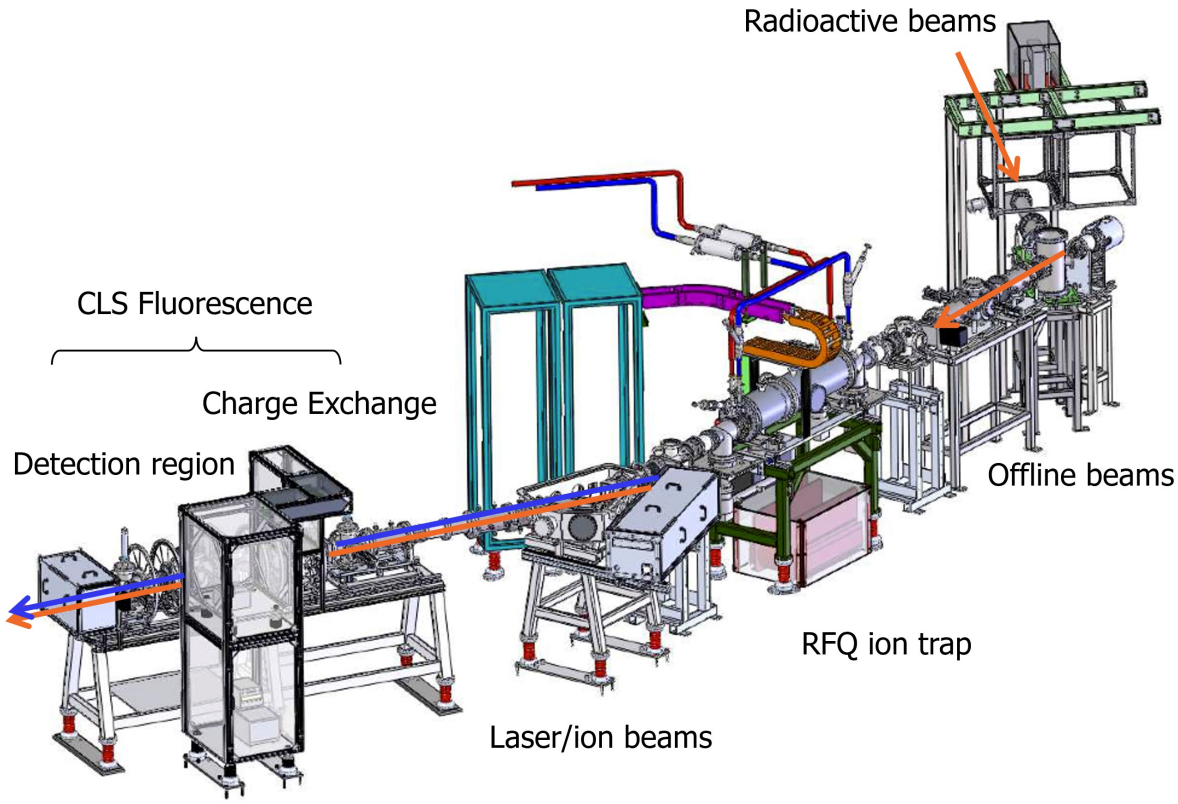

Figure 29: Technical 3D model of the BECOLA facility.

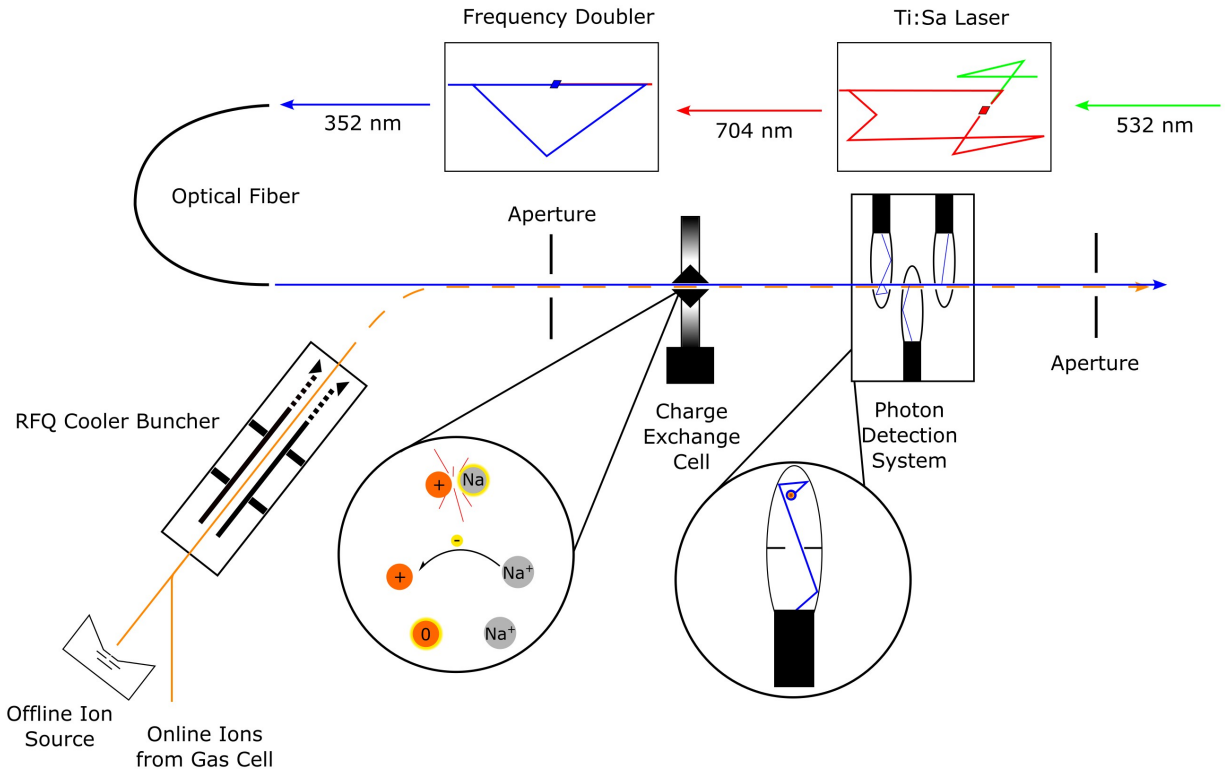

Figure 30: Cartoon diagram of the BECOLA facility and the laser system.

3.2.1 Laser System Overview

A continuous-wave Titanium-sapphire laser (Matisse TS, Sirah Lasertechnik) was pumped by a solid state Nd-YAG laser (Millenia eV, Spectra Physics) to produce a 704 nm Near-Infrared (NIR) laser beam. Frequencies in the NIR regime of the electromagnetic spectrum range from 700 nm–2500 nm. The 704 nm light was directed into a cavity-based frequency doubler (WaveTrain, Spectra Physics) to produce 352 nm light which was transported to the BECOLA beamline via an optical fiber. Spectroscopy was performed using 300 μW of laser power, which was stabilized using a laser power controller (Brock Electro-Optics Corp). The Matisse laser frequency was stabilized by side-of-fringe locking to a reference cavity. Feedback from a wavelength meter (WSU30, HighFinesse) was used to control the length of the cavity for long-term stabilization. This wavelength meter was calibrated every minute using a frequency-stabilized helium-neon laser (SL 03, SIOS Meßtechnik) and was compared to an iodine saturation-absorption spectroscopy setup [100]. A detailed description of the entire system (Fig. 31) can be found in Appx. C.

The light was focused into a polarization maintaining optical fiber using a telescope to increase the transport efficiency through the fiber. The typical transmission frequency through the polarization maintaining fiber was 30%. A BEOC laser power controller (LPC) with a liquid-crystal waveplate was placed before the entrance to the beamline to mitigate power fluctuations caused by the polarization of light through the fiber as well as from the laser itself, and maintain the laser power at 300 μW when taking isotope shift measurements. The use of the laser power controller kept a constant baseline for the hyperfine spectra. A half wave plate was placed before the optical fiber to reduce power oscillations from polarization in the optical fiber. Another telescope was placed after the optical fiber exit to focus the beam at the photon detection region with a 1.2 mm diameter (Fig. 35) and minimize stray scattered light inside of the beamline (Fig. 32). The laser beam path through the beamline was optimized by looking at the photon counts on the photomultiplier tubes, adjusting the vertical and horizontal knobs on the mirrors to minimize background photons. Two irises were inserted at 3 mm inside of the beamline to help align the beam and also to cut down on unwanted background. The use of a CCD camera was critical to alignment to ensure the beam was not walked off during optimization (Fig. 33). A circular beam profile was observed with the CCD camera (Fig. 35).

Typical background rates for the PMTs with the laser at 300 μW are shown in Tab. 3, with $< 45,000$ counts/s being extremely optimized. Using the anticollinear geometry, these photon counts were higher at typically 80,000 counts/s. The origin of this consistently higher background rate with the anticollinear geometry is still unknown. Changes in temperature, vibrations, and other factors that changed the alignment of the mirrors facilitated the need for daily alignment procedures. Due to its tedious nature, the amount of time dedicated to alignment affected the overall photon counts in the background. Apart from the alignment of

the mirrors, the focus of the laser light was systematically changed the background reached a local minimum. Once the minimum was reached, the mirrors would be walked and the focus would be adjusted iteratively sometimes for days at a time. Alignment on power was also performed a as last step. The 3 mm apertures on either side of the beamline were also adjusted as a final alignment.

PMT0	PMT1	PMT2
73 000	82 000	101 000

Table 3: Laser background in counts/s at 300 μW throughout the experiment.

A scanning potential on the charge exchange cell changes the kinetic energy of the ions, which in turn Doppler-shifts the laser frequency. This allows one to precisely set the laser to a specific frequency and perform a voltage scan around resonances. The laser can then be stabilized for long periods of time using an external calibration method such as a HeNe laser and wavemeter. An alternative is to have a stabilized, constant beam energy and scan the frequency of the laser. If the beam energy can be stabilized effectively, then the uncertainty lies in the laser frequency as it is scanned across the resonance. This method presents its own challenges since the laser may mode-hop or the frequency scan speed could be inconsistent since laser cannot be calibrated or stabilized while it is scanning.

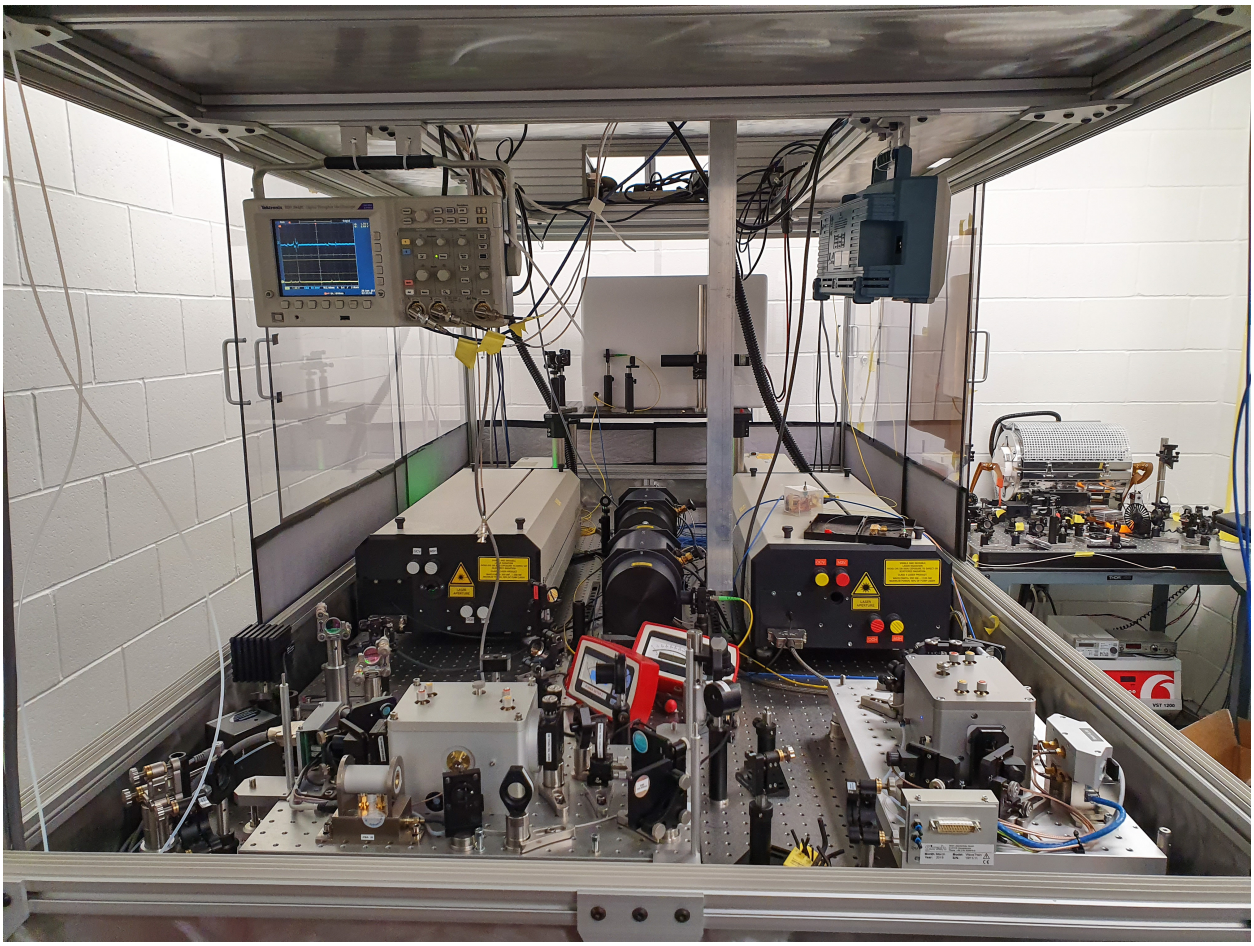

Figure 31: BECOLA laser system. WaveTrain frequency doublers (front left and right, characterized by their small grey resonator boxes). Ti:Sa CW laser (middle left). Dye laser (middle right). HeNe (back center, in front of white styrofoam box). Wavemeter (back center, inside styrofoam box). Iodine cell (right, outside of laser enclosure). A vertical pipe is seen hanging in the middle of the enclosure which is part of the CW laser light transport system.

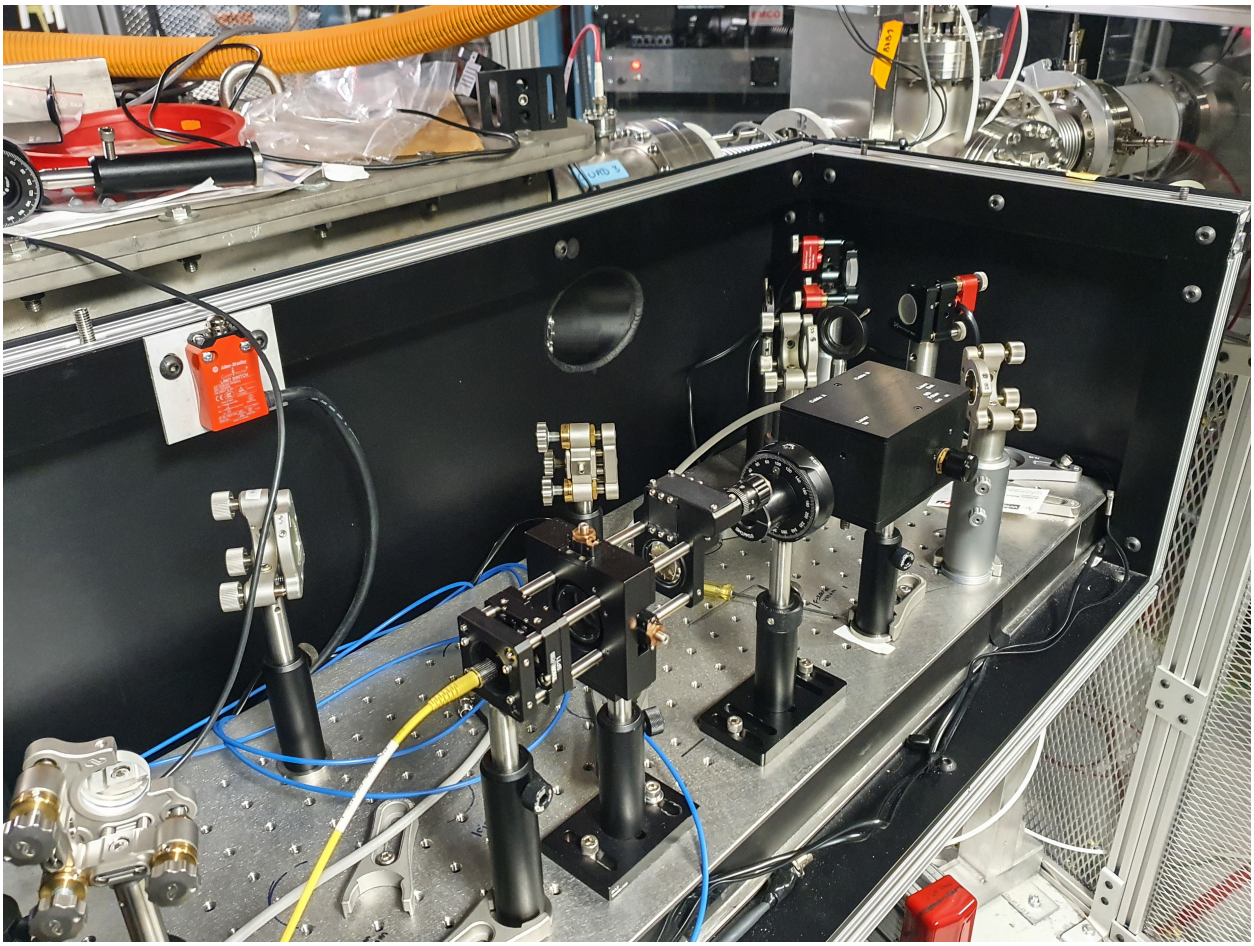

Figure 32: Injection side of the BECOLA beamline. The yellow optical fiber output passed through a telescope and a half-wave plate before entering the LPC and being injected into the beamline.

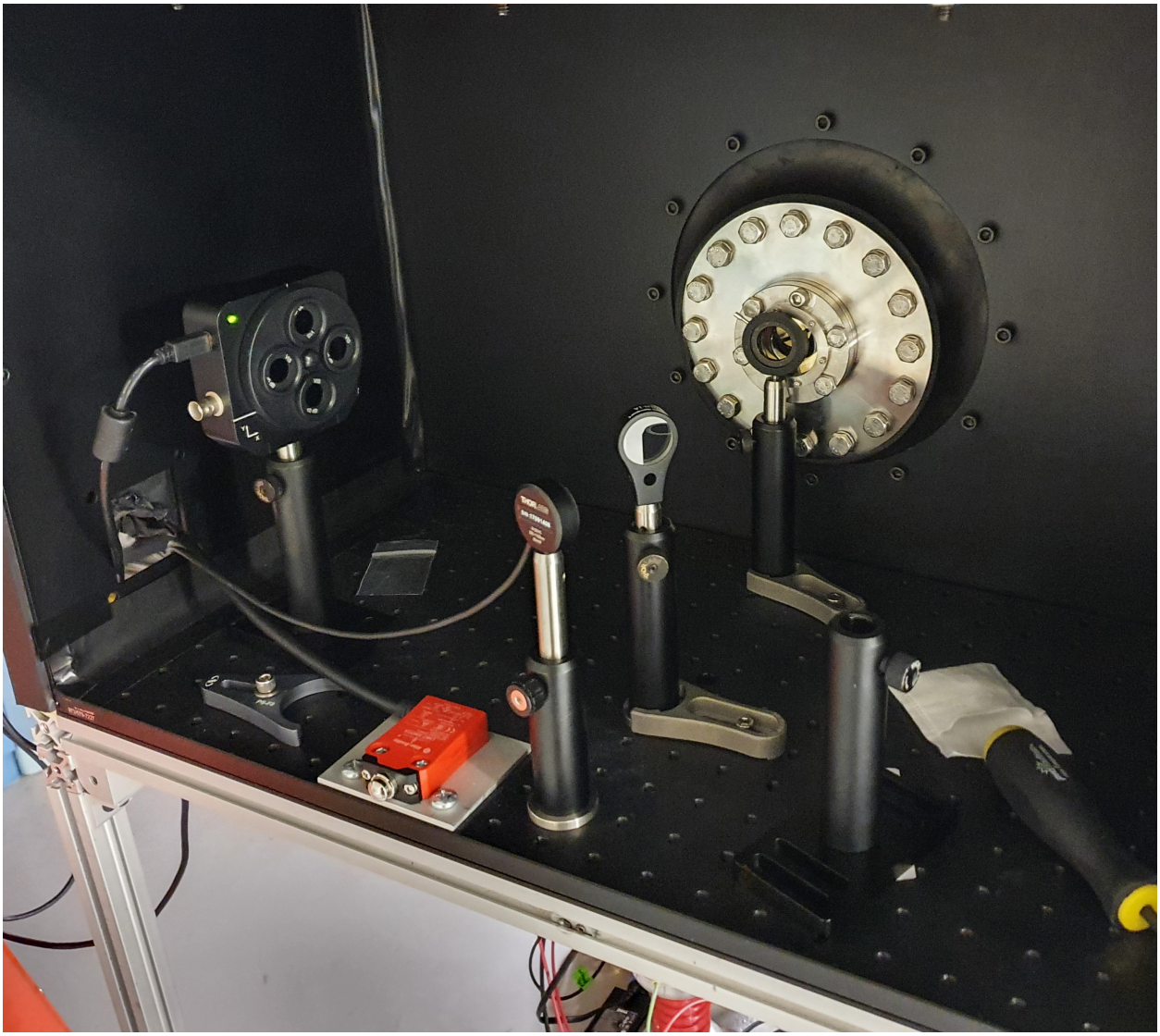

Figure 33: Other end of the beamline. add arrows showing the beam path. Beam splitter used to send one part of the beam to the CCD camera (to check to make sure the doubler is locked and blue light is going through) and other to the power meter to check stability of the power. This also allows for optimization through the beamline with the power meter.

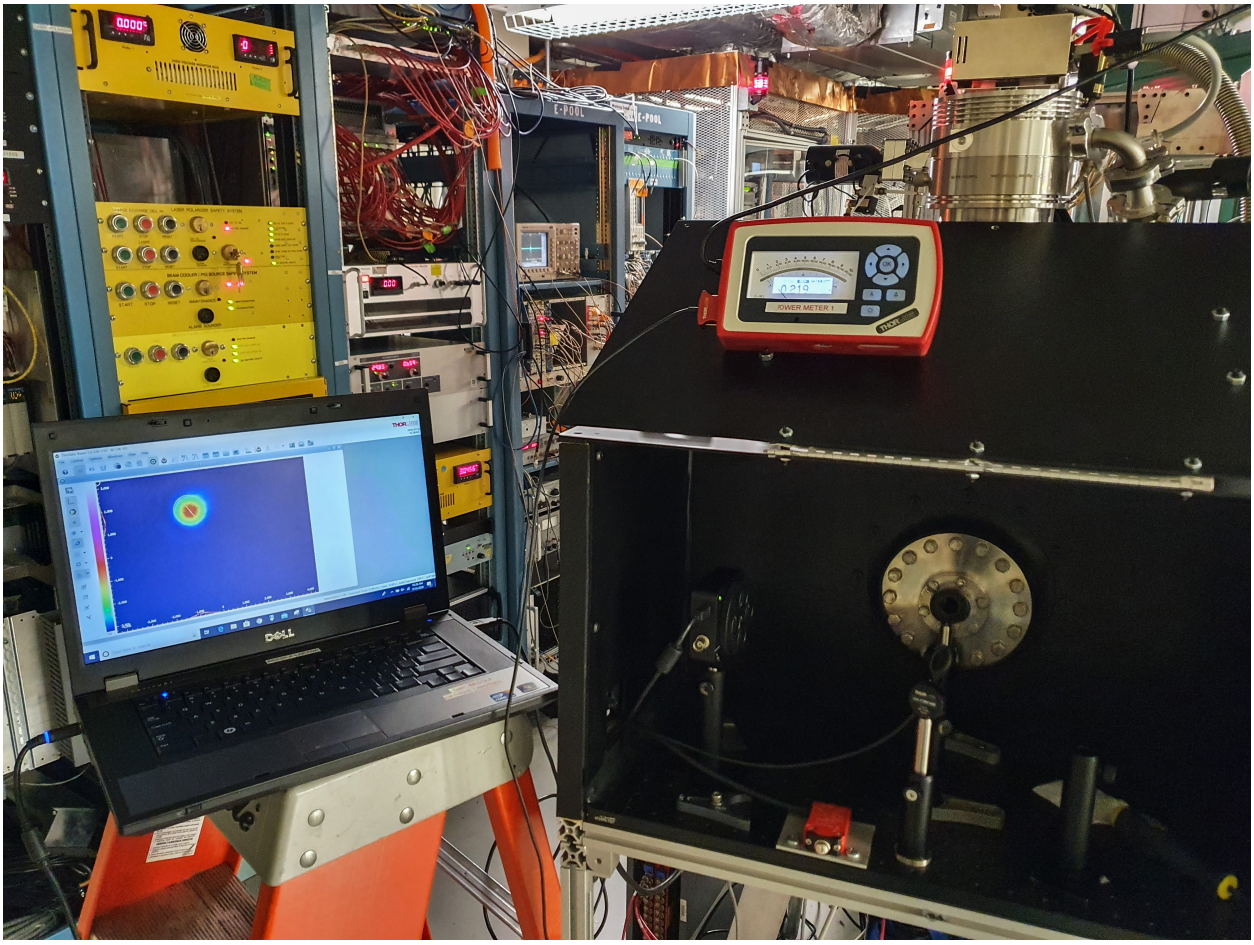

Figure 34: CCD camera (Thorlabs) and powermeter setup at the end of the beamline. The computer is turned towards the computer area so that it can be monitored at all times during the experiment.

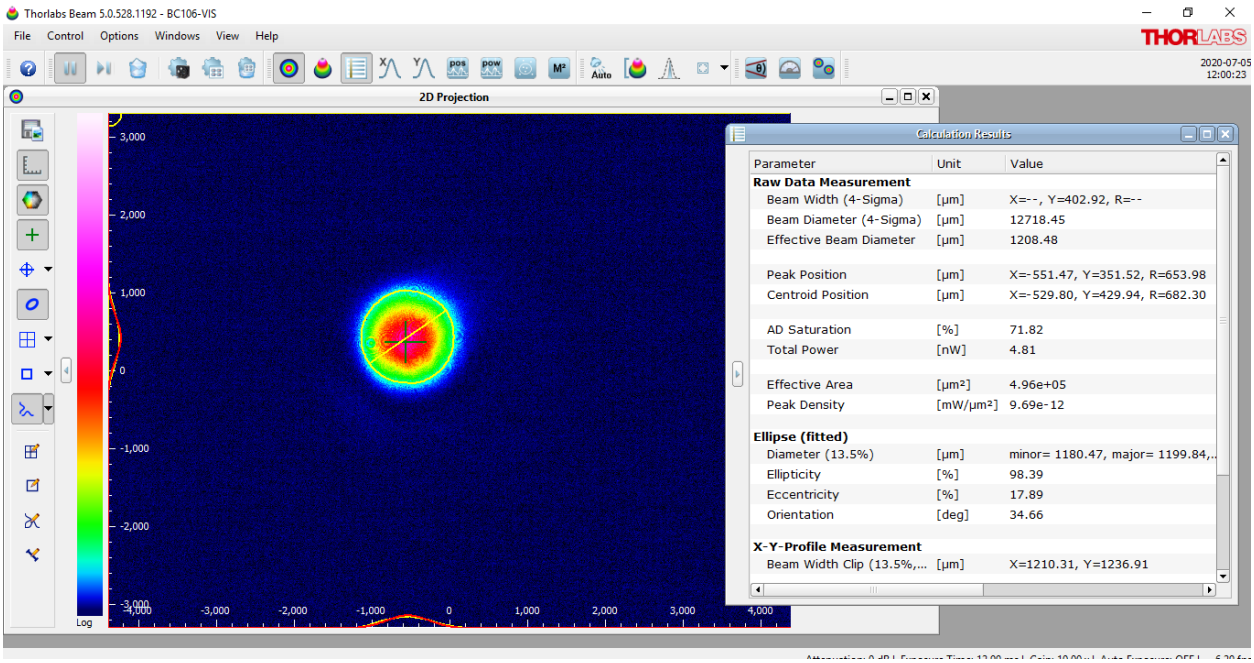

Figure 35: Screen shot of Gaussian beam profile used for Ni spectroscopy with an effective beam diameter of 1.2 μm. The measurement was performed using Thorlabs Beam software [101].

3.2.2 Photon Detection System

The photon detection system consisted of three photomultiplier tubes (PMTs), each with their own fluorescence capture units. PMT0 contained a system which focused on maximizing signal (Photon Detection System A), while PMT1 and PMT2 contained an upgraded system (Photon Detection System B) which focused on reducing background to maximize the signal to noise ratio (SNR).

The upgraded units on PMT1 and PMT2 had two main components, an ellipsoidal 4π mirror and a compound parabolic concentrator, which worked together to improve the signal to noise ratio by gathering fluorescence while preventing stray light from entering the PMTs. The background light which was filtered by these units had two origins: stray light that has diffracted off of apertures in the beamline and beam-related background from de-excitation processes which were not from the laser (such as CEC processes) [73]. A 4π solid angle was chosen for the ellipsoidal mirror in order to guide the maximum amount of fluorescence photons to the PMT (Fig. 36). The mirror isolated the fluorescence spatially, being able to collect photons what would otherwise have been lost in the beamline during fluorescence due to their initial propagation direction (Fig. 36). Stay light, shown in blue on the same figure, was reflected at a steeper angle and thus rejected by the following component of the PDS, the compound parabolic concentrator. Shown in Fig. 37, the CPC collected fluorescence photons and guided them to the PMT. Photons travelling at steeper angles, such as with stray light, were rejected by the mirror, making multiple consecutive bounces before leaving the CPC.

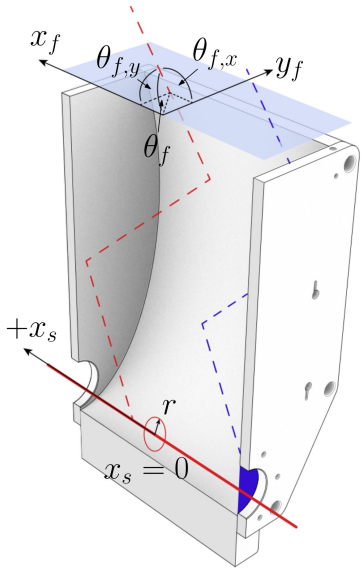

Figure 36: Elliptical portion of the photon detection system from Ref. [73] which isolates the beam spatially.

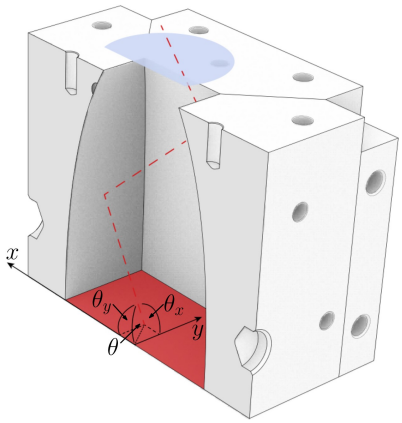

Figure 37: CPC portion of the photon detection system from Ref. [73] which rejects stray light from entering the PMTs.

While the upgraded system (CPC + Elliptical Reflector) focuses on reducing background noise, the original system on PMT0 focused on maximizing signal. As shown in Fig. 38, the original system was a bowl-shaped ellipsoidal reflective surface that directed fluorescence photons to the PMTs. Simulations showing the geometric distribution of photons arriving at the focal plane detailed in [74] show the differences between the two photon detection systems. The ellipsoidal reflector was made out of aluminum with a theoretical reflectance of $> 80\%$ over a wide range of wavelengths (300–1000 nm) [64]. The photomultiplier tube was placed at one of the focal points of the ellipsoidal reflector. Both systems are shown in Fig. 39. In addition, a line of focus for the ellipsoidal reflector was added in Fig 40.

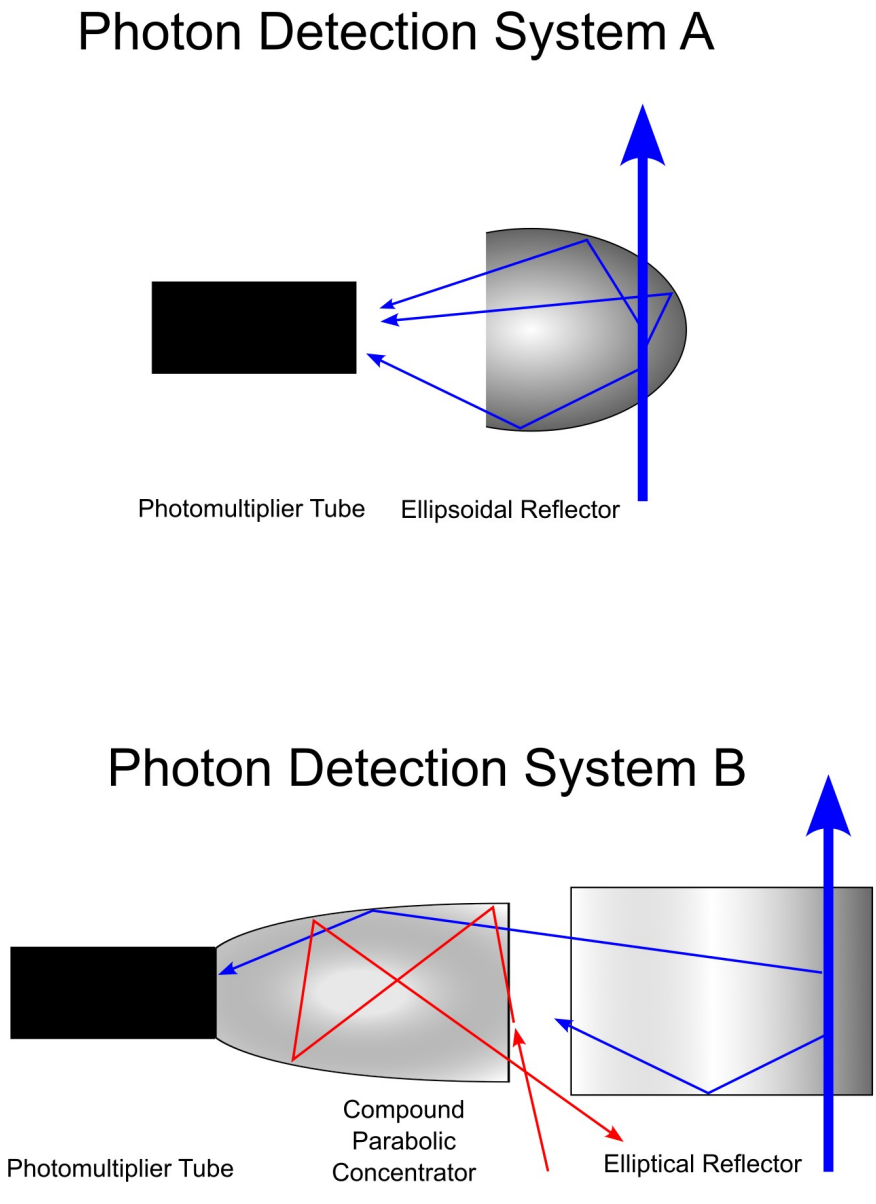

Figure 38: Schematic diagram comparing both photon detection systems.

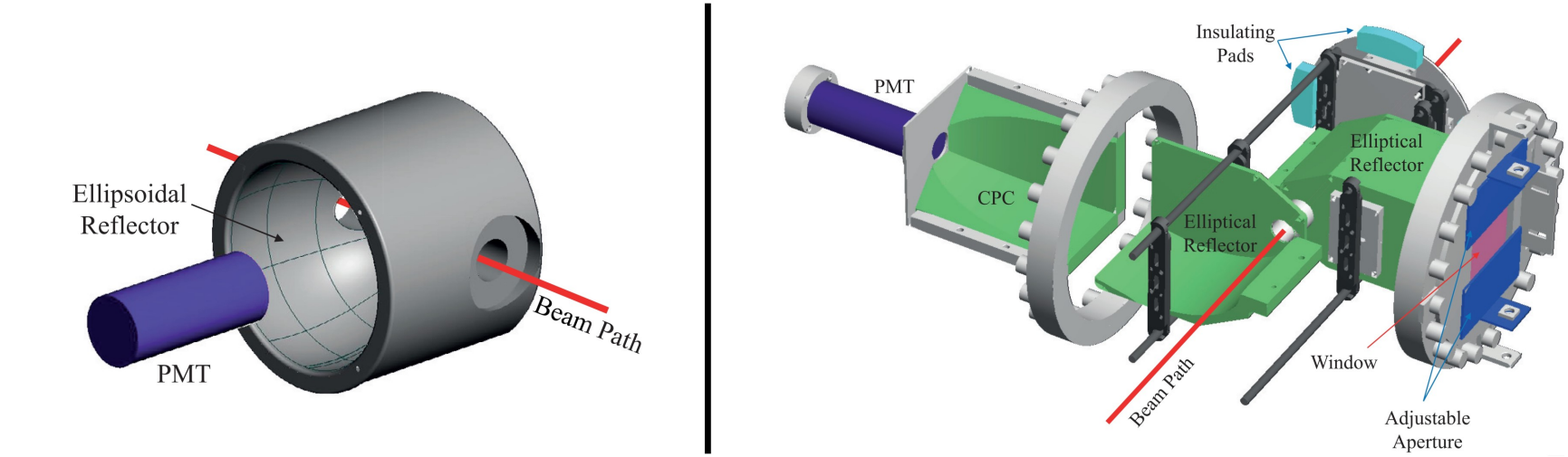

Figure 39: 3D models of Photon Detection System A (left) and Photon Detection System B (right).

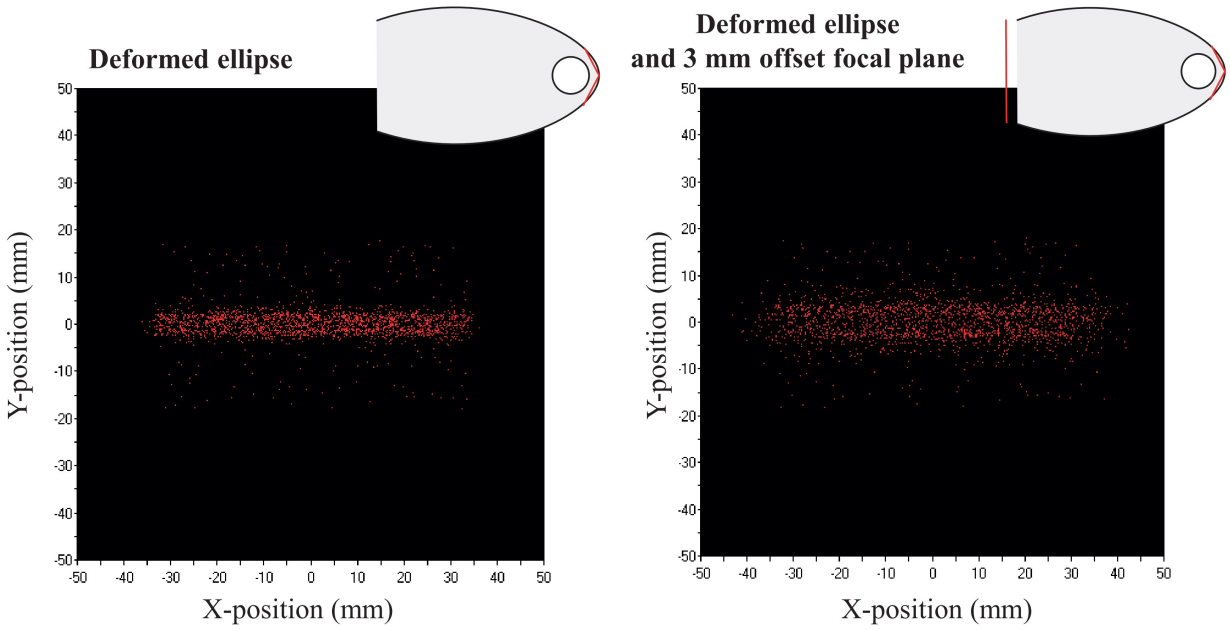

Figure 40: Simulations on possible systematic differences and their effect on photons arriving at the focal plane of the ellipsoidal mirror taken from Ref. [74]. (a) A slight crease is added the point of the ellipse. (b) The signal splits into two parts if the location of the aperture is now in an ideal position.

3.2.3 Offline Ion Source

An offline ion source is critical to BECOLA in order to extract the rms charge radii from King-plot analyses, perform calibration measurements during online experiments, and provide a reference for isotope shift measurements. Ions for stable Ni isotopes were produced using a Penning Ionization Gauge (PIG) ion source, which was a discharge plasma sputter source [102]. A diagram is shown in Fig. 41. The source consisted of two Ni cathodes on either side of a central anode disk [68]. The cathodes used were natural Ni, meaning that all isotopes were produced according to their natural abundance. A helium-buffer gas flooded the plasma discharge region in order to generate and sustain a plasma. He ions in the gas were accelerated towards both cathodes due to a potential difference of ∼600 V between the anode and cathodes. These ions were sputtered onto the Ni cathodes, which released not only Ni ions, but also fast electrons which travelled back towards the anode and collided with more buffer gas ions-perpetuating the plasma. An electromagnet created from a hollow copper coil surrounded the plasma discharge region in order to confine these discharge electrons with an axial magnetic field, containing them within spiral paths [102]. The Ni ions were released through a hole in one of the cathodes where they were extracted with a conically-shaped extraction electrode and transported to the RFQ cooler/buncher ion trap. The majority of the ions that were extracted from the source were from the buffer gas, approximately 10^3 times more than Ni, and they were filtered out with the RFQ cooler/buncher.

In the process of Ni ion beam tuning, the same apertures used to perform alignment of the laser beam were used to increase the overlap between the laser and the ion bunches. The transmission efficiency of the ion beam was obtained for 3-3 mm aperture diameters. When the ion beam was going through these apertures, it had a transmission efficiency of $\eta_{\text{transport}} \approx 50\%$. Observing the beam current through Faraday cups (Beam Observation Boxes) placed through the beamline (BOB0, BOB1, BOB2) yielded beam currents shown in Tab. 4 when the apertures were inserted. The locations for BOB0, BOB1, and BOB2 were after the cooler/buncher but before the aperture, directly in front of the CEC, and directly after the CEC, respectively.

D1203 (μA)	BOB0 (nA)	BOB1 (nA)	BOB2 Neutral (pA)
2.6	2.0	1.0	510

Table 4: Beam currents from the PIG source along the BECOLA beamline.

The PIG source was typically cleaned every few weeks to remove the nickel residue forming on the anode and, if need be, flip the cathodes to a fresh surface for ionization. PIG source settings used throughout the experiment are shown in Tab. 5. Variations in these parameters depended upon the condition of the cathodes and anode inside of the source. For example: higher leakage currents were indicative that the source needed

to be cleaned. Different combinations of valve position (which influenced the buffer gas pressure), magnet amperage, and cathode voltage were used to maintain the plasma inside of the source as the cathodes degraded from use.

An extraction electrode was used to defocus the ion beam to control the number of ions entering the cooler buncher to prevent overfilling the ion trap within the buncher (Sec. 3.2.4). One way to verify that the trap is not overfilled is a narrow time of flight spectrum (Fig. 45), which is typically around 1 μs (FWHM). The cooler may also be adjusted to mitigate overfilling. For a bunch pressure of 1.4 mTorr a cooling time of no more than 5 ms was necessary, and a high repetition rate was employed to maintain fewer ions per bunch [99].

Extractor Voltage (V)	-2280
Magnet (A)	1.4
Cathode Voltage (V)	-148
Leakage Current (A)	14
Valve Position (%)	31
Buffer Gas Pressure (μTorr)	13
CC Gauge Pressure (μTorr)	6

Table 5: Settings for the PIG source used throughout the nickel experiment.

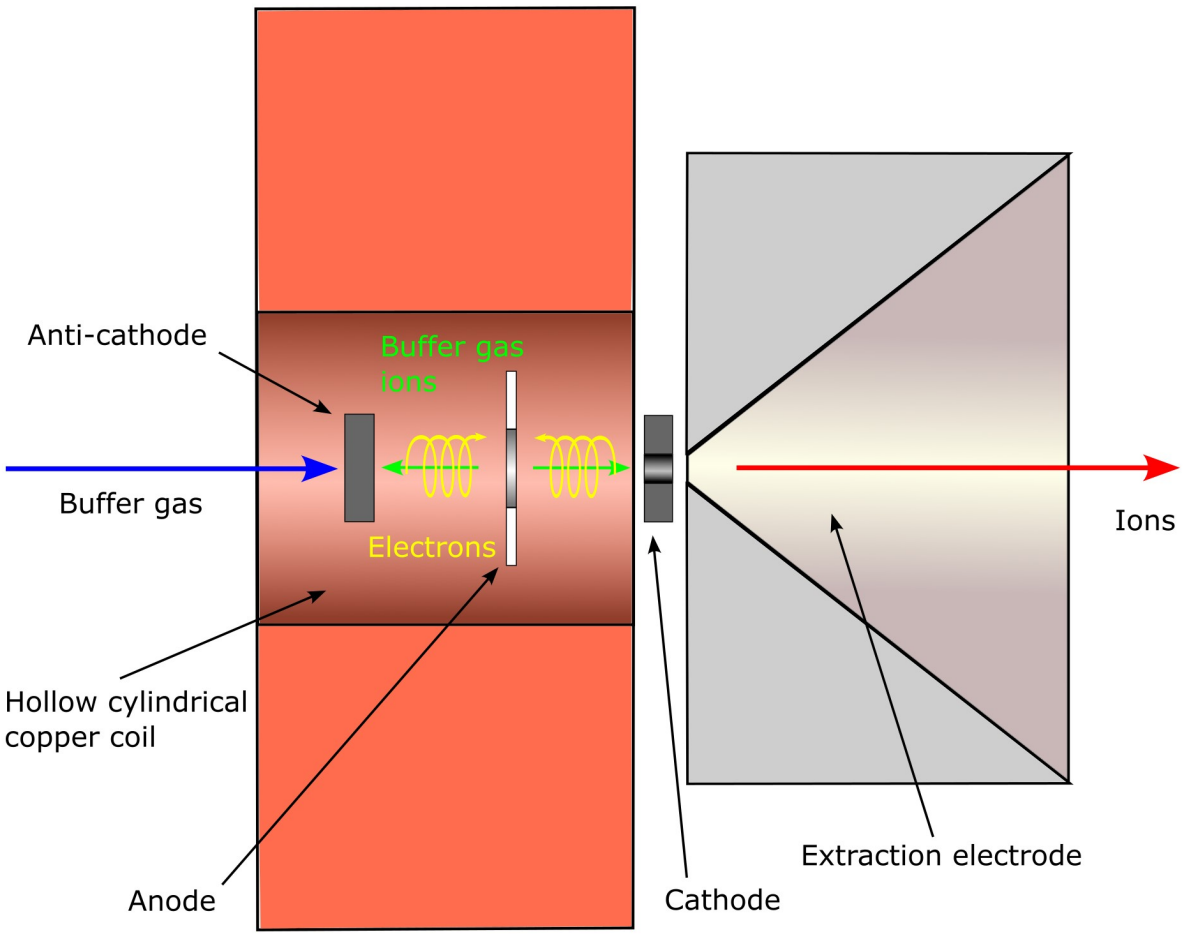

Figure 41: PIG source diagram.

3.2.4 Radiofrequency Quadrupole Cooler/Buncher Ion Trap

A radio-frequency quadrupole (RFQ) cooler/buncher ion trap (Fig. 43) was employed to trap ions from on-line or offline ion sources and send beam bunches for high resolution and high sensitivity hyperfine spectrum measurements at BECOLA [64]. The RFQ ion beam cooler contained four rods placed such that, if viewed from the cross-section, the centers of the rods formed vertices of a square [99]. An oscillating potential is applied to the rods, with adjacent rods of opposite polarity. This oscillating potential yielded a quadrupole potential. Frequencies of the oscillating potential between the quadrupole electrodes contained the ion beam, allowing the beam to be contained instead of diverting it into the walls of the apparatus. Collisions with a buffer gas slowed the ion beam down in order for it to be trapped. A differential pumping system for the buffer gas was used to maintain a higher pressure in the cooling region (when most of the transverse energy spread of the ions is removed) while maintaining a lower pressure in the buncher (here ions are accumulated to form a pulse). Longitudinal confinement was achieved by employing static electric fields to move ions through the buffer gas. Instead of cutting electrodes into several straight segments, long diagonal wedges were cut to create a uniform drag field over an arbitrarily long distance. Segmented RFQ electrodes (Fig. 43) were added to the end of the cooler/buncher in order to guide the beam longitudinally through the buffer gas and formed a trap for the beam bunching. Beam cooling and bunching was used at BECOLA because the buffer gas reduced the beam emittance while bunching increased background suppression.

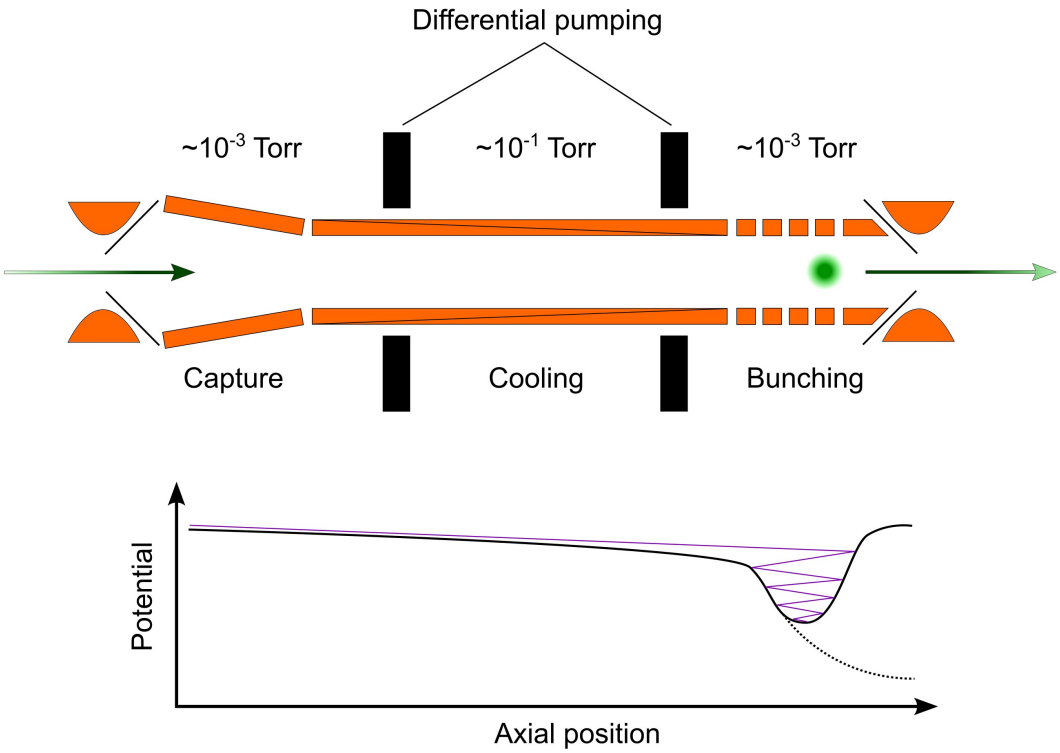

Figure 42: RFQ Cooler buncher schematic based upon Ref. [99] showing the ion capture, cooling, and bunching regions.

A hyperbolic ring electrode at the entrance was used to decelerate the beam as well as provide cylindrically symmetric quadrupole field to focus the beam in the RFQ (trapping) region, while a cone electrode was included to mitigate penetration of the RF field into the deceleration region. Flaring electrodes at the beginning of the cooler/buncher were used in order to enhance the acceptance of the system. Once the beam was transported into the cooler, ions needed to be transported and bunched with as few losses as possible. A large pseudopotential (Sec. 3.2.5) is critical to efficiently transport ions. The electrodes were designed with a tight electrode spacing to result in stronger confining pseudopotential, but also done such that there was lower risk of an RF discharge. The large pseudopotentials are important to accomodate high beam currents, where space charge effects work to defocus the beam and results in losses when ions come into contact with electrode surfaces. In order to eject the ions, the voltage from a switching electrode was switched down to permit the ion pulse to leave the trap and reaccelerate to approx 30 keV. The energy spread of the ion beam, which arises from longitudinal emittance, limits the resolution of the CLS measurement. Therefor it was important that the beam cooler buncher delivered a beam with as small energy spread as possible. The emittance achievable by beam cooling is limited by the temperature of the buffer gas. The ratio of the He buffer gas pressure between the cooling and trapping regions was approximately 100 : 1, respectively, with the trapping region at approximately 1 mTorr. A differential pumping channel was used to separate

the sections of high and low pressure gas within the cooler/buncher. A helium inlet feeds gas into the high pressure cooling region, which gas flow out of the cooler is restricted by the differential pumping channel. The buncher region of the vacuum chamber was pumped directly by a turbomolecular pump.

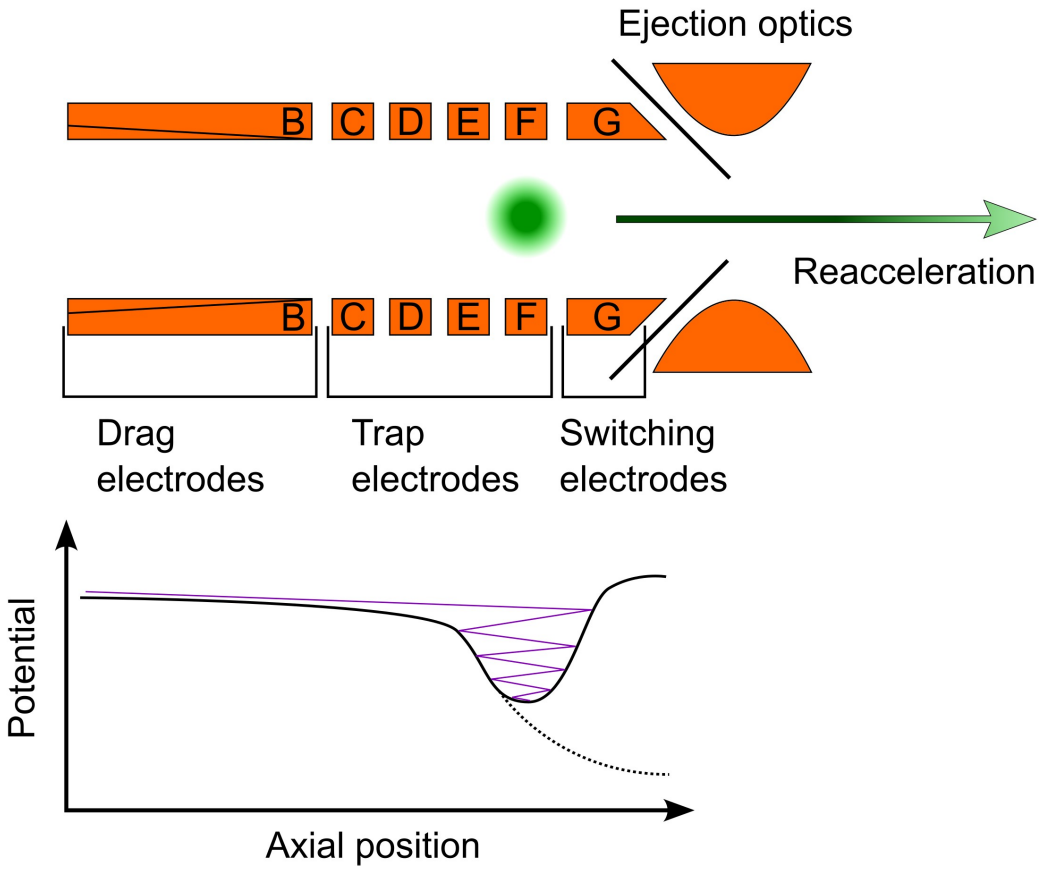

Figure 43: Diagram of the end of the RFQ cooler/buncher based upon Ref. [99]. The segmented C and D trap electrodes were grounded, while E and F had $-0.2\,\mathrm{V}$ and $-4.2\,\mathrm{V}$ of applied voltage, respectively. The E switching electrodes had a $19.8\,\mathrm{V}$ potential that was flipped to $-15\,\mathrm{V}$ to eject the trapped ions.

3.2.5 Stability of Ni Ions in the RFQ

In the cooler, ions were kept in the trap due to oscillations around a saddle-point of a potential [99]. The RFQ cooler/buncher acts as a mass filter when the ion is driven away from the saddle point before the potential has time to switch to the opposite polarity and keep the ion confined. The Mathieu stability parameter calculates at which RF voltages (volt-peak) the ions are stable and which are not. Since voltages with allowable q depend on the mass of the ion, it is advantageous to use a buffer gas that is largely different from the ion of interest. Otherwise there will be increased contamination in the ion beam due to the gas not being filtered out. The importance of knowing the Mathieu parameter is shown in the plot below, where different q values are plotted as a function of RF peak-to-peak Voltage. For this experiment, He buffer gas was the best choice because it filtered out around 13 V peak-to-peak (Fig. 44), leaving a disparity between the voltage at which Ni isotopes start to be unstable in the ion trap. This instability is characterized by the q parameter, where stable ion motion is $q < 0.908$ [103]. The q values in Fig. 44 were calculated (for a linear quadrupole) using

$$q = \frac{4eV_{\mathrm{RF}}}{mr_0^2\omega_{\mathrm{RF}}^2} \tag{58}$$

where e is the elementary charge, V_{RF} is the peak RF amplitude, m is the mass of the ion, r_0 is the distance from the central axis to the RFQ electrode, and ω_{RF} is the RF angular frequency. At BECOLA, $r_0 = 0.0035\,\mathrm{m}$ and $\omega = 2\pi f$ in rad/s where $f = 1.2\,\mathrm{MHz}$. Equation 58 originates from a gradient pseudopotential, where the ion is held in the trap by oscillating back and forth towards the saddle-point of the potential. Looking at an equation of motion, the solution to the Laplace equation in a linear quadrupole geometry is

$$\Phi = \frac{\Phi_0}{2r_0^2}\left(y^2 - x^2\right) \tag{59}$$

where Φ_0 is the potential applied across the adjacent electrodes. The potential Φ_0 will oscillate in time t [99].

$$\Phi_0 = V_{\mathrm{RF}}\cos\left(\omega_{\mathrm{RF}}t\right) \tag{60}$$

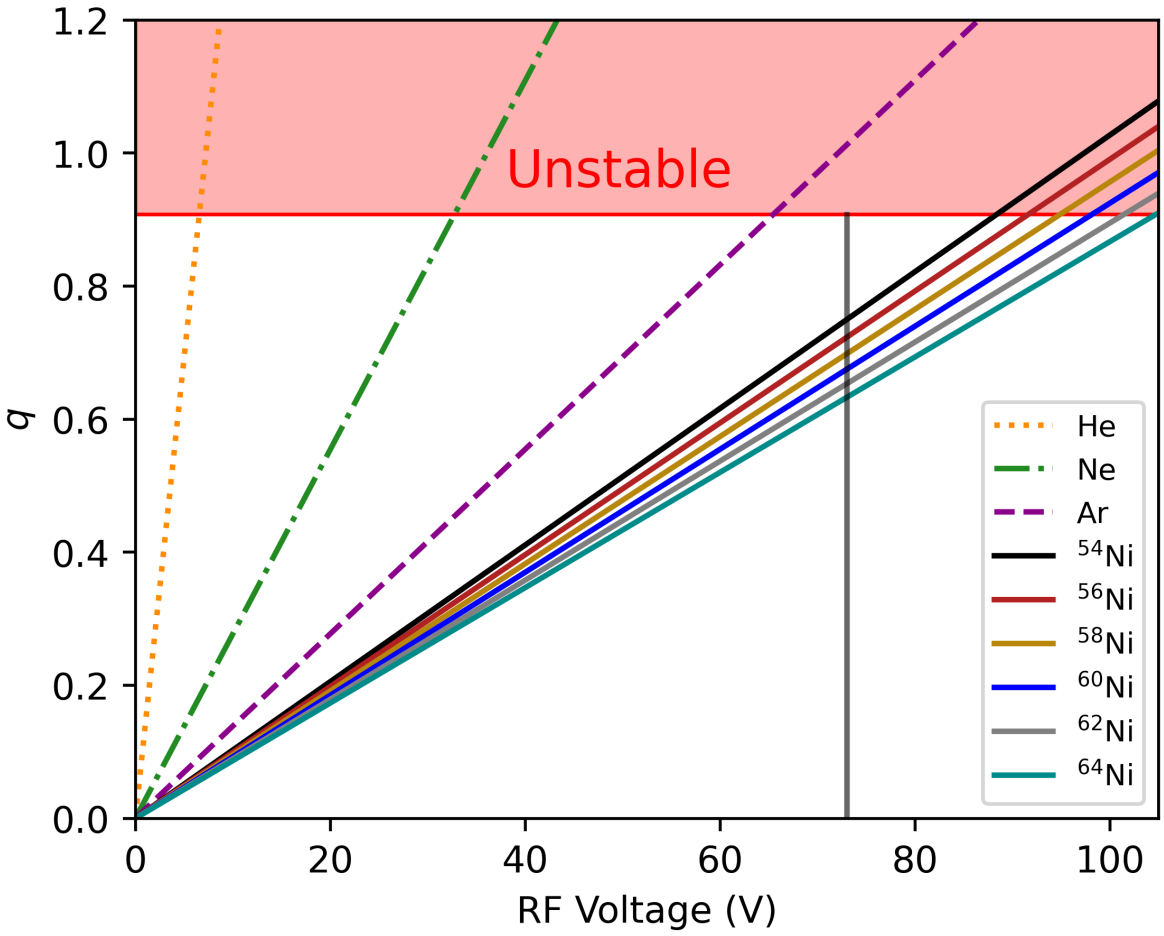

Figure 44: Stability for various buffer gasses and ^{54}Ni in the RFQ cooler buncher. The RF voltage on the x-axis is the peak voltage. The red horizontal line indicates the point at $q = 0.908$, where beyond this point the ion motion is unstable. Masses used in these calculations were taken from Ref. [104]. The RF voltage used in this experiment was 73 V (grey vertical band), a setting which filters out all three buffer gases but also keeps all Ni ions. A He buffer gas was used for the PIG source.

3.2.6 Time of Flight Spectrum from the RFQ Cooler/Buncher

A width of typically 1 μs was achieved from the offline ion source by reducing the amount of ions (typically limited to $< 10^6$) entering the cooler/buncher until a narrow time structure was observed, such as the one shown in Fig. 45. The background was suppressed by performing a time cut, which selects the data within the bunch and cuts out the unwanted background. This is not possible to do with a DC ion beam, where the ions are flowing through the photon detection region continuously and any cut in time would also cut out signal. Bunched beam spectroscopy adds this time cut advantage allowing an improvement to the signal to noise ratio [72]. Background can be suppressed by a factor of 10^6, assuming the bunch is released once per second and perfect bunching efficiency [74]. The time spectrum in Fig. 45 is for ^{58}Ni. The measurement time for each isotope varied due to their natural abundances (Tab. 6).

Stable Isotope	Natural Abundance (%)
^{58}Ni	68.08
^{60}Ni	26.22
^{61}Ni	0.01
^{62}Ni	3.63
^{64}Ni	0.93

Table 6: Table of stable Ni isotope natural abundances. These are the ions that are produced from the PIG source. Note that BECOLA did not measure ^{61}Ni, however it is part of the natural abundaces of Ni.

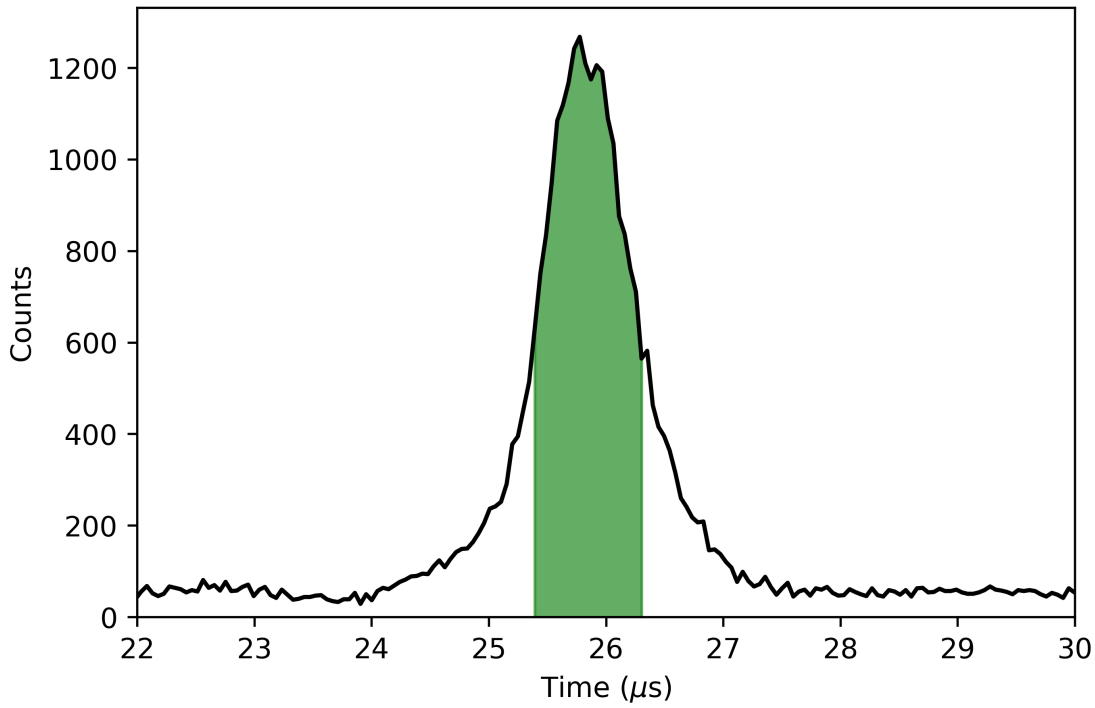

Figure 45: Time spectrum for offline Ni ion beam from the PIG source. All naturally occurring nickel isotopes are contained in this time spectrum. The green shaded area spans a width of 1μs.

3.2.7 Charge Exchange Cell

A sodium-loaded charge exchange cell (CEC) was used to neutralize incoming Ni ions to atoms using collisions with the alkali vapor. The CEC had a vertical design, and Na metal was heated in a reservoir at the bottom where vapor travelled up to the interaction region. Condensation at the top of the cell, due to a lower temperature sustained by an oil bath, allowed the Na to be recycled and reheated when it reached the bottom of the reservoir. A cartoon showing the basic components of the charge exchange cell is shown below in Fig. 46. The typical temperature associated with the bottom of the charge exchange cell was 423°C with a heating current of 3.3 A.

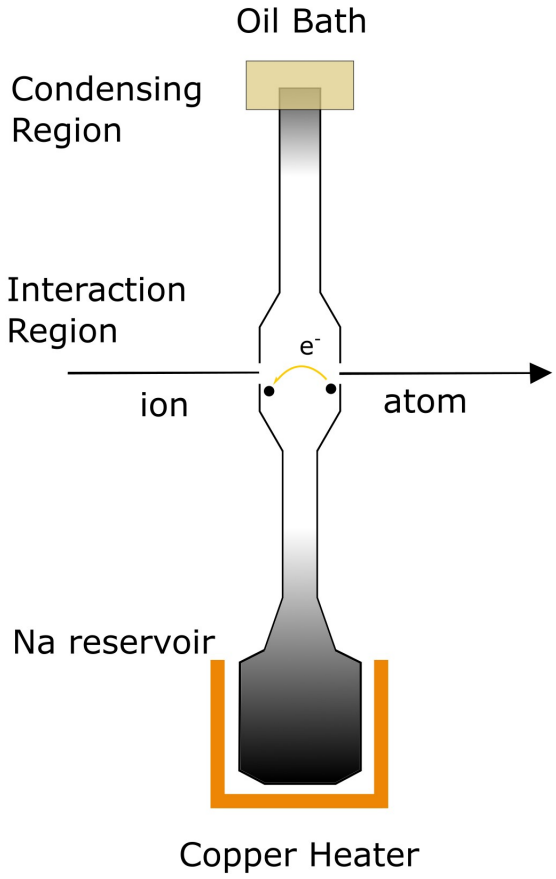

Figure 46: Cartoon CEC diagram. The gradient within the cell represents the concentration and evaporation of sodium within the CEC. A more detailed schematic can be found in Ref. [105].

The distribution of electronic states (Fig. **??**) populated in the charge exchange reactions (fractionalization) is dependent on the first ionization energies of both the alkali-metal vapor and the state of interest in the incident ion, as well as the density of other states (level density) [68]. Due to spontaneous decays, this distribution changes with time and is referred to as a cascade decay. Within the cascade decay, the population is redistributed to lower energy levels and depending on the level density, atomic lifetimes, and branching ratios of each transition with the cascade decay, the population of the outgoing atomic beam may

1. be fragmented across many levels
2. remain in a near resonant metastable state which is directly populated in the charge exchange reactions
3. be accumulated in a low-energy metastable state after the cascade decay.

The charge exchange process is

$$X^{+}(i) + A(j) \rightarrow X(f) + A^{+}(g) + \Delta E \tag{61}$$

where $X^{+}(i)$ is the incident ion beam in the electronic state i, $A(j)$ is the alkali atom in state j, $X(f)$ is the outgoing atom in state f, and $A^{+}(g)$ is the alkali ion in state g. The ΔE term at the end of Eq. 61 is the energy difference between the final and initial electronic states, and can result in three cases [65]:

1. $\Delta E = 0$; referred to as a resonant process
2. $\Delta E < 0$; outgoing atomic beam gains energy, broadening the energy distribution of the beam by a maximum of ΔE
3. $\Delta E > 0$; energy is required for the charge-exchange process to occur and the energy is taken from the kinetic energy of the incident ion beam.

Where $\Delta E \neq 0$ are inelastic collisions between the ion and alkali vapor, where energy is given or taken from the kinetic energy of the ionic or atomic beam and result in an asymmetric resonance line shape. An clear example of the result of these inelastic collisions is shown in Figs. 85,97, where each of the main hyperfine peaks is accompanied by a satellite peak caused by the charge exchange cell. In Ni isotopes, the asymmetry in the spectrum Fig. 47 due to these collisions is less pronounced although still present.

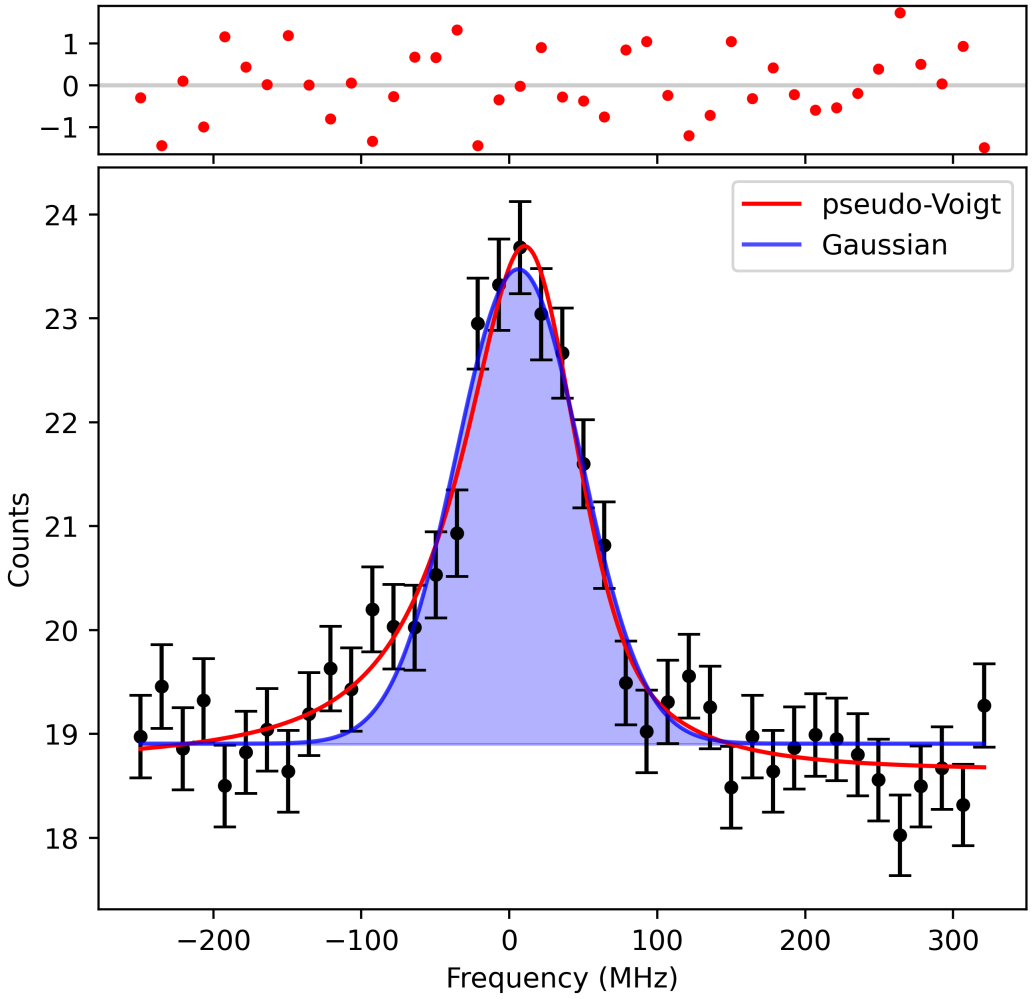

Figure 47: Spectrum of ^{64}Ni using an asymmetric pseudo-Voigt function. The asymmetric tail seen on the left side of the peak is due to the charge exchange process. As a reference, a symmetric Gaussian curve fit is shown in blue. Notice on the left- and right-hand sides the difference between the red and blue curves, as well as the top.

Depending on the CEC temperature, which affected the charge exchange efficiency, the degree of asymmetry in the lineshape of the Ni spectra would change. A charge exchange efficiency of 50% was employed throughout the experiment in order to maintain a rather symmetric lineshape while having a decent efficiency (typically 50%). Taking into account the population fraction that is in the electronic state targeted for spectroscopy, the total efficiency for neutral atoms ready for spectroscopy after the CEC dropped to 7.5%. Ni electronic populations after the charge exchange process can be found in Ref. [68]. This total efficiency was deemed an adequate balance between lineshape symmetry and charge exchange efficiency, since as the CEC temperature was increased the lineshape becomes more asymmetric due to inelastic collisions described above. This efficiency calculated by deflecting the ion beam and seeing the ratio between neutral and ion beams and is detailed in Appx. B.4.

3.2.8 High Voltage Read-Out

High voltages were applied both at the RFQ and the charge exchange cell: the FuG high voltage from the RFQ accelerated the ions at approximately 30 keV while the Matsusada high voltage on the top of the CEC was applied to change the beam energy and scan over the resonant frequency. Both of these were read out by a digital volt meter (DVM) connected to a high voltage divider. A high voltage divider is a series of resistors that effectively attenuate the amount of voltage sent to the DVM in order to accurately and precisely read out the voltage. The FuG HV power supply, which supplied a potential to the RFQ, was connected to an Ohmlabs voltage divider with a ratio of 9997.7048 : 1. The Matsusada HV power supply on the CEC had a voltage divider ratio of 201.0037 : 1. A number of high voltage dividers (Fig. 48) were constructed at BECOLA by Kristian König and Yuan Liu. The BECOLA-1 high voltage divider, which is currently in use, has a ratio of 2980.32 : 1.

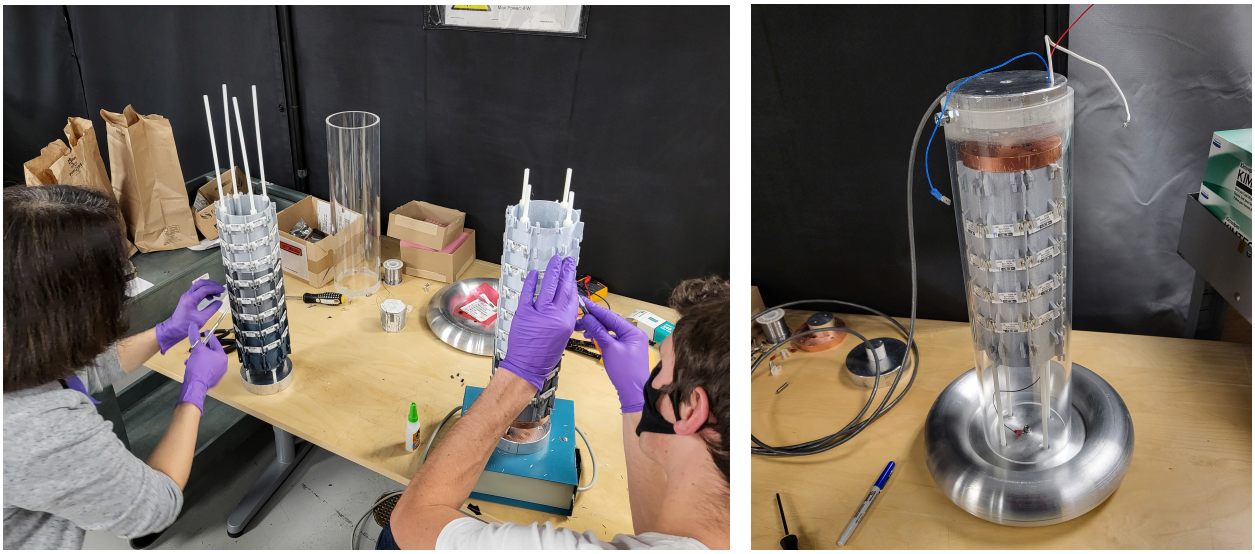

Figure 48: High voltage dividers under construction at BECOLA.

4 Data Analysis

4.1 Laser Frequencies for Isotope Shift Measurements

The electronic measurement of a large scanning voltage that would cover all isotopes could easily lead to uncertainties of a few MHz even if devices with 10^{-4} relative accuracy are applied [77]. The beam path was observed to change while changing the scanning potential. This was avoided by scanning small voltage ranges. The laser frequencies calculated using Eq. 16 for each measurement range are shown in Tab. 7.

Isotope	−1670 V	−800 V	−60 V	50 V	750 V	1370 V	1375 V
^{54}Ni	–	–	–	–	–	425.624 179	–
^{58}Ni	425.631 897	425.625 060	425.619 700	425.618 884	425.613 600	425.608 870	425.608 827
^{60}Ni	425.624 180	425.617 700	425.612 426	425.611 628	425.606 433	425.601 785	425.601 742
^{62}Ni	425.617 078	425.610 710	425.605 520	425.604 733	425.599 622	–	425.595 006
^{64}Ni	425.610 326	425.604 060	425.958 950	425.598 175	425.593 145	–	425.588 602

Table 7: Laser frequencies in terahertz (THz) used for isotope shift measurements at BECOLA. The top column labels show the voltage scan location the laser frequencies were used with. A 40 volt scan range was performed around the voltage headers shown.

4.2 Import of Data

Values for the scanning voltage were taken from a high precision digital volt meter (DVM) for each voltage step during data taking. These values from the DVM were converted to Volts using the voltage divider ratio. The ion beam energy was then determined using

$$E_{\mathrm{kin,\,ion}} = U_{\mathrm{Fug}} \times R_{\mathrm{Fug}} - U_{\mathrm{Mat}} \times R_{\mathrm{Mat}} = E_{\mathrm{FuG}} - E_{\mathrm{Mat}} \tag{62}$$

Detailed in Sec. 4.4, rest-frame frequency can be used as a method of calibration, enabling the precise determination of the FuG high voltage power supply which accelerates the ions. If the calibrated FuG voltage for a data set was known, appropriate equation for the beam energy is shown in Eq. 63 where $E_{\mathrm{FuG\,cal}}$ is the calibrated beam energy in volts.

$$E_{\mathrm{kin,\,ion}} = E_{\mathrm{FuG\,cal}} - U_{\mathrm{Mat}} \times R_{\mathrm{Mat}} \tag{63}$$

The data was binned in the following way. The x bin edges of a histogram were created by making an array that spanned the maximum and minimum beam energies in steps of the unique number of voltage steps plus one. The y bin edges were the unique number of time steps. Due to the limit on the speed of the DAQ hardware, there is a small lag that can affect the data and sometimes the scans per voltage are not

uniform across the measurement. This was also taken into account and remedied by normalizing each of the bins by the number of scans in each bin (Fig. 49).

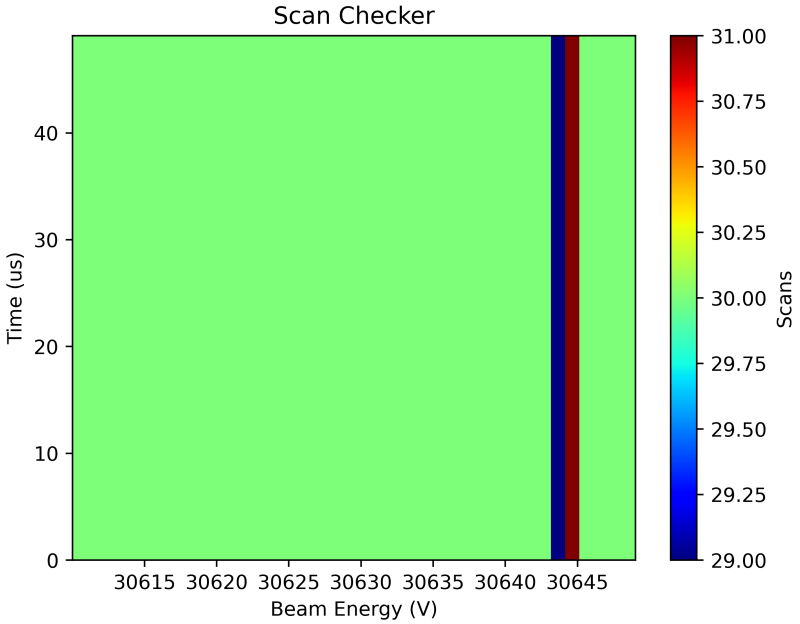

Figure 49: Histogram that checks the number of scans per bin. In the ideal case, all of the bins should have 30 scans. However, due to a lag in the DAQ, one bin has 29 scans while the other right next to it has 31.

4.3 Time Cut Selection

In order to take advantage of the bunch beam spectroscopy a time cut was made which selected only the data within the ion bunch and cut out unwanted background. In order to make the best cut, the center and width were shifted systematically to find the best signal to noise ratio. The centroid uncertainty was also taken into consideration when choosing the time cut, where a local minimum appeared during systematic analysis. The center of the time cut was different for each PMT due to the time of flight between the detectors, where, due to their positions, PMT1 and PMT2 were delayed, relative to PMT0, by 0.91μs and 1.25μs, respectively (Fig. 50). The time of flight spectrum for ^{54}Ni is shown in Fig. 51. This spectrum is much noisier compared to Fig. 45, however, this highlights the bunched beam spectroscopy advantage because by performing the time cut the hyperfine spectrum can be extracted despite the noise. Although one could proceed with the spectroscopic analysis at this point, high voltage calibrations were performed using the rest-frame frequency.

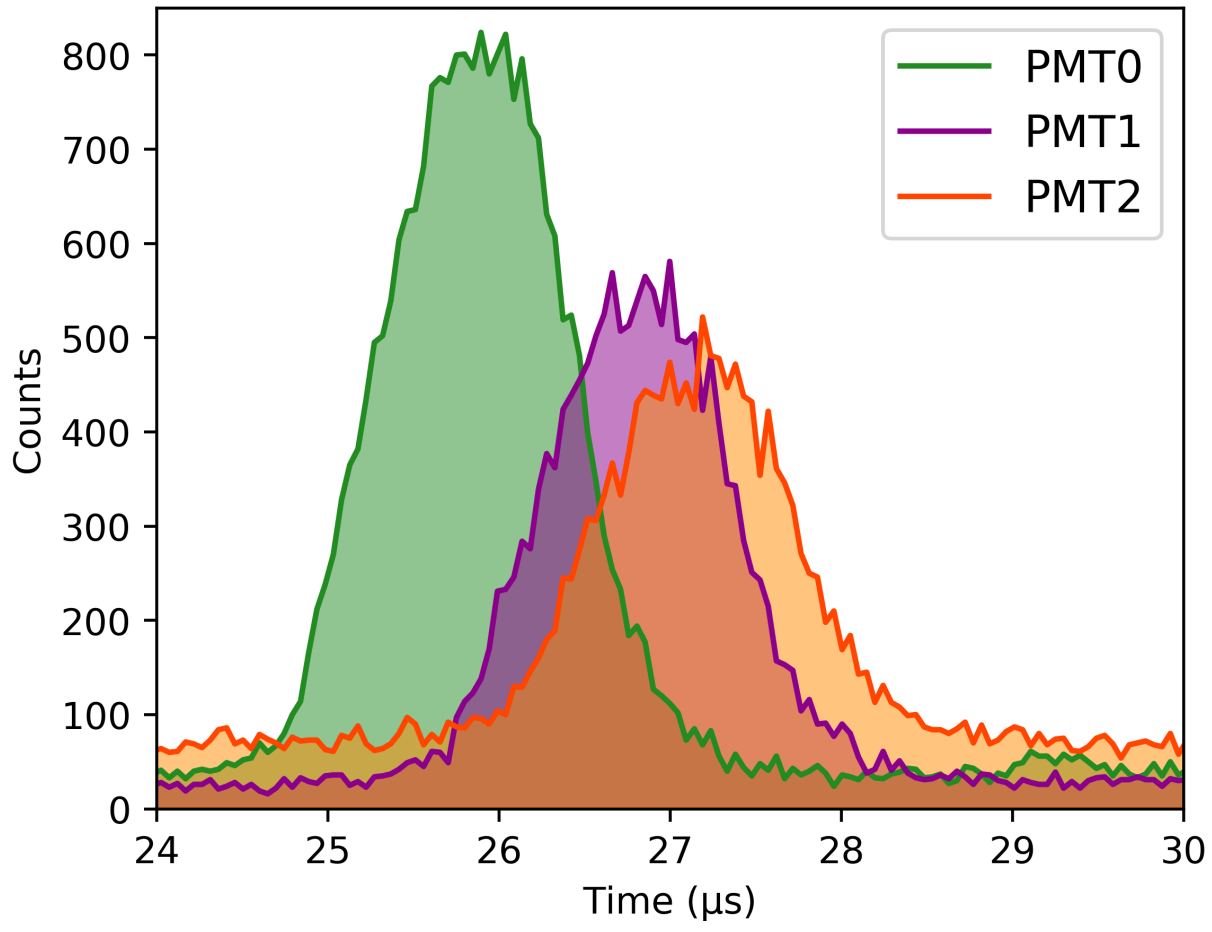

Figure 50: Time of flight spectra for all three PMTs for ^{60}Ni.

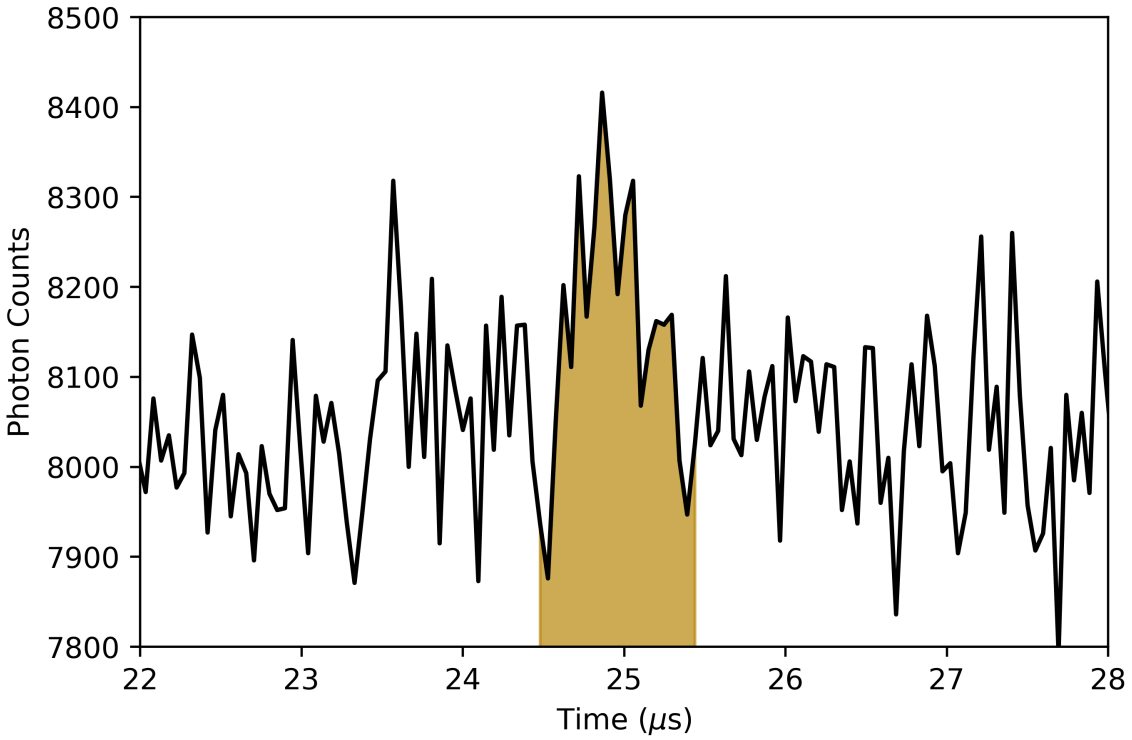

Figure 51: Time of flight spectrum for ^{54}Ni. The gold shaded region spans a width of 1μs.

4.4 Rest-frame Frequency Determination

Two sets of DC- and Bunch-mode measurements (four total) were used in rest-frame frequency calculation (Fig. 52). Data from all three PMTs were summed together before performing a fit. The rest-frame frequencies [77] were determined using the method described below, with alternative methods in Appx. H.

The determination for the rest-frame frequency is as follows:

1. Find an initial guess for the rest-frame frequency ν_0 using the hyperfine fit results.

$$\nu_{0\,\text{guess}}^2 = \nu_{c\,\text{fit}} \cdot \nu_{a\,\text{fit}} \tag{64}$$

2. Find the transition sensitivity with the rest-frame frequency guess ν_0.

$$S_{\text{transition}} = \frac{2\nu_{0\,\text{guess}}}{\text{mass}} \cdot \frac{\nu_{\text{laser}}^2}{\nu_{\text{laser}}^2 - \nu_{0\,\text{guess}}} \tag{65}$$

3. Find the beam energy using the fit result.

$$E_{\text{kin}} = \frac{mc^2}{2} \cdot \frac{(\nu_{\text{fit}} - \nu_{\text{laser}})^2}{\nu_{\text{fit}}\nu_{\text{laser}}} \tag{66}$$

4. Find the difference in beam energy between the colinear/anticolinear measurements.

$$\Delta U_{\text{scan}} = E_{\text{kin col}} - E_{\text{kin acol}} \tag{67}$$

5. Finally, determine the rest-frame frequency ν_0.

$$\nu_0 = \sqrt{\nu_{\text{col laser}}(\nu_{\text{acol laser}} - \Delta U_{\text{scan}} S_{\text{transition}})} \tag{68}$$

Before taking the weighted average of all the rest-frame frequencies to obtain the final result (blue band in Fig. 52), the following uncertainties were added to the total statistical uncertainty of the black points in the figure using Gaussian error propagation:

1. *Fit uncertainty*, $\left(\leq 0.6/\sqrt{2}\right)$ MHz: The maximum fit uncertainty between different fit functions used to determine the rest-frame frequency. The $\sqrt{2}$ term comes from the fact that $\nu_a \approx \nu_c$. Then

   (a) $\nu_0^2 = \nu_c \cdot \nu_a$

   (b) $\nu_0^2 \approx \nu_c \cdot \nu_c \approx 2\nu_c$

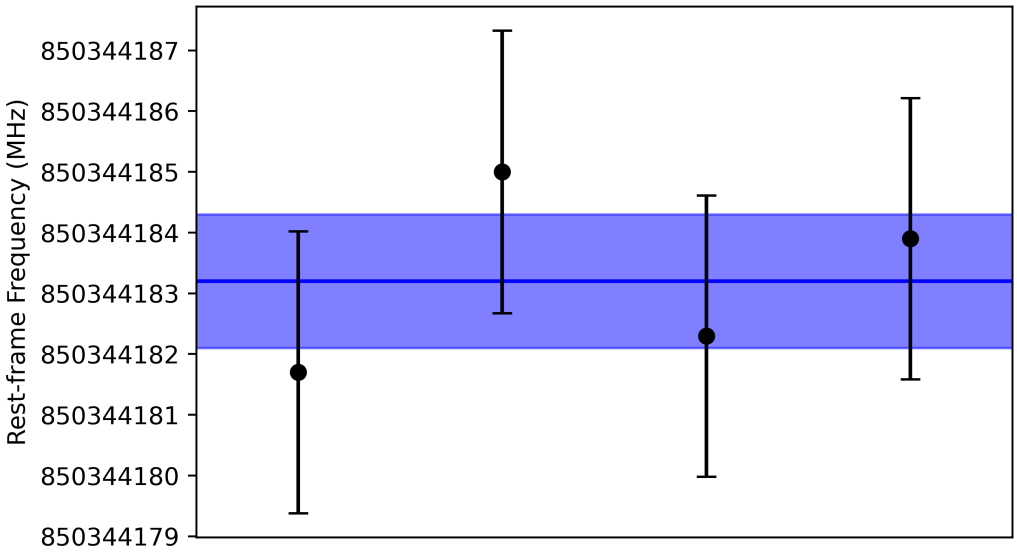

Figure 52: Rest-frame frequencies from DC- and Bunch- mode collinear-anticollinear measurements of ^{60}Ni, two sets each. The blue band shows the weighted mean of the four data points and the statistical uncertainty. The rest-frame frequency from these data was $850\,344\,183.2 \pm 1.1$ MHz., with a ± 20 MHz systematic uncertainty.

(c) $\nu_0 \approx \sqrt{2}\sqrt{\nu_c}$

(d) $\nu_0/\sqrt{2} \approx \sqrt{\nu_c}$

2. *Voltage drifts*, (2.2) MHz: The voltage drifted during the approximately one hour period it took to switch the laser system to the collinear/anticollinear frequencies. Performing the measurements in alternating order (collinear-anticollinear-anticollinear-collinear) allows the voltage fluctuations to be treated statistically because doing so compensates the effect of drifts of the acceleration voltage, which are mainly due to temperature fluctuations.

The systematic uncertainties for the rest-frame frequency are listed below, where the total 20 MHz uncertainty is dominated by the wavelength meter frequency measurement.

1. *Frequency measurement*, 20 MHz (1.4 MHz): The uncertainty in the WSU30 wavelength meter used at BECOLA has a 1σ uncertainty of 10 MHz, which after the frequency doubler becomes 20 MHz. This uncertainty was investigated in Refs. [106, 107], where it originates from a constant offset for measurements at the same wavelength if frequently calibrated with the same reference laser. On top of this offset, only relatively small variations have been observed, translating to a 1 MHz uncertainty

at 1σ [77]. The uncertainty can be determined using

$$\sigma_{\nu_{0,\mathrm{var}}} = \frac{1}{\sqrt{2}}\sigma_{\nu_{\mathrm{WM-var}}} \times 2 = 1.4\,\mathrm{MHz} \tag{69}$$

2. *Lineshape*, 1 MHz: Detailed in Sec. 3.2.7, the resonance lineshape is asymmetric due to inelastic collisions with Na atoms in the CEC. Data fitting was compared using an asymmetric pseudo-Voigt [108] and a symmetric pseudo-Voigt, and discrepancies between resulting ν_0 values are below 1 MHz.

3. *Beam alignment*, 0.8 Mhz: The misalignment between collinear and anticollinear laser beams was estimated to be less than 1 mrad. The maximum frequency deviation was calculated by using Eq. 70, with α being the angles between the atomic beam and collinear or anticollinear geometry. The laser light path spanned a distance of 2.1 m with two 3 mm apertures leading to a maximal angular deviation of 2 mrad. By restricting $\alpha < 2\,\mathrm{mrad}$ and $|\alpha_\mathrm{c} - \alpha_\mathrm{a}| < 1\,\mathrm{mrad}$, the largest deviation is 0.8 MHz.

$$(\Delta\nu_{0,\mathrm{align}})^2 = \nu_\mathrm{c}\nu_\mathrm{a}\gamma^2(1-\beta\cos\alpha_\mathrm{c})(1+\beta\cos\alpha_\mathrm{a}) \tag{70}$$

4.5 High Voltage Calibration and Interpolation

With the rest-frame frequency determined, the high voltage as well as the beam energy could be calibrated for each reference isotope measurement. One method for determining the calibrated high voltage is shown below. An alternative method can be found in Appx. I.

1. Choose an initial beam energy guess and perform a fit to the data

$$E_{\mathrm{kin\,guess}} = 29\,850\,\mathrm{V} \tag{71}$$

2. Determine the beam energy using the rest-frame frequency.

$$E_{\mathrm{kin\,rest}} = \frac{\mathrm{mass}}{2} \cdot \frac{(\nu_0 - \nu_\mathrm{laser})^2}{\nu_0\nu_\mathrm{laser}} \tag{72}$$

3. Determine the beam energy using the fit centroid.

$$E_{\mathrm{kin\,fit}} = \frac{\mathrm{mass}}{2} \cdot \frac{(\nu_\mathrm{fit} - \nu_\mathrm{laser})^2}{\nu_\mathrm{fit}\nu_\mathrm{laser}} \tag{73}$$

4. Find the beam energy offset using the beam energies from Steps 2 and 3.

$$E_{\text{kin offset}} = E_{\text{kin rest}} - E_{\text{kin fit}} \tag{74}$$

5. Determine the calibrated beam energy using the offset.

$$E_{\text{kin cal}} = E_{\text{kin guess}} + E_{\text{kin offset}} \tag{75}$$

In order to obtain the most accurate isotope shift and produce the clearest spectrum for ^{54}Ni, the voltage needed to be calibrated approximately every 6 hours (Fig. 53). By interpolating this voltage between two calibration measurements, using the time stamp on each data file, a more precise beam energy for each measurement could be obtained (Fig. 54). Voltage interpolation was also performed on ^{62,64}Ni measurements which were typically 20 and 60 minutes, respectively, a much longer scan time when compared to ^{58,60}Ni which were typically 5 minutes. The errorbars in Fig. 53 originate from:

1. *Fit uncertainty*, ≤ 0.6 MHz: Same as described in Sec. 4.4.

2. *Lineshape*, 1 MHz: Same as described in Sec. 4.4.

3. *Local wavelength-meter variations*, 2 MHz: A 1 MHz uncertainty of the wavelength meter reading was considered. To account for frequency doubling, this value was multiplied by a factor of two.

4. *Helium-neon laser drift*, 2 MHz: Drifts of the He:Ne laser frequency, which is used to calibrate the wavelength meter, vary from day-to-day.

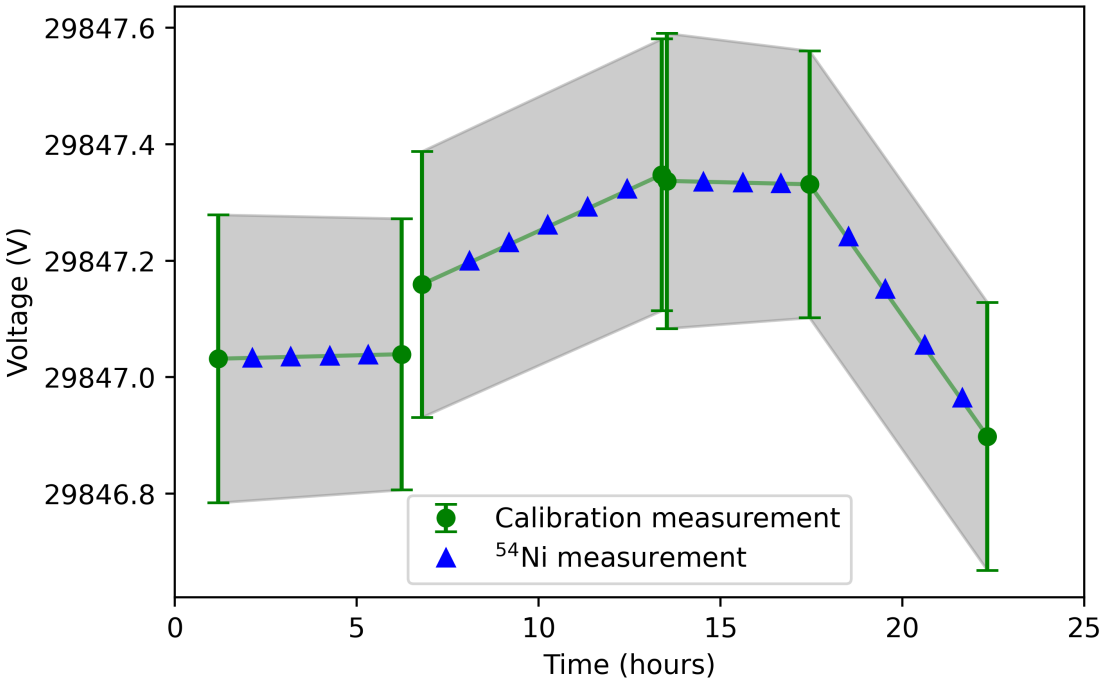

Figure 53: Calibration voltages (green) and ^{54}Ni measurements (blue), with their respective voltages as a function of time. Calibration measurements were performed approximately every six hours.

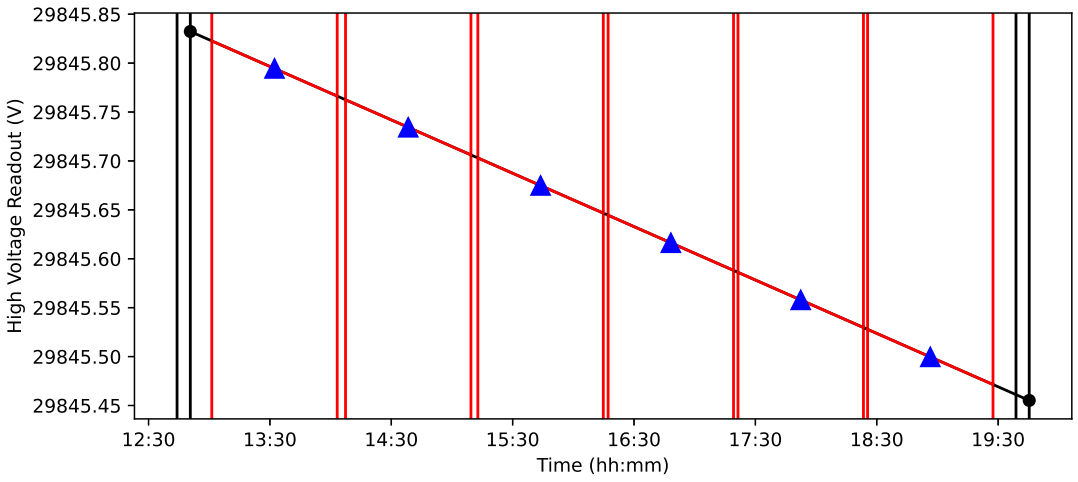

Figure 54: Beam energy interpolation for ^{54}Ni measurements (red) using stable ^{60}Ni as the two calibration measurements (black). The black and red vertical lines are the boundaries of the measurement time. Black points are the calibration measurements, and blue triangles are the interpolated voltage values.

4.6 Fitting Hyperfine Spectra

The resulting spectrum for ^{54}Ni is shown in Fig. 56 using an asymmetric pseudo-Voigt from Ref. [108]. The full width at half maximum (γ_0), asymmetry (a), and fraction (f) were constrained in the least-squares minimization fit for the ^{54}Ni spectrum. The values for those constraints were obtained from stable ^{60}Ni spectra. Although there are many functions that can be used to fit spectra, it is important to have meaningful parameters in the lineshape model that have direct correspondence to physical phenomena. A pseudo-Voigt function is the sum of two components: a Gaussian curve that describes the broadening mechanisms and a Lorentzian curve which describes the natural lineshape. An asymmetric pseudo-Voigt from Ref. [108] is detailed below where its general form is

$$y(\nu) = \underbrace{f L(\nu)}_{\text{Lorentzian}} + \underbrace{(1-f)\, G(\nu)}_{\text{Gaussian}} \tag{76}$$

where f is the fraction of Lorentzian to Gaussian with a range from 0 to 1; a value of $f = 0$ indicates a pure Gaussian and $f = 1$ indicates a pure Lorentzian. As shown in the previous equation, there are two components to a pseudo-Voigt function:

1. The Gaussian component
$$G(\nu) = \frac{A}{\gamma_0}\sqrt{\frac{4\,\ln(2)}{\pi}}\, e^{-4\,\ln(2)\left(\frac{\nu-\nu_0}{\gamma_0}\right)^2} \tag{77}$$

2. and the Lorentzian component
$$L(\nu) = \frac{\frac{2A}{\pi\gamma_0}}{1+4\left(\frac{\nu-\nu_0}{\gamma_0}\right)^2} \tag{78}$$

where ν_0 is the centroid, ν is the frequency, γ_0 is the full width at half maximum (FWHM), and A is the area under the peak. In order to obtain an asymmetry in the lineshape, we make a substitution for γ_0 with $\gamma(\nu)$, where

$$\gamma(\nu) = \frac{2\gamma_0}{1+e^{a(\nu-\nu_0)}} \tag{79}$$

and a is the asymmetry parameter. The asymmetric portion of the function is used to describe inelastic collisions with the sodium vapor detailed in Sec. 3.2.7. The baseline was represented by a constant because the background itself remained constant. If, for example, the power were to drift during the measurement, the background would increase and a linear baseline would be more appropriate. Also included below in Fig. 57 are the hyperfine spectra for the stable Ni isotopes. As aside, the `LMFIT` package in `python` does not contain an asymmetric pseudo-Voigt presented here; only symmetric Voigt and symmetric pseudo-Voigt functions. `LMFIT` does have an asymmetric Voigt function (`SkewedVoigt`), however, its fits are widely unpredictable

and can do a poor job at estimating the centroid (see Appx. D).

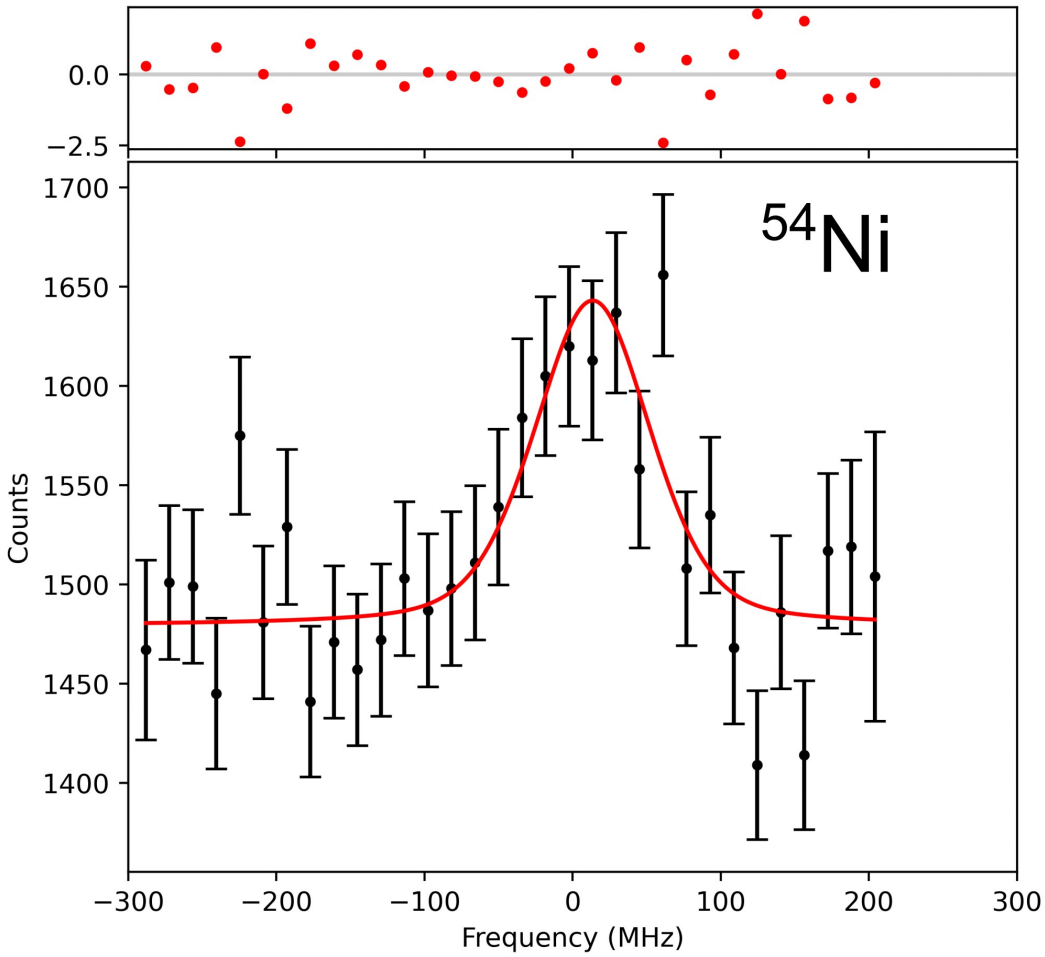

Figure 55: Hyperfine spectrum for ^{54}Ni after 8454 scans. Uncertainties in the data points are the standard deviation on each photon count (see Sec. B.3).

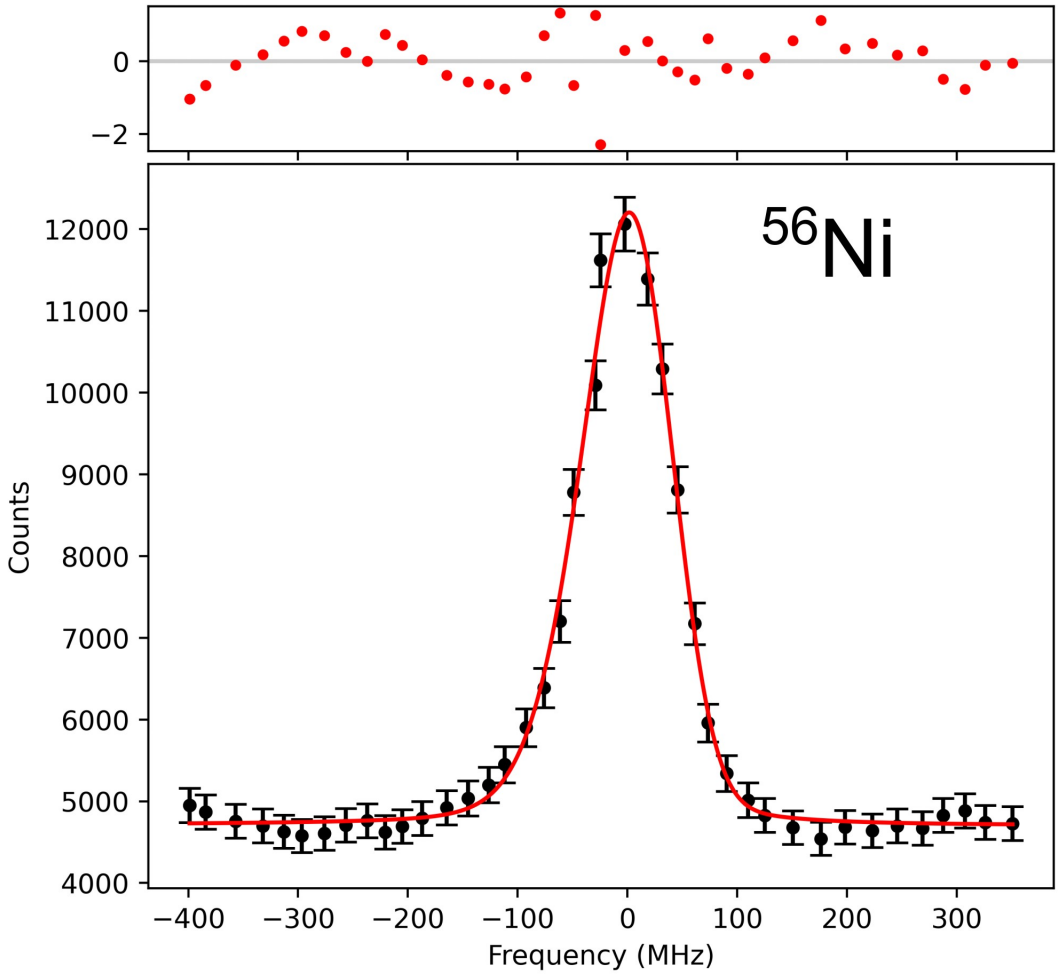

Figure 56: Hyperfine spectrum for ^{56}Ni. Uncertainties in the data points are the standard deviation on each photon count (see Sec. B.3).

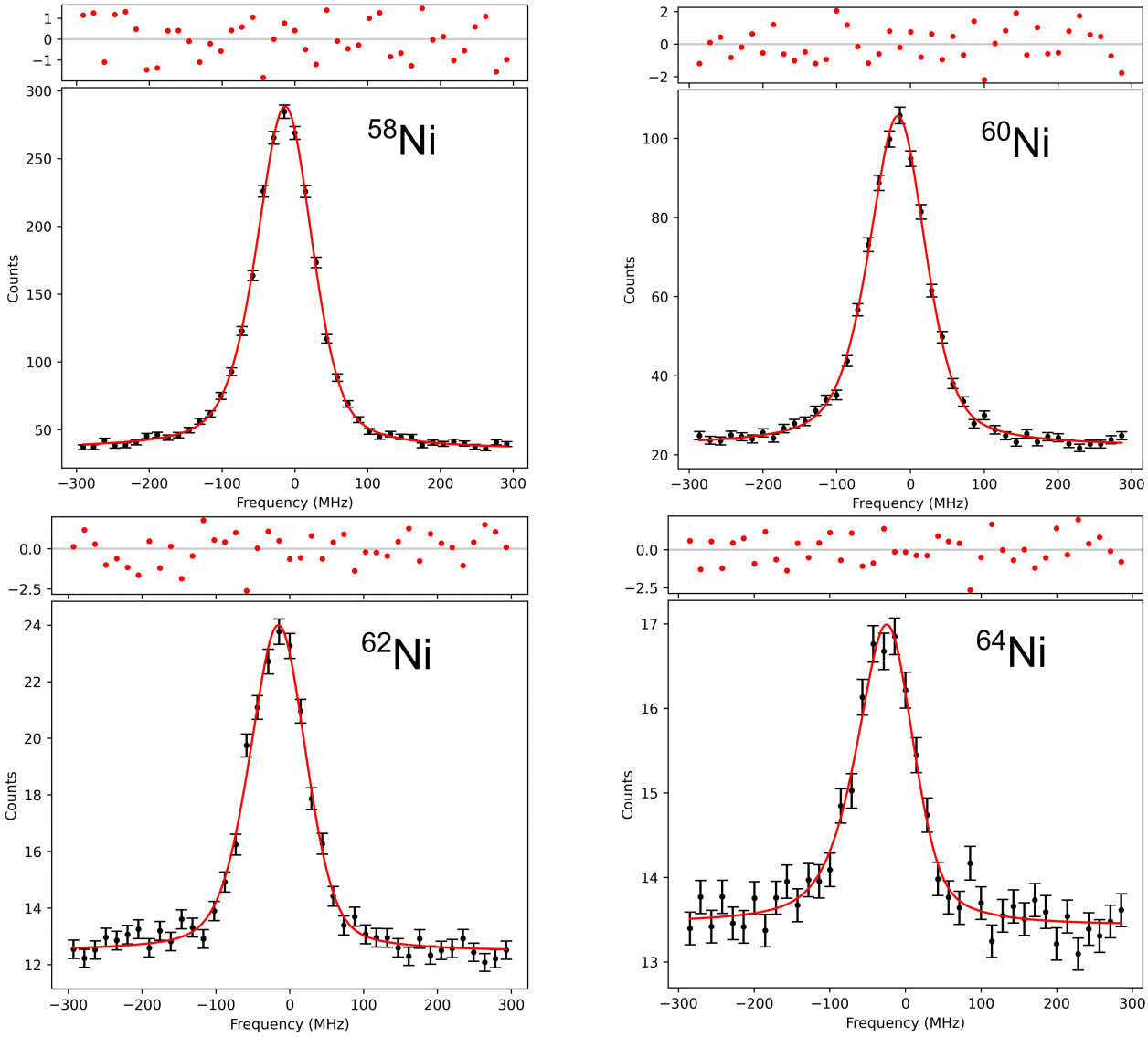

Figure 57: Spectra for stable Ni isotopes. ^{58}Ni after two scans (top left), ^{60}Ni after three scans (top right), ^{62}Ni after twenty scans (bottom left), ^{64}Ni after sixty scans (bottom right). Uncertainties in the data points are the standard deviation on each photon count (see Sec. B.3).

4.7 Isotope Shift Measurements

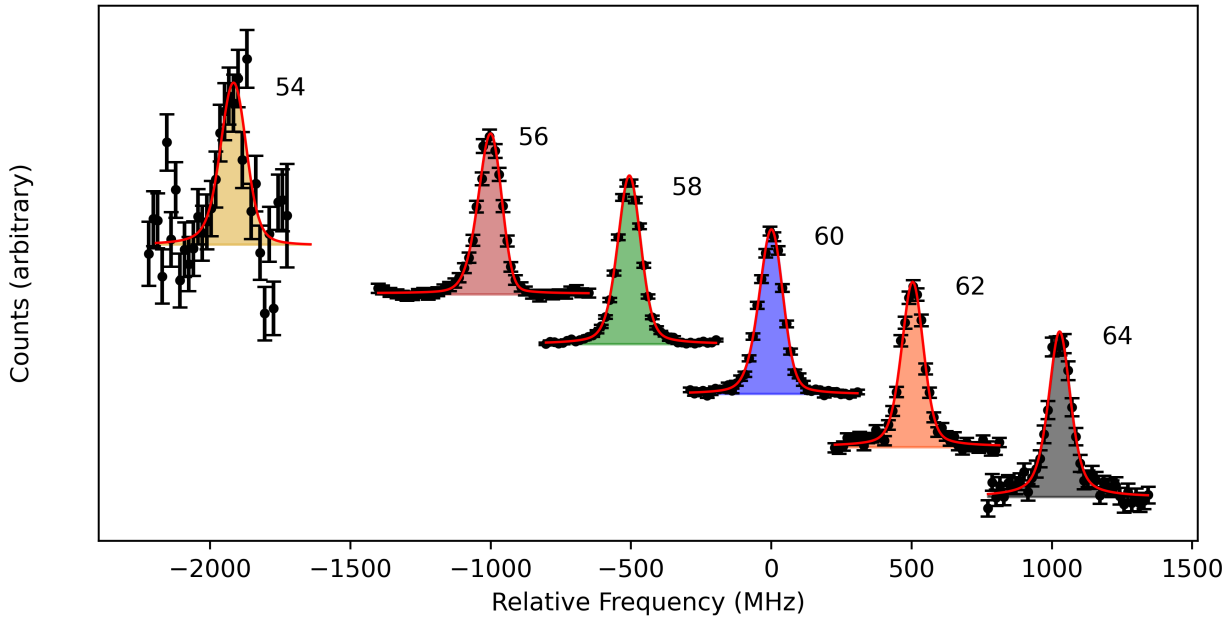

Figure 58: Nickel spectra for even isotopes measured at BECOLA relative to ^{60}Ni.

Typical resonance spectra for stable nickel isotopes are shown above in Fig. 58. A weighted average of isotope shift measurements was taken for each day of data. ^{60}Ni was chosen as the reference isotope due to the achievable accuracy of the differential mean-square charge radius. When plotting the uncertainty of the differential mean-square charge radius $\sigma_{\delta\langle r^2\rangle^{54,A'}}$ as a function of isotope shift for ^{54}Ni, ^{60}Ni is favored in terms of the reference isotope [83].

Table 8: Resonance spectra for even-even nickel isotopes measured at BECOLA.

$\nu^{58,60}$ (MHz)	$\nu^{62,60}$ (MHz)	$\nu^{64,60}$ (MHz)
-506.3 ± 2.3	504.4 ± 2.7	1028.2 ± 2.6

The following systematic uncertainties were added in quadrature to isotope shift results (Fig. 59) at each beam energy before taking the weighted average over all of the results:

1. *Beam energy determination*, < 0.3 MHz: The uncertainty of the beam energy determination based on the collinear and anticollinear approach was below 0.3 eV. [77].

2. *Line shape*, 0.5 MHz: Comparisons between symmetric and asymmetric pseudo-Voigt functions yielded deviations of up to 0.5 MHz.

3. *Bunching*, 2 MHz: A systematically different isotope shift is observed when using DC-mode versus bunched-mode for the ion beam. The origin of this discrepancy is unclear. Conservatively, a 2 MHz contribution that brides the gap outside the combined fit uncertainties was added.

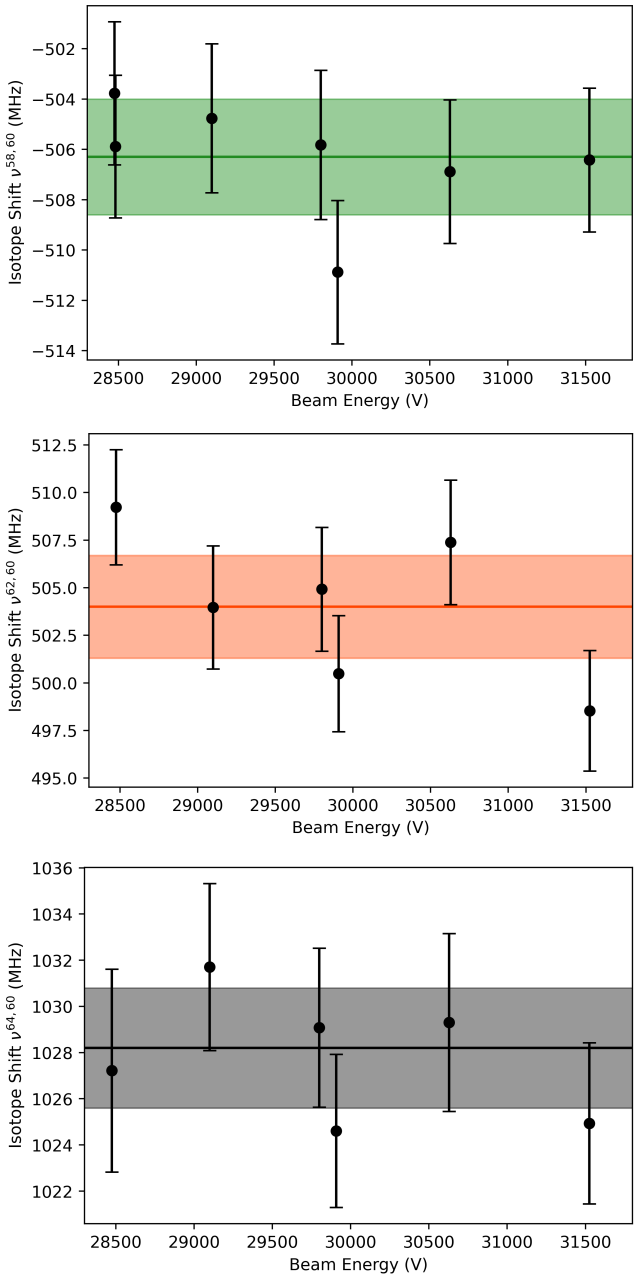

Figure 59: Isotope shifts (^{58}Ni (top), ^{62}Ni (middle), ^{64}Ni (bottom)) for stable Ni isotopes at each beam energy relative to ^{60}Ni. The band is the weighted average of all data points within the plot.

A combination of three different approaches were used to obtain the final isotope shift value between ^{58,60}Ni. The wavelength meter result is shown in the table above. The other two approaches are the rest-frame frequencies from the collinear-anticollinear measurements [77] and referencing the laser frequency to a well-known natural transition line in diatomic iodine (I_2) [100]. The results from all three methods, shown in the table below, agree with each other and the weighted average between all three was taken to obtain the final isotope shift for ^{58,60}Ni.

Table 9: Isotope shift between ^{58,60}Ni.

Method	$\nu^{58,60}$ (MHz)	σ_{stat} (MHz)	σ_{tot} (MHz)
Wavelength Meter	−506.3	1.1	–
Iodine Reference	−507.0	0.9	–
$\text{Mean}_{\text{meter, iodine}}$	−506.7	0.8	2.2
Col./Acol.	−505.6	–	3.9
Final	−506.4	–	1.9

4.8 Model-independent Charge Radii

In order to perform the King-plot, values for model-independent charge radii were extracted from Fricke. The model-independent rms charge radii were calculated by combining the tabulated values [57] for the Barrett radii $R_{k\alpha}$ and for the ratio of radial moments V_2 from electron scattering. The resulting rms radii calculated from the procedure described in Section 2.5 (Tab. 2) are shown below in Tab. 10. Differential root mean squared charge radii extracted using Eq. 55 are shown in Tab. 11.

Table 10: Model-independent RMS charge radii. Left of the dividing line are the final results for ms charge radii, while on the right are the values from Ref. [57] used to deduce them. All $R_{k\alpha}$ values are listed in fm. V_2 values are unitless.

Isotope	rms charge radii (fm)	$R_{k\alpha}$	$\sigma R_{k\alpha\,\text{exp}}$	$\sigma R_{k\alpha\,\text{theo}}$	$\sigma R_{k\alpha\,\text{tot}}$	V_2
$R(^{58}\text{Ni})$	3.7698 ± 0.0016	4.8386	0.0007	0.0019	0.0020	1.283517
$R(^{60}\text{Ni})$	3.8059 ± 0.0017	4.8865	0.0007	0.0020	0.0021	1.283944
$R(^{54}\text{Fe})$	3.6880 ± 0.0017	4.7358	0.0009	0.0020	0.0022	1.284120

Table 11: Differential MS charge radii from Ref. [57].

$\delta\langle r^2\rangle^{A,A'}$	(fm^2)
$\delta\langle r^2\rangle^{58,60}$	-0.2731 ± 0.0048
$\delta\langle r^2\rangle^{62,60}$	0.2266 ± 0.0048
$\delta\langle r^2\rangle^{64,60}$	0.3631 ± 0.0048

4.9 The King-plot

Once the differential ms charge radii were extracted and the isotope shifts were deduced, the King-plot analysis (Fig. 60) was performed. A linear regression analysis procedure taken from Ref. [85] was used, and details on the linear regression can be found in Appx. J. The α parameter was stepped until the final uncertainty in K_α was at a minimum, in this case when $\alpha = 388$.

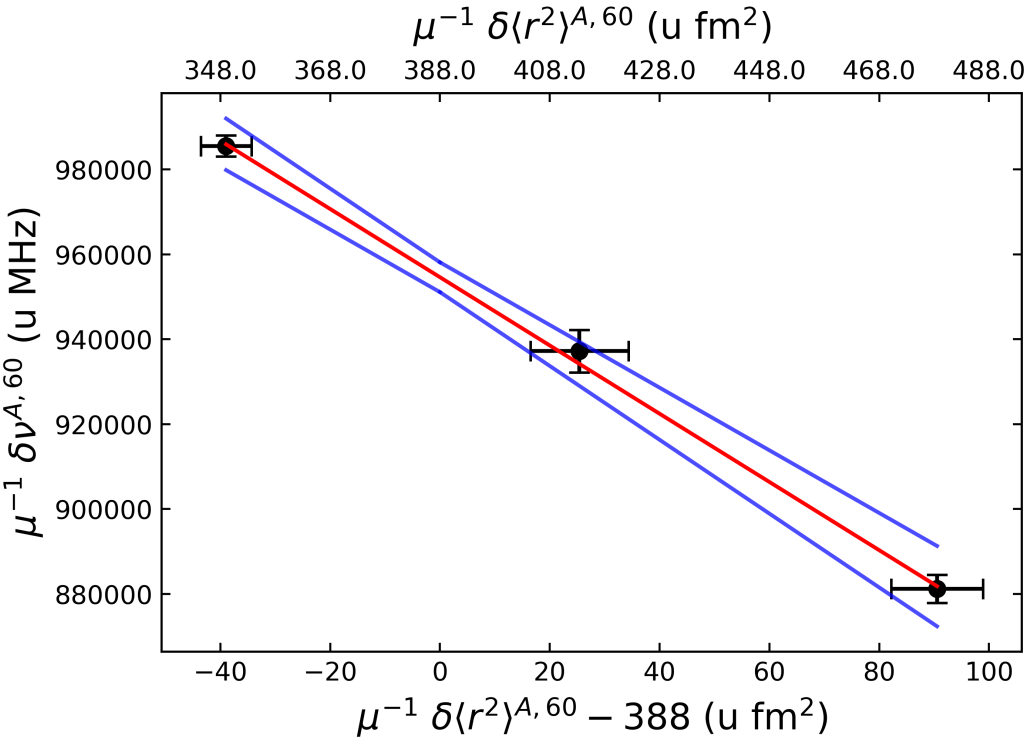

Figure 60: King-plot shifting the alpha term. The top x-axis shows the shifted α parameter. The bottom x-axis shows the new ajusted points from the linear regression analysis.

Table 12: King-plot results

F	K_0	K_α	α	$\delta\langle r^2\rangle^{54,60}$
-804 ± 66	1266 ± 26	954.0 ± 3.5	388	-0.522 ± 0.020

Table 13: A table for all of the relevant data to perform the King-plot analysis. The uncertainties in $\mu^{A,A'}$ are on the order of 3.8×10^{-12} and are negligible.

A, A'	$\delta\langle r^2\rangle^{A,A'}$ (fm^2)	$\delta\nu^{A,A'}$ (MHz)	$\mu^{A,A'}$ (amu)
$58, 60$	-0.2731 ± 0.0048	-506.4 ± 1.9	-0.00057470
$60, 62$	0.2266 ± 0.0048	504.4 ± 2.7	0.00053821
$60, 64$	0.3631 ± 0.0048	1028.2 ± 2.6	0.00104329

4.10 Difference in Mirror Pair Charge Radii

In order to get the difference in mirror pair charge radii, one must convert the differential mean squared charge radius from the King-plot to the absolute charge radius. To extract the absolute charge radius for ^{54}Ni, the literature value for ^{60}Ni from Fricke which was extracted above (Tab. 10) must be used in conjunction with the differential mean squared charge radius from the King-plot (Tab. 12). The charge radius was extracted using

$$R\left(X\right)^{A} = \sqrt{\left(R\left(X\right)^{A'}\right)^{2} + \delta\langle r^{2}\rangle^{A,A'}} \tag{80}$$

where X is the element of interest. For our purposes this equation then becomes

$$R\left(\mathrm{Ni}\right)^{54} = \sqrt{\left(R\left(\mathrm{Ni}\right)^{60}\right)^{2} + \delta\langle r^{2}\rangle^{54,60}} \tag{81}$$

and the charge radius of ^{54}Ni is $3.737\,(3)$ fm.

With the charge radii from both mirror pairs known, the difference in mirror pair charge radii can be deduced using

$$\Delta R_{\mathrm{ch}} = R\left(^{54}\mathrm{Ni}\right) - R\left(^{54}\mathrm{Fe}\right) \tag{82}$$

to get $\Delta R_{\mathrm{ch}} = 0.049\,(4)$ fm.

5 Results

5.1 Density Functional Theory and the Skyrme Interaction

In nuclear Density Functional Theory (DFT) [109], effective internucleon interaction is represented by the Energy Density Functional (EDF) adjusted to experimental data and often also to selected nuclear matter parameters [53]. DFT has been used in nuclear models to successfully reproduce characteristics like binding energies, kinks in the systematics of charge radii, and odd-even staggering along the isotopic chain [110, 109, 111, 112, 113, 53, 114]. Self-consistent mean-field models use effective interactions in place of true nucleon-nucleon interactions to achieve descriptions of nuclei beyond present-day capabilities of *ab-initio* calculations [109]. The total binding energy from the Skyrme [115, 116] interaction is given by the sum of the kinetic energy, Skyrme energy density functional that models the effective interaction between nucleons, the Coulomb energy, the pair energy, and corrections for spurious motion [109].

5.2 Quadrupole Deformation as a Correction to Spherical Radii

Because quadrupole correlations increase the rms radii [43, 117], quadrupole deformation effects were taken into account as a correction to the calculations for spherical nuclei [60, 114]. While performing this correction two **Conditions** are enforced:

1. the nuclear matter density is saturated and the average interior density remains constant
2. deformation is not the same between neutron and proton matter

5.2.1 Bohr Collective Model to Evaluate the Change in RMS Radius

The Bohr Hamiltonian starts as an expansion of the nuclear surface in terms of its multipole degrees of freedom is shown in Eq. 83, where R_0 is a spherical radius of the nucleus, $Y_{\lambda,\mu}(\theta,\phi)$ is the spherical harmonic, and $\alpha_{\lambda,\mu}$ is a coefficient dependent on the β value. β, in this case, is a transformed y coordinate from a coordinate system obtained from the Euler-angle rotation $\theta = (\alpha, \beta, \gamma)$.

$$R(\theta,\phi) = R_0 \left[1 + \sum_{\lambda,\mu} \alpha_{\lambda,\mu} Y_{\lambda,\mu}\left(\theta,\phi\right) \right] \tag{83}$$

The volume integral of Eq.83, to the order of β^2, is

$$\begin{aligned} I_0 &= \int_\Omega \int_0^{R(\theta,\phi)} r^2 dr\, d\Omega \\ &= \frac{1}{3}\int_\Omega \left[R\left(\theta,\phi\right)\right]^3 d\Omega \\ &= \frac{R_0^3}{3}\left[4\pi + 3\alpha_0\sqrt{4\pi} + 3\sum_\lambda \beta_\lambda^2\right] \end{aligned} \tag{84}$$

In order to impose **Condition 1** (conservation of the nuclear volume),

$$\alpha_{0,q} = -\frac{\beta_q^2}{\sqrt{4\pi}}, \tag{85}$$

where q indicates the proton ($q = p$), neutron ($q = n$), or matter distributions ($q = m$). With $q = m$ for matter and **Condition 1** imposed, the volume integral I_0 becomes

$$I_0 = \frac{4\pi R_{0,m}^3}{3} \tag{86}$$

The I_2 volume integral to the order of β^2 for r^2 can be obtained in a similar fashion where

$$\begin{aligned} I_2 &= \int_\Omega \int_0^{R(\theta,\phi)} r^4 dr\, d\Omega \\ &= \frac{R_0^5\left(4\pi + 5\alpha_0\sqrt{4\pi} + 10\beta^2\right)}{5} \\ &= \frac{R_0^5}{5}(4\pi + 5\beta^2) \end{aligned} \tag{87}$$

Using I_0 and I_2 the matter mean-square radius is

$$\langle r^2\rangle = \frac{I_2}{I_0} = \underbrace{\langle r^2\rangle_{0,m}}_{\text{Spherical}}\underbrace{\left[1 + \frac{5}{4\pi}\beta_m^2\right]}_{\text{Deformation}} \tag{88}$$

where the spherical ms radius with no deformation is

$$\langle r^2\rangle_{0,m} = \frac{3R_{0,m}^2}{5} \tag{89}$$

If $\beta_p = \beta_n = \beta_m$, then Eq.88 could be used for protons. However, because we are imposing **Condition 2** where $\beta_p \neq \beta_n$, assumptions must be made about the α_0 term. We take $\alpha_{0,p} = \alpha_{0,n} = \alpha_{0,m}$ for the volume

correction, and substitute $\alpha_{0,q}$ from Eq.85 to obtain the ms radius of the protons (Eq. 90).

$$\begin{aligned}\langle r^2\rangle_p &= \langle r^2\rangle_{0,p}\left[1+\frac{2\alpha_{0,p}}{\sqrt{4\pi}}+\frac{7}{4\pi}\beta_p^2\right] \\ &= \langle r^2\rangle_{0,p}\left[1-\frac{2}{4\pi}\beta_m^2+\frac{7}{4\pi}\beta_p^2\right]\end{aligned} \tag{90}$$

For $\lambda = 2$, the β_p are related to the $B\left(E2,\uparrow\right)_p$ (in units of e^2) for 0^+ to 2^+ states by

$$\beta_p = \frac{4\pi\sqrt{B\left(E2,\uparrow\right)_p}}{5a_q\langle r^2\rangle_{0,p}} \tag{91}$$

where $a_q = Z$ for protons (β_n has $a_q = N$ and β_m has $a_q = A$). The $B(E2,\uparrow)_n$ and $B(E2,\uparrow)_m$ are much less known, but $B(E2,\uparrow)_p$ can be compared to experimental results.

5.2.2 Determination of $B(E2,\uparrow)_p$ for ^{54}Ni

The $B(E2,\uparrow)_p$ for ^{54}Ni has not been determined experimentally and therefor needed to be theoretically calculated in order to obtain β_p (Eq. 91) and perform the deformation correction. $B(E2,\uparrow)_p$ depend on the $E2$ matrix elements (Eq. 92), which were calculated in the fp model space with the GFPX1A [118] and KB3G [119] Hamiltonians.

$$M_q = \sqrt{B\left(E2,\uparrow\right)_p} \tag{92}$$

The full matrix element was obtained with "effective charges", e_q, that arise from the coupling of the fp nucleons to the $2\hbar\omega$ giant quadrupole resonances where the $E2$ matrix elements are denoted by A_q. For mirror symmetry we assume that $A_p(^{54}\text{Ni}) = A_n(^{54}\text{Fe})$ and $A_n(^{54}\text{Ni}) = A_p(^{54}\text{Fe})$. We can write the full matrix element (Eq. 93) in terms of its isoscalar (0) and isovector (1) contributions

$$M_p = M_0 + M_1 = A_0e_0 + A_1e_1 \tag{93}$$

where $A_0 = \frac{A_p+A_n}{2}$, $A_1 = \frac{A_p-A_n}{2}$, $e_0 = e_p + e_n$, and $e_1 = e_p - e_n$. $E2$ transitions are dominated by the isoscalar matrix element A_0 and the isoscalar effective charge, $e_0 = 2.0 \pm 0.1$ [120]. While the $B(E2)$ values for ^{54}Ni are not known experimentally, the values for ^{54}Fe are. Once the A_p and e_p are known for the full matrix element, calculations using ^{54}Fe can be compared to experiment and then used to find the $B(E2)$ and subsequently β_p for ^{54}Ni. The $E2$ matrix elements calculated for both the GPFX1A and KB3G interactions for ^{54}Fe are shown in Tab.14.

In the case of ^{54}Fe, $M_p > M_n$ since the wave functions for the 0^+ and 2^+ states are dominated (about 50%) by the configuration with two proton $0f_{7/2}$ holes in a ^{56}Ni closed-shell configuration. The main contribution to

Interaction	A_p	A_n	A_0	A_1
GPFX1A	16.5	7.9	12.2	4.3
KB3G	14.8	6.0	10.4	4.4

Table 14: A_q matrix elements for ^{54}Fe in units of fm^2.

the radius shift is from the isoscalar M_1 term. The isovector effective charge e_1 was determined by comparing the $E2$ transition in ^{51}Fe-^{51}Mn mirror pair [121]. That data was reanalyzed with GPX1A (Tab. 15). The e_1 is reduced from its free nucleon value of one, due to coupling of the fp nucleons to the isovector giant-quadrupole resonance. Based on these results we adopt a refined value of $e_1 = 0.44 \pm 0.10$. Using the new

Interaction	A_1	e_1
KB3G	5.86	0.37 ± 0.08
GPFX1A (Ref. [121] harmonic-oscillator parameter)	4.56	0.47
GPFX1A (new harmonic-oscillator parameter)	4.85	0.44 ± 0.10

Table 15: GPFX1A isovector results.

value of $e_1 = 0.44 \pm 0.10$, the values of $e_p = 1.22$ and $e_n = 0.78$ were obtained. The results for $B(E2)$ values for ^{54}Fe are shown below, showing that the theoretical results agree with the experimental value.

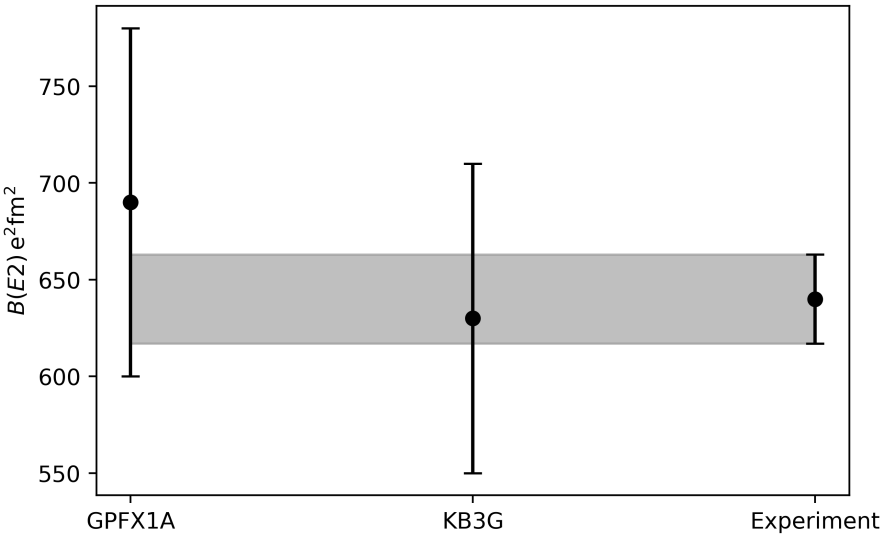

Figure 61: Theoretical $B(E2,\uparrow)$ values from Ref. [60] compared to experiment [122] for ^{54}Fe. Values left to right are 690 ± 90, 630 ± 80, and 640 ± 23 for GPFX1A, KB3G, and experiment, respectively.

The theoretical errors are dominated by the error in e_0. For a given value of M_1, we can used the experimental $M_p(\text{exp}) = 25.3 \pm 0.5\, e\text{fm}^2$ [122] to constrain M_0 using

$$M_0 = M_p(\text{exp}) - M_1. \tag{94}$$

The results for the ^{54}Fe and ^{54}Ni β values are shown in the table below. The $B(E2) = 460 \pm 40\, e^2\text{fm}^4$ for

Isotope	β_p	β_n	β_m
^{54}Fe	0.186 ± 0.004	0.147 ± 0.007	0.166 ± 0.005
^{54}Ni	0.147 ± 0.007	0.186 ± 0.004	0.166 ± 0.005

Table 16: β_q values between mirror radii. Notice that due to the mirror symmetry $\beta_p(^{54}\text{Ni})$ is equivalent to $\beta_n(^{54}\text{Fe})$ and vice versa.

^{54}Ni. The difference between the ^{54}Fe and the ^{54}Ni results between the GPFX1A and KB3G interactions is very small since the A_1 values are almost the same. Although the theoretical $B(E2)$ for should be close to the experimental value, the predicted $B(E2)$ for ^{54}Ni should be verified experimentally. Its resulting contribution to ΔR_{ch} is a shift of $-0.0131 \pm 0.0017\,\text{fm}$, with the error in ΔR_{ch} dominated by the error in e_1.

The quadrupole correlations are explicitly contained in the CHFB + 5DCH calculations using the D1S Hamiltonian given in Refs. [123, 124]. They obtain $\Delta R_{\text{ch}}(\text{deformed}) = 0.058$ fm that goes with $L = 22.3$ MeV [125] for D1S. Their $B(E2)$ values are 1310 and $1580\, e^2\text{fm}^2$ for ^{54}Fe and ^{54}Ni, respectively. This does not agree with experiment or the shell-model calculations, presumably because the ^{56}Ni core is too soft compared to experiment and the shell model.

Figure 62 shows the β-correction in practice with theoretical (red x's) and experimental (black points) charge radii for $N = 28$ isotones ranging from ^{48}Ca to ^{56}Ni. It is clear that the theoretical β_2 correction for deformation reproduces experimental results significantly well. The straight line across represents a spherical nucleus, where, if the nuclei were spherical, they would lie along the line. Because in reality each of the isotones in between are deformed, the experimental values deviate from the line and the β_2 correction successfully accounts for that deformation.

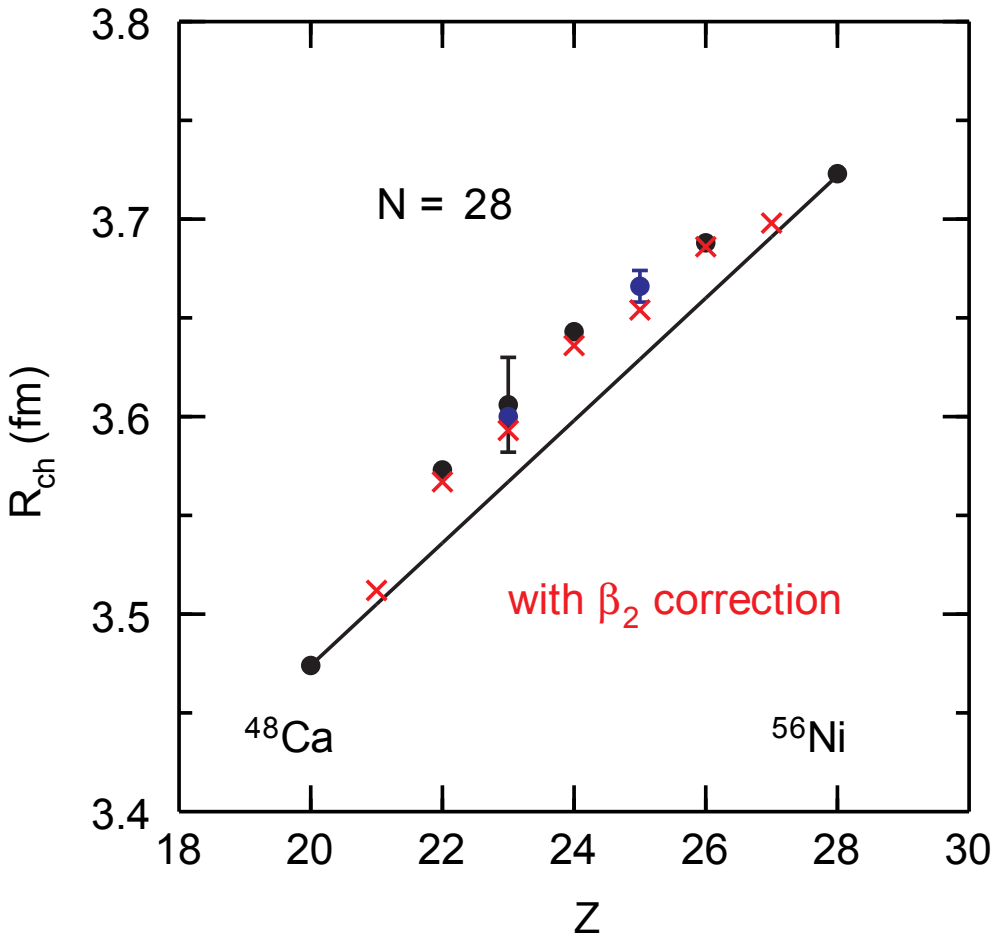

Figure 62: Charge radii for $N = 28$ isotones ranging from ^{48}Ca to ^{56}Ni. Experimental values are represented by the black circles and the Skyrme results with the β_2 correction are shown as red x's. The straight black line is to demonstrate the deformity of radii going between the magic numbers 20 and 28, showing that if they were indeed spherical they would lie along the line. Figure courtesy of B. Alex Brown.

5.3 Constraints on L Using the $A = 54$ Mirror Pair

The quadrupole correction for $\Delta R_{\rm ch}$ is added to the Skyrme and COvariant Density Functional (CODF) calculations performed in the spherical basis. CODF is the relativistic description of nuclear systems (relativistic mean-field calculation). The Skyrme results for $\Delta R_{\rm ch}$ are the colored points in Fig. 63 each with constraints in the form of the neutron skin thickness, based on ^{208}Pb: 0.12 (red), 0.16 (orange), 0.20 (green), and 0.24 (blue) fm. The CODF results are shown as crosses. Theoretical uncertainties are the grey dashed lines, which again have an uncertainty dominated by the e_1 effective charge. The experimental $\Delta R_{\rm ch}$ result is shown as the grey band. Using Fig. 63 a constraint of $21 \leq L \leq 88$ MeV was placed by taking the points at which the theoretical uncertainty (grey dashed lines) and the experimental result (grey band) intersected. Discussed in [126], Skyrme results for the $A = 36$ mirror pair were found to be sensitive to the isoscalar (IS) and isoscalar plus isovector (IS + IV) forms of the spin-orbit potential. However, the calculations for the $A = 54$ pair are insensitive to the forms, with the IS result about 0.003 fm larger in $\Delta R_{\rm ch}$, which is negligible when compared to the uncertainty in $\Delta R_{\rm ch}$ and the shift observed in $A = 36$ (Sec. 5.4.1) [60]. Due to this insensitivity, the 48 Skyrme energy-density functionals shown in Fig. 63 are the results of the IS + IV form. Results from GW170817 [7] and PREX-2 [25] are shown in the top part of Fig. 63, showing good agreement with the astrophysical results but limited agreement with PREX-2. The BECOLA result supports a soft EOS, which implies a smaller, more compact neutron star. This disagrees with the stiff EOS tendency from PREX-2.

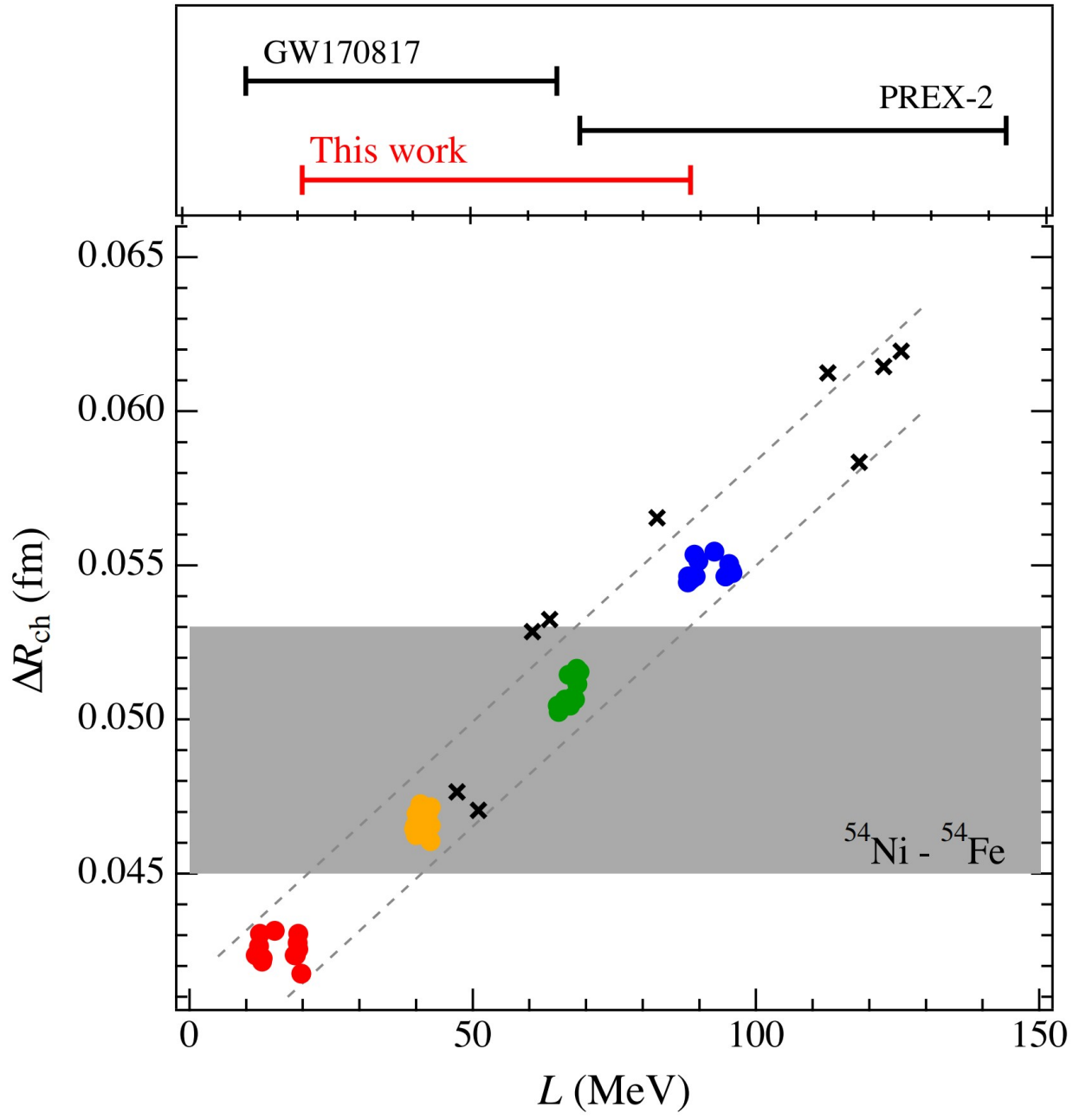

Figure 63: $\Delta R_{\rm ch}$ as a function of L at ρ_0. The experimental result is shown as a horizontal gray band. The solid circles are results of Skyrme EDF and the crosses are for the CODF calculations. The dashed lines indicate theoretical error bounds. The upper figure shows comparison with the GW170817 and the PREX-2.

5.4 Constraints on L in Other Mass Systems

5.4.1 L Results for $A = 36$ and $A = 38$ Based on Ca

The first mirror charge radii pairs used to constrain L were based on neutron deficient Ca isotopes with pairs ^{38}Ca-^{38}Ar and ^{36}Ca-^{36}S [126]. As of today, the $A = 36$ pair has the largest $|N - Z| = 4$ of any known mirror pairs and therefor has the highest sensitivity to L. Also, the ^{36}Ca-^{36}S mirror partners are stable nuclei and their charge radii are well known [57]. The proton radius used to calculate theoretical charge radii was from 2018 CODATA, which is the smaller radius of $r_{\mathrm{p}} = 0.8414 \pm 0.0019\,\mathrm{fm}$ compared to the previously recommended value of $r_{\mathrm{p}} = 0.8775 \pm 0.0051\,\mathrm{fm}$. The difference between theoretical charge radii using the old or more recent value of the proton radius is negligible when placing constraints on L, where the difference of $\Delta R_{\mathrm{ch}} = 0.001\,\mathrm{fm}$ was observed. The linear correlation between the ΔR_{ch} and L can be seen, however there is a 0.10 fm offset between them. This difference can be accounted for based on the functional used for the spin-orbit potential. This potential contains both isoscalar (IS) and isovector (IS + IV) parts. However, in the CODF formalism the spin-orbit potential is dominated by just the IS form. The isospin contributions largely come from isoscalar-scalar ("sigma") and isoscalar-vector ("omega") mesons, which results in a very strong split-orbit interaction. The difference between the Skyrme and CODF forms leads to some changes in the isotope shifts [127, 128], and the Skyrme calculations were recalculated with the isoscalar form (with its strength adjusted to reproduce the spin-orbit splittings). The recalculated results between Skyrme and CODF formalisms agreed with each other after the adjustment was made.

In this analysis, the IMSRG calculations may be treated as predictions because the parameters of the underlying family of chiral NN plus $3N$ interactions have been determined completely in $A \leq 4$ nuclei. The viability of using difference in mirror pair charge radii to constrain next-generation chiral interactions, although more work on quantifying the theoretical unceratinties of IMSRG and other ab initio approaches is still required. The Skyrme IS + IV form and CODF provide consistent results with $15 \leq L \leq 70\,\mathrm{MeV}$, and the addition of an isovector spin-orbit potential for Skyrme would move the lower limit to $5 \leq L \leq 70\,\mathrm{MeV}$. This result is about a factor of 3 more precise than the value of L deduced from PREX-2 [25].

Constraints on the L parameter from $A = 36$, 38 are consistent with those from $A = 54$, supporting a soft neutron EOS. Although a promising observation, the L constraints cannot be compared directly because the $A = 36$, 38 charge radii were not calculated using the β-correction (see Sec. 6.2).

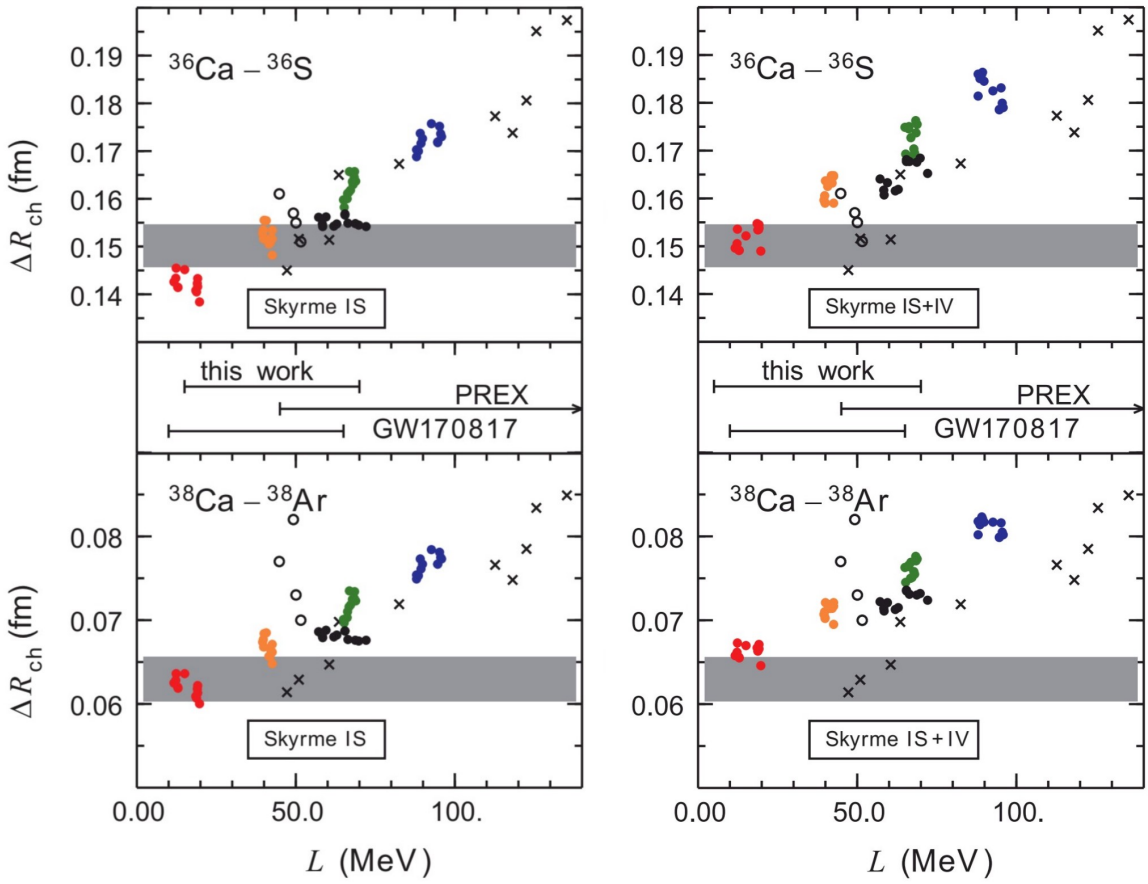

Figure 64: Constraints on L for the $A = 36$ and $A = 38$ systems [126]. Solid circles indicate results from Skyrme EDF, crosses are from CODF, and open circles are from IMSRG calculations. The colored circles have constraints from the neutron skin of ^{208}Pb, with red = 0.12 fm, orange = 0.16 fm, green = 0.20 fm, and blue = 0.24 fm. Black filled circles are a set of 12 Skyrme EDFs with additional constraints that the EDFs reproduce *ab initio* calculations for the low-density neutron equation of state and the maximum mass of a neutron star ($2.1\,M_\odot$).

5.5 Constraints on the Neutron Skin for ^{48}Ca

5.5.1 Constraints on the Neutron Skin for ^{48}Ca Using $A = 54$

The experimental value for the $A = 54$ pair constrained the $0.15 \leq \Delta R_{\rm np}(^{48}{\rm Ca}) \leq 0.21$ fm as shown in Fig. 65 to be compared with the CREX results. The published results $\Delta R_{\rm np}(^{48}{\rm Ca}) = 0.121 \pm 0.026$ [129] agree with the prediction from BECOLA at the lower bound, and in fact trends towards an even softer neutron EOS. This neutron skin thickness agrees with the soft EOS, again showing disparity from the PREX results. All anticipated constraints on $\Delta R_{\rm np}(^{48}{\rm Ca})$ are shown in Fig. 67.

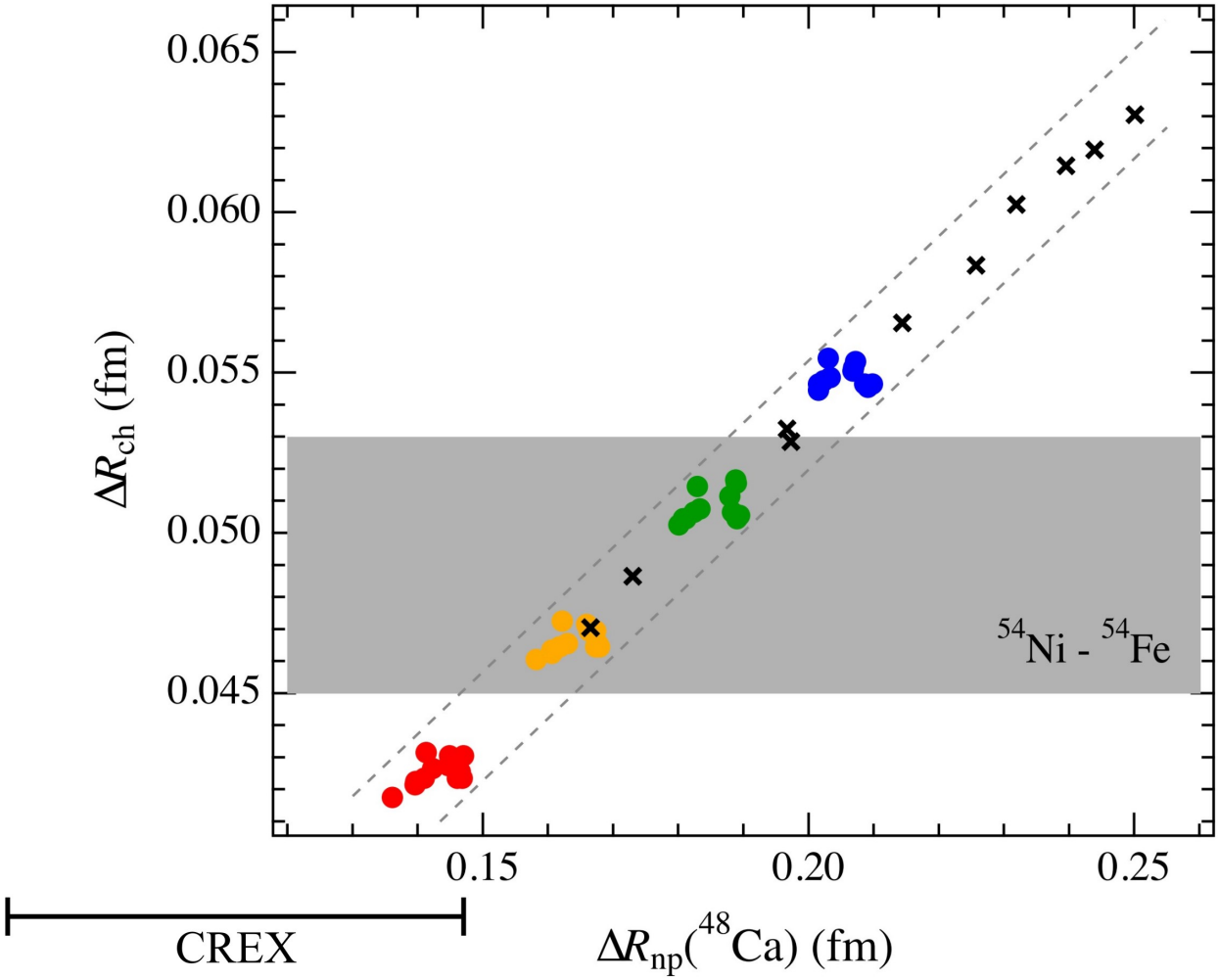

Figure 65: $\Delta R_{\rm np}(^{48}{\rm Ca})$ constrained by the mirror charge radii results for $A = 54$ [60]. The black band on the bottom left of the figure shows the experimental value from CREX [129].

5.5.2 Constraints on the Neutron Skin for ^{48}Ca Using $A = 36$

There is a significant discrepancy between the results of two forms of the Skyrme IS and IS+IV when placing constraints on $\Delta R_{\rm np}$ for ^{48}Ca. The shift in the theoretical points, shown in Fig. 66, is due to a sign change when looking at $A = 36$ $\left(0d_{3/2}\right)$ versus $A = 48$ $\left(0f_{7/2}\right)$. IMSRG calculations agree with the IS + IV Skyrme results based on the $p-$wave form of the interaction. Nevertheless, both results agree with the published value for $\Delta R_{\rm np}$ $\left(^{48}\text{Ca}\right)$ [129].

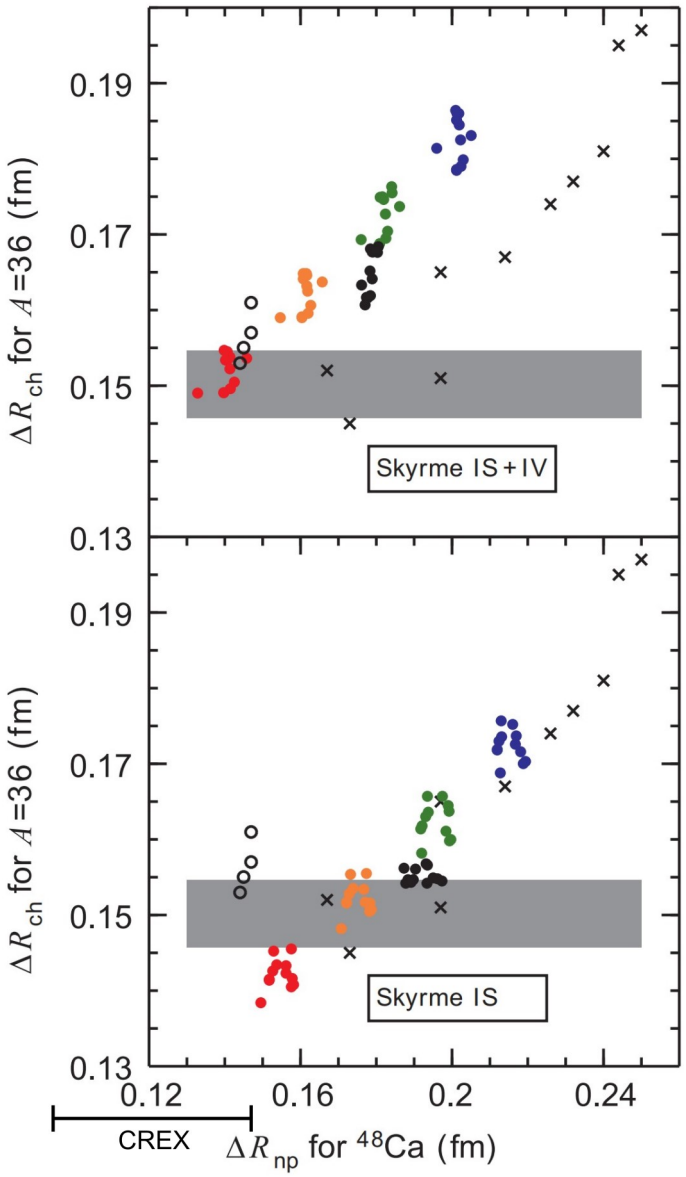

Figure 66: Constraints on $\Delta R_{\rm np}$ for ^{48}Ca using the $A = 36$ results from the ^{36}Ca-^{36}S [126]. The black band on the bottom left of the figure shows the experimental value from CREX [129].

All of the predictions made by BECOLA for $\Delta R_{\rm ch}$ are plotted below compared to the published CREX results. Although all of the predictions agree with Ref. [129].

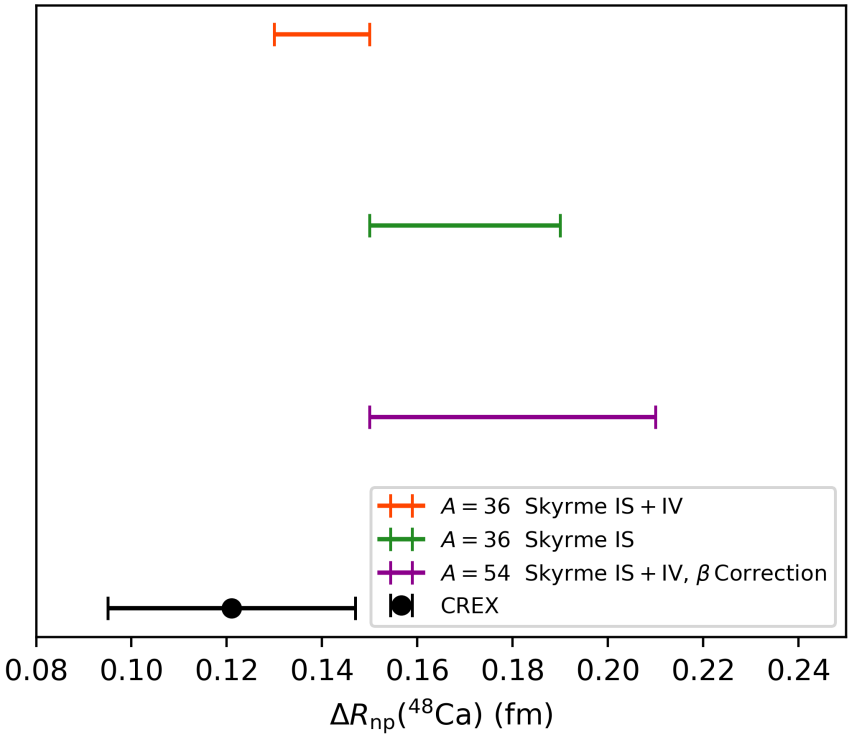

Figure 67: BECOLA predictions for $\Delta R_{\rm np}\left({}^{48}{\rm Ca}\right)$ deduced from $\Delta R_{\rm ch}$ for $A = 36$ and $A = 54$ compared to the CREX experimental result [129].

6 Discussion

6.1 BECOLA L Constraints in Comparison to World Results

The Skyrme and CODF calculations show a clear correlation between $\Delta R_{\rm ch}$ and L. The experimental value shown in grey (Fig. 63) sets a constraint on L between $21 \leq L \leq 88$ MeV, consistent with the GW170817 neutron star merger results [7] and also shown in the top bar of Fig. 63. This lower L value is consistent with a soft neutron matter EOS, implying smaller, more compact neutron star radius. In contrast, the $L = 106 \pm 37$ MeV value taken from the PREX-I and PREX-II data (PREX-2) [25] implies a stiff neutron matter EOS, with the 1σ PREX uncertainty band barely overlapping the constraint from $\Delta R_{\rm ch}$. It is worth noting that over 100 analyses from terrestrial experiments and astrophysical observations also support a soft EOS [130], and some of those results are shown in the figure below (Fig. 68).

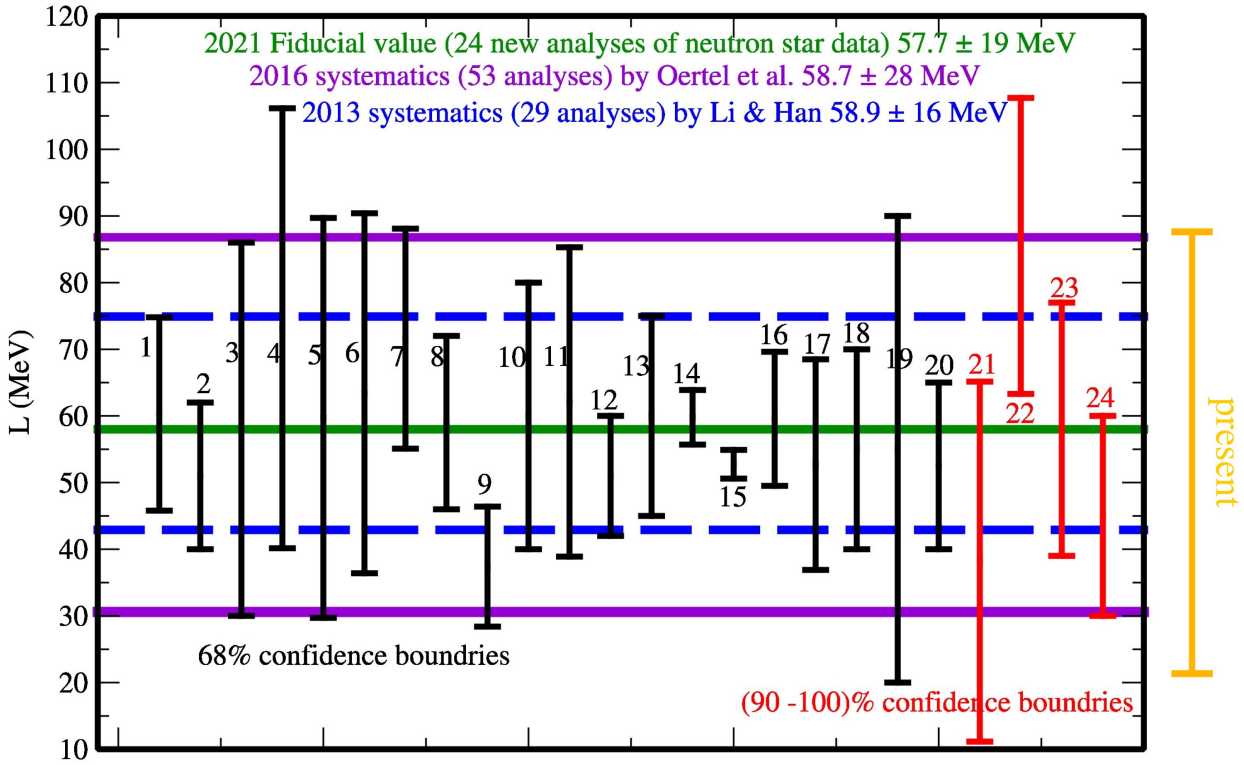

Figure 68: World results from Ref. [130], with the majority tending towards a lower L value and a soft EOS. The BECOLA result from $A = 54$ is shown on the right side of the figure in gold.

6.2 β_2 Correction for $A = 36$

It is noted that our previous results on the mirror pair ^{36}Ca-^{36}S indicates the range of $5 \leq L \leq 70$ MeV [126], which is consistent with the present results. However, the $A = 36$ and $A = 38$ results do not include

the quadrupole correlation and has an ambiguity in the form of the spin orbit force. This ambiguity is that the isovector and isoscalar Skyrme EDFs produce different results, shifting the theoretical points vertically and their comparison is shown in Fig.64. Once experimental $B(E2)$ for the $A = 36$ pair become available, the range from the $A = 36$ will be updated. The $A = 36$ results were not shown in Fig.63 because it would not have been a like-for-like comparison.

6.3 Assessment of Model Dependencies

6.3.1 Comparison to a Global Fit Model

Ref.[14] brings into discussion the stringency of the constraints on L using the method of mirror pair charge radii. They performed a statistical correlation analysis (such as in Refs. [11, 131]) between $\Delta R_{\rm ch}$ and L, obtaining a coefficient of determination (CoD) that describes how correlated one variable is to another. The rich form of the pairing interaction that reproduces the odd-even staggering of nuclear charge radii, Fy(Δr, HFB), was used for the trend analysis [132, 53, 14]. It was performed with three different models: Bardeen-Cooper-Schrieffer (BCS), Hartree-Fock-Bogoliubov (HFB), and Hartree-Fock with an Equal Filling Approximation (HF+EFA). The HFB formalism is the one of focus for this analysis, since the simpler BCS approximation can impact the radial behavior of nucleonic densities and produce unphysical results [14]. This is because the BCS pairing approximation breaks down when applied to nuclei which are weakly bound [109, 133], acquiring an unphysical spurious proton gas component [44].

Error ellipsoids computed with Skryme are shown in Fig. 69 (left), where they found that while $\Delta R_{\rm np}$ was highly correlated to L, $\Delta R_{\rm ch}$ had a weaker correlation. It is emphasized that the error ellipsoids are wider for $\Delta R_{\rm ch}$ and depend appreciably on the treatment of pairing correlations. For this reason they add the HF+EFA result in the figure, because it is devoid of pairing correlations making the ellipsoid smaller and the COD larger, automatically implying stronger correlation between $R_{\rm ch}$ and $R_{\rm np}$. Essentially, when pairing is turned on, such as with HFB, the correlation gets weaker and vice versa. The authors from Ref. [14] state that the large correlations between $R_{\rm ch}$ and L in Ref. [134] were reported as such because pairing correlations and parameters in the EDFs are ignored, automatically implying strong correlation. The broader error ellipsoids with $\Delta R_{\rm ch}$, when compared to the thinner ellipsoid on $\Delta R_{\rm np}$, imply other terms in the EDF parameterization are affecting them (Fig. 69 (middle)). Theoretical $\Delta R_{\rm ch}$ are plotted in Fig. 69 (right) comparing results from BCS and HFB. It can be seen that the treatment of pairing affects $\Delta R_{\rm ch}$ for both the ^{36}Ca-^{36}S and ^{48}Ni-^{48}Ca pairs, shifting the BCS relative to HFB. It is noted that the ^{54}Ni nucleus is more bound than ^{36}Ca or ^{48}Ni, and as such the disagreement between BCS and HFB is expected to be less. For the ^{54}Ni-^{54}Fe pair both the BCS and HFB with the Fayans model agree within themselves and with

experimental results. This implies that the ^{54}Ni-^{54}Fe mirror pair is not susceptible to the continuum effects. Within their theoretical framework, it is not the globalization of the model that decreases the correlation, but the missing terms in the Skyrme interaction (pairing). They conclude by saying that while there is a correlation between $R_{\rm ch}$ and L, it cannot provide a stringent constraint on L within their model. On the other side of the discussion, using the β correction makes the analysis more specific to the mirror pair and reduces the uncertainty in a parameter-free comparison.

Including both sides of this discussion on the stringency in the constraint on L paints a more complete picture, and I again emphasize that *all* methods that determine L are *model dependent*, and it is important to have different observables to add to the systematics in constraining the slope parameter L. With that said, the difference in mirror pair charge radii is a novel purely electromagnetic experimental method that adds another valuable piece in this ongoing puzzle to constrain the neutron matter EOS.

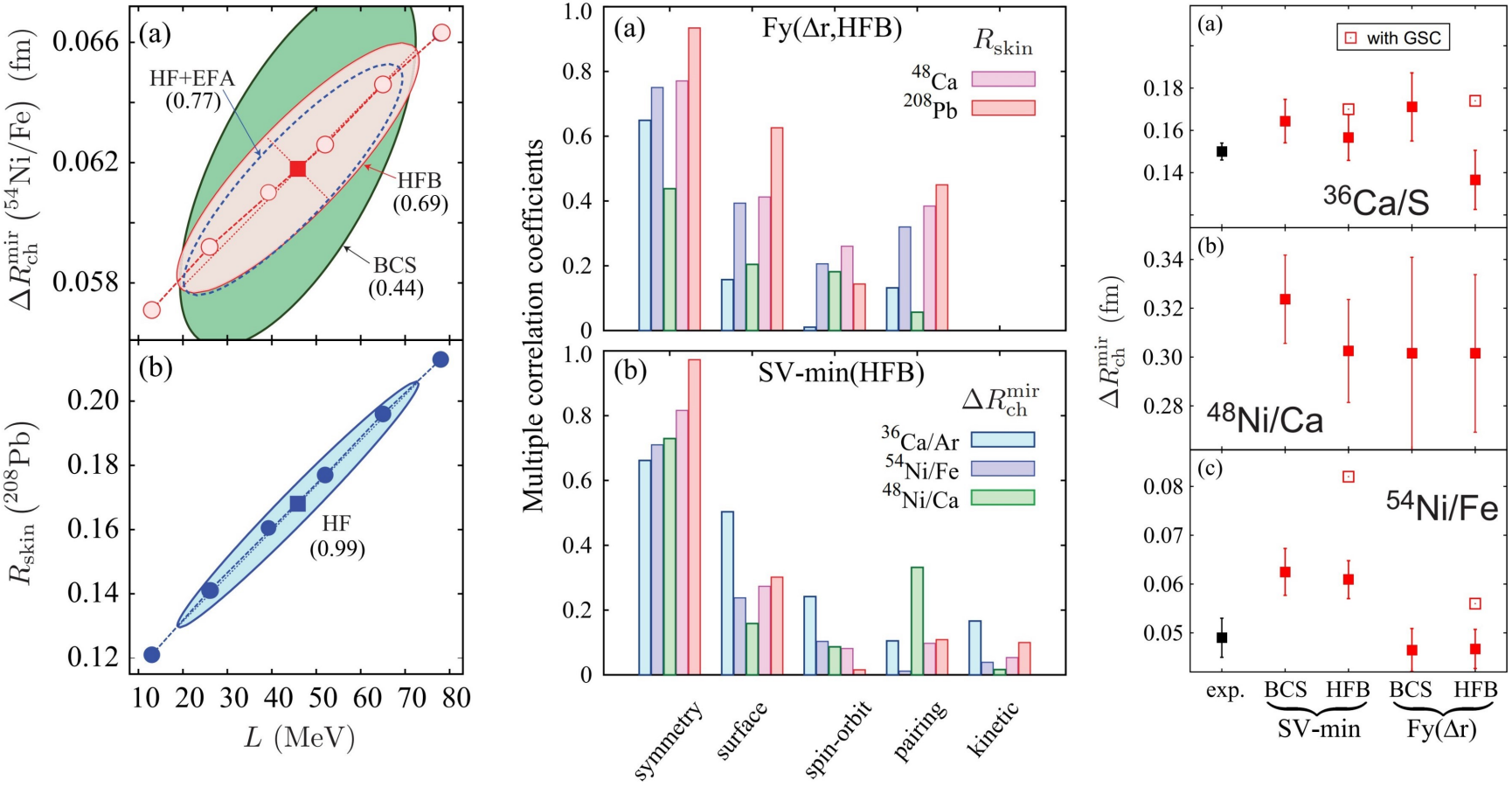

Figure 69: Results from Ref. [14]. (left) Error ellipsoids from the trend analysis for $\Delta R_{\rm ch}$ and $\Delta R_{\rm np}$ to L using Skyrme. (middle) Multiple correlation coefficients between various observables and model parameters. (right) Theoretical $\Delta R_{\rm ch}$ calculated with SV-min and FY(Δr) EDFs in BCS and HFB variants.

6.3.2 Analysis of Parity-violating Asymmetry for ^{208}Pb and ^{48}Ca

The PREX and CREX experiments are considered the golden standard as an avenue to obtain the neutron skin. A reevaluation of the neutron skin from ^{208}Pb constrained $L = 54 \pm 8$ [135], a stark contrast to $L = 106 \pm 37$ [25]. The model-dependent step ($\mathcal{M}$) which carries out the extraction $A_{\rm PV} \xrightarrow{\mathcal{M}} L$ should be treated with caution. The dependence on a nuclear model enters through two avenues [12]:

1. the description of the parity-violating response

2. the nuclear model of electroweak charge distribution of the atomic nucleus

A host of studies [130, 136, 137, 138, 139, 140, 141, 142, 143, 144, 145] found it difficult to accept the PREX-2 values of $\Delta R_{\rm np}$ and resulting L, and conclude that there is tension between the $\Delta R_{\rm np}$ and $\alpha_{\rm D}$ [146]. Some of these references consider the value of $\Delta R_{\rm np}$ (from Ref. [17]) as a measured quantity, ignoring its model-dependent extraction. Ref. [12] performed a comprehensive theoretical investigation of $A_{\rm PV}$ and $\alpha_{\rm D}$, assessing the impact of $A_{\rm PV}$ in ^{208}Pb and ^{48}Ca on EDFs.

Correlations between different nuclear properties were calculated and error ellipsoids for $\alpha_{\rm D}J$, L, and $\Delta R_{\rm np}$ are shown in Fig. 70. The 1σ uncertainties for the mean values of measured $A_{\rm PV}$ are shown by the grey bands. Fig. 70 shows that theoretical predictions for $A_{\rm PV}$ tend to overestimate ^{208}Pb and underestimate ^{48}Ca. Most of the theoretical results shown do not overlap or barely overlap at a 1σ level with the experimental data on $A_{\rm PV}$, indicating a tension between PREX-2 and CREX values of $A_{\rm PV}$ viewed through the lens of quantified nuclear models [12].

Trends in $\alpha_{\rm D}$ and $A_{\rm PV}$ were investigated as well, shown in Fig. 71. In the lower panel, the results from $\alpha_{\rm D}$ line up along a linear trend in the direction of the intersection between the mean values for $A_{\rm PV}$ from both isotopes. However, looking at the top panel it is shown that the $A_{\rm PV}$ trends do not approach the intersection and are pointed in the wrong direction, suggesting that a simultaneous fit of both $A_{\rm PV}$ values cannot produce a consistent explanation of PREX-2 and CREX measurements [12].

From these inconsistent results it seems that either something within the theoretical framework is misguided and/or something within the experimental analysis is amiss.

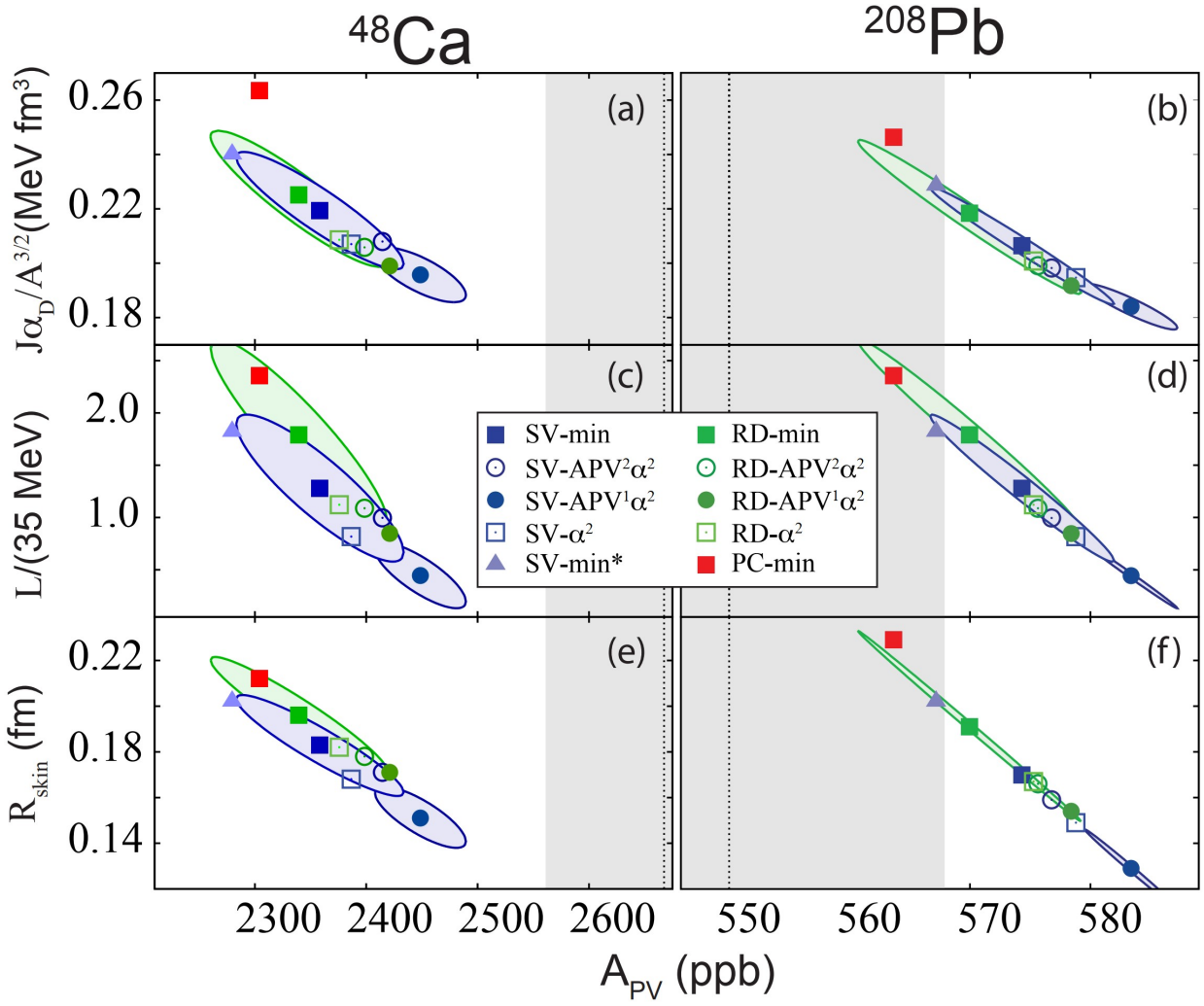

Figure 70: Trends of $\alpha_{\rm D}J$, L, and $\Delta R_{\rm np}$ with $A_{\rm PV}$ for ^{48}Ca (left), and ^{208}Pb (right) taken from Ref. [12]. Grey bands indicate the mean values of measured $A_{\rm PV}$ at 1σ. The black dashed line indicates the mean value. Different EDFs are shown by the symbols on the legend.

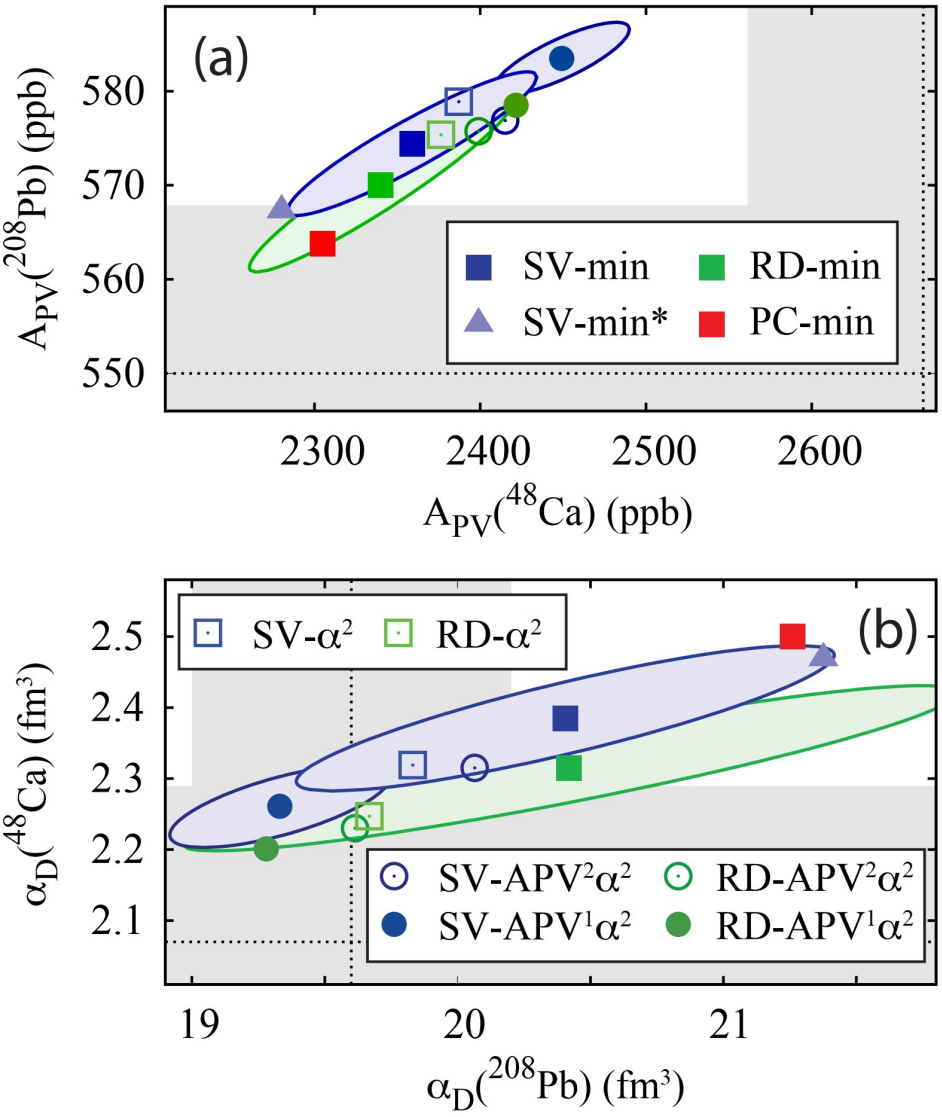

Figure 71: Trends of $A_{\rm PV}$ (top) and $\alpha_{\rm D}$ (bottom), each plotting ^{208}Pb and ^{48}Ca against each other. The grey bands indicate the 1σ uncertainties in the mean values of measured observables. The black dashed line indicates the mean value.

6.4 Future Prospects

6.4.1 Difference in Mirror Charge Radii of ^{32}Si-^{32}Ar

The most recent study in mirror charge radii was based on Si isotopes. Fluorescence spectra for silicon isotopes ^{28,29,30,32}Si for the $3s^2 3p^2 \rightarrow 3s^2 3p 4s$ transition were measured and their isotope shifts were deduced relative to the rest-frame frequency for ^{28}Si. Analysis to deduce the constraints on L are ongoing, however, the preliminary value agrees with the $A = 54$ system. Details on this analysis can be found in Appx. F. Isotope shift measurements were performed on ^{28,29,30,32}Si isotopes (Fig. 72). The spectra for these Si isotopes are more asymmetric than those shown from Ni due to the densely populated electronic states. These measurements were performed with a DC beam because the rate of these ions was sufficient. The transition used for these measurements was not cyclic, meaning that each atom could only be excited once before decaying to another state not accessible to the laser frequency. Because of this issue, an acousto-optic modulator (AOM) was used to chop the laser light so that light was only exciting the atoms at the photon detection region. Using the AOM prevented the unwanted loss of atoms in the correct ground state to excite the $3s^2 3p^2 \rightarrow 3s^2 3p 4s$ transition, because exciting them too early would mean less fluorescent atoms at the photon detection region. Using the ^{32}Si-^{32}Ar pair gives an $|N - Z| = 4$, which means that is is more sensitive to L than the $A = 54$ results. A preliminary constraint has been placed between $L \leq 60\,\text{MeV}$, consistent with other mass systems. Details will be discussed elsewhere [147]).

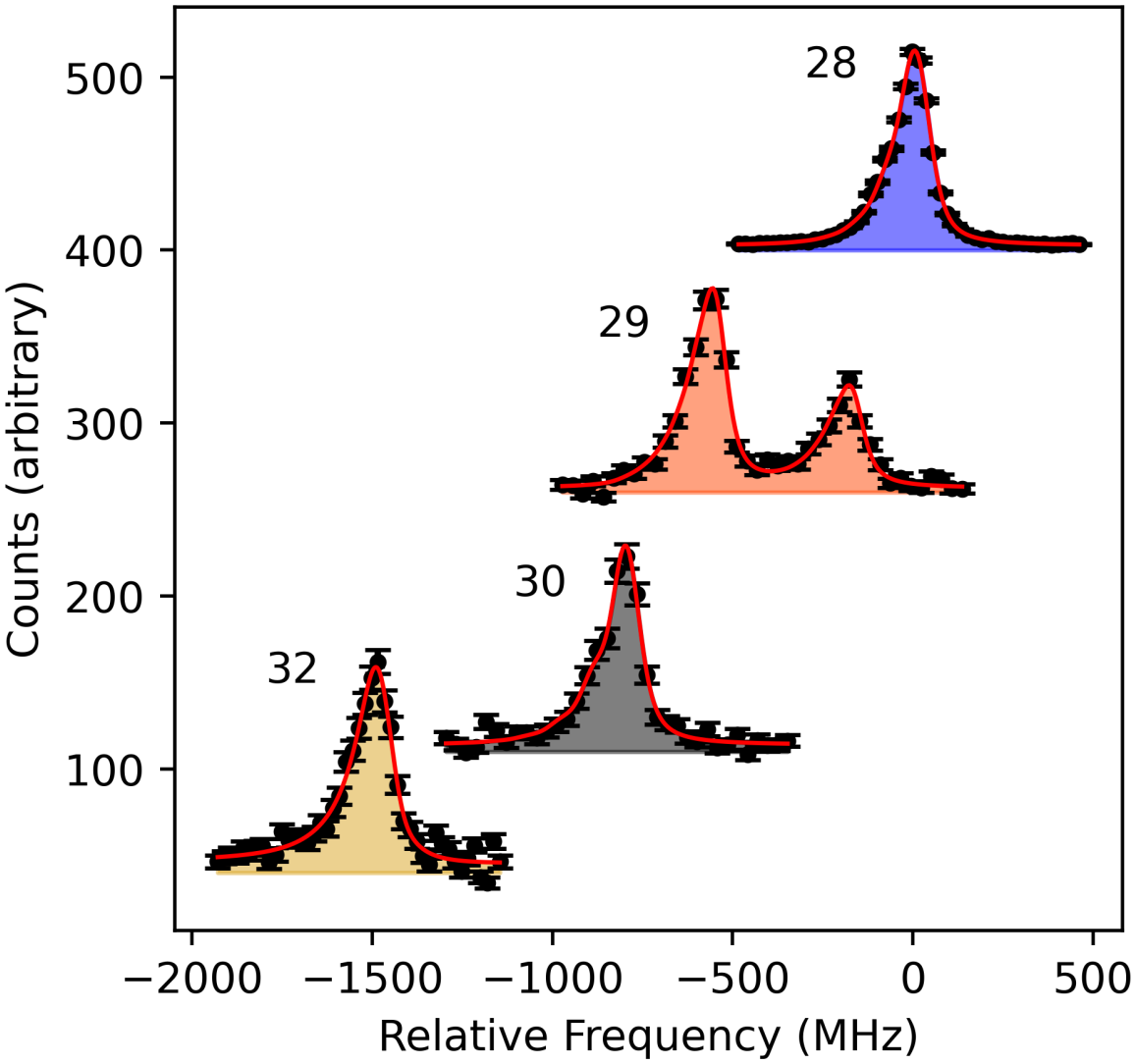

Figure 72: Silicon spectra for isotopes measured at BECOLA relative to ^{28}Si.

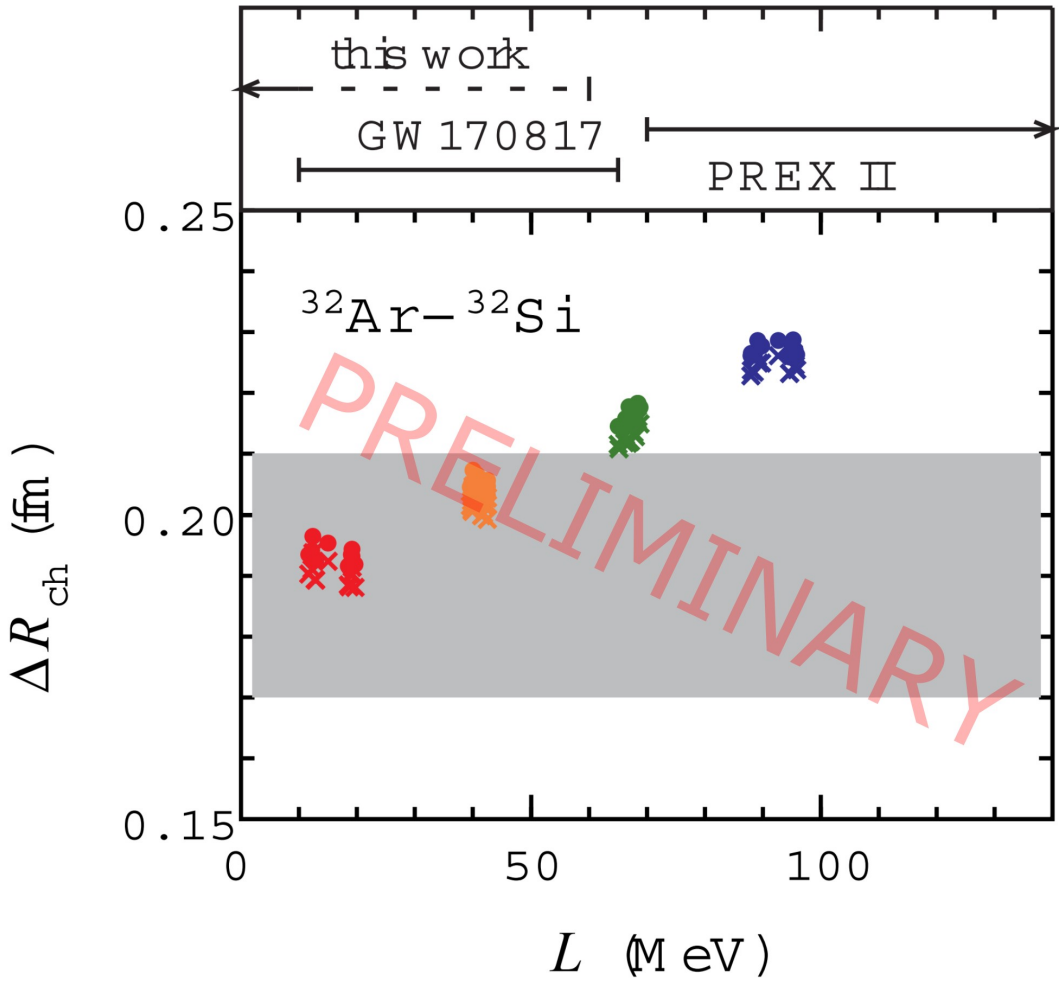

Figure 73: Correlation between L and $\Delta R_{\rm ch}$ for the ^{32}Si-^{32}Ar mirror pair, placing a preliminary constraint $L \leq 60\,\text{MeV}$. Filled circles are results from Skyrme EDFs with constraints on the neutron skin of ^{208}Pb, with red = 0.12 fm, orange = 0.16 fm, green = 0.20 fm, and blue = 0.24 fm. Colored $\times$'s are from CODF, with the same constraints as the filled circles. Figure courtesy of B. Alex Brown.

6.4.2 Limitations of Current Studies

While Ca mirror charge radii contains the largest $|N-Z|$ so far, the ambiguity in theoretical calculations does not enable confident constraints on L using this method and the study must be updated once $B\,(E2)$ values are available to perform the quadrupole correction. The Ni $A = 54$ analysis, while containing a rather large statistical uncertainty, is ultimately limited by the uncertainty in absolute charge radii and its smaller $|N-Z| = 2$, and solicits a measurement of ^{52}Ni to enable tighter constraints.

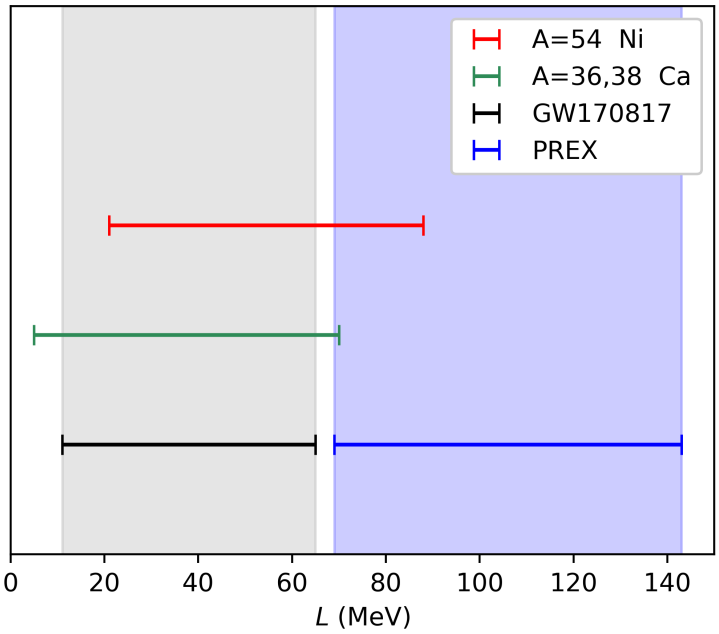

Figure 74: Constraints on L measured at BECOLA for $A = 36, 38$ [126] and $A = 54$ [60] compared to GW170817 [7] and PREX-2 [25].

6.4.3 Future Studies

Studying the $A = 52$ mirror pair with Ni and Cr would provide tighter constraint on L with an $|N-Z| = 4$. Using this mirror pair is also convenient because the ^{52}Cr nucleus is stable and its charge radius has already been measured. Adding to that convenience, the King-plot analysis has already been performed on stable Ni isotopes and its atomic factors extracted, making the deduction of the $R_{\mathrm{ch}}(^{52}\mathrm{Ni})$ straightforward. The ^{52}Ni has a half-life of 40.8 ms and is possible with FRIB. Currently the BECOLA-RISE collaboration with MIT is performing resonance ionization spectroscopy experiments and developing a powerful new technique that may be useful in studying future mirror pairs. As stated previously, the limiting factor for using mirror nuclei to deduce L is that larger $|N-Z|$ approaches the proton dripline, even though it provides a tighter

constraint on L in the process. The largest $|N-Z|$ possible with technique is $|N-Z|=6$ with the ^{22}Si-^{22}O pair, however, currently both of those charge radii are currently unknown and there are not many systematic charge radius measurements for either of these isotopic chains, making the extraction of atomic factors more challenging. Developments such as resonance ionization spectroscopy at BECOLA and the advancement of rare isotope facilities like FRIB will facilitate the opportunity to study this extreme mirror pair with the hopes of placing the tightest constraints on L possible with the $\Delta R_{\rm ch}$ technique. Further theoretical studies are encouraged, including *ab-initio* calculations for the correlation between $\Delta R_{\rm ch}$ and L.

7 Summary

The nuclear equation of state has remained a hot topic in nuclear physics in past decades due to its relation to astrophysics and heavy nuclei. Its wide application, as well as its illusive nature stemming from model-dependence and contradictory results, add to this allure, compelling many different experimental and theoretical approaches to constrain pure neutron matter. The symmetry energy describes nuclear matter as it moves away from stability, and extrapolations to higher densities with pure neutron matter show large variations in its softness or stiffness. By constraining the slope of the symmetry energy (the L parameter), which is correlated to the neutron skin thickness in neutron rich nuclei, the softness or stiffness of the neutron equation of state can be described. All constraints on L are model-dependent and although most of them agree within 1σ they have tendencies to favor either the soft or stiff equation of state. Constraints on L obtained from the PREX favor a stiff equation of state, while astrophysical results from the GW170817 neutron star merger favor a soft equation of state.

Isotope shifts of the hyperfine structure of ^{54,58,60,62,64}Ni relative to ^{60}Ni were measured at the BECOLA facility using bunched beam collinear laser spectroscopy. The ^{54}Ni ($I^\pi = 0^+,\ t_{1/2} = 114\,\text{ms}$) measurement was performed for the first time with beams obtained at the National Superconducting Cyclotron Laboratory (NSCL) at Michigan State University. The $3d^9 4s\,^3D_3 \rightarrow 3d^9 4p\,^3P_2$ transition at 352 nm was probed for laser resonant fluorescence measurement with a rate of $\sim 13\,\text{atom/s}$ at the photon detection region. Isotope shifts for stable Ni isotopes resulted in a total uncertainty of less than 3 MHz, dominated by the systematic uncertainty of the beam energy due to the limited beam rate. The ^{54}Ni hyperfine spectrum is dominated by statistical uncertainty due to the beam rate at BECOLA. A King-plot analysis was performed which extracted the atomic factors necessary to deduce the differential mean-squared charge radius, an essential step necessary to extract the charge radius of ^{54}Ni. Obtaining its charge radius ($R(^{54}\text{Ni}) = 3.737 \pm 0.003\,\text{fm}$) presented an opportunity to place constraints on the slope of the symmetry energy by using the difference in mirror pair charge radii to be $\Delta R_{\text{ch}} = 0.049 \pm 0.004\,\text{fm}$.

The difference in mirror pair charge radii for the ^{54}Ni-^{54}Fe pair place constraints $21 \leq L \leq 88\,\text{MeV}$ which is in good agreement with the neutron star merger results and supportive of a soft EOS. In comparison to world data, there is a tendency to favor a soft equation of state and there is still some ambiguity as to whether the soft or stiff tendencies are statistical or if there is some systematic shift. The response to such an ambiguity is that more experimental and theoretical approaches, and analytical methods should be used to add to the systematics of L.

The model-dependence on the L parameter has sparked a debate on the uncertainty in the contraint using the difference in mirror pair charge radii. The present DFT theory with Skyrme EDF used to deduce

the correlation between L and $\Delta R_{\rm ch}$ includes a β_2 correction obtained from the $B(E2,\uparrow)$, which corrects for the quadrupole deformation of the nucleus. The $B(E2,\uparrow)$ for ^{54}Ni has not yet been measured and calculated using the shell model with the GXPF1 interaction, which was benchmarked by a good agreement with experimental $B(E2,\uparrow)$ of the mirror ^{54}Fe nucleus. The calculated charge radii using the β_2-corrected Skyrme model well reproduce experimental charge radii of the $N = 28$ isotones between Ca and Ni, making this model specifically tuned for this region.

Another DFT model, which contains the rich form of pairing interaction, was applied to investigate the correlation between L and $\Delta R_{\rm ch}$. The model was fitted to global experimental parameters and contains the rich forms of the pairing interaction. It shows a moderately weaker correlation between L and $\Delta R_{\rm ch}$ compared to the one for L and $\Delta R_{\rm np}$. The global fit model suggests that the difference of mirror charge radii cannot set a stringent constraint on L.

It is important to emphasize that *all* determinations of L are more or less model dependent. In order to further assess the model dependence to constrain L better, more theoretical and experimental works are encouraged. A prime example of model dependence playing a critical role in its relationship to the EOS is exhibited by PREX-2, the experiment which was considered a benchmark for the neutron skin value. The reevaluation of the PREX-2 data resulted in agreement with the soft EOS, a contradiction to the initial PREX-2 analysis. The model-dependent step leading to the neutron skin was evaluated differently, and produced a stark difference in the L parameter constraint. PREX and CREX results also cannot be accomodated experimentally or theoretically, fronting a challenge to relate ^{208}Pb and ^{48}Ca to each other and bringing into question not only theoretical, but experimental evaluations of the data.

The difference in mirror charge radii provides a purely electromagnetic observable, similar to the PREX, as an avenue to constrain the L parameter. Mirror pairs with higher $|N - Z|$ should be considered such as ^{52}Ni-^{52}Cr and ^{22}Si-^{22}O, since their sensitivity to determine L is higher and becomes less susceptive to the systematics of theoretical calculations.

REFERENCES

[1] P. Atkins and J. de Paula. *Physical Chemistry: Thermodynamics, Structure, and Change.* Tenth Edition. Oxford University Press, 41 Madison Avenue, New York, NY 10010, 2014.

[2] R. Knight. *Physics for Scientists and Engineers: A Strategic Approach.* Third Edition. Pearson Education, 2013.

[3] M. Baldo and G.F. Burgio. The nuclear symmetry energy. *Progress in Particle and Nuclear Physics*, 91:203–258, 2016.

[4] B. Alex Brown. Lecture notes in nuclear structure physics. 2020.

[5] C. J. Horowitz and J. Piekarewicz. Neutron star structure and the neutron radius of ^{208}pb. *Phys. Rev. Lett.*, 86:5647–5650, Jun 2001.

[6] Andrew W. Steiner, James M. Lattimer, and Edward F. Brown. The neutron star mass–radius relation and the equation of state of dense matter. *The Astrophysical Journal Letters*, 765(1):L5, feb 2013.

[7] C. Raithel and F. Özel. Measurement of the nuclear symmetry energy parameters from gravitational-wave events. *The Astrophysical Journal*, 885(2):121, Nov 2019.

[8] B. Alex Brown. Neutron radii in nuclei and the neutron equation of state. *Phys. Rev. Lett.*, 85:5296–5299, Dec 2000.

[9] B. Alex Brown. Mirror charge radii and the neutron equation of state. *Phys. Rev. Lett.*, 119:122502, Sep 2017.

[10] P.-G. Reinhard and W. Nazarewicz. Nuclear charge and neutron radii and nuclear matter: Trend analysis in skyrme density-functional-theory approach. *Phys. Rev. C*, 93:051303, May 2016.

[11] P.-G. Reinhard and W. Nazarewicz. Information content of a new observable: The case of the nuclear neutron skin. *Phys. Rev. C*, 81:051303, May 2010.

[12] Paul-Gerhard Reinhard, Xavier Roca-Maza, and Witold Nazarewicz. Combined theoretical analysis of the parity-violating asymmetry for ^{48}ca and ^{208}pb, 2022.

[13] M. B. Tsang, J. R. Stone, F. Camera, P. Danielewicz, S. Gandolfi, K. Hebeler, C. J. Horowitz, Jenny Lee, W. G. Lynch, Z. Kohley, R. Lemmon, P. Möller, T. Murakami, S. Riordan, X. Roca-Maza, F. Sammarruca, A. W. Steiner, I. Vidaña, and S. J. Yennello. Constraints on the symmetry energy and neutron skins from experiments and theory. *Phys. Rev. C*, 86:015803, Jul 2012.

[14] Paul-Gerhard Reinhard and Witold Nazarewicz. Information content of the differences in the charge radii of mirror nuclei. *Phys. Rev. C*, 105:L021301, Feb 2022.

[15] X. Roca-Maza, M. Centelles, X. Viñas, and M. Warda. Neutron skin of ^{208}Pb, nuclear symmetry energy, and the parity radius experiment. *Phys. Rev. Lett.*, 106:252501, Jun 2011.

[16] S. Abrahamyan, *et al.*, and PREX Collaboration. Measurement of the neutron radius of ^{208}Pb through parity violation in electron scattering. *Phys. Rev. Lett.*, 108:112502, Mar 2012.

[17] D. Adhikari, *et al.*, and PREX Collaboration. Accurate determination of the neutron skin thickness of ^{208}Pb through parity-violation in electron scattering. *Phys. Rev. Lett.*, 126:172502, Apr 2021.

[18] J. Piekarewicz. Pygmy resonances and neutron skins. *Phys. Rev. C*, 83:034319, Mar 2011.

[19] J. Piekarewicz, B. K. Agrawal, G. Colò, W. Nazarewicz, N. Paar, P.-G. Reinhard, X. Roca-Maza, and D. Vretenar. Electric dipole polarizability and the neutron skin. *Phys. Rev. C*, 85:041302, Apr 2012.

[20] D. M. Rossi, P. Adrich, F. Aksouh, H. Alvarez-Pol, T. Aumann, J. Benlliure, M. Böhmer, K. Boretzky, E. Casarejos, M. Chartier, A. Chatillon, D. Cortina-Gil, U. Datta Pramanik, H. Emling, O. Ershova, B. Fernandez-Dominguez, H. Geissel, M. Gorska, M. Heil, H. T. Johansson, A. Junghans, A. Kelic-Heil, O. Kiselev, A. Klimkiewicz, J. V. Kratz, R. Krücken, N. Kurz, M. Labiche, T. Le Bleis, R. Lemmon, Yu. A. Litvinov, K. Mahata, P. Maierbeck, A. Movsesyan, T. Nilsson, C. Nociforo, R. Palit, S. Paschalis, R. Plag, R. Reifarth, D. Savran, H. Scheit, H. Simon, K. Sümmerer, A. Wagner, W. Waluś, H. Weick, and M. Winkler. Measurement of the dipole polarizability of the unstable neutron-rich nucleus ^{68}Ni. *Phys. Rev. Lett.*, 111:242503, Dec 2013.

[21] B. P. Abbott, *et al* LIGO Scientific Collaboration, and Virgo Collaboration. Gw170817: Observation of gravitational waves from a binary neutron star inspiral. *Phys. Rev. Lett.*, 119:161101, Oct 2017.

[22] B. P. Abbott, B. P. Abbott, *et al* LIGO Scientific Collaboration, and Virgo Collaboration. Gw170817: Measurements of neutron star radii and equation of state. *Phys. Rev. Lett.*, 121:161101, Oct 2018.

[23] Carolyn A. Raithel. Constraints on the neutron star equation of state from gw170817. *The European Physical Journal*, 55:80, May 2019.

[24] Hong Shen, Fan Ji, Jinniu Hu, and Kohsuke Sumiyoshi. Effects of symmetry energy on the equation of state for simulations of core-collapse supernovae and neutron-star mergers. *The Astrophysical Journal*, 891(2):148, mar 2020.

[25] Brendan T. Reed, F. J. Fattoyev, C. J. Horowitz, and J. Piekarewicz. Implications of prex-2 on the equation of state of neutron-rich matter. *Phys. Rev. Lett.*, 126:172503, Apr 2021.

[26] B. Alex Brown, G. Shen, G. C. Hillhouse, J. Meng, and A. Trzcińska. Neutron skin deduced from antiprotonic atom data. *Phys. Rev. C*, 76:034305, Sep 2007.

[27] J. Zenihiro, H. Sakaguchi, T. Murakami, M. Yosoi, Y. Yasuda, S. Terashima, Y. Iwao, H. Takeda, M. Itoh, H. P. Yoshida, and M. Uchida. Neutron density distributions of ^{204,206,208}Pb deduced via proton elastic scattering at $E_p = 295$ mev. *Phys. Rev. C*, 82:044611, Oct 2010.

[28] C. M. Tarbert, D. P. Watts, D. I. Glazier, P. Aguar, J. Ahrens, J. R. M. Annand, H. J. Arends, R. Beck, V. Bekrenev, B. Boillat, A. Braghieri, D. Branford, W. J. Briscoe, J. Brudvik, S. Cherepnya, R. Codling, E. J. Downie, K. Foehl, P. Grabmayr, R. Gregor, E. Heid, D. Hornidge, O. Jahn, V. L. Kashevarov, A. Knezevic, R. Kondratiev, M. Korolija, M. Kotulla, D. Krambrich, B. Krusche, M. Lang, V. Lisin, K. Livingston, S. Lugert, I. J. D. MacGregor, D. M. Manley, M. Martinez, J. C. McGeorge, D. Mekterovic, V. Metag, B. M. K. Nefkens, A. Nikolaev, R. Novotny, R. O. Owens, P. Pedroni, A. Polonski, S. N. Prakhov, J. W. Price, G. Rosner, M. Rost, T. Rostomyan, S. Schadmand, S. Schumann, D. Sober, A. Starostin, I. Supek, A. Thomas, M. Unverzagt, Th. Walcher, L. Zana, and F. Zehr. Neutron skin of ^{208}Pb from coherent pion photoproduction. *Phys. Rev. Lett.*, 112:242502, Jun 2014.

[29] E. Lipparini and S. Stringari. Sum rules and giant resonances in nuclei. *Physics Reports*, 175(3):103–261, 1989.

[30] M. Miorelli, S. Bacca, N. Barnea, G. Hagen, G. R. Jansen, G. Orlandini, and T. Papenbrock. Electric dipole polarizability from first principles calculations. *Phys. Rev. C*, 94:034317, Sep 2016.

[31] A. Tamii, I. Poltoratska, P. von Neumann-Cosel, Y. Fujita, T. Adachi, C. A. Bertulani, J. Carter, M. Dozono, H. Fujita, K. Fujita, K. Hatanaka, D. Ishikawa, M. Itoh, T. Kawabata, Y. Kalmykov, A. M. Krumbholz, E. Litvinova, H. Matsubara, K. Nakanishi, R. Neveling, H. Okamura, H. J. Ong, B. Özel-Tashenov, V. Yu. Ponomarev, A. Richter, B. Rubio, H. Sakaguchi, Y. Sakemi, Y. Sasamoto, Y. Shimbara, Y. Shimizu, F. D. Smit, T. Suzuki, Y. Tameshige, J. Wambach, R. Yamada, M. Yosoi, and J. Zenihiro. Complete electric dipole response and the neutron skin in ^{208}Pb. *Phys. Rev. Lett.*, 107:062502, Aug 2011.

[32] X. Roca-Maza, M. Brenna, G. Colò, M. Centelles, X. Viñas, B. K. Agrawal, N. Paar, D. Vretenar, and J. Piekarewicz. Electric dipole polarizability in ^{208}pb: Insights from the droplet model. *Phys. Rev. C*, 88:024316, Aug 2013.

[33] T. Hashimoto, A. M. Krumbholz, P.-G. Reinhard, A. Tamii, P. von Neumann-Cosel, T. Adachi, N. Aoi, C. A. Bertulani, H. Fujita, Y. Fujita, E. Ganioğlu, K. Hatanaka, E. Ideguchi, C. Iwamoto, T. Kawabata, N. T. Khai, A. Krugmann, D. Martin, H. Matsubara, K. Miki, R. Neveling, H. Okamura, H. J. Ong, I. Poltoratska, V. Yu. Ponomarev, A. Richter, H. Sakaguchi, Y. Shimbara, Y. Shimizu, J. Simonis, F. D. Smit, G. Süsoy, T. Suzuki, J. H. Thies, M. Yosoi, and J. Zenihiro. Dipole polarizability of ^{120}Sn and nuclear energy density functionals. *Phys. Rev. C*, 92:031305, Sep 2015.

[34] J. Birkhan, M. Miorelli, S. Bacca, S. Bassauer, C. A. Bertulani, G. Hagen, H. Matsubara, P. von Neumann-Cosel, T. Papenbrock, N. Pietralla, V. Yu. Ponomarev, A. Richter, A. Schwenk, and A. Tamii. Electric dipole polarizability of ^{48}Ca and implications for the neutron skin. *Phys. Rev. Lett.*, 118:252501, Jun 2017.

[35] X. Roca-Maza, X. Viñas, M. Centelles, B. K. Agrawal, G. Colò, N. Paar, J. Piekarewicz, and D. Vretenar. Neutron skin thickness from the measured electric dipole polarizability in ^{68}Ni, ^{120}Sn, and ^{208}Pb. *Phys. Rev. C*, 92:064304, Dec 2015.

[36] Z. Z. Li, Y. F. Niu, and W. H. Long. Electric dipole polarizability in neutron-rich sn isotopes as a probe of nuclear isovector properties. *Phys. Rev. C*, 103:064301, Jun 2021.

[37] Ning Wang and Tao Li. Shell and isospin effects in nuclear charge radii. *Phys. Rev. C*, 88:011301, Jul 2013.

[38] Bao-An Li and Xiao Han. Constraining the neutron–proton effective mass splitting using empirical constraints on the density dependence of nuclear symmetry energy around normal density. *Physics Letters B*, 727(1):276–281, 2013.

[39] Bao-An Li. Nuclear symmetry energy extracted from laboratory experiments. *Nuclear Physics News*, 27(4):7–11, 2017.

[40] W.G. Lynch and M.B. Tsang. Decoding the density dependence of the nuclear symmetry energy. *Physics Letters B*, 830:137098, 2022.

[41] B.A. Brown and W.D.M. Rae. The shell-model code nushellx@msu. *Nuclear Data Sheets*, 120:115–118, 2014.

[42] Wilfried Nörtershäuser. Laser spectroscopy of radioactive isotopes - survey.

[43] B A Brown, C R Bronk, and P E Hodgson. Systematics of nuclear RMS charge radii. *Journal of Physics G: Nuclear Physics*, 10(12):1683–1701, dec 1984.

[44] A. J. Miller, K. Minamisono, A. Klose, D. Garand, C. Kujawa, J. D. Lantis, Y. Liu, B. Maaß, P. F. Mantica, W. Nazarewicz, W. Nörtershäuser, S. V. Pineda, P.-G. Reinhard, D. M. Rossi, F. Sommer, C. Sumithrarachchi, A. Teigelhöfer, and J. Watkins. Proton superfluidity and charge radii in proton-rich calcium isotopes. *Nature Physics*, 15, May 2019.

[45] I. Angeli and K.P. Marinova. Table of experimental nuclear ground state charge radii: An update. *Atomic Data and Nuclear Data Tables*, 99(1):69–95, 2013.

[46] Takaharu Otsuka, Alexandra Gade, Olivier Sorlin, Toshio Suzuki, and Yutaka Utsuno. Evolution of shell structure in exotic nuclei. *Rev. Mod. Phys.*, 92:015002, Mar 2020.

[47] C. Gorges, L. V. Rodríguez, D. L. Balabanski, M. L. Bissell, K. Blaum, B. Cheal, R. F. Garcia Ruiz, G. Georgiev, W. Gins, H. Heylen, A. Kanellakopoulos, S. Kaufmann, M. Kowalska, V. Lagaki, S. Lechner, B. Maaß, S. Malbrunot-Ettenauer, W. Nazarewicz, R. Neugart, G. Neyens, W. Nörtershäuser, P.-G. Reinhard, S. Sailer, R. Sánchez, S. Schmidt, L. Wehner, C. Wraith, L. Xie, Z. Y. Xu, X. F. Yang, and D. T. Yordanov. Laser spectroscopy of neutron-rich tin isotopes: A discontinuity in charge radii across the $n = 82$ shell closure. *Phys. Rev. Lett.*, 122:192502, May 2019.

[48] T. Day Goodacre, A. V. Afanasjev, A. E. Barzakh, L. Nies, B. A. Marsh, S. Sels, U. C. Perera, P. Ring, F. Wienholtz, A. N. Andreyev, P. Van Duppen, N. A. Althubiti, B. Andel, D. Atanasov, R. S. Augusto, J. Billowes, K. Blaum, T. E. Cocolios, J. G. Cubiss, G. J. Farooq-Smith, D. V. Fedorov, V. N. Fedosseev, K. T. Flanagan, L. P. Gaffney, L. Ghys, A. Gottberg, M. Huyse, S. Kreim, P. Kunz, D. Lunney, K. M. Lynch, V. Manea, Y. Martinez Palenzuela, T. M. Medonca, P. L. Molkanov, M. Mougeot, J. P. Ramos, M. Rosenbusch, R. E. Rossel, S. Rothe, L. Schweikhard, M. D. Seliverstov, P. Spagnoletti, C. Van Beveren, M. Veinhard, E. Verstraelen, A. Welker, K. Wendt, R. N. Wolf, A. Zadvornaya, and K. Zuber. Charge radii, moments, and masses of mercury isotopes across the $n = 126$ shell closure. *Phys. Rev. C*, 104:054322, Nov 2021.

[49] Paul-Gerhard Reinhard and Witold Nazarewicz. Nuclear charge densities in spherical and deformed nuclei: Toward precise calculations of charge radii. *Phys. Rev. C*, 103:054310, May 2021.

[50] U. C. Perera, A. V. Afanasjev, and P. Ring. Charge radii in covariant density functional theory: A global view. *Phys. Rev. C*, 104:064313, Dec 2021.

[51] Felix Sommer, Kristian König, Dominic M. Rossi, Nathan Everett, David Garand, Ruben P. de Groote, Jason D. Holt, Phillip Imgram, Anthony Incorvati, Colton Kalman, Andrew Klose, Jeremy Lantis, Yuan Liu, Andrew J. Miller, Kei Minamisono, Takayuki Miyagi, Witold Nazarewicz, Wilfried Nörtershäuser, Skyy V. Pineda, Robert Powel, Paul-Gerhard Reinhard, Laura Renth, Elisa Romero-Romero, Robert Roth, Achim Schwenk, Chandana Sumithrarachchi, and Andrea Teigelhöfer. Charge radii of ^{55,56}Ni reveal a surprisingly similar behavior at $n = 28$ in ca and ni isotopes. *Phys. Rev. Lett.*, 129:132501, Sep 2022.

[52] W. A. Friedman and G. F. Bertsch. Whence the odd-even staggering in nuclear binding? *The European Physical Journal A*, 41:109–113, Jul 2009.

[53] P.-G. Reinhard and W. Nazarewicz. Toward a global description of nuclear charge radii: Exploring the fayans energy density functional. *Phys. Rev. C*, 95:064328, Jun 2017.

[54] G. D. Alkhazov, A. E. Barzakh, V. A. Bolshakov, V. P. Denisov, V. S. Ivanov, Yu. Ya. Sergeyev, I. Ya. Chubukov, V. I. Tikhonov, V. S. Letokhov, V. I. Mishin, S. K. Sekatsky, and V. N. Fedoseyev. Odd-even staggering in nuclear charge radii of neutron-rich europium isotopes. *Zeitschrift für Physik A Atomic Nuclei*, 337:257–259, 09 1990.

[55] Ann-Marie Mårtensson-Pendrill, Anders Ynnerman, Håkan Warston, Ludo Vermeeren, Roger E. Silverans, Alexander Klein, Rainer Neugart, Christoph Schulz, Peter Lievens, and The ISOLDE Collaboration. Isotope shifts and nuclear-charge radii in singly ionized $^{40--48}$Ca. *Phys. Rev. A*, 45:4675–4681, Apr 1992.

[56] Ludo Vermeeren, Peter Lievens, Roger E Silverans, Uwe Georg, Matthias Keim, Alexander Klein, Rainer Neugart, Michael Neuroth, Fritz Buchinger, and the ISOLDE Collaboration. The mean square nuclear charge radius of ^{39}ca. *Journal of Physics G: Nuclear and Particle Physics*, 22(10):1517, oct 1996.

[57] G. Fricke and K. Heilig. *Nuclear Charge Radii*. Springer, Berline Heidelberg, 2004.

[58] K. Minamisono, D. M. Rossi, R. Beerwerth, S. Fritzsche, D. Garand, A. Klose, Y. Liu, B. Maaß, P. F. Mantica, A. J. Miller, P. Müller, W. Nazarewicz, W. Nörtershäuser, E. Olsen, M. R. Pearson, P.-G. Reinhard, E. E. Saperstein, C. Sumithrarachchi, and S. V. Tolokonnikov. Charge radii of neutron deficient ^{52,53}Fe produced by projectile fragmentation. *Phys. Rev. Lett.*, 117:252501, Dec 2016.

[59] R. F. Garcia Ruiz, M. L. Bissell, K. Blaum, A. Ekström, N. Frömmgen, G. Hagen, M. Hammen, K. Hebeler, J. D. Holt, G. R. Jansen, M. Kowalska, K. Kreim, W. Nazarewicz, R. Neugart, G. Neyens, W. Nörtershäuser, T. Papenbrock, J. Papuga, A. Schwenk, J Simonis, K. A. Wendt, and D. T. Yordanov. Unexpectedly large charge radii of neutron-rich calcium isotopes. *Nature Physics*, 12:594–598, Feb 2016.

[60] Skyy V. Pineda, Kristian König, Dominic M. Rossi, B. Alex Brown, Anthony Incorvati, Jeremy Lantis, Kei Minamisono, Wilfried Nörtershäuser, Jorge Piekarewicz, Robert Powel, and Felix Sommer. Charge radius of neutron-deficient ^{54}Ni and symmetry energy constraints using the difference in mirror pair charge radii. *Phys. Rev. Lett.*, 127:182503, Oct 2021.

[61] Jonathan Billowes and P Campbell. High-resolution laser spectroscopy for the study of nuclear sizes and shapes. *Journal of Physics G*, 21:707–739, 1995.

[62] Laser spectroscopy of nickel isotopes with a new data acquisition system at isolde.

[63] Electronic population manipulation in an rfq ion trap for the study of rare transition metal isotopes. 2020.

[64] K. Minamisono, P.F. Mantica, A. Klose, S. Vinnikova, A. Schneider, B. Johnson, and B.R. Barquest. Commissioning of the collinear laser spectroscopy system in the becola facility at nscl. *Nuclear Instruments and Methods in Physics Research Section A: Accelerators, Spectrometers, Detectors and Associated Equipment*, 709:85–94, 2013.

[65] A. Klose, K. Minamisono, and P. F. Mantica. Collinear laser spectroscopy on the ground state and an excited state in neutral ^{55}mn. *Phys. Rev. A*, 88:042701, Oct 2013.

[66] D. M. Rossi, K. Minamisono, B. R. Barquest, G. Bollen, K. Cooper, M. Davis, K. Hammerton, M. Hughes, P. F. Mantica, D. J. Morrissey, R. Ringle, J. A. Rodriguez, C. A. Ryder, S. Schwarz, R. Strum, C. Sumithrarachchi, D. Tarazona, and S. Zhao. A field programmable gate array-based time-resolved scaler for collinear laser spectroscopy with bunched radioactive potassium beams. *Review of Scientific Instruments*, 85(9):093503, 2014.

[67] D. M. Rossi, K. Minamisono, H. B. Asberry, G. Bollen, B. A. Brown, K. Cooper, B. Isherwood, P. F. Mantica, A. Miller, D. J. Morrissey, R. Ringle, J. A. Rodriguez, C. A. Ryder, A. Smith, R. Strum, and C. Sumithrarachchi. Charge radii of neutron-deficient ^{36}K and ^{37}K. *Phys. Rev. C*, 92:014305, Jul 2015.

[68] C.A. Ryder, K. Minamisono, H.B. Asberry, B. Isherwood, P.F. Mantica, A. Miller, D.M. Rossi, and R. Strum. Population distribution subsequent to charge exchange of 29.85kev ni+ on sodium vapor. *Spectrochimica Acta Part B: Atomic Spectroscopy*, 113:16–21, 2015.

[69] A. J. Miller, K. Minamisono, D. M. Rossi, R. Beerwerth, B. A. Brown, S. Fritzsche, D. Garand, A. Klose, Y. Liu, B. Maaß, P. F. Mantica, P. Müller, W. Nörtershäuser, M. R. Pearson, and C. Sumithrarachchi. First determination of ground state electromagnetic moments of ^{53}Fe. *Phys. Rev. C*, 96:054314, Nov 2017.

[70] R. Neugart. Laser spectroscopy on mass-separated radioactive beams. *Nuclear Instruments and Methods in Physics Research*, 186(1):165–175, 1981.

[71] H. J. Andrä, A. Gaupp, and W. Wittmann. New method for precision lifetime measurements by laser excitation of fast-moving atoms. *Phys. Rev. Lett.*, 31:501–504, Aug 1973.

[72] S.L. Kaufman. High-resolution laser spectroscopy in fast beams. *Optics Communications*, 17(3):309–312, 1976.

[73] Bernhard Maaß, Kristian König, Jörg Krämer, Andrew J. Miller, Kei Minamisono, Wilfried Nörtershäuser, and Felix Sommer. A 4π fluorescence detection region for collinear laser spectroscopy. 2020.

[74] Andrew Jacob Miller. Measurements of charge radii of neutron-deficient calcium using collinear laser spectroscopy at becola. *Dissertation*, 2019.

[75] Nist atomic spectra database.

[76] W. Demtröder. *Laser Spectroscopy 1: Basic Principles*. Fifth Edition.

[77] Kristian König, Kei Minamisono, Jeremy Lantis, Skyy Pineda, and Robert Powel. Beam energy determination via collinear laser spectroscopy. *Phys. Rev. A*, 103:032806, Mar 2021.

[78] A. E. Siegmen. *Lasers*. University Science Books, 1986.

[79] Atomic spectral line database from cd-rom 23 of r. l. kurucz.

[80] Atam P. Arya. *Fundamentals of Atomic Physics*. Allyn and Bacon, Inc., 470 Atlantic Avenue, Boston, 1971.

[81] Paul Siddons, Charles S Adams, Chang Ge, and Ifan G Hughes. Absolute absorption on rubidium d lines: comparison between theory and experiment. *Journal of Physics B: Atomic, Molecular and Optical Physics*, 41(15):155004, jul 2008.

[82] Ove Axner, Jörgen Gustafsson, Nicolò Omenetto, and James D. Winefordner. Line strengths, a-factors and absorption cross-sections for fine structure lines in multiplets and hyperfine structure components in lines in atomic spectrometry—a user's guide. *Spectrochimica Acta Part B: Atomic Spectroscopy*, 59(1):1–39, 2004.

[83] Kristian König, Felix Sommer, Jeremy Lantis, Kei Minamisono, Wilfried Nörtershäuser, Skyy Pineda, and Robert Powel. Isotope-shift measurements and king-fit analysis in nickel isotopes. *Phys. Rev. C*, 103:054305, May 2021.

[84] Wilfried Nörtershäuser and Christopher Geppert. *Nuclear Charge Radii of Light Elements and Recent Developments in Collinear Laser Spectroscopy*. Springer Berlin Heidelberg, Berlin, Heidelberg, 2014.

[85] Derek York, Norman M. Evensen, Margarita López Martınez, and Jonás De Basabe Delgado. Unified equations for the slope, intercept, and standard errors of the best straight line. *American Journal of Physics*, 72(3):367–375, 2004.

[86] R. Jenkins, R. Manne, R. Robin, and C. Senemaud. Iupac—nomenclature system for x-ray spectroscopy. *X-Ray Spectrometry*, 20(3):149–155, 1991.

[87] R. Pohl and *etal.*. The size of the proton. *Nature*, 466:213–216.

[88] Randolf Pohl, François Nez, Luis M. P. Fernandes, Fernando D. Amaro, François Biraben, João M. R. Cardoso, Daniel S. Covita, Andreas Dax, Satish Dhawan, Marc Diepold, Adolf Giesen, Andrea L. Gouvea, Thomas Graf, Theodor W. Hänsch, Paul Indelicato, Lucile Julien, Paul Knowles, Franz Kottmann, Eric-Olivier Le Bigot, Yi-Wei Liu, José A. M. Lopes, Livia Ludhova, Cristina M. B. Monteiro, Françoise Mulhauser, Tobias Nebel, Paul Rabinowitz, Joaquim M. F. dos Santos, Lukas A. Schaller, Karsten Schuhmann, Catherine Schwob, David Taqqu, João F. C. A. Veloso, Aldo Antognini, and null null. Laser spectroscopy of muonic deuterium. *Science*, 353(6300):669–673, 2016.

[89] Randolf Pohl, Ronald Gilman, Gerald A. Miller, and Krzysztof Pachucki. Muonic hydrogen and the proton radius puzzle. *Annual Review of Nuclear and Particle Science*, 63(1):175–204, oct 2013.

[90] R.C. Barrett. Model-independent parameters of the nuclear charge distribution from muonic x-rays. *Physics Letters B*, 33(6):388–390, 1970.

[91] B. Dreher, J. Friedrich, K. Merle, H. Rothhaas, and G. Lührs. The determination of the nuclear ground state and transition charge density from measured electron scattering data. *Nuclear Physics A*, 235(1):219–248, 1974.

[92] G.A. Rinker and J. Speth. Nuclear polarization in muonic atoms. *Nuclear Physics A*, 306(3):397–405, 1978.

[93] B.-M. Sherrill. Scientific Opportunities with the NSCL Coupled Cyclotron Facility. *Progress of Theoretical Physics Supplement*, 146:60–69, 03 2002.

[94] S.M. Austin and L.A.K. Simon. *Up from nothing: The Michigan state university cyclotron laboratory.* 01 2015.

[95] Yang Dong and Huo Junde. Nuclear data sheets for $a = 54$. *Nuclear Data Sheets*, 121:1–142, 2014.

[96] D.J. Morrissey, B.M. Sherrill, M. Steiner, A. Stolz, and I. Wiedenhoever. Commissioning the a1900 projectile fragment separator. *Nuclear Instruments and Methods in Physics Research Section B: Beam Interactions with Materials and Atoms*, 204:90–96, 2003. 14th International Conference on Electromagnetic Isotope Separators and Techniques Related to their Applications.

[97] K. Cooper, C.S. Sumithrarachchi, D.J. Morrissey, A. Levand, J.A. Rodriguez, G. Savard, S. Schwarz, and B. Zabransky. Extraction of thermalized projectile fragments from a large volume gas cell. *Nuclear Instruments and Methods in Physics Research Section A: Accelerators, Spectrometers, Detectors and Associated Equipment*, 763:543–546, 2014.

[98] C.S. Sumithrarachchi, D.J. Morrissey, S. Schwarz, K. Lund, G. Bollen, R. Ringle, G. Savard, and A.C.C. Villari. Beam thermalization in a large gas catcher. *Nuclear Instruments and Methods in Physics Research Section B: Beam Interactions with Materials and Atoms*, 463:305–309, 2020.

[99] Bradley Barquest. an advanced ion guode for beam cooling and bunching for collinear laser spectroscopy of rare isotopes.

[100] Robert Powel, Makenna Koble, Julian Palmes, Nathan Everett, Phillip Imgram, Kristian König, Jeremy Lantis, Kei Minamisono, Wilfried Nörtershäuser, Ryan Parker, Skyy Pineda, Felix Sommer, and Andrew Klose. Improved wavelength meter calibration in near infrared region via doppler-free spectroscopy of molecular iodine. *Applied Physics B*, 127:104, 2021.

[101] Thorlabs. Thorlabs beam.

[102] Z. Nouri, R. Li, R.A. Holt, and S.D. Rosner. A penning sputter ion source with very low energy spread. *Nuclear Instruments and Methods in Physics Research Section A: Accelerators, Spectrometers, Detectors and Associated Equipment*, 614(2):174–178, 2010.

[103] N.V. Konenkov, M. Sudakov, and D.J. Douglas. Matrix methods for the calculation of stability diagrams in quadrupole mass spectrometry. *Journal of the American Society for Mass Spectrometry*, 13(6):597–613, 2002.

[104] Meng Wang, W. J. Huang, F. G. Kondev, G. Audi, and S. Naimi. The ame 2020 atomic mass evaluation (ii). tables, graphs and references*. *Chinese Physics. C, High Energy Physics and Nuclear Physics*, 45(3), 3 2021.

[105] A. Klose, K. Minamisono, Ch. Geppert, N. Frömmgen, M. Hammen, J. Krämer, A. Krieger, C.D.P. Levy, P.F. Mantica, W. Nörtershäuser, and S. Vinnikova. Tests of atomic charge-exchange cells for collinear laser spectroscopy. *Nuclear Instruments and Methods in Physics Research Section A: Accelerators, Spectrometers, Detectors and Associated Equipment*, 678:114–121, 2012.

[106] M. and Verlinde, K. Dockx, S. Geldhof, K. König, D. Studer, T. E. Cocolios, R. P. de Groote, R. Ferrer, Yu. Kudryavtsev, T. Kieck, I. Moore, W. Nörtershäuser, S. Raeder, P. Van den Bergh, P. Van Duppen, and K. Wendt. On the performance of wavelength meters: Part 1—consequences for medium-to-high-resolution laser spectroscopy. page 85, 04 2020.

[107] Kristian König, Phillip Imgram, Jörg Krämer, Bernhard Maaß, Konstantin Mohr, Tim Ratajczyk, Felix Sommer, and Wilfried Nörtershäuser. On the performance of wavelength meters: Part 2—frequency-comb based characterization for more accurate absolute wavelength determinations. *Applied Physics B*, 86:86.

[108] Aaron L. Stancik and Eric B. Brauns. A simple asymmetric lineshape for fitting infrared absorption spectra. *Vibrational Spectroscopy*, 47(1):66–69, 2008.

[109] Michael Bender, Paul-Henri Heenen, and Paul-Gerhard Reinhard. Self-consistent mean-field models for nuclear structure. *Rev. Mod. Phys.*, 75:121–180, Jan 2003.

[110] Z. Patyk, A. Baran, J. F. Berger, J. Dechargé, J. Dobaczewski, P. Ring, and A. Sobiczewski. Masses and radii of spherical nuclei calculated in various microscopic approaches. *Phys. Rev. C*, 59:704–713, Feb 1999.

[111] S. Goriely, S. Hilaire, M. Girod, and S. Péru. First gogny-hartree-fock-bogoliubov nuclear mass model. *Phys. Rev. Lett.*, 102:242501, Jun 2009.

[112] M. Kortelainen, T. Lesinski, J. Moré, W. Nazarewicz, J. Sarich, N. Schunck, M. V. Stoitsov, and S. Wild. Nuclear energy density optimization. *Phys. Rev. C*, 82:024313, Aug 2010.

[113] R Utama, Wei-Chia Chen, and J Piekarewicz. Nuclear charge radii: density functional theory meets bayesian neural networks. *Journal of Physics G: Nuclear and Particle Physics*, 43(11):114002, oct 2016.

[114] B. Alex Brown and Kei Minamisono. β^2 corrections to spherical energy-density functional calculations for root-mean-square charge radii. *Phys. Rev. C*, 106:L011304, Jul 2022.

[115] T. H. R. Skyrme. Cvii. the nuclear surface. *The Philosophical Magazine: A Journal of Theoretical Experimental and Applied Physics*, 1(11):1043–1054, 1956.

[116] D. Vautherin and D. M. Brink. Hartree-fock calculations with skyrme's interaction. i. spherical nuclei. *Phys. Rev. C*, 5:626–647, Mar 1972.

[117] G F Bertsch. Monopole moments and the β-vibration in deformed nuclei. *The European Physical Journal A*, 55(12):248, dec 2019.

[118] M Honma, T Otsuka, B A Brown, and T Mizusaki. Shell-model description of neutron-rich pf-shell nuclei with a new effective interaction gxpf 1. *The European Physical Journal A - Hadrons and Nuclei*, 25, sep 2005.

[119] A. Poves, J. Sánchez-Solano, E. Caurier, and F. Nowacki. Shell model study of the isobaric chains a=50, a=51 and a=52. *Nuclear Physics A*, 694(1):157–198, 2001.

[120] M. Honma, T. Otsuka, B. A. Brown, and T. Mizusaki. New effective interaction for pf-shell nuclei and its implications for the stability of the $n = z = 28$ closed core. *Phys. Rev. C*, 69:034335, Mar 2004.

[121] R. du Rietz, J. Ekman, D. Rudolph, C. Fahlander, A. Dewald, O. Möller, B. Saha, M. Axiotis, M. A. Bentley, C. Chandler, G. de Angelis, F. Della Vedova, A. Gadea, G. Hammond, S. M. Lenzi, N. Mărginean, D. R. Napoli, M. Nespolo, C. Rusu, and D. Tonev. Effective charges in the fp shell. *Phys. Rev. Lett.*, 93:222501, Nov 2004.

[122] K. L. Yurkewicz, D. Bazin, B. A. Brown, C. M. Campbell, J. A. Church, D. C. Dinca, A. Gade, T. Glasmacher, M. Honma, T. Mizusaki, W. F. Mueller, H. Olliver, T. Otsuka, L. A. Riley, and J. R. Terry. Nuclear structure in the vicinity of $n = z = 28$ ^{56}Ni. *Phys. Rev. C*, 70:054319, Nov 2004.

[123] J. Dechargé and D. Gogny. Hartree-fock-bogolyubov calculations with the $d1$ effective interaction on spherical nuclei. *Phys. Rev. C*, 21:1568–1593, Apr 1980.

[124] J.F. Berger, M. Girod, and D. Gogny. Time-dependent quantum collective dynamics applied to nuclear fission. *Computer Physics Communications*, 63(1):365–374, 1991.

[125] J. P. Delaroche, M. Girod, J. Libert, H. Goutte, S. Hilaire, S. Péru, N. Pillet, and G. F. Bertsch. Structure of even-even nuclei using a mapped collective hamiltonian and the d1s gogny interaction. *Phys. Rev. C*, 81:014303, Jan 2010.

[126] B. A. Brown, K. Minamisono, J. Piekarewicz, H. Hergert, D. Garand, A. Klose, K. König, J. D. Lantis, Y. Liu, B. Maaß, A. J. Miller, W. Nörtershäuser, S. V. Pineda, R. C. Powel, D. M. Rossi, F. Sommer, C. Sumithrarachchi, A. Teigelhöfer, J. Watkins, and R. Wirth. Implications of the ^{36}Ca $-^{36}$ S and ^{38}Ca $-^{38}$ Ar difference in mirror charge radii on the neutron matter equation of state. *Phys. Rev. Research*, 2:022035, May 2020.

[127] M. M. Sharma, G. Lalazissis, J. König, and P. Ring. Isospin dependence of the spin-orbit force and effective nuclear potentials. *Phys. Rev. Lett.*, 74:3744–3747, May 1995.

[128] P.-G. Reinhard and H. Flocard. Nuclear effective forces and isotope shifts. *Nuclear Physics A*, 584(3):467–488, 1995.

[129] D. Adhikari, H. Albataineh, D. Androic, K. A. Aniol, D. S. Armstrong, T. Averett, C. Ayerbe Gayoso, S. K. Barcus, V. Bellini, R. S. Beminiwattha, J. F. Benesch, H. Bhatt, D. Bhatta Pathak, D. Bhetuwal, B. Blaikie, J. Boyd, Q. Campagna, A. Camsonne, G. D. Cates, Y. Chen, C. Clarke, J. C. Cornejo, S. Covrig Dusa, M. M. Dalton, P. Datta, A. Deshpande, D. Dutta, C. Feldman, E. Fuchey, C. Gal, D. Gaskell, T. Gautam, M. Gericke, C. Ghosh, I. Halilovic, J.-O. Hansen, O. Hassan, F. Hauenstein, W. Henry, C. J. Horowitz, C. Jantzi, S. Jian, S. Johnston, D. C. Jones, S. Kakkar, S. Katugampola, C. Keppel, P. M. King, D. E. King, K. S. Kumar, T. Kutz, N. Lashley-Colthirst, G. Leverick, H. Liu, N. Liyanage, J. Mammei, R. Mammei, M. McCaughan, D. McNulty, D. Meekins, C. Metts, R. Michaels, M. Mihovilovic, M. M. Mondal, J. Napolitano, A. Narayan, D. Nikolaev, V. Owen, C. Palatchi, J. Pan, B. Pandey, S. Park, K. D. Paschke, M. Petrusky, M. L. Pitt, S. Premathilake, B. Quinn, R. Radloff, S. Rahman, M. N. H. Rashad, A. Rathnayake, B. T. Reed, P. E. Reimer, R. Richards, S. Riordan, Y. R. Roblin, S. Seeds, A. Shahinyan, P. Souder, M. Thiel, Y. Tian, G. M. Urciuoli, E. W. Wertz, B. Wojtsekhowski, B. Yale, T. Ye, A. Yoon, W. Xiong, A. Zec, W. Zhang, J. Zhang, and X. Zheng. Precision determination of the neutral weak form factor of ^{48}Ca. *Phys. Rev. Lett.*, 129:042501, Jul 2022.

[130] Bao-An Li, Bao-Jun Cai, Wen-Jie Xie, and Nai-Bo Zhang. Progress in constraining nuclear symmetry energy using neutron star observables since gw170817. *Universe*, 7(6), 2021.

[131] F. J. Fattoyev and J. Piekarewicz. Accurate calibration of relativistic mean-field models: Correlating observables and providing meaningful theoretical uncertainties. *Phys. Rev. C*, 84:064302, Dec 2011.

[132] S.A. Fayans, S.V. Tolokonnikov, E.L. Trykov, and D. Zawischa. Nuclear isotope shifts within the local energy-density functional approach. *Nuclear Physics A*, 676(1):49–119, 2000.

[133] J. Dobaczewski, W. Nazarewicz, T. R. Werner, J. F. Berger, C. R. Chinn, and J. Dechargé. Mean-field description of ground-state properties of drip-line nuclei: Pairing and continuum effects. *Phys. Rev. C*, 53:2809–2840, Jun 1996.

[134] Junjie Yang and J. Piekarewicz. Difference in proton radii of mirror nuclei as a possible surrogate for the neutron skin. *Phys. Rev. C*, 97:014314, Jan 2018.

[135] Paul-Gerhard Reinhard, Xavier Roca-Maza, and Witold Nazarewicz. Information content of the parity-violating asymmetry in ^{208}Pb. *Phys. Rev. Lett.*, 127:232501, Nov 2021.

[136] Reed Essick, Ingo Tews, Philippe Landry, and Achim Schwenk. Astrophysical constraints on the symmetry energy and the neutron skin of ^{208}Pb with minimal modeling assumptions. *Phys. Rev. Lett.*, 127:192701, Nov 2021.

[137] Reed Essick, Philippe Landry, Achim Schwenk, and Ingo Tews. Detailed examination of astrophysical constraints on the symmetry energy and the neutron skin of ^{208}Pb with minimal modeling assumptions. *Phys. Rev. C*, 104:065804, Dec 2021.

[138] Elias R. Most and Carolyn A. Raithel. Impact of the nuclear symmetry energy on the post-merger phase of a binary neutron star coalescence. *Phys. Rev. D*, 104:124012, Dec 2021.

[139] William G. Newton and Gabriel Crocombe. Nuclear symmetry energy from neutron skins and pure neutron matter in a bayesian framework. *Phys. Rev. C*, 103:064323, Jun 2021.

[140] Bhaskar Biswas. Impact of prex-ii and combined radio/nicer/xmm-newton's mass–radius measurement of psr j0740+6620 on the dense-matter equation of state. *The Astrophysical Journal*, 921(1):63, nov 2021.

[141] J.M. Lattimer. Neutron stars and the nuclear matter equation of state. *Annual Review of Nuclear and Particle Science*, 71(1):433–464, 2021.

[142] Francesca Sammarruca and Randy Millerson. Analysis of the neutron matter equation of state and the symmetry energy up to fourth order of chiral effective field theory. *Phys. Rev. C*, 104:034308, Sep 2021.

[143] J. T. Zhang, X. L. Tu, P. Sarriguren, K. Yue, Q. Zeng, Z. Y. Sun, M. Wang, Y. H. Zhang, X. H. Zhou, and Yu. A. Litvinov. Systematic trends of neutron skin thickness versus relative neutron excess. *Phys. Rev. C*, 104:034303, Sep 2021.

[144] Baishan Hu, Weiguang Jiang, Takayuki Miyagi, Zhonghao Sun, Andreas Ekström, Christian Forssén, Gaute Hagen, Jason D. Holt, Thomas Papenbrock, S. Ragnar Stroberg, and Ian Vernon. Ab initio predictions link the neutron skin of 208pb to nuclear forces. *Nature Physics*, 18(10):1196–1200, aug 2022.

[145] Yeunhwan Lim and Jeremy W. Holt. Neutron star radii, deformabilities, and moments of inertia from experimental and ab initio theory constraints on the 208pb neutron skin thickness. 2022.

[146] J. Piekarewicz. Implications of prex-2 on the electric dipole polarizability of neutron-rich nuclei. *Phys. Rev. C*, 104:024329, Aug 2021.

[147] Publication under preparation.

[148] John R. Taylor. *An Introduction to Error Analysis: The Study of Uncertainties in Physical Measurements*. 2 edition, 1996.

[149] Sirah Lasertechnik. Matisse user's guide: Version 2.2.

[150] R. W. P. Drever, J. L. Hall, F. V. Kowalski, J. Hough, G. M. Ford, A. J. Munley, and H. Ward. Laser phase and frequency stabilization using an optical resonator. *Applied Physics B*, 31:97–105, June 1983.

[151] M. Brieger, H. Büsener, A. Hese, F. v.Moers, and A. Renn. Enhancement of single frequency sgh in a passive ring resonator. *Optics Communications*, 38(5):423–426, 1981.

[152] Grant R. Fowles. *Introduction to Modern Optics, Second Edition*. Dover Publications, Inc., New York, 1986.

[153] W. Gins. Satlas: Statistical analysis toolbox for laser spectroscopy.

[154] C. Granados, P. Creemers, R. Ferrer, L. P. Gaffney, W. Gins, R. de Groote, M. Huyse, Yu. Kudryavtsev, Y. Martínez, S. Raeder, S. Sels, C. Van Beveren, P. Van den Bergh, P. Van Duppen, K. Wrzosek-Lipska, A. Zadvornaya, A. E. Barzakh, B. Bastin, P. Delahaye, L. Hijazi, N. Lecesne, F. Luton, J. Piot, H. Savajols, J.-C. Thomas, E. Traykov, R. Beerwerth, S. Fritzsche, M. Block, X. Fléchard, S. Franchoo, L. Ghys, H. Grawe, R. Heinke, T. Kron, P. Naubereit, K. Wendt, M. Laatiaoui, I. Moore, V. Sonnenschein, M. Loiselet, E. Mogilevskiy, and S. Rothe. In-gas laser ionization and spectroscopy of actinium isotopes near the $n = 126$ closed shell. *Phys. Rev. C*, 96:054331, Nov 2017.

[155] Dennis R. Phillips, Raphael M. Kudela, Virginia T. Hamilton, and Mark A. Brzezinski. *Isotope Production and Applications in the 21st Century*. 2000.

[156] B. E. Kane. A silicon-based nuclear spin quantum computer. *Nature*, 1998.

[157] A. Mutschler, A. Lemasson, O. Sorlin, D. Bazin, C. Borcea, R. Borcea, Z. Dombrádi, J.-P. Ebran, A. Gade, H. Iwasaki, E. Khan, A. Lepailleur, F. Recchia, T. Roger, F. Rotaru, D. Sohler, M. Stanoiu, S. R. Stroberg, J. A. Tostevin, M. Vandebrouck, D. Weisshaar, and K. Wimmer. A proton density bubble in the doubly magic ^{34}si nucleus. *Nature Physics*, 13:152–156, 02 2017.

[158] Fairbank Jr. W.M. Lee, S.A. Measurements of the hyperfine structure and isotope shifts of the $3s^23p^2{}^3p_2 \rightarrow 3s3p^3{}^3d_3^0$ transition in silicon. *Physical Review A*, 82:042515, 10 2010.

[159] Hoover M. Holmes, J. Isotope shift in the first spectrum of silicon (si i). *Journal of the Optical Society of America*, 52:86247–250, 03 1962.

[160] isomet.com. Ao frequency shifting - application note.

[161] S. Malbrunot-Ettenauer, S. Kaufmann, S. Bacca, C. Barbieri, J. Billowes, M. L. Bissell, K. Blaum, B. Cheal, T. Duguet, R. F. Garcia Ruiz, W. Gins, C. Gorges, G. Hagen, H. Heylen, J. D. Holt, G. R. Jansen, A. Kanellakopoulos, M. Kortelainen, T. Miyagi, P. Navrátil, W. Nazarewicz, R. Neugart, G. Neyens, W. Nörtershäuser, S. J. Novario, T. Papenbrock, T. Ratajczyk, P.-G. Reinhard, L. V. Rodríguez, R. Sánchez, S. Sailer, A. Schwenk, J. Simonis, V. Somà, S. R. Stroberg, L. Wehner, C. Wraith, L. Xie, Z. Y. Xu, X. F. Yang, and D. T. Yordanov. Nuclear charge radii of the nickel isotopes $^{58-68,70}$Ni. *Phys. Rev. Lett.*, 128:022502, Jan 2022.

[162] FRIB. Mass explorer.

[163] Takaharu Otsuka, Michio Honma, and Takahiro Mizusaki. Structure of the $N = Z = 28$ closed shell studied by monte carlo shell model calculation. *Phys. Rev. Lett.*, 81:1588–1591, Aug 1998.

[164] C. Gorges, L. V. Rodríguez, D. L. Balabanski, M. L. Bissell, K. Blaum, B. Cheal, R. F. Garcia Ruiz, G. Georgiev, W. Gins, H. Heylen, A. Kanellakopoulos, S. Kaufmann, M. Kowalska, V. Lagaki, S. Lechner, B. Maaß, S. Malbrunot-Ettenauer, W. Nazarewicz, R. Neugart, G. Neyens, W. Nörtershäuser, P.-G. Reinhard, S. Sailer, R. Sánchez, S. Schmidt, L. Wehner, C. Wraith, L. Xie, Z. Y. Xu, X. F. Yang, and D. T. Yordanov. Laser spectroscopy of neutron-rich tin isotopes: A discontinuity in charge radii across the $n = 82$ shell closure. *Phys. Rev. Lett.*, 122:192502, May 2019.

[165] Björn Jonson. Light dripline nuclei. *Physics Reports*, 389(1):1–59, 2004.

[166] W. Geithner, T. Neff, G. Audi, K. Blaum, P. Delahaye, H. Feldmeier, S. George, C. Guénaut, F. Herfurth, A. Herlert, S. Kappertz, M. Keim, A. Kellerbauer, H.-J. Kluge, M. Kowalska, P. Lievens, D. Lunney, K. Marinova, R. Neugart, L. Schweikhard, S. Wilbert, and C. Yazidjian. Masses and charge radii of $^{17--22}$Ne and the two-proton-halo candidate ^{17}Ne. *Phys. Rev. Lett.*, 101:252502, Dec 2008.

[167] J. Lee, X. X. Xu, K. Kaneko, Y. Sun, C. J. Lin, L. J. Sun, P. F. Liang, Z. H. Li, J. Li, H. Y. Wu, D. Q. Fang, J. S. Wang, Y. Y. Yang, C. X. Yuan, Y. H. Lam, Y. T. Wang, K. Wang, J. G. Wang, J. B. Ma, J. J. Liu, P. J. Li, Q. Q. Zhao, L. Yang, N. R. Ma, D. X. Wang, F. P. Zhong, S. H. Zhong, F. Yang, H. M. Jia, P. W. Wen, M. Pan, H. L. Zang, X. Wang, C. G. Wu, D. W. Luo, H. W. Wang, C. Li, C. Z. Shi, M. W. Nie, X. F. Li, H. Li, P. Ma, Q. Hu, G. Z. Shi, S. L. Jin, M. R. Huang, Z. Bai, Y. J. Zhou, W. H. Ma, F. F. Duan, S. Y. Jin, Q. R. Gao, X. H. Zhou, Z. G. Hu, M. Wang, M. L. Liu, R. F. Chen, and X. W. Ma. Large isospin asymmetry in ^{22}Si/^{22}O mirror gamow-teller transitions reveals the halo structure of ^{22}Al. *Phys. Rev. Lett.*, 125:192503, Nov 2020.

[168] V. Lapoux, V. Somà, C. Barbieri, H. Hergert, J. D. Holt, and S. R. Stroberg. Radii and binding energies in oxygen isotopes: A challenge for nuclear forces. *Phys. Rev. Lett.*, 117:052501, Jul 2016.

[169] Andreas Ekström and Gaute Hagen. Global sensitivity analysis of bulk properties of an atomic nucleus. *Phys. Rev. Lett.*, 123:252501, Dec 2019.

[170] Rituparna Kanungo, I Tanihata, and A Ozawa. Observation of new neutron and proton magic numbers. *Physics Letters B*, 528(1):58–64, 2002.

[171] C. Samanta and S. Adhikari. Extension of the bethe-weizsäcker mass formula to light nuclei and some new shell closures. *Phys. Rev. C*, 65:037301, Feb 2002.

[172] O. Sorlin and M.-G. Porquet. Nuclear magic numbers: New features far from stability. *Progress in Particle and Nuclear Physics*, 61(2):602–673, 2008.

[173] M. Kumawat, G. Saxena, M. Kaushik, R. Sharma, and S.K. Jain. Description of nuclei with magic number z (n) = 6. *Canadian Journal of Physics*, 96(12):1413–1419, 2018.

[174] D. S. Ahn, N. Fukuda, H. Geissel, N. Inabe, N. Iwasa, T. Kubo, K. Kusaka, D. J. Morrissey, D. Murai, T. Nakamura, M. Ohtake, H. Otsu, H. Sato, B. M. Sherrill, Y. Shimizu, H. Suzuki, H. Takeda, O. B. Tarasov, H. Ueno, Y. Yanagisawa, and K. Yoshida. Location of the neutron dripline at fluorine and neon. *Phys. Rev. Lett.*, 123:212501, Nov 2019.

[175] Takaharu Otsuka, Toshio Suzuki, Jason D. Holt, Achim Schwenk, and Yoshinori Akaishi. Three-body forces and the limit of oxygen isotopes. *Phys. Rev. Lett.*, 105:032501, Jul 2010.

[176] E. K. Warburton, J. A. Becker, and B. A. Brown. Mass systematics for a=29–44 nuclei: The deformed a∼32 region. *Phys. Rev. C*, 41:1147–1166, Mar 1990.

[177] A. Poves, J. Retamosa, M. J. G. Borge, and O. Tengblad. Halo signals in the beta decay of ^{28}o. *Zeitschrift für Physik A Hadrons and Nuclei*, Dec 1994.

[178] Á. Koszorús, X. F. Yang, W. G. Jiang, S. J. Novario, S. W. Bai, J. Billowes, C. L. Binnersley, M. L. Bissell, T. E. Cocolios, B. S. Cooper, R. P. de Groote, A. Ekström, K. T. Flanagan, C. Forssén, S. Franchoo, R. F. Garcia Ruiz, F. P. Gustafsson, G. Hagen, G. R. Jansen, A. Kanellakopoulos, M Kortelainen, W. Nazarewicz, G. Neyens, T. Papenbrock, P.-G. Reinhard, C. M. Ricketts, B. K. Sahoo, A. R. Vernon, and S. G. Wilkins. Apr 2021.

[179] M Avgoulea, Yu P Gangrsky, K P Marinova, S G Zemlyanoi, S Fritzsche, D Iablonskyi, C Barbieri, E C Simpson, P D Stevenson, J Billowes, P Campbell, B Cheal, B Tordoff, M L Bissell, D H Forest, M D Gardner, G Tungate, J Huikari, A Nieminen, H Penttilä, and J Äystö. Nuclear charge radii and electromagnetic moments of radioactive scandium isotopes and isomers. *Journal of Physics G: Nuclear and Particle Physics*, 38(2):025104, jan 2011.

[180] Á. Koszorús, L.J. Vormawah, R. Beerwerth, M.L. Bissell, P. Campbell, B. Cheal, C.S. Devlin, T. Eronen, S. Fritzsche, S. Geldhof, H. Heylen, J.D. Holt, A. Jokinen, S. Kelly, I.D. Moore, T. Miyagi, S. Rinta-Antila, A. Voss, and C. Wraith. Proton-neutron pairing correlations in the self-conjugate nucleus 42sc. *Physics Letters B*, 819:136439, 2021.

[181] Kristian König, Stephan Fritzsche, Gaute Hagen, Jason D. Holt, Andrew Klose, Jeremy Lantis, Yuan Liu, Kei Minamisono, Takayuki Miyagi, Witold Nazarewicz, Thomas Papenbrock, Skyy Pineda, Robert Powel, and Paul-Gerhard Reinhard. Surprising charge-radius kink in the sc isotopes at $n = 20$. *Publication under preparation.*

Appendix A Useful Equations

Below is a list of equations that were used and referenced in this thesis, collecting them here all here to mitigate any confusion when their names are referenced.

A.1 The Weighted Mean

The weighted mean used in this analysis is

$$\bar{x} = \frac{\sum_i^n \left(\frac{x_i}{\sigma_i^2}\right)}{\sum_i^n \left(\frac{1}{\sigma_i^2}\right)} \tag{95}$$

where x and σ_i are the elements and their uncertainties, respectively, and the uncertainty of the weighted mean is

$$\sigma_{\bar{x}} = \sqrt{\frac{1}{\sum_i^n \sigma_i^{-2}}} \tag{96}$$

A.2 The Standard Error of the Mean

The standard error of the mean is

$$\sigma_{\bar{x}} = \frac{\sigma}{\sqrt{n}} \tag{97}$$

where n is the number of observations of the sample and σ is the standard deviation.

A.3 The Standard Deviation

The standard deviation is

$$\sigma = \sqrt{\frac{\sum \left(x_i - \mu\right)^2}{n}} \tag{98}$$

where μ is the mean of the population.

A.4 Exact Error Propagation Formula

The exact error propagation formula for an equation f is

$$\sigma_f = \sqrt{\left(\frac{\partial f}{\partial a}\sigma_a\right)^2 + \left(\frac{\partial f}{\partial b}\sigma_b\right)^2 \cdots} \tag{99}$$

A.5 Signal to Noise Ratio

$$\mathrm{SNR} = \frac{\mathrm{Signal\,Height} - \mathrm{Background\,Noise}}{\sqrt{\mathrm{Background\,Noise}}} \tag{100}$$

A.6 Differential Mean-squared Charge Radius

$$\delta\langle r^2\rangle^{A,A'} = \frac{\delta\nu^{A,A'} - \mu^{A,A'}K_\alpha}{F} + \mu^{A,A'}\alpha \tag{101}$$

A.7 Uncertainty in the Differential Mean-squared Charge Radius

$$\sigma_{\delta\langle r^2\rangle^{A,A'}} = \sqrt{\left(\frac{1}{F}\sigma_{\nu^{A,A'}}\right)^2 + \left(\left(\alpha - \frac{K_\alpha}{F}\right)\sigma_{\mu^{A,A'}}\right)^2 + \left(-\frac{\mu^{A,A'}}{F}\sigma_{K_\alpha}\right)^2 + \left(\left(\frac{-\nu^{A,A'} + \mu^{A,A'}K_\alpha}{F^2}\right)\sigma_F\right)^2} \tag{102}$$

A.8 Uncertainty in the Mass Coefficient

$$\sigma_{\mu^{A,A'}} = \sqrt{\left(\frac{1}{(m_A + m_e)^2}\sigma_{m_A}\right)^2 + \left(-\frac{1}{(m_{A'} + m_e)^2}\sigma_{m_{A'}}\right)^2 + \left(\frac{(m_{A'} - m_A)(m_A + m_{A'} + 2m_e)}{(m_A + m_e)^2(m_{A'} + m_e)^2}\sigma_{m_e}\right)^2} \tag{103}$$

Appendix B Relevant Derivations

B.1 Deriving the Nuclear Equation of State and Nuclear Pressure

We can also characterize nuclear matter with an equation of state. We start with identifying the density of nucleus

$$\rho = \frac{A}{V} \tag{104}$$

and the energy density

$$\varepsilon = \frac{E}{V} \tag{105}$$

where A is the total number of nucleons, V is the nuclear volume, and E is the energy. Using these two equations we are able to obtain an equation of state, Eq. 106, for nuclear matter [4].

$$\left[\frac{E}{A}\right] = \frac{\varepsilon}{\rho} \tag{106}$$

The pressure inside of the nucleus can be defined in terms of the energy density with

$$P(\rho) = \rho \frac{\partial \varepsilon}{\partial \rho} - \varepsilon \tag{107}$$

The asymmetry parameter is

$$I = \frac{N - Z}{A} \tag{108}$$

The difference between the symmetric matter equation of state and neutron matter equation of state is the symmetry energy, which is the energy you gain due to the symmetry (or asymmetry) of the system

$$E_{\text{sym}} = \frac{E}{A}_{I=1}(\rho) - \frac{E}{A}_{I=0}(\rho) \tag{109}$$

and is shown in Fig. 1.

B.2 Deriving the Velocity Component β

1. Start with the relativistic expression for the kinetic energy K_E, taking note that $E = mc^2$.

$$K_E = qU = mc^2 - m_0c^2 \tag{110}$$

2. Convert the mass component in terms of m_0 by substituting into m.

$$m = m_0\gamma = m_0\sqrt{\frac{1}{1-\beta^2}} \tag{111}$$

We now have

$$K_E = qU = m_0\sqrt{\frac{1}{1-\beta^2}}c^2 - m_0c^2 \tag{112}$$

❖ Note the Lorentz term γ comes from

$$\gamma^2 = \frac{c^2}{c^2-v^2} = \frac{1}{1-\frac{v^2}{c^2}} = \frac{1}{1-\beta^2} \longrightarrow \gamma = \sqrt{\frac{1}{1-\beta^2}} = \frac{1}{\sqrt{1-\beta^2}} \tag{113}$$

3. Rearrange the equation so that

$$\frac{qU}{m_0c^2} = \sqrt{\frac{1}{1-\beta^2}} - 1 \tag{114}$$

4. Solve for β.

$$\beta = \sqrt{1 - \frac{1}{\frac{q^2U^2}{m_0^2c^4} + \frac{2qU}{m_0c^2} + 1}} \tag{115}$$

5. To make this equation match Eq. 18, we must put the mass in units of eV/c^2, thus yielding

$$\beta = \sqrt{1 - \frac{1}{\frac{q^2U^2}{m^2} + \frac{2qU}{m} + 1}} \tag{116}$$

by making the substitution

$$m_0 = \frac{m}{c^2} \tag{117}$$

B.3 Standard Deviation of the Poisson Distribution

The Poisson distribution describes the results of experiments in which we count events that occur at random but at a definite average rate. If you count the occurrences of an event of this type in a chosen time interval T and obtain ν counts, then the best estimate for the true average number in time T is ν, and the uncertainty is $\sqrt{\nu}$. Its derivation is described in below, adapted from Ref. [148].

The Poisson distribution is defined by Eq. 118, which in the context of laser spectroscopy can be thought of as the probability of a certain number of counts ν within an interval of time. The variable μ is the average number of counts expected if the counting experiment is repeated many times.

$$P_\mu(\nu) = e^{-\mu}\frac{\mu^\nu}{\nu!} \tag{118}$$

To establish significance in the parameter μ, we calculate the average number of counts $\bar{\nu}$. This average is found by summing over all possible values of ν, each multiplied by its probability:

$$\bar{\nu} = \sum_{\nu=0}^{\infty} \nu P_{\mu}(\nu) = \sum_{\nu=0}^{\infty} \nu e^{-\mu} \frac{\mu^{\nu}}{\nu!} \tag{119}$$

The first term in the sum is dropped because it is zero, and $\nu/\nu!$ can be replaced by $1/(\nu-1)$. This yields

$$\bar{\nu} = \mu e^{-\mu} \sum_{\nu=1}^{\infty} \frac{\mu^{\nu-1}}{(\nu-1)!} \tag{120}$$

Thus the infinite sum is

$$\sum_{\nu=1}^{\infty} \nu e^{-\mu} \frac{\mu^{\nu}}{\nu!} = 1 + \mu + \frac{\mu^2}{2!} + \frac{\mu^3}{3!} + \cdots = e^{\mu} \tag{121}$$

Notice that Eq. 121 is just the exponential function e^{μ}. This means that the $e^{-\mu}$ in Eq. 120 is exactly cancelled by the sum, resulting in

$$\bar{\nu} = \mu \tag{122}$$

Now that the value of μ has been established, the standard deviation can be derived. The standard deviation of any distribution after a large number of trials is the root-mean-square deviation from the mean (Eq. 123).

$$\sigma_{\nu}^2 = \overline{(\nu - \bar{\nu})^2} = \overline{\nu^2} - \bar{\nu}^2 \tag{123}$$

Knowing that $\bar{\nu} = \mu$ and using $\overline{\nu^2} = \mu^2 + \mu$, the standard deviation is

$$\sigma_{\nu} = \sqrt{\mu} \tag{124}$$

Thus, in hyperfine spectra throughout this thesis the errorbars on the data points are the square-root of the counts (Eq. 124).

B.4 Calculating the Charge Exchange Efficiency

In order to calculate the CEC efficiency at BECOLA, three measurements need to be performed: the beam current of the ion beam (I_{-50}), the total beam current (I_{+50}), and the beam current of neutral atoms ($I_{+50+1000}$). The reason for the three measurements is because the Faraday cup cannot differentiate between ions and atoms. A system of equations can be solved to find the conversion efficiency C using the three equations listed below, where $I(+)$ is a singly charged ion current and $I(0)$ is a neutralized atom current.

1. -50 V repelling voltage applied to the Faraday cup

$$I_{-50} = I(+) \tag{125}$$

2. +50 V repelling voltage applied to the Faraday cup

$$I_{+50} = I(+)\,(1 + C) + CI(0) \tag{126}$$

3. +50 V repelling voltage applied to the Faraday cup +1000 V ion kicker

$$I_{+50+1000} = CI(0) \tag{127}$$

Solving this system of equations the conversion efficiency is

$$C = \frac{I_{+50} - I_{-50} - I_{+1000}}{I_{-50}} \tag{128}$$

The CEC efficiency is given by

$$\eta_{\mathrm{CEC}} = \frac{I(0)}{I(+) + I(0)} \tag{129}$$

By using Eq. 129, the efficiency may also be expressed as

$$\eta_{\mathrm{CEC}} = \frac{\frac{I_{+50+1000}}{C}}{I_{-50} + \frac{I_{+50+1000}}{C}} \tag{130}$$

Appendix C The BECOLA Continuous Wave Laser System

C.1 Principles of Lasers

The word "laser" is an acronym which stands for Light Amplification by Stimulated Emission of Radiation. A broad description of a laser is that it is a device that generates or amplifies light. All lasers contain 3 essential elements [78]:

1. a gain medium, which is in general pumped by an external source and acts as an amplifier for electromagnetic radiation
2. a pumping process to excite the gain medium
3. optical feedback elements that increase the path length through the gain medium, allowing the beam of radiation to bounce back and forth repeatedly through the medium.

When the gain medium is excited by the pump it must achieve population inversion, where more atoms in the medium are in a higher quantum energy level than in a lower one. Once this condition is achieved, the electromagnetic radiation within a narrow band of frequencies will be amplified. The resulting light that comes out of the laser is coherent and monochromatic (narrow line width), meaning that it is in phase and of a single frequency. Narrow line width lasers are essential for atomic spectroscopy because they are able to excite specific electronic transitions that reveal critical information about the nucleus.

C.2 Titanium Sapphire Laser

The following description of the Ti:Sapphire laser used at BECOLA is taken from Ref. [149].

This laser gets its name via its laser gain medium, which is a Titanium-doped Sapphire. Frequency-selective elements that have an impact on the free-spectral range (FSR) are the mirror set, thin etalon, and thick etalon. The FSR is the spacing between the modes within a resonator in terms of optical frequency, and in the case of this overall laser system is 160 MHz. The birefringent (BiFi) filter is used for course frequency selection. This optical element consists of three quartz plates stacked together and oriented at the Brewster angle with respect to the incident light. When scanning the BiFi, the optic is rotated and thus rotates the polarization of the incoming beam. It also works as a polarization filter: incoming p-polarized light sees no reflection at the Brewster angle whereas the s-polarized light will encounter high losses due to reflection. The incoming light is resolved into two orthogonal components. They see different refractive indices and hence will propagate with different phase velocities, experiencing a slight displacement with respect to each other.

The polarization of the incoming light is rotates to a certain degree depending on its wavelength. for a certain orientation of the optical axis with respect to the polarization of the incoming beam there are only a finite number of wavelengths for which the polarization will remain unchanged, of these wavelengths the quartz (SiO_2) plate acting as a full-wave plate. accordingly, the light oscillating with one of these wavelengths will come out of the quartz plate and see no losses whereas the remaining wavelength with the BiFi is achieved by rotating the quartz plate with an angle ρ with respect to the plates surface normal. In this way, the optical axis of the quartz crystal will also be rotated, hence yielding new wavelength of the incoming light which there is no change of the polarization state, therefore no losses through reflection at Brewsters incidence.

The piezo etalon is formed by two prisms with parallel base sides, functioning as a Fabry-Perot interferometer with an air gap. One prism is mounted to a piezoelectric actuator to control the air gap thickness. This optical element ensures that all except one longitudinal mode have high loses and therefor lasing at this mode is not possible. Therefore, the spacing of the etalon must be matched to a multiple of the favored longitudinal mode's wavelength, and this spacing is actively controlled.

The combination of the birefringent filter and the piezo etalon is not sufficient to guarantee single-mode single-frequency laser operation Therefore there is another frequency filter: a solid state Fabry-Perot etalon, called the thin etalon. Its position in relation to the laser beam can be adjusted with the help of a motor-controlled mount. It is adjusted so that it give no direct reflections from the etalon's facettes into the laser beam paths to avoid complicated laser intensity dynamics. For the TE one of its modes' frequency has to be the same as the laser resonator mode's frequency. For this purpose the reflection from one facette is monitored and compared to the total laser intensity. A control loop will adjust the TE position so that the ratio of these two signals is kept constant.

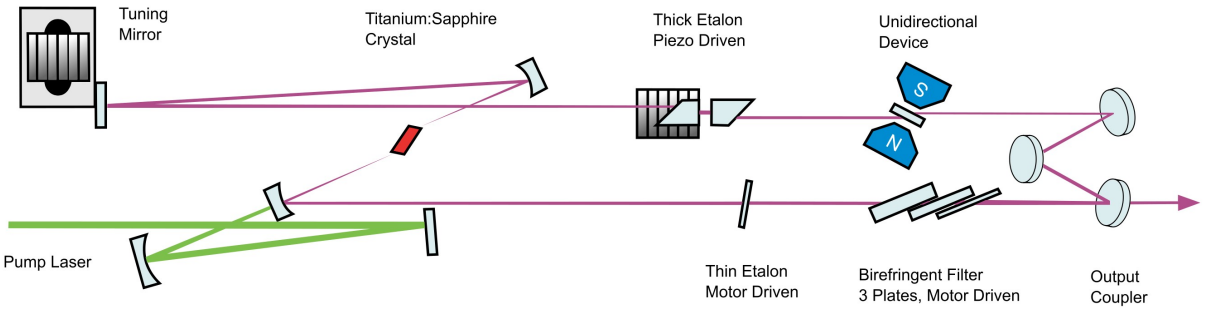

Figure 75: Matisse TS diagram.

A schematic of the Ti:Sa laser is shown below. This laser covers a wvelength range of 700-1000 nm,

C.3 Second Harmonic Generation via WaveTrain Ring Cavity

Second harmonic light 77 was generated by directing the N-IR 708 nm Matisse TS output into an optical cavity where the light does many passes through a nonlinear crystal. Light passes through an Electro-Optic Modulator (EOM) to create sidebands for active stabilization using the Pound-Drever-Hall method [150]. The light was mode matched and phase matched to the cavity and the crystal.

A ring cavity is formed by deflecting the beam path using the prism. The resonator is tuned by translating the prism via the piezoelectric transducer. Both the prism and nonlinear crystal are cut for Brewster's angle to minimize reflection losses. These resonator losses are the main limiting factor for the power enhancement and hence for the SHG conversion efficiency. The main task in constructing a resonance doubler with highest efficiency is therefor to reduce the losses. This delta configuration shown in Fig. 76 reduces the dimensions of the resonator and increases the spectral width of the resonator modes. This reduces the linewidth requirements for the laser source to be doubled. The purpose of the resonator is the amplify the

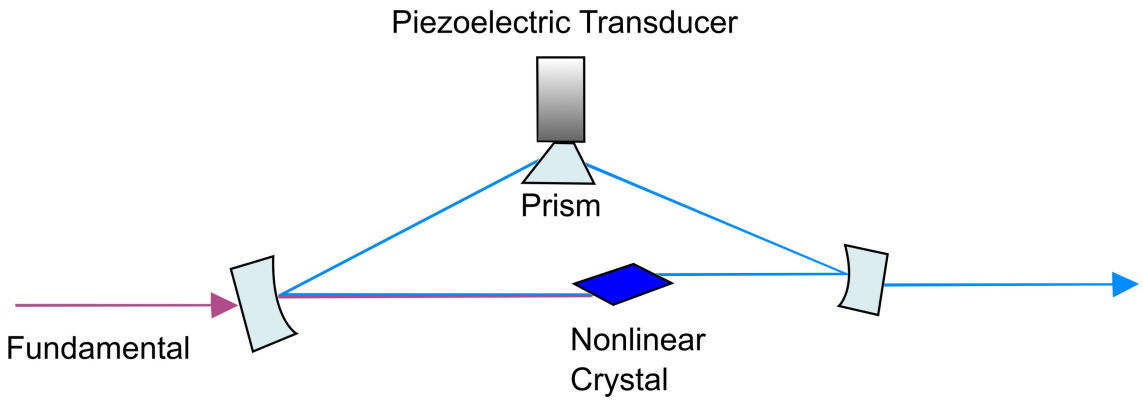

Figure 76: Spectraphysics WaveTrain Delta cavity diagram.

signal of the lightwave, storing the energy of many light round-trips to obtain an increase of the injected light power by constructive superposition with the resonator. If the nonlinear crystal is arranged inside such a resonator the conversion efficiency is increased [151]. Crystal structures are generally isotropic, meaning that the polarization produced in the crystal by a given electric field is varies in a manner that depends on the direction of the applied field in relation to the crystal lattice [152]. This results in the speed of propagation of a light wave in the crystal is a function of the direction of propagation and polarization of the light. The displacement of the electron under the action of an external field $\vec{E}$, as well as the resulting polarization $\vec{P}$, depends on the direction of the field as well as its magnitude. The dependence of $\vec{P}$ on $\vec{E}$ is expressible as

a tensor relation in the form

$$\begin{bmatrix} P_x \\ P_y \\ P_z \end{bmatrix} = \epsilon_0 \begin{bmatrix} \chi_{11} & \chi_{12} & \chi_{13} \\ \chi_{21} & \chi_{22} & \chi_{23} \\ \chi_{31} & \chi_{32} & \chi_{33} \end{bmatrix} \begin{bmatrix} E_x \\ E_y \\ E_z \end{bmatrix} \quad \text{abbreviated,} \quad \overrightarrow{P} = \epsilon_0 \boldsymbol{\chi} \overrightarrow{E} \tag{131}$$

where $\boldsymbol{\chi}$ is the susceptibility tensor. Second harmonic generation process is a nonlinear optical process that results in the doubled frequency of the fundamental light. In ordinary light sources, the radiation fields are much smaller than the fields that bind the electrons to the atoms and hence the radiation acts as a small perturbation [152]. If the radiation field is comparable to the atomic fields $\left(\sim 10^8\,\mathrm{V/cm}\right)$, then the relation between the polarization and radiation field is no longer a linear one. In an isotropic medium, the relation between $\overrightarrow{P}$ on $\overrightarrow{E}$ is expressed as a series expansion (Eq. 132) involving on the magnitudes since the directions of the polarization coincides with that of the field.

$$P = \epsilon_0 \left(\chi E + \chi^{(2)} E^2 + \chi^{(3)} E^3 \cdots \right) \tag{132}$$

For crystals, $\overrightarrow{P}$ on $\overrightarrow{E}$ are not necessarily parallel and the expansion is normally written as the sum of two terms

$$\mathbf{P} = \mathbf{P}^{\mathrm{L}} + \mathbf{P}^{\mathrm{NL}} \tag{133}$$

where linear polarization is

$$\mathbf{P}^{\mathrm{L}} = \epsilon_0 \boldsymbol{\chi} \mathbf{E} \tag{134}$$

and the nonlinear polarization is given by

$$\mathbf{P}^{\mathrm{NL}} = \epsilon_0 \chi^{(2)} E^2 + \epsilon_0 \chi^{(3)} E^3 \cdots \tag{135}$$

If the impressed field $\overrightarrow{E}$ is a light wave of angular frequency ω, then the second harmonic polarization $\overrightarrow{P}\,(2\omega)$ arises from the term $\epsilon_0 \chi^{(2)} E^2$ (Eq. 136).

$$P_i\,(2\omega) = \sum_i \sum_j \chi^{(2)}_{ijk} E_j E_k \tag{136}$$

The amount of second harmonic light that is produced depends critically on the form the $\chi^{(2)}$ tensor.

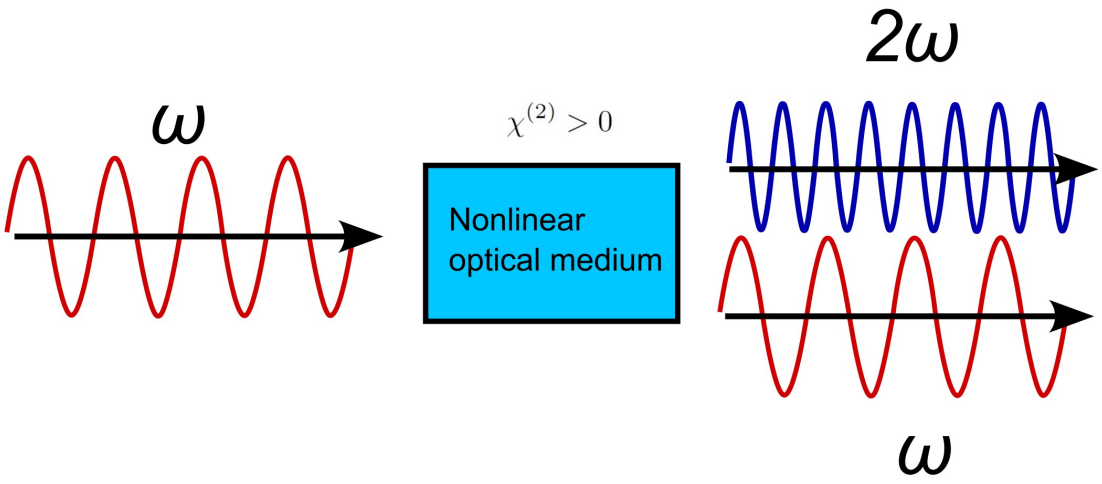

Figure 77: Simple explanation of a nonlinear optical medium producing second harmonic light.

Appendix D Software Development for Analysis

The BECOLA DAQ stores data in `.mda` (Microsoft Access Add-in) files, which are in binary format. Although various file converters exist for this data format, BECOLA has its own which can be used by making the converter file executable using `chmod +x mda2ascii_64`. The command `mda2ascii_64 -mt1f DBEC_*.mda` was used to convert the `.mda` files to `.asc` (ASCII) format. Using `-mt1f` instead of `-1f` gets rid of the headers in the data, allowing it to be read more easily into Python using `pandas` package. The resulting data structure found in the ASCII file contains various columns, and those of interest are shown in the table below.

Column Number	Value
0	run
1	region
2	vstep
4	time_step
8	dac_mat_set
11	dac_read_dvm
13	fug_voltagedivider_read
15	time
16	pmt_0
17	pmt_1
18	pmt_2

Once the ASCII file is read into Python using a `pandas` data frame, you will notice that there are still headers as a series of hashes that interfere when trying to make arrays of the data for analysis. To delete these headers, you may use something on the order of `data = dataframe[(dataframe['run'] != '#')]`.

My data analysis program, `Skeleton.py`, is a script that uses a series of tools in the form of Classes to perform the analysis. Using this method, `Skeleton.py` is the file from which all others branch fromand contains all of the controls. A general outline is shown below, where `ExperimentalParameters.py`, `Hyperfine_Fit.py`, `Operations.py`, and `Import_Data.py` are all class files. The `ExperimentalParameters` and `Operations` classes are used broadly throughout the `Skeleton` to perform, as their names suggest, operations or retrieve experimental parameters pertaining to the experimental data. Apart from those shown in the figure, these operations can check initial control settings and abort the program if necessary. The experimental parameters provide values from laser frequencies and masses to initial guesses for fitting.

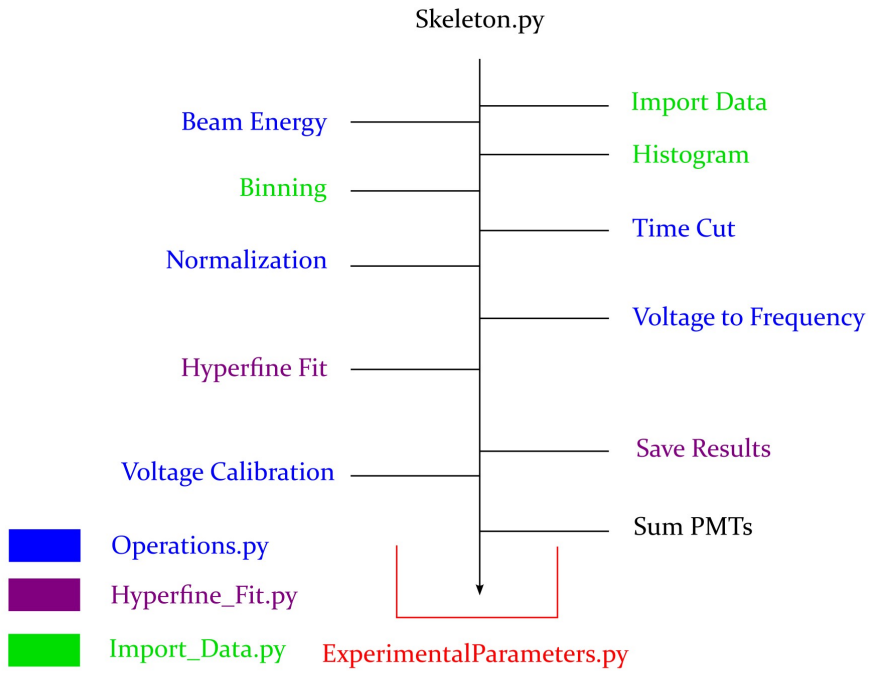

Figure 78: Skeleton placeholder

Separately, there is a Multiple file script to sum exported data from the Skeleton.

The python packages that are used within my software are `pandas`, `csv`, `matplotlib`, `numpy`, `sys`, `sympy`, `lmfit`, and `scipy`. The different functions that this software package includes are:

- Bunch/DC Mode options
- Collinear/Anticollinear Options
- Hyperfine Spectrum Simulation
- Export Data and Fit Results
- Save Figures
- Multiple Functions
  - Pseudo Voigt
  - Voigt
  - Skewed Voigt
  - Custom Asymmetric Pseudo Voigt
  - Satellite peak Options

- Normalization Options
- Time Gate Position/Width Selection
- Free and Fixed heights
- Calculate Isotope Shifts
- Voltage Calibration procedure
- AOM quick settings and frequency shift
- Frequency double/triple/quadrupule quick setting
- Tools
  - Voltage Interpolation
  - King-Plot
  - Rest-frame frequency determination
  - Doppler-shifted resonance frequency calculator

The analysis was consistent between all functions with the exception of the SkewedVoigt LMFIT function. It is unclear why this function does not estimate the centroid correctly. In my experience, fixing the gamma parameter tends to help produce more sensible results-however, I do not trust it and would not recommend using the SkewedVoigt function from LMFIT. As such, the asymmetric pseudo-Voigt should be sufficient.

There is limited space on the BECOLA I:/drive and therefore data files from the DAQ are stored on the Linux machine, which is not accessible to the local machine without using PuTTY and the Fishtank. In order to run Python scripts through the Fishtank, an environment needs to be created. This can be done in the steps below, where the third step executes the environment and the fourth executes the script.

1. `module load anaconda/python3.5`
2. `python3 -m venv env`
3. `source env/bin/activate`
4. `python Skeleton.py`

As an aside, while writing this thesis it has come to my attention that there exists a Python spectroscopy analysis software called SATLAS (Statistical Analysis Toolbox for Laser Spectroscopy)[153] which as been used in Ref.[154] and may be of use to the reader.

Appendix E Development at BECOLA

E.1 Laser Light Transport System

For transitions with deep UV transitions attained from the frequency-quadrupled light and pulsed laser systems, an optical fiber cannot be used due to the process of solarization, which damages the optical fiber over time. At BECOLA solarization damage has been observed in time scales as low as days at less than 1 mW of laser power, lowering the transmission efficiency through the fiber optic cable [63]. The alternative is to use a system of mirrors to transport light from one room to another. A major issue, however, is the stability of the laser beam position because small fluctuations influence the laser beam position considerably due to the long lever arm. The light needed to be transported over 15 m from room 1440 to 1361B. This is a problem because depending on the level of fluctuation, the Doppler-shifted spectrum will be effected as well as how much time the laser beam spends overlapped with the ion beam. A typical experiment at BECOLA uses approximately 300 μW of laser power, providing an estimate for how much initial laser power is needed to obtain an acceptable resonance spectrum. A rough estimate for the amount of power after a system of mirrors is

$$P_f = P_i R^N \tag{137}$$

where R is the reflectivity of the mirror, N is the number of mirrors, P_i is the initial power, and P_f is the power at the end of the system.

The ceiling-based light transport system (Fig. 79,80) consisted of an aluminum extrusion suspended above the laser enclosure, supported on either side by I-beams of the original roof structure. A small breadboard was attached to the aluminum extrusion, where optics could be mounted. Local sources of fluctuation include:

1. Opening and closing of doors (1361B and 1440)
2. Laser box vibrations (1361B)
3. Laser power fluctuations, changing the perceived position on the CCD camera
4. Air conditioning wind (1440)
5. Height of the mirror mount posts

Figure 79: Front view of the CW light transport system. The black anodized aluminum extrusion (center) is clamped to the I-beams on both sides. A periscope mount with one 45°mirror is attached to a twelve-inch post, directing light towards the hanging breadboard (left) which is clamped to the left I-beam.

Figure 80: Back view of the CW laser light transport system. The beam pipe entrance which sends the light to 1361B and the BECOLA beamline can be seen directly underneath the breadboard, above the door.

Measurements were performed with different tests for sources of beam jitter. Opening and closing the laser room door had a significant effect on the laser beam jitter. Sorbothane was added to the clamps and underneath all of the components of the light-transport structure with negligible improvement. A PID loop using the CCD camera and a picomotor was programmed to compensate for beam position drift (Fig. 81,82). Using this system, spectroscopy of Ni with fourth harmonic light was achieved. Unfortunately, after a few months of measurements, the vibrations could not be dampened reliably and the stability was still dependent on the activity within the building. As a response, a floor-based light transport system was constructed (Fig. 83). Standard deviations of the beam jitter in the x and y directions across data sets were 140 μm and 70 μm, respectively. This jitter should be investigated further.

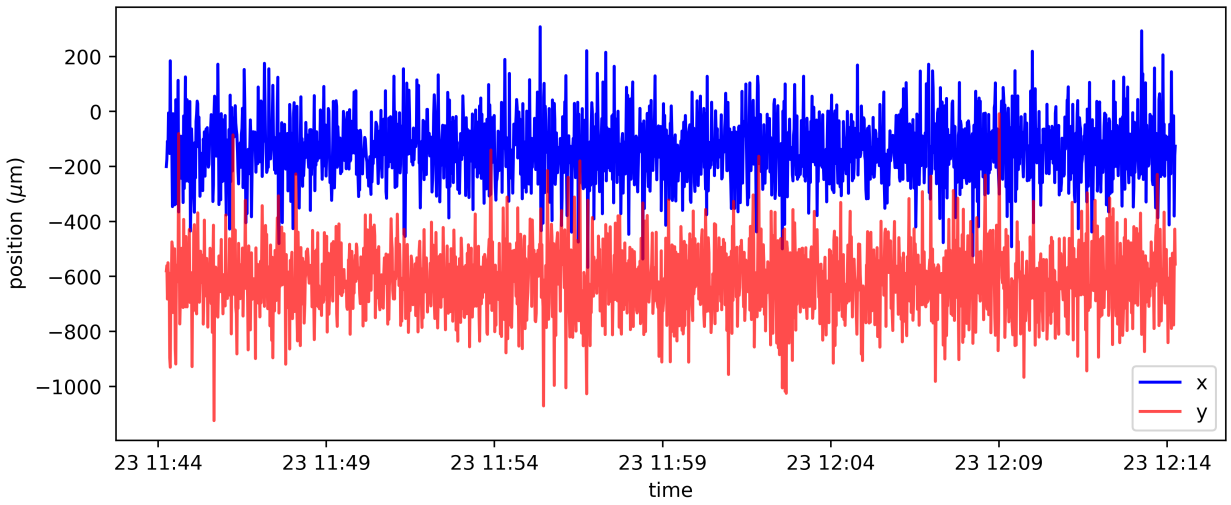

Figure 81: Laser beam stability over a period of 30 minutes. The PID loop was active and the CCD camera was placed at the breadboard right before injection into the BECOLA beamline.

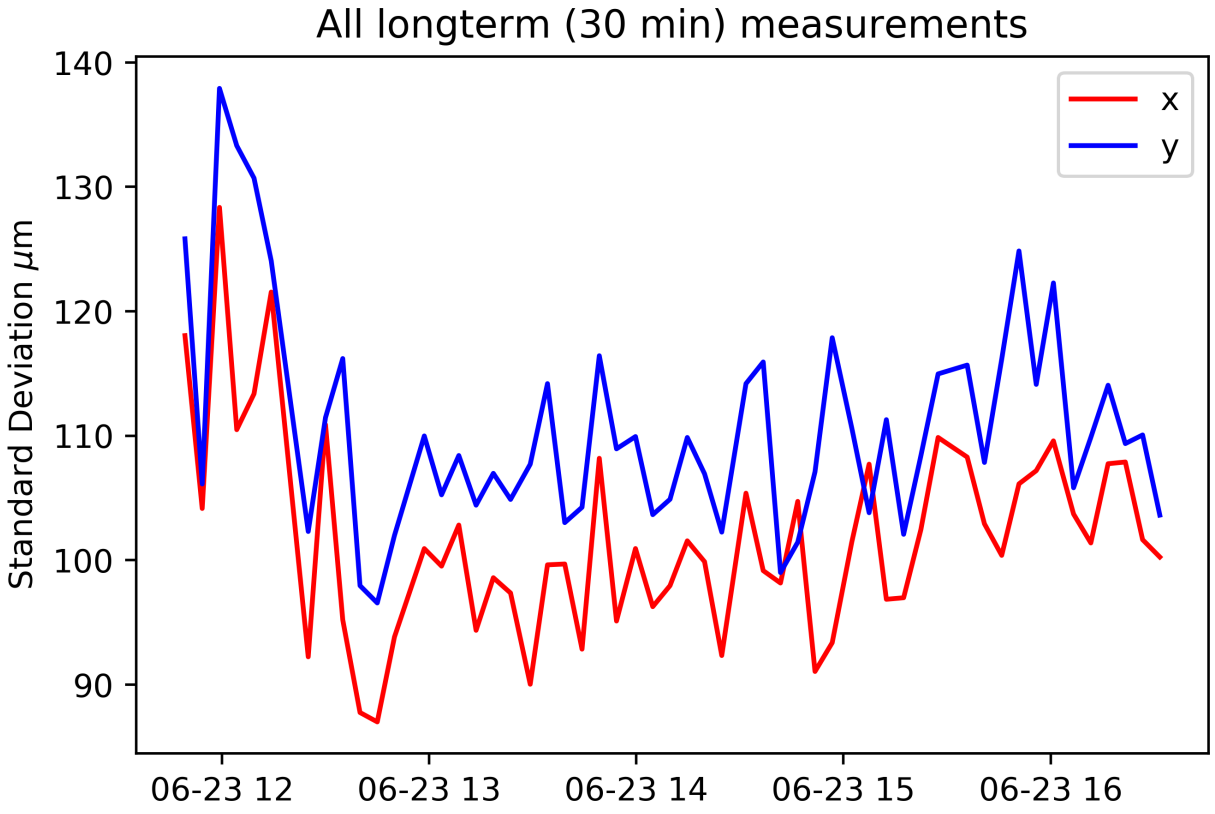

Figure 82: Standard deviations of beam stability for 30 minute measurements over a period of four hours. There is an increased jitter around 12:00, and the y direction is more susceptible to vibrations than with x.

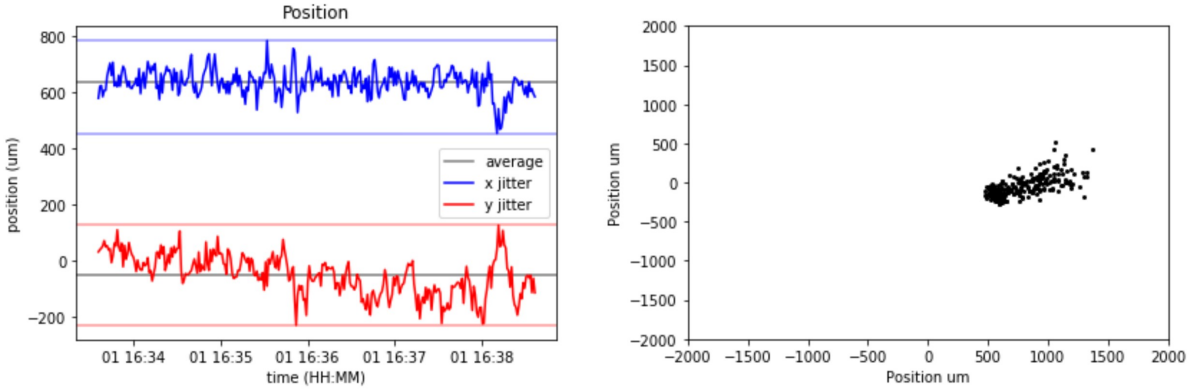

Figure 83: Floor-based light transport system data.

E.2 RISE Collaboration and the Future of BECOLA

A Resonance Ionization Spectroscopy Experiment (RISE) collaboration between BECOLA and MIT began its commissioning of a resonance ionization beamline (Fig. 84) began at the beginning of 2022. The vacuum components and other hardware were installed, and the internal irises were calibrated. The injection-seeded pulsed laser installation was a large part of the installation time. It was pumped by the ORNL laser system and timed by the quantum composer. Different multi-step ionization schemes were attempted and spectra for different transitions of ^{27}Al were collected. PAC proposals for FRIB have been accepted for neutron deficient aluminum and molecules of exotic thorium isotopes. Current efforts are in preparation for the $^{22-26}$Al experiment, where ^{22,23}Al are proton-halo and proton-skin candidates. A sample spectrum for ^{27}Al is shown below in Fig. 85, which will be used for determining the isotope shift of exotic Al isotopes produced at FRIB.

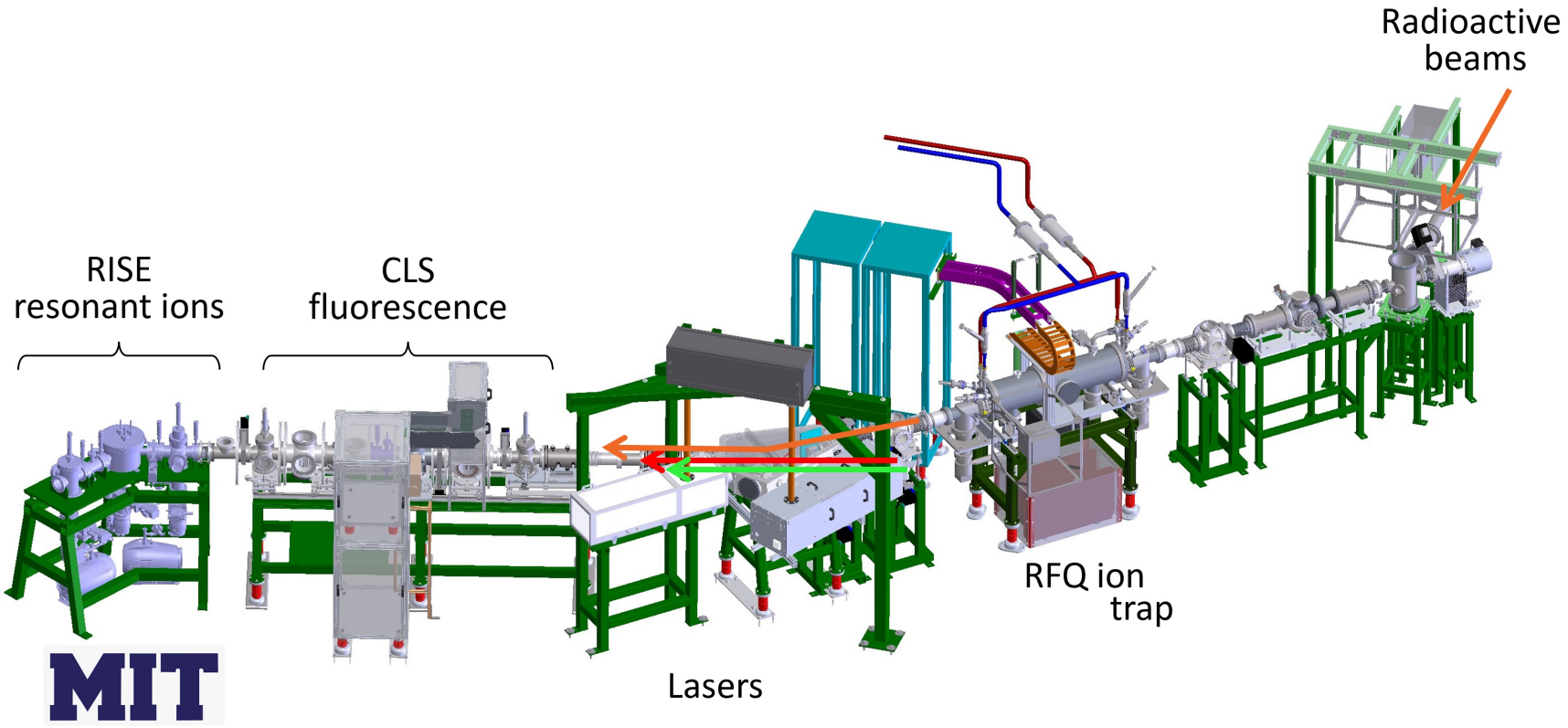

Figure 84: The BECOLA-RISE beamline. The shaded blue portion at the end (left-most side of the figure labeled 'MIT') is the contribution from the collaboration to detect resonant ions produced by high powered pulsed lasers and multi-step ionization schemes. Radioactive beam direction is shown as the orange arrows while the lasers are in green and red.

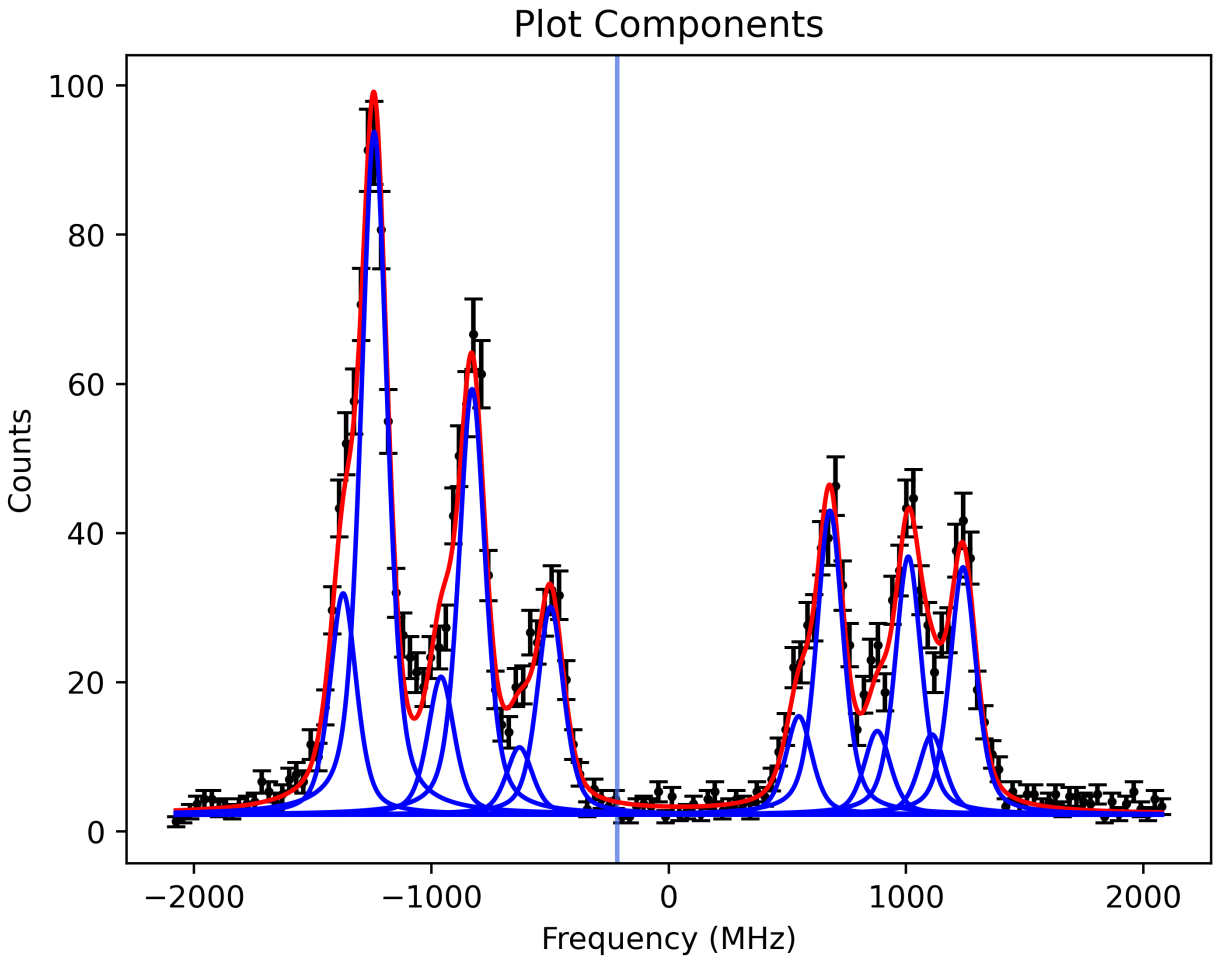

Figure 85: ^{27}Al spectrum for the $D_{3/2} \rightarrow S_{1/2}$ transition that shows a satellite peak on the left side of each main hyperfine peak due to charge exchange. These fit components are shown in blue, beneath the red fitline. The vertical line indicates the centroid of the fit.

To conclude this section, an example of hyperfine splitting tree (Fig. 86) is shown below.

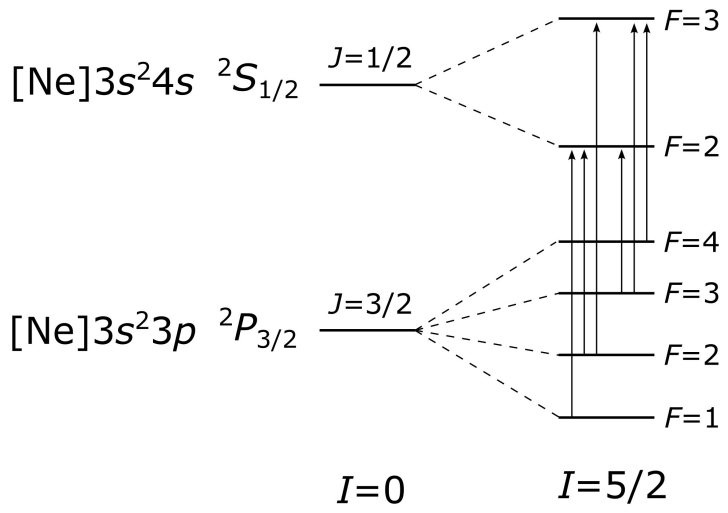

Figure 86: Example hyperfine splitting tree for an ^{27}Al transition, showing how when the nuclear spin is $I = 0$ only the fine structure splitting is present. Adding a nucleus with non-zero nuclear spin leads to hyperfine splitting.

E.2.1 Iris Calibration

The irises within the new beamline components were calibrated, taking measurements in both closing and opening to counteract hysteresis. Below is a plot showing the best fit to the data. A quadratic fit was chosen to reproduce the data due to friction between the interlocking petals of the iris. When doing precise alignment of the pulsed laser systems through the BECOLA-RISE beamline, I set the irises to their minimum diameters that still allowed light to pass through without getting clipped. These settings, which are written here for future reference but also taped to each of the micrometers on the beamline, are shown in Tab. 17. If matching these settings, it is best to start in one direction (either opening or closing) to reach the micrometer value to avoid hysteresis. For clarity, irises 1 and 3 are the original black micrometers that slide in and out of the beamline vertically, each with 3, 5 and 7 mm apertures. Irises 2, 4, and 5 have the variable apertures that were designed at MIT with a range from 0 to 40 mm in diameter. The main reason the aperture settings are not all the same throughout the beamline is because the center of the iris is not perfectly in the center of the beamline nor perfectly along the z-axis of the laser light through the beamline.

Iris Number	Micrometer Setting (mm)
1	39.5
2	28.24
3	44.5
4	30
5	39

Table 17: Iris positions for laser alignment.

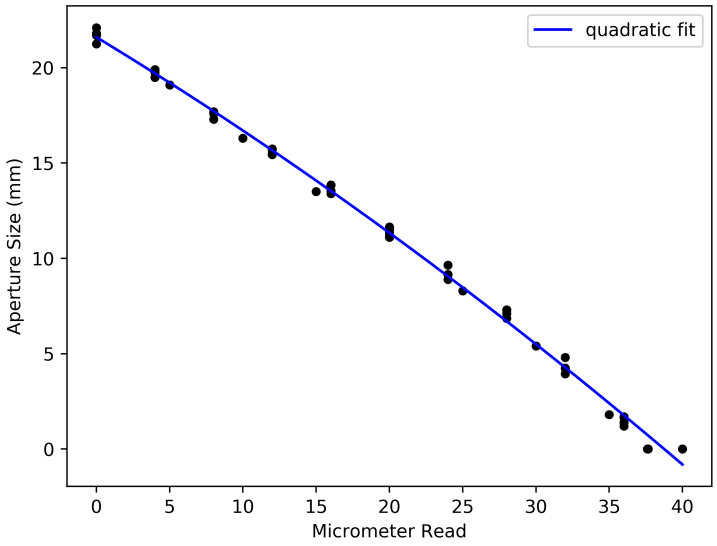

Figure 87: Iris calibration for the 3 new irises designed by MIT along the BECOLA-RISE beamline.

E.2.2 Injection-seeded Pulsed Laser System Frequency Shift

The injection-seeded and pulsed laser systems were setup in 1440 after two new 8X4 laser tables were installed. A discrepancy in the injection-seeded laser output was measured based on the setpoint. Depending on the setpoint of the laselock (using side of fringe locking method), the frequency was also shifted as shown in Fig. 88 by a maximum of 15 MHz. These frequency measurements were done by coupling the output laser light into a WS30 wave meter, where the uncertainty on each point is 3 MHz. The fastest solution to this issue was to use the output of the injection-seeded laser to lock the Ti:Sa.

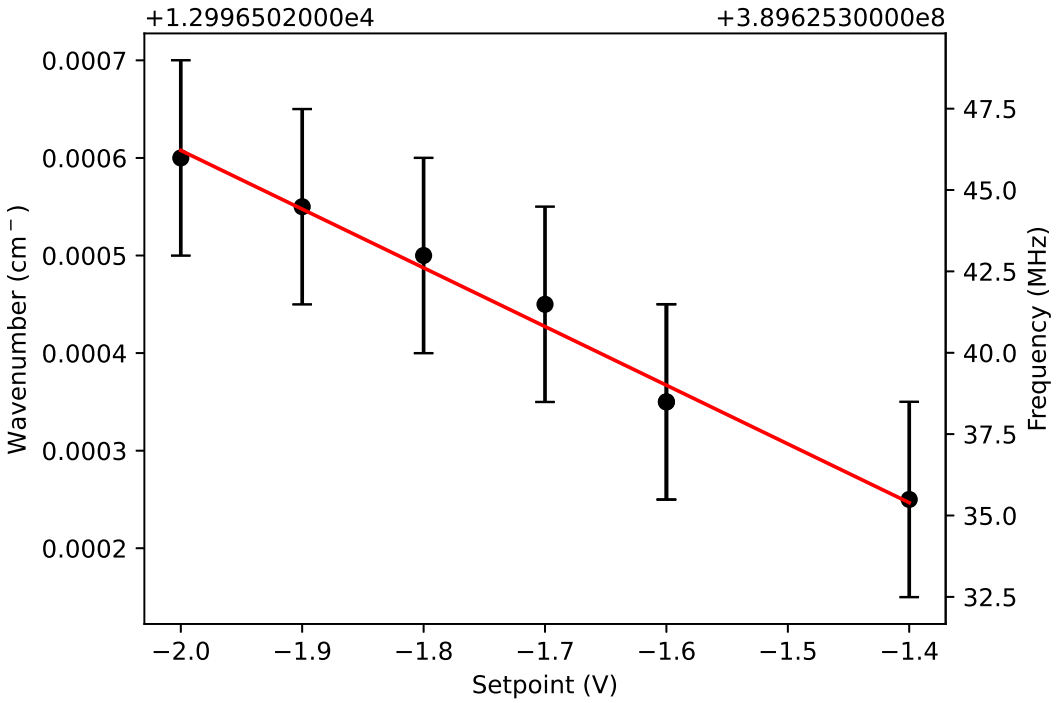

Figure 88: Shift in wavenumber of the output of the injection-seeded laser as a function of the setpoint on the LaseLock. The maximum uncertainty for the laser frequency if the output frequency is unknown is 15 MHz.

E.3 ORNL Laser System Calibrations

Laser calibrations are shown in the plots below for the ORNL laser system.

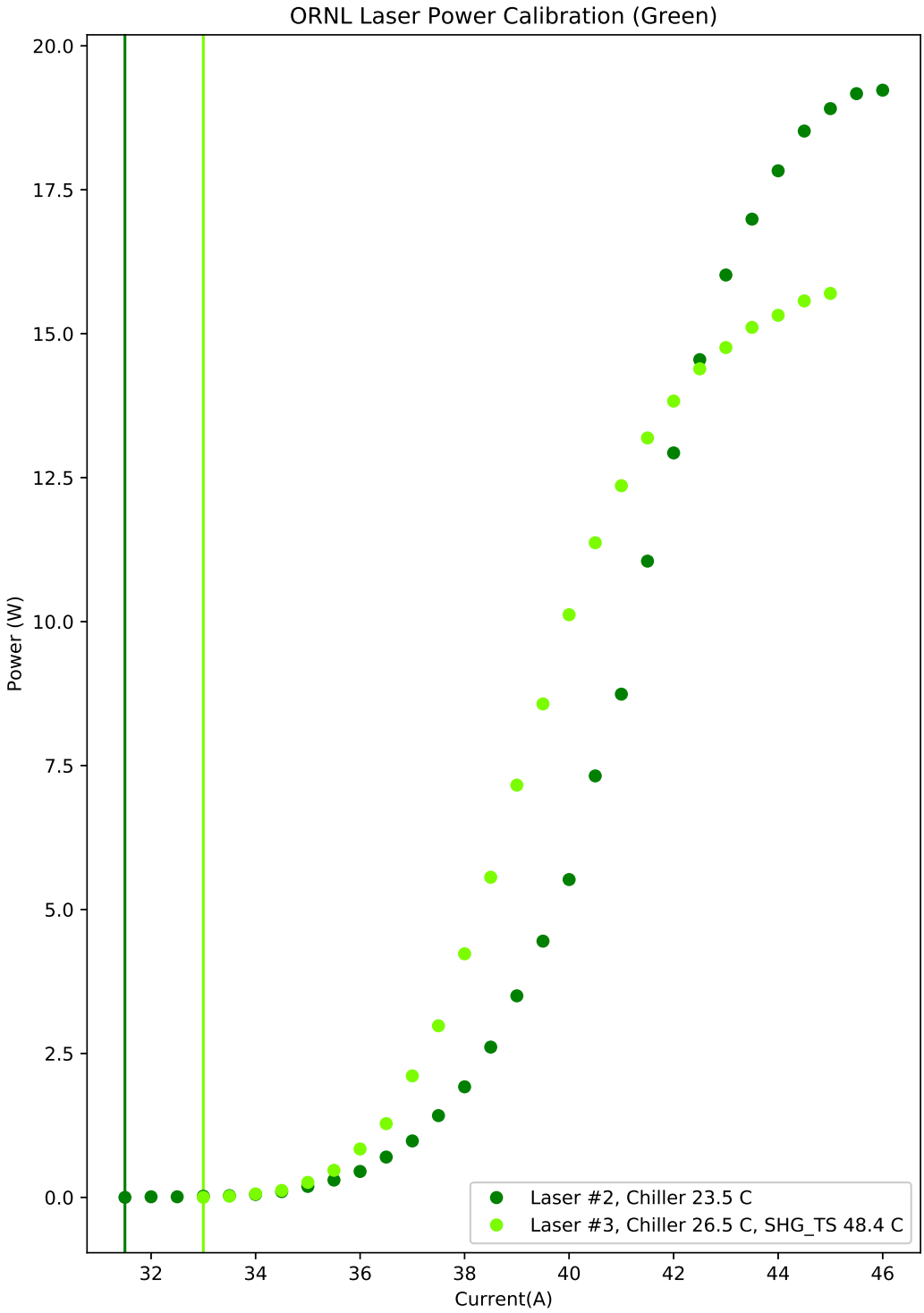

Figure 89: ORNL Calibration Curves of 532 nm light for Lasers 2 and 3.

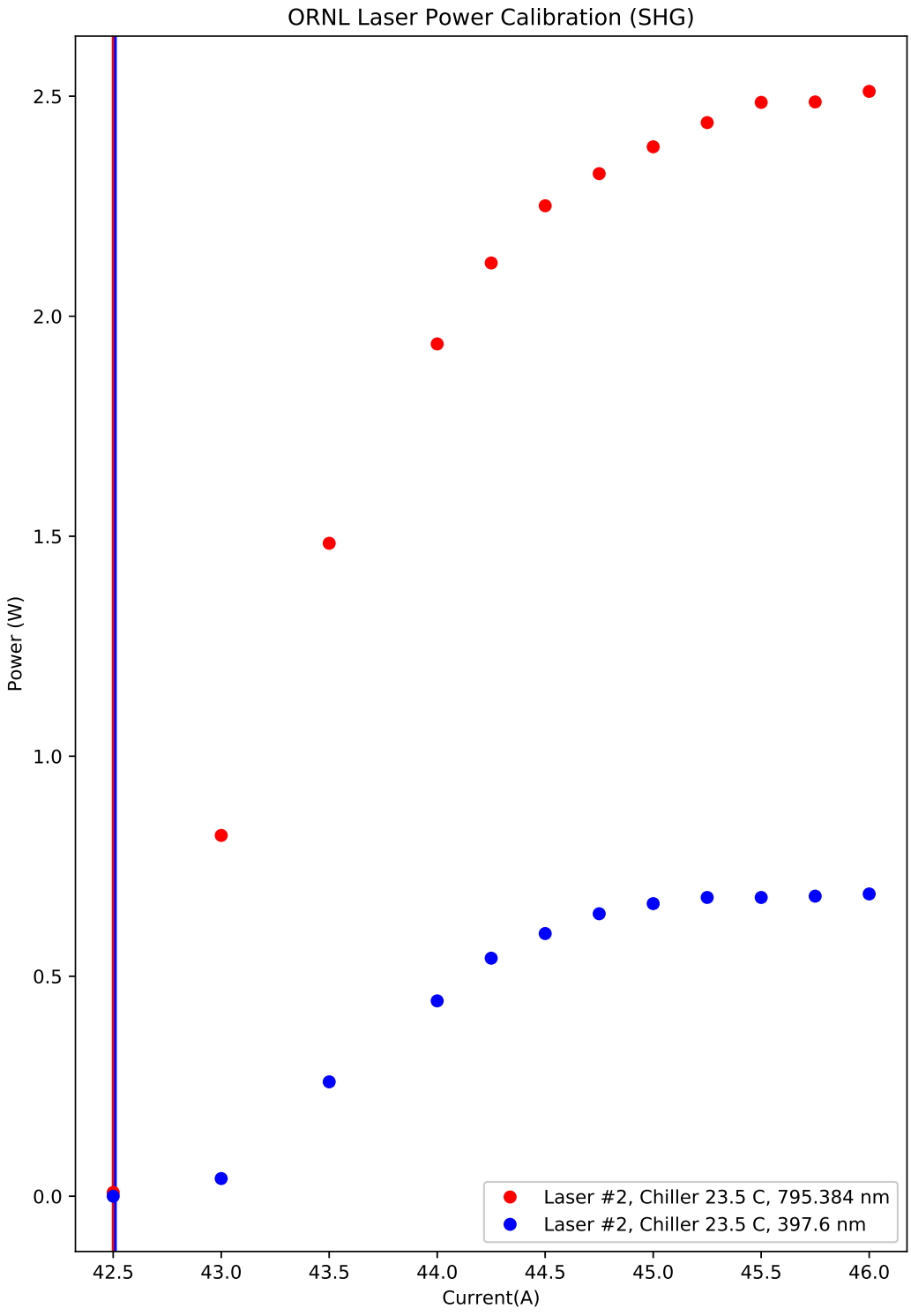

Figure 90: Curves for fundamental (red) light and SHG (blue).

Appendix F Silicon at BECOLA

F.1 PIG Source with Silicon Cathodes

Thus far, cathodes of Ca, Mn, Fe, Ni, Sc, Zr, Sn-Ca, Si-C, Si-Cu, Si, Pd, and Al have successfully produced ion beams for spectroscopy at BECOLA. However, some cathodes require less maintenance than others and are easier to produce stable ion beams for spectroscopic studies. Silicon in particular was a challenge because the source required maintenance extremely frequently. Due to its high conductivity, a Si-C amalgam was used to attempt a silicon ion beam. This ion beam was extremely dirty and spectroscopy of Si was not achieved.The cathode itself was brittle which made maintenance challenging. In the end both Si-Cu and pure silicon cathodes worked, however the maintenance was necessary every two days (Fig. 92). Pictures for all of the Si cathodes used at BECOLA are shown in Fig. 91.

Figure 91: Silicon cathodes placed into the PIG source. Si-C (left), Si-Cu (middle), Si (right). Notice the slightly more metallic color near the hole on the Si-C and Si-Cu cathodes, suggesting that the distribution of silicon is not uniform throughout.

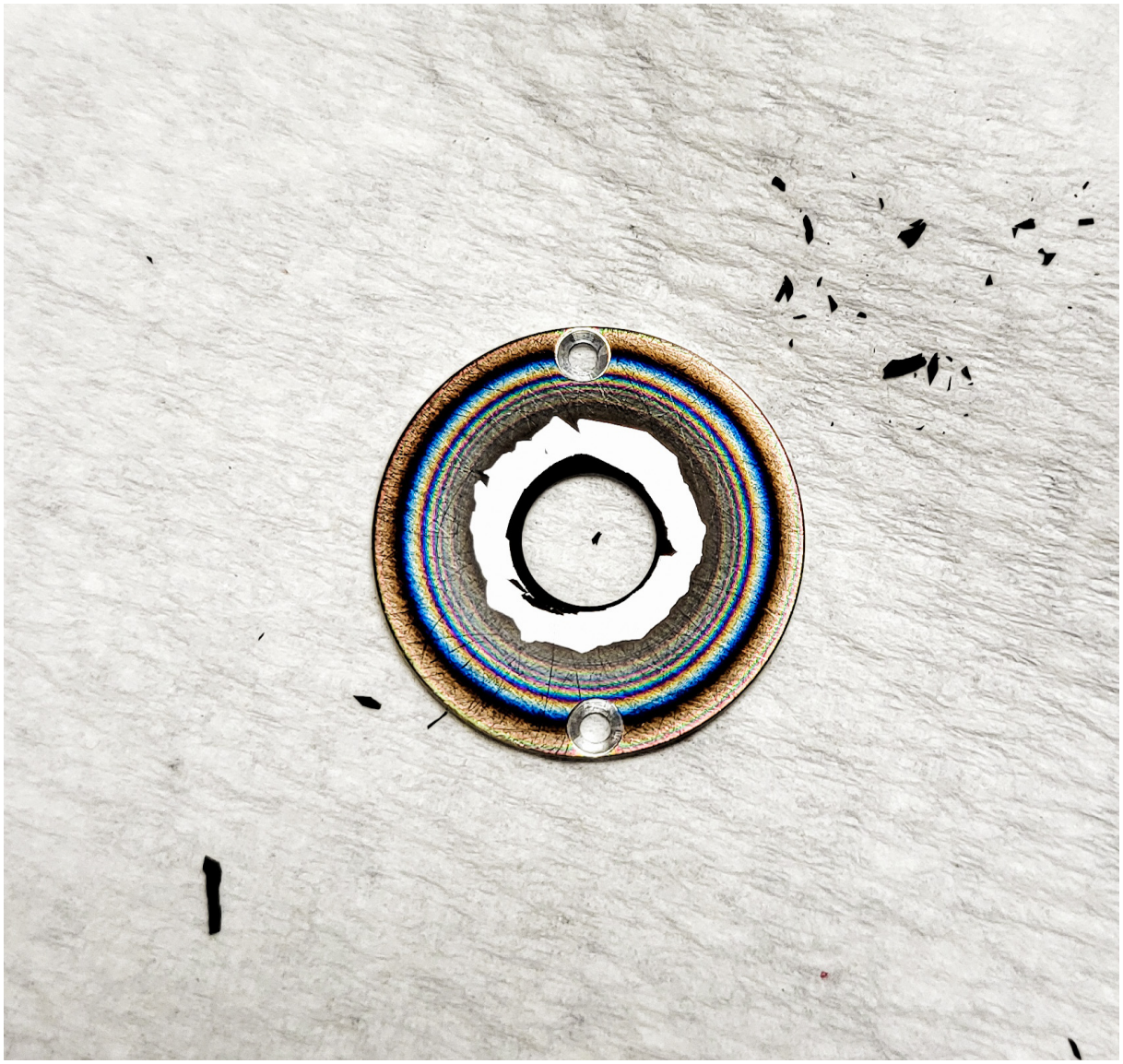

Figure 92: A picture of the anode during the cleaning of the PIG source. Fragments have been chipped off to reveal the anode.

The reason for including these details is if BECOLA decides to use Si cathodes in the future. Si is interesting in general for its chemical and nuclear properties, from biological importance [155] to applications to quantum computing [156] and the ^{34}Si 'bubble nucleus' [157]. Laser spectroscopy on ^{31}Si has only been simulated [158], and PAC proposals have been submitted to study ^{34}Si. I should also point out that silicon spectral studies are scarce, with only a meager 2 publications [159, 158] currently in the literature (excluding BECOLA's contributions).

F.2 Modifications to the Photon Detection System

A 3D-printed holder for PMT1 and PMT2 was installed onto the beamline. Filters were added to block out unwanted fluorescence light.

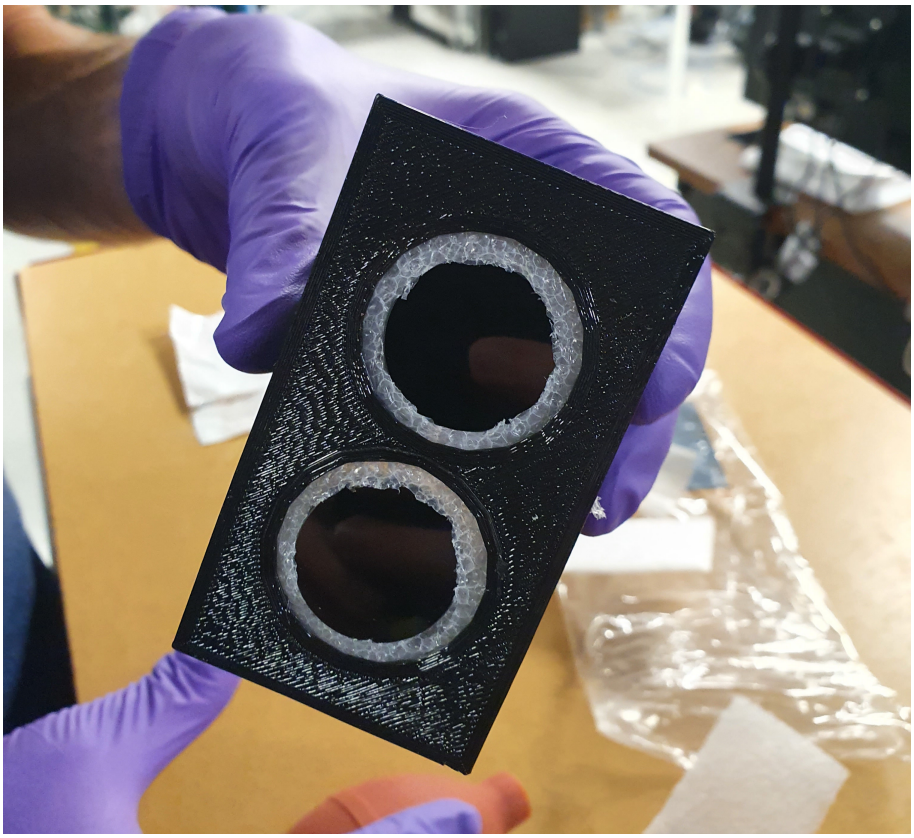

Figure 93: Two PMTs situated in a custom 3D printed holder. Filters were placed in front of the PMTs to select only the fluorescence light and increase the signal to noise ratio.

F.3 Spectroscopy of Silicon

F.3.1 Use of Fourth Harmonic Light

The effort to measure the $3s^2 3p^3 \rightarrow 3s^2 3p^2$ transition ($A_2 1 = 4.54 \times 10^7$) [75] was not successful. Therefor the $3s^2 4s \rightarrow 3s^2 3p 4s$ transition was used to obtain the spectra below (Fig. 97). A feedback system was used to stabilize the laser beam using the CCD camera and LabVIEW. In the end we moved the entire WaveTrain to 1361B. The transition using FHG (fourth harmonic generation) it did not work for Si but did for Ni. A comparison between the FHG spectrum using the CCD camera stabilization and the new feedback system would be interesting.

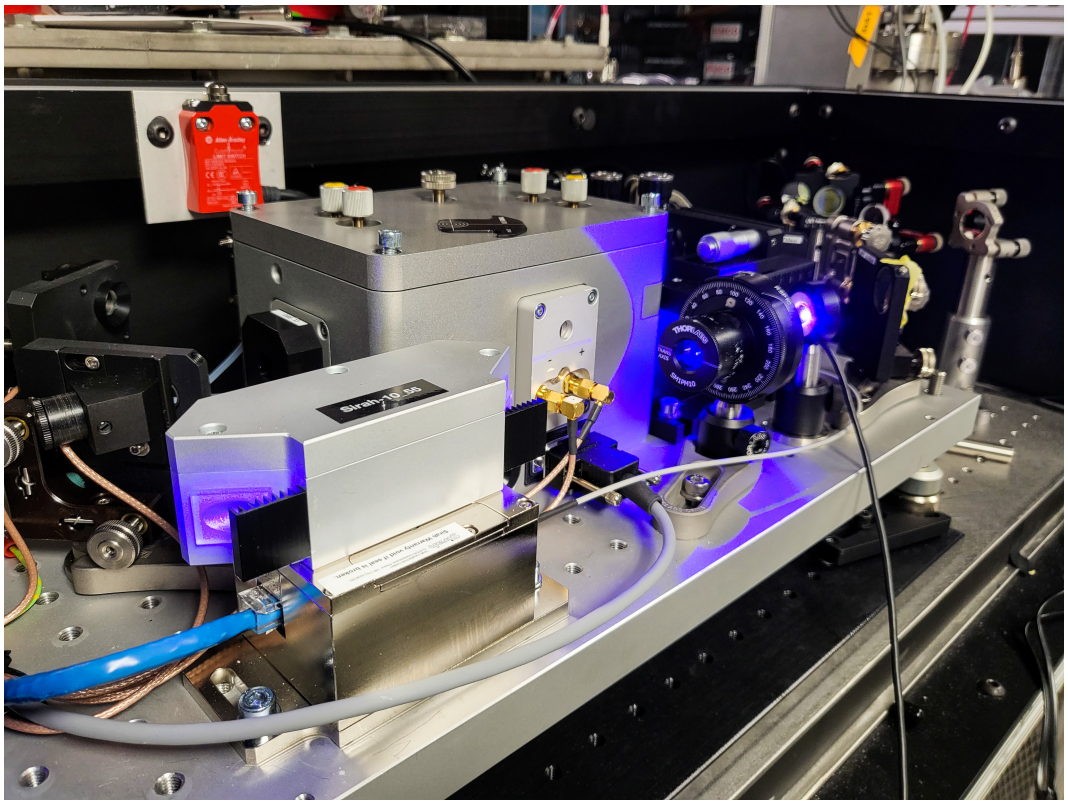

Figure 94: The WaveTrain was directly mounted to the breadboard in 1361B in order to produce FHG light at sufficient power for spectroscopy.

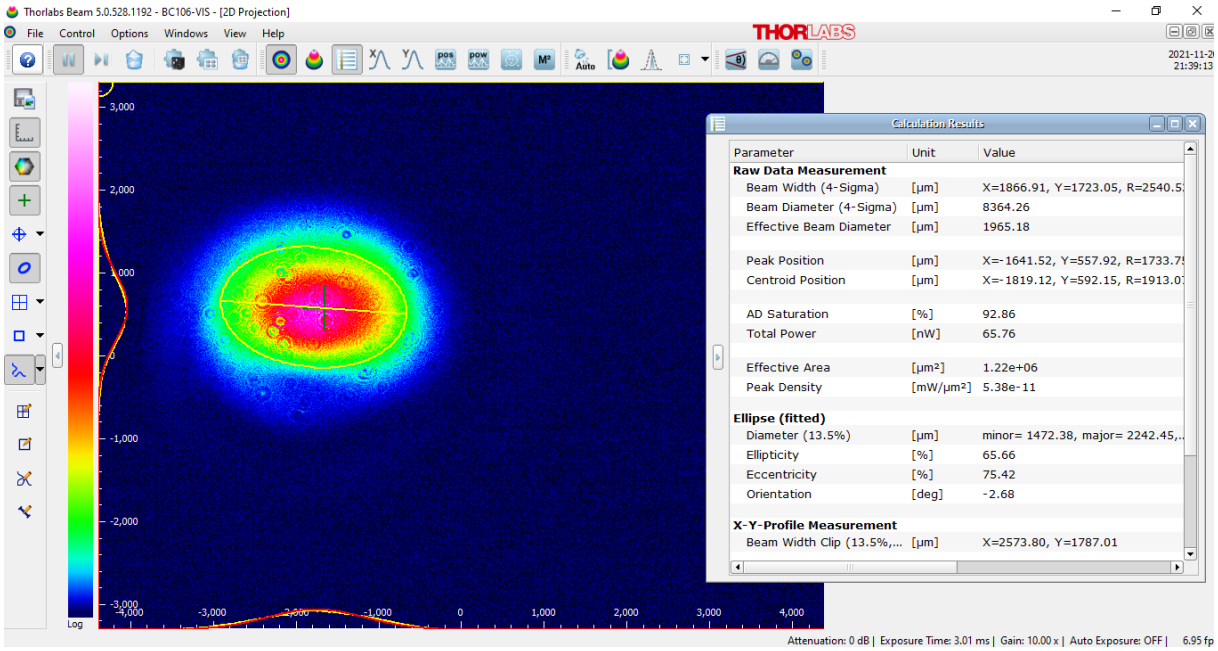

Figure 95: Laser beam profile used for spectroscopy of ^{32}Si using Thorlabs Beam software [101]. The effective beam diameter was 2 μm, significantly larger than the one used for Ni (Fig. 35). The profile itself is also more oblong, whose shape origin is unknown.

F.3.2 Use of an Acousto-optic Modulator

In order to obtain a better signal to noise ratio and acoust-optic modulator was used. An acousto-optic modulator (AOM) is a device that can chop light at a specific frequency. A voltage is applied at an RF frequency which excites a sound wave to a crystal, typically quartz, which changes the refractive index as the light passes through. The sound wave applies pressure to the crystal, and this pressure changes its refractive index. The RF frequency from the AOM was measured using a frequency counter and an oscilloscope with $\nu_{\mathrm{RF}} = 179.34\,\mathrm{MHz}$ and $\nu_{\mathrm{RF}} = 180.0\,\mathrm{MHz}$, respectively. This meant that the chopped 1st order the laser frequency was shifted by $\nu_{\mathrm{RF}} \approx 180\,\mathrm{MHz}$. Depending on the angle at which the light travels through the crystal, the 1st order light will be above or below relative to the 0th order light. The orientation is important because a positive or negative frequency shift will result depending on the input beam angle. A diagram is shown in Fig. 96. The pulsing of the AOM was timed with a frequency generator and the BECOLA DAQ in order to have laser light only at the photon detection region for spectroscopy. The coincidence between the DAQ and photon counts allowed pulsed AOM light to pass through the beamline to excite the Si atoms.

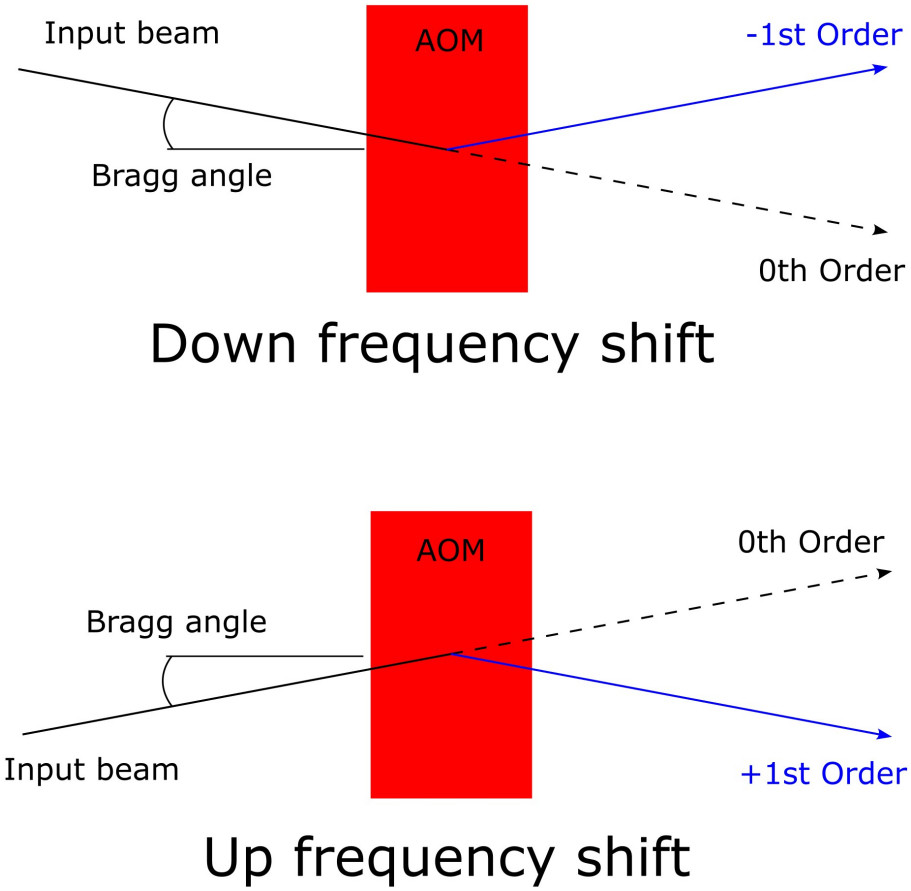

Figure 96: AOM frequency shifting diagram modeled from Ref. [160]. The resulting frequency of 1st order light is given by $\nu_{\pm 1\text{st order}} = \nu_{\text{input}} \pm \nu_{\text{RF}}$, where ν_{RF} is the frequency of the RF carrier of the AOM. For a down frequency shift the RF frequency is subtracted from the input frequency. The opposite sign is used for an up frequency shift, hence the $\pm$ sign in the equation.

F.3.3 Si Spectra

The rest-frame frequency for ^{28}Si with the $3s^2 4s \rightarrow 3s^2 3p 4s$ transition was determined to be 767 393 807.0 ± 1.4 MHz.

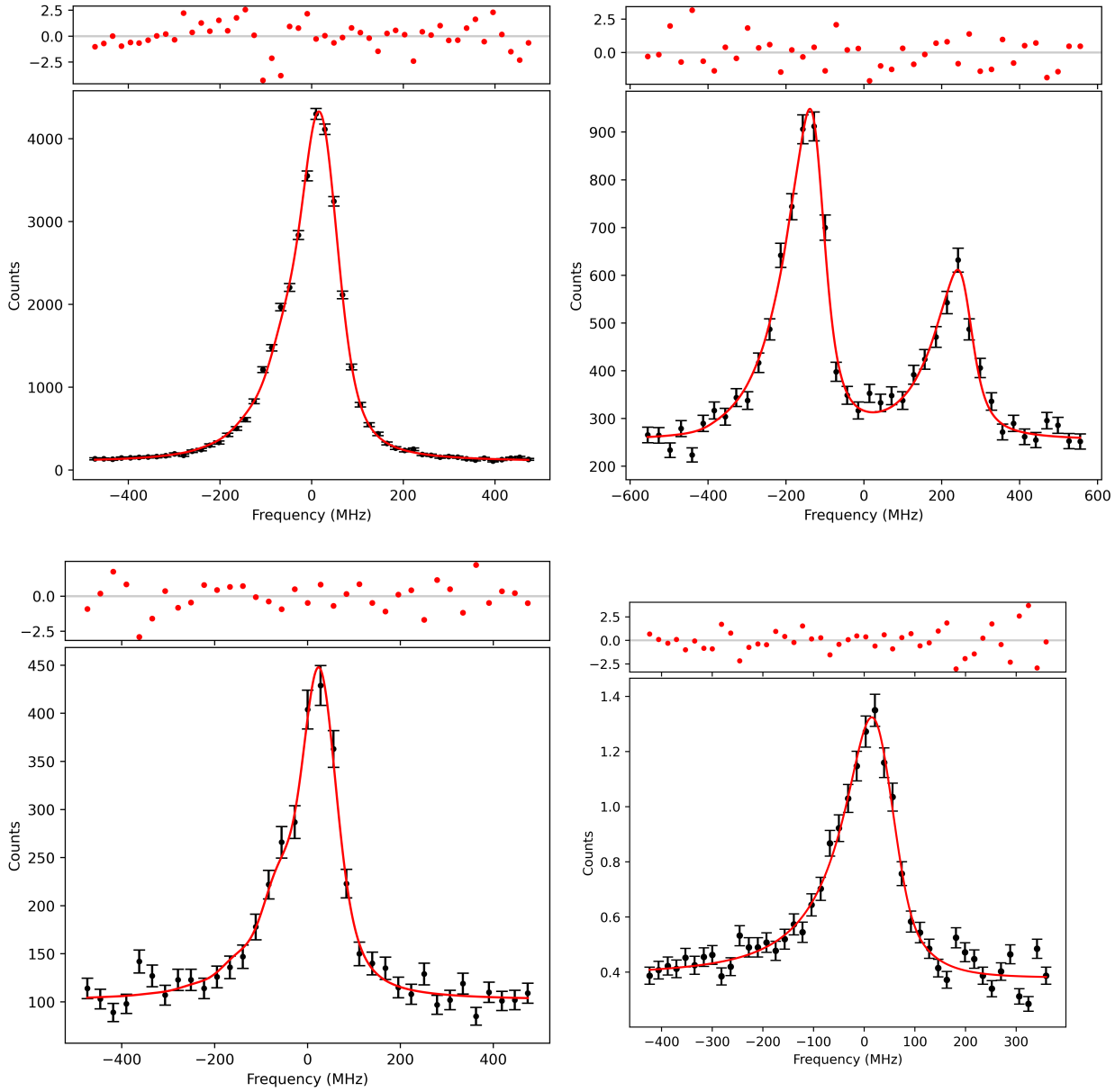

Figure 97: Spectra for all measured Si isotopes. ^{28}Si (top left), ^{29}Si (top right), ^{30}Si (bottom left), ^{32}Si (bottom right).

Beam current for ^{32}Si is shown below in Fig. 98.

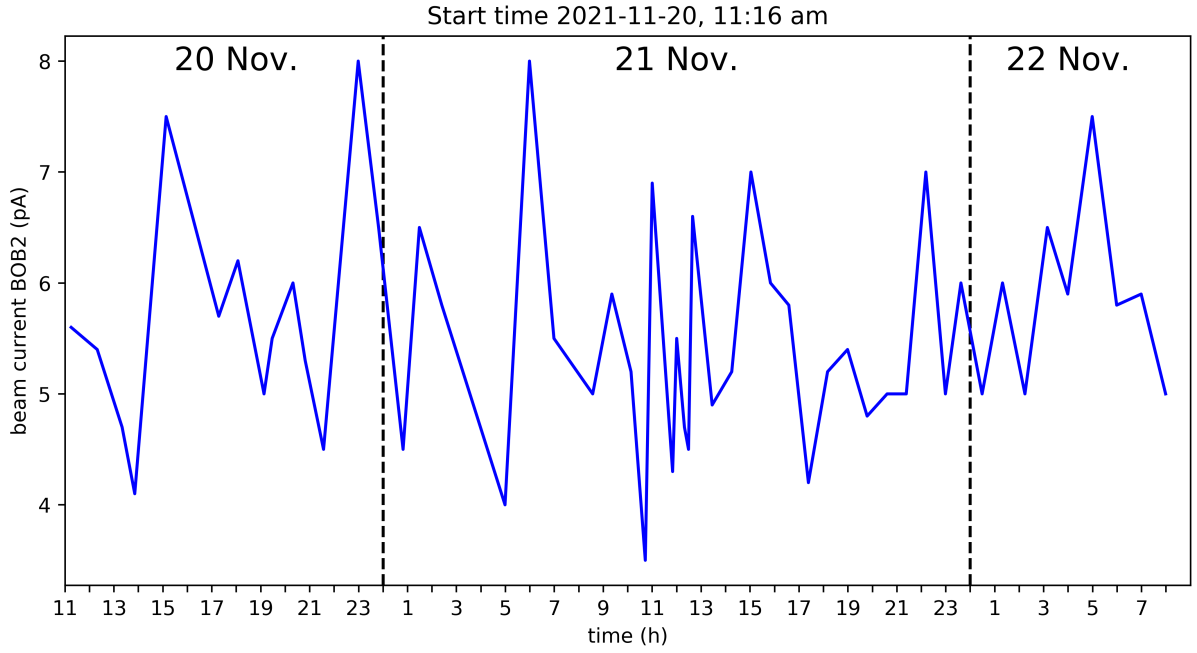

Figure 98: ^{32}Si beam current from the BMIS source measured from BOB2 in pA. An average current of 5.58 ± 0.99 pA was collected at BOB2 over the course of the experiment.

F.3.4 Constraints on L

The $A = 32$ system with Si, while with its larger $|N - Z|$, has large uncertainties with the atomic factors extracted from the King-plot analysis since there are so few isotopes within the Si isotopic chain that have known charge radii. Any gain in precision with the ^{32}Si-^{32}Ar pair is unrequited due to the large atomic factor uncertainty, resulting in a constraint similar to that obtained with the $A = 54$ system.

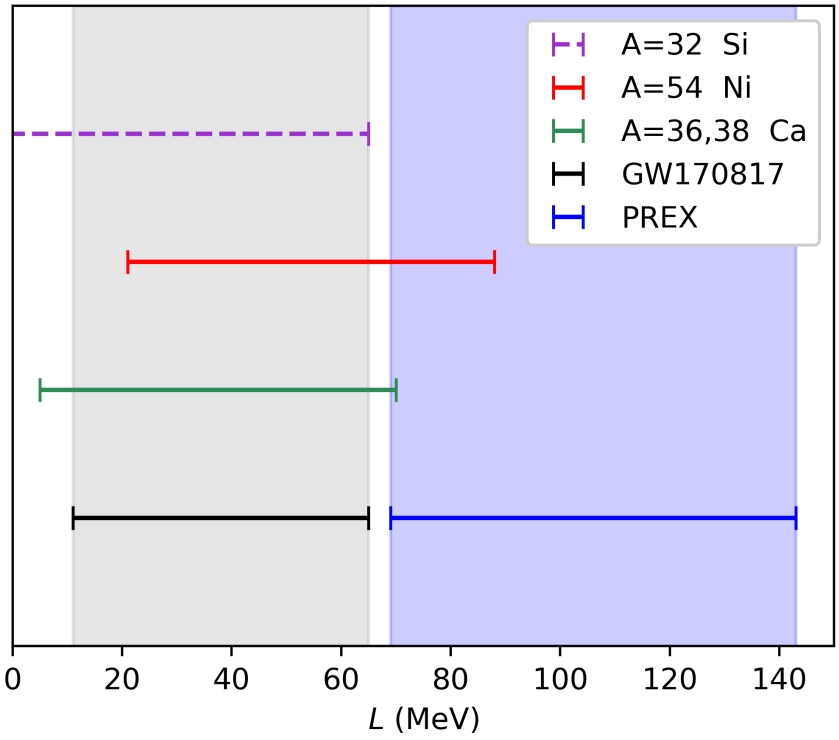

Figure 99: Constraints on L measured at BECOLA for $A = 36, 38$ [126] and $A = 54$ [60] compared to GW170817 [7] and PREX-2 [25]. The preliminary value for $A = 32$ is shown as the dashed line.

Appendix G Miscellaneous Analysis

G.1 Choosing the Best Number of Satellite Peaks

When observing asymmetric hyperfine peaks due to the charge exchange process (Sec. 3.2.7), the use of satellite peaks within the hyperfine fit may be appropriate. However, there is nothing stopping you from adding as many peaks as you want to perfectly reproduce the fit, and you can add as many as you like. This is an issue, and there are three aspects that you can observe as you make your decision on how many peaks to add. The first of these is the residuals of your fit for a visual confirmation. The residuals are essentially the difference between the data points and your best fit. Ideally these would be minimized. The second is the fit uncertainty, and you can take note of how the uncertainty in the fit increases or decreases depending on the amount of satellite peaks you have added. The third is the chi-squared value, which tests the goodness of fit.

You may also look at the Akaike- and Bayesian- information criterion (AIC and BIC, respectively), which estimates the quality of your fit model. This parameter deals with the risk of overfitting and underfitting your data and evaluates the trade-off between the goodness of fit of the model and how simple it is. In general, a lower AIC scores and larger BIC scores are better. All of these statistical tools are included in the `python` package `LMFIT`. Lastly, pay attention that the direction for your peaks is correct in order to correctly reproduce the asymmetry with collinear and anticollinear measurements as shown in Fig. 100.

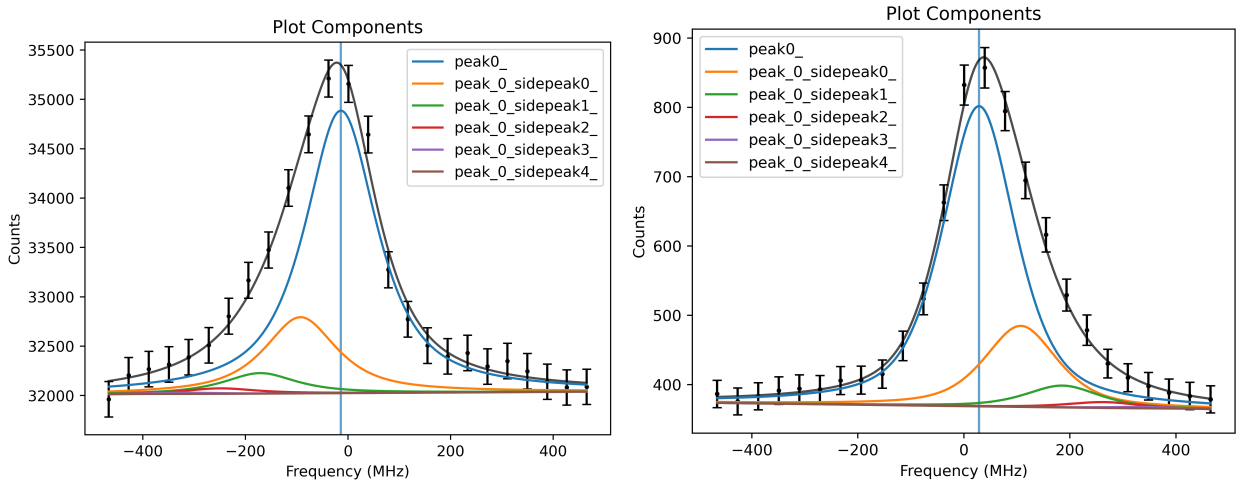

Figure 100: Hyperfine spectra for ^{28}Si in collinear (left) and anticollinear (right) geometries.

G.2 Choosing the Best Time Cut for Bunched Beam Spectroscopy

The time cut on the bunched beam may be systematically shifted in width and position to find the best cut for each isotope. A minimum centroid uncertainty and a maximum SNR should correspond to each other when setting the e.g. width of the time cut width Fig. 101.

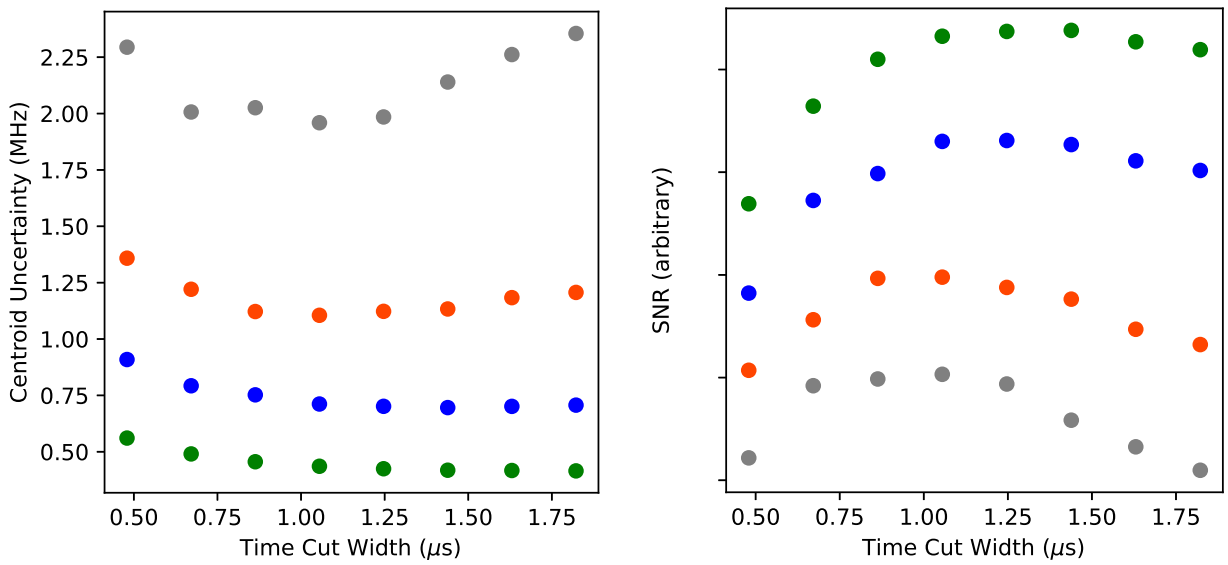

Figure 101: Centroid uncertainty (left) and SNR (right) for stable Ni isotopes as a function of time cut width. Isotopes correspond to these colors: ^{58}Ni (green), ^{60}Ni (blue), ^{62}Ni (orange), ^{64}Ni (grey).

Appendix H Rest-Frame Frequency Determination (with steps)

H.1 Determining the Rest-Frame Frequency Method 1 (6 Steps)

Use steps 1-5 to determine the rest-frame frequency for each colinear/anticolinear measurement pair. The determination for the rest-frame frequency is as follows:

1. Find an initial guess for the rest-frame frequency ν_0 using the hyperfine fit results.

$$\nu_{0\,\text{guess}}^2 = \nu_{c\,\text{fit}} \cdot \nu_{a\,\text{fit}} \tag{138}$$

2. Find the transition sensitivity with the rest-frame frequency guess ν_0.

$$S_{\text{transition}} = \frac{2\nu_{0\,\text{guess}}}{\text{mass}} \cdot \frac{\nu_{\text{laser}}^2}{\nu_{\text{laser}}^2 - \nu_{0\,\text{guess}}} \tag{139}$$

3. Find the beam energy using the fit result.

$$E_{\text{kin}} = \frac{mc^2}{2} \cdot \frac{(\nu_{\text{fit}} - \nu_{\text{laser}})^2}{\nu_{\text{fit}}\nu_{\text{laser}}} \tag{140}$$

4. Find the difference in beam energy between the colinear/anticolinear measurements.

$$\Delta U_{\text{scan}} = E_{\text{kin col}} - E_{\text{kin acol}} \tag{141}$$

5. Finally, determine the rest-frame frequency ν_0.

$$\nu_0 = \sqrt{\nu_{\text{col laser}}(\nu_{\text{acol laser}} - \Delta U_{\text{scan}} S_{\text{transition}})} \tag{142}$$

H.2 Determining the Rest-Frame Frequency Method 2: Converging Frequency (6 Steps)

1. Using the laser frequencies $\nu_{\text{col laser}}$ and $\nu_{\text{acol laser}}$, which are the laser frequencies the laser is set to in the laboratory for the experiment, make an initial guess for the rest-frame frequency using

$$\nu_{0\,\text{guess}}^2 = \nu_{c\,\text{laser}} \cdot \nu_{a\,\text{laser}} \tag{143}$$

2. Based on the result from step (1.), find the sensitivity of the transition frequency. Let us start with

the collinear laser frequency for ν_{laser}.

$$S_{\text{transition}} = \frac{2\nu_{0\,\text{guess}}}{mc^2} \cdot \frac{\nu_{\text{laser}}^2}{\nu_{\text{laser}}^2 - \nu_{0\,\text{guess}}} \tag{144}$$

3. Fit the hyperfine spectra in terms of voltage to determine its center V_c for a collinear-anticollinear pair, then take the difference between the fit results to find ΔU_{scan}

4. Using the results from steps 1-3, find the corrected rest-frame frequency using

$$\nu_0 = \sqrt{\nu_{\text{col laser}}(\nu_{\text{acol laser}} - \Delta U_{\text{scan}} S_{\text{transition}})} \tag{145}$$

5. Repeat steps 1-4 to make subsequent iterations in determining the rest-frame frequency by sustituting the result from step 4 into $\nu_{0\,\text{guess}}$. The result should converge within about 5 iterations when taking the difference between the initial and final ν_0 of each iteration.

6. Repeat steps 1-5 using the anticollinear laser frequency. The results from collinear and anticollinear should converge.

H.3 Determining the Rest-Frame Frequency Method 3: Converging E_{kin} and ν_0 (19 Steps)

This next method utilizes the collinear-anticollinear determinations in parallel to perform new guesses to converge the rest-frame frequency. The beam energies for each collinear and anticollinear will converge independently, and the rest-frame frequencies from both geometries will converge with each other.

1. Same as Step 1. in Method 2 above

2. Starting with the collinear case, determine the beam kinetic energy using

$$V_{\text{main}} = E_{\text{kin}} = \frac{mc^2}{2} \cdot \frac{(\nu_{0\,\text{guess}} - \nu_{\text{laser}})^2}{\nu_{0\,\text{guess}}\nu_{\text{laser}}} \tag{146}$$

3. Fit the hyperfine spectra in terms of voltage to determine its center V_c for the collinear-anticollinear pair

4. Using, in this instance, the collinear V_c (c stands for center, not collinear), determine the beam energy at the fit center using

$$E_{\text{kin c}} = V_{\text{main}} - V_c \tag{147}$$

5. Using Eq. 18, find the beam velocity β, and then solve for the rest-frame frequency using

$$\nu_0 = \nu_{\text{laser}} \sqrt{\frac{1-\beta}{1+\beta}} \tag{148}$$

6. Using the fit centers from step (3.), find the average V_c and add it to V_{main}

7. Repeat steps (4.) and (5.) to get ν_0. We thus far have two determinations (iterations) for ν_0 on the collinear side. To continue iterations, we must now analyze the anticollinear side as well in order to provide new initial guesses for V_{main}. Once the anticollinear iterations are caught up to the number of iterations on collinear side, we can continue with both the collinear and anticollinear iterations in parallel.

8. Use step (4.) to find $E_{\text{kin c}}$, using the *collinear* V_{main} (determined in step (2.)) with the anticollinear fit result V_c

9. Use step (5.) to determine ν_0 using the anticollinear laser frequency

10. Find $\Delta\nu_0$. For the sake of checking how far the convergence of the frequency is, you can take the difference between the collinear ν_0 from your first iteration (in this case the first time you solved Step (5.)) and the result from step (9.). Since you are comparing the first iterations of col/acol, they will not be too close yet. We now will move on to the second iteration on the anticollinear side.

11. Repeat step (8.), using the collinear V_{main} from the second iteration. Then repeat steps (9.) and (10.). You should notice that the result from step (10.) is smaller upon the second iteration meaning the rest-frame frequencies are beginning to converge. We can now move back to the collinear iteration.

12. Take the difference between the collinear-anticollinear fit results to get ΔV_c

13. Use the equation below to find ΔV, where $g = \Delta V_c/0.02$. Use the most current iteration (if going through this step for the first time, you would be starting iteration 3, using the values from iteration number 2).

$$\Delta V = \Delta\nu_0 \cdot \frac{\Delta V_c}{g} \tag{149}$$

14. Find the new V_{main} by adding ΔV to the most recent collinear V_{main}

15. Repeat steps 4 and 5.

16. Switch to the anticollinear side, using step (4.) with the collinear V_{main} and the anticollinear V_c to get the kinetic energy.

17. Repeat steps 4 and 5 to get the rest-frame frequency.

18. Determine $\Delta\nu_0$ and ΔV for the new iteration

19. Repeat steps (14.-18.) until both $\Delta\nu_0$ and ΔV approach 0 and the rest-frame frequencies converge.

H.4 Uncertainty for the Rest-frame frequency

The exact error propagation formula yields

$$\sigma_{\nu_0} = \sqrt{\left(\frac{\nu_a}{2\sqrt{\nu_c\nu_a}}\sigma_{\nu_c}\right)^2 + \left(\frac{\nu_c}{2\sqrt{\nu_c\nu_a}}\sigma_{\nu_c}\right)^2} \tag{150}$$

for the uncertainty of a pair of collinear-anticollinear measurements. Because the difference between ν_a or ν_c to the $\sqrt{\nu_a\nu_c}$ term is very small (approximately 1%), they can be treated as essentially the same number. Since they are in fraction, they simplify to 1 and the simplified total uncertainty equation becomes

$$\sigma_{\nu_0} \approx \frac{1}{2}\sqrt{\sigma_{\nu_c}^2 + \sigma_{\nu_a}^2} \tag{151}$$

Appendix I Determining the Calibrated Voltage (with steps)

Once the rest-frame frequency is determined, not only can ν_0 be used to find the isotope shift, but also to calibrate the beam energy.

I.1 Calculating the Calibrated Voltage

Beam energy determination using the rest-frame frequency is as follows:

1. Choose an initial beam energy guess and perform a fit to the data

$$E_{\text{kin guess}} = 29\,850\,\text{V} \tag{152}$$

2. Determine the beam energy using the rest-frame frequency.

$$E_{\text{kin rest}} = \frac{\text{mass}}{2} \cdot \frac{(\nu_0 - \nu_{\text{laser}})^2}{\nu_0 \nu_{\text{laser}}} \tag{153}$$

3. Determine the beam energy using the fit centroid.

$$E_{\text{kin fit}} = \frac{\text{mass}}{2} \cdot \frac{(\nu_{\text{fit}} - \nu_{\text{laser}})^2}{\nu_{\text{fit}} \nu_{\text{laser}}} \tag{154}$$

4. Find the beam energy offset using the beam energies from Steps 2 and 3.

$$E_{\text{kin offset}} = E_{\text{kin rest}} - E_{\text{kin fit}} \tag{155}$$

5. Determine the calibrated beam energy using the offset.

$$E_{\text{kin cal}} = E_{\text{kin guess}} + E_{\text{kin offset}} \tag{156}$$

I.2 Calibrating the Voltage by Iterative Fits

Stepping the beam energy and performing iterative fits until the fit centroid converges with the rest-frame frequency is an alternative to steps 1-5 above.

1. Choose an initial guess for the beam energy or the high voltage power supply (e.g. $U_{\text{FuG}} = 29\,850$).

2. Perform an initial hyperfine fit and get the centroid value.

3. Compare the centroid value from your fit to the rest-frame frequency.

4. Step U_{FuG} again (e.g. $U_{\mathrm{FuG}} = 29\,848$).

5. Fit the hyperfine spectrum again and compare the fit centroid to the rest-frame frequency.

6. Take note if the difference between ν_0 and ν_{fit} is getting larger or smaller, and if need be change the direction of your high voltage steps accordingly (in this example we are decreasing the value of U_{FuG}, but you may need to increase it instead).

7. Keep stepping the voltage until the fit result matches the rest-frame frequency $\nu_{\mathrm{fit}} = \nu_0$. Once these two frequencies match up, you have the calibrated value for the high voltage and also the calibrated beam energy.

Appendix J Linear Regression Analysis for the King-plot

The following procedure for the best straight line was taken from Ref. [85]. We start with the equation of a line $y = a + bx$, where a is the y intercept and b is the slope.

1. Choose an approximate initial value for b. This can be done, for example, with a simple curve fit to the King-plot without adjusting any values (i.e. using `python` or literature value). Remember that b is the initial guess for the F atomic factor.

2. Determine weights for each point (X_i, Y_i). These are the weights on the charge radii and isotope shifts, and are represented by

$$\omega(X_i) = \frac{1}{\sigma^2(X_i)} \quad \text{and} \quad \omega(Y_i) = \frac{1}{\sigma^2(Y_i)} \tag{157}$$

3. Use these weights, with the value of b and the correlations r_i between the x and y errors of the ith point to evaluate W_i (Eq. 158) where $\alpha_i = \sqrt{\omega(X_i)\omega(Y_i)}$. For clarity, r_i is the correlation coefficient between the X_i and Y_i errors. In this case, we set $r_i = 0$ because we are trying to minimize the correlation between a and b (K and F).

$$W_i = \frac{\omega(X_i)\omega(Y_i)}{\omega(X_i) + b^2\omega(Y_i) - 2br_i\alpha_i} \tag{158}$$

4. Use the observed points (X_i, Y_i) and W_i to calculate $\bar{X}$ and $\bar{Y}$, from which U_i and V_i, and hence β_i can be evaluated for each point.

$$\bar{X} = \frac{\sum W_i X_i}{\sum W_i} \quad \text{and} \quad \bar{Y} = \frac{\sum W_i Y_i}{\sum W_i} \tag{159}$$

$$U_i = X_i - \bar{X} \quad \text{and} \quad V_i = Y_i - \bar{Y} \tag{160}$$

$$\beta_i = W_i \left[\frac{U_i}{\omega(Y_i)} + \frac{bV_i}{\omega(X_i)} - (bU_i + V_i)\frac{r_i}{V_i} \right] \tag{161}$$

5. Use W_i, U_i, V_i, and β_i in the expression for b in

$$b = \frac{\sum W_i \beta_i V_i}{\sum W_i \beta_i U_i} \tag{162}$$

   to calculate an improved value for b.

6. Use the new b and repeat steps (3.),(4.), and (5.).

7. From this final value for b (F atomic factor), together with the final $\bar{X}$ and $\bar{Y}$, calculate a (K atomic

factor) using

$$a = \bar{Y} - b\bar{X} \tag{163}$$

8. For each point (X_i, Y_i) calculate the adjusted values x_i, where

$$x_i = \bar{X} + \beta_i \tag{164}$$

The x_i and upcoming y_i are the last-squares adjusted points, expectation values of X_i and Y_i.

9. Use the adjusted x_i, together with W_i, to calculate $\bar{x}$ and u_i where

$$\bar{x} = \frac{\sum W_i x_i}{\sum W_i} \quad \text{and} \quad u_i = x_i - \bar{x} \tag{165}$$

10. From W_i, $\bar{x}$, and u_i, calculate the uncertainties σ_b and σ_a with

$$\sigma_b = \frac{1}{\sum W_i u_i^2} \quad \text{and} \quad \sigma_a = \frac{1}{\sum W_i} + \bar{x}^2 \sigma_b^2 \tag{166}$$

Appendix K Nickel Charge Radii and Future Experiments

K.1 Charge Radii of Ni Isotopes Across the $N = Z = 28$ Shell Closure

Although not the main focus of this thesis, the determination of the ^{54}Ni charge radius refines and characterizes the kink structure across the $N = 28$ shell closure (along with ^{55,56}Ni) for the nickel chain, especially considering it is the most neutron-deficient Ni nucleus whose charge radius has been extracted thus far Fig. 102. The nickel chain is also the heaviest element whose systematics span across the $N = 28$ shell closure. In Fig. 102, four sets of experimental results and two sets of theoretical results are shown. Neutron deficient charge radii measured at BECOLA are plotted in red [60, 51], while neutron rich charge radii for the rest of the isotopic chain are shown in blue [161].The remaining two sets of experimental values from Refs. [57, 45] are taken from tabulated values in a compilation of charge radii. Theoretical calculations, Skyrme and Fayans, agree with experimental results for different regions of the chain. Skyrme tends to agree well in the middle of the chain, while struggling to reproduce the kink structure at $N = 28$. Fayans on the other hand reproduces the kink structure much better than Skyrme, but deviates after the kink only to converge back at around $N = 36$. The odd-even staggering in the chain is also much more pronounced with Fayans than with Skyrme.

The charge radii for neutron deficient nickel isotopes reveal a similarity between the kink at $N = 28$ in Ca and Ni [51], which is surprising due to the fact that the ^{56}Ni core is supposed to be much 'softer' than the ^{48}Ca core. This 'soft' nature is due to its larger $B\left(E2,\uparrow\right)$ value, where the probability of the $N = Z = 28$ canonical configuration in the wave function of the ^{56}Ni ground state is only 49% [163]. To avoid confusion, the word 'soft' in this context refers to the core of the nucleus due to configuration mixing; this terminology is not linked to the 'soft' or 'stiff' EOS discussion. Adding to the validity of this 'soft' nature, the nuclear magnetic moments of neighboring isotopes are inconsistent with single-particle estimates [51].

The kink structure was characterized by a three-point indicator [164]

$$\Delta_{kn}^{(3)} R_{\mathrm{ch}}\left(A\right) = \frac{1}{2}\left[R_{\mathrm{ch}}\left(A+k\right) - 2R_{\mathrm{ch}}\left(A\right) + R_{\mathrm{ch}}\left(A-k\right)\right] \tag{167}$$

which quantifies its strength at the $N = Z = 28$ shell closure and is shown in the figure below. The $k = 1$ corresponds to the odd-even staggering while $k = 2$ characterizes the curvature. Studying ^{56}Ni is interesting because it is the first self-conjugate doubly-magic radioactive nucleus that has been measured using laser spectroscopy to characterize the shell closure. By looking at Fig. 103, the three-point indicator value is extremely close to that of K and, more importantly, Ca. The radii for these chains have been plotted in the bottom left of the figure, comparing all of the radius chains to each other. One can see that Mn and Fe, who

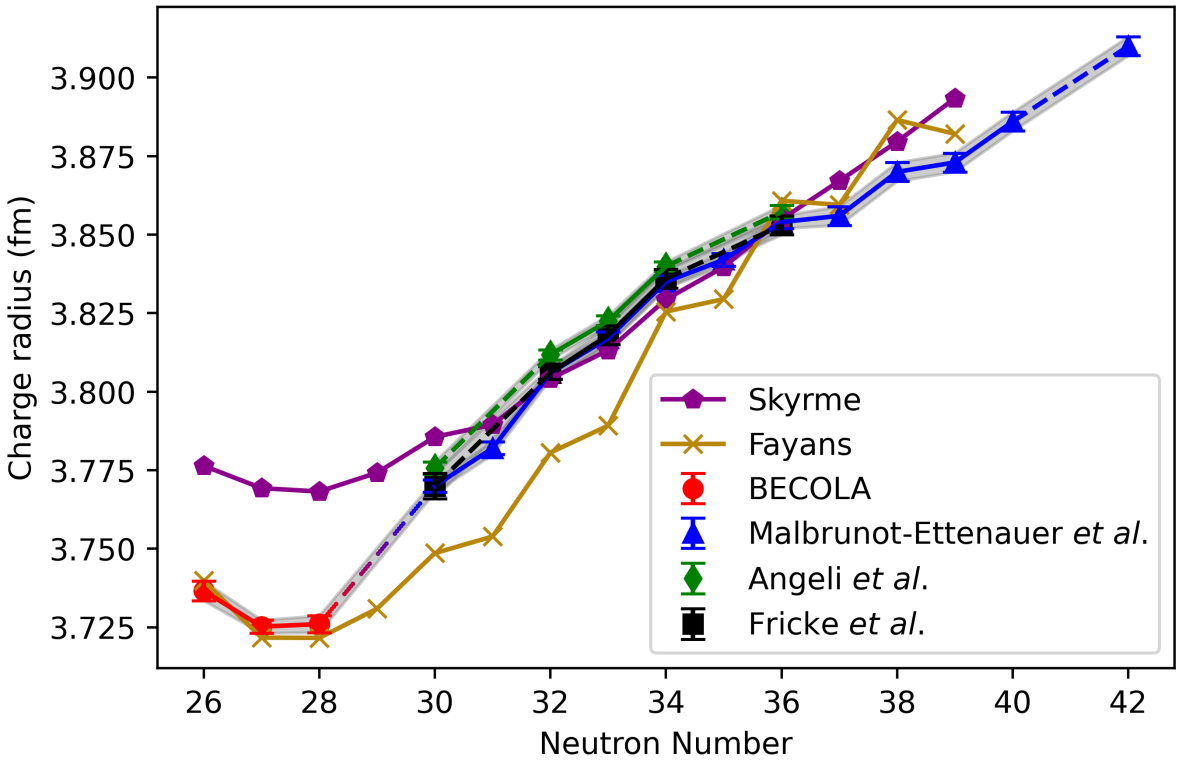

Figure 102: Theoretical and Experimental charge radii of nickel isotopes [45, 60, 51, 57, 161]. Dashed lines indicate missing measurements in the chain. The red circles (BECOLA) and blue triangles (Malbrunot-Ettenauer *et al.*) are experimental results. Green diamonds (Angeli *et al.*) and black squares (Fricke *et al.*) are also experimental results, but from tabulated compilations. Fayans calculations are courtesy of W. Nazarewicz and P.-G. Reinhard, while Skyrme results are from the FRIB Mass Explorer [162].

have different three-point indicator values, differ from K, Ca, and Ni.

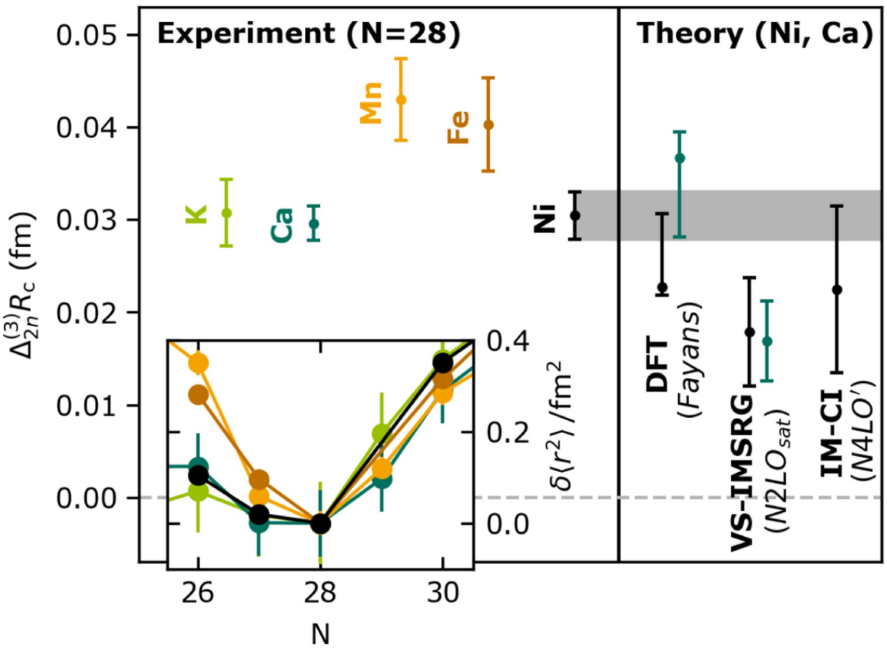

Figure 103: Three-point indicator showing the similarity between Ca and Ni for the $N = 28$ shell closure taken from Ref. [51].

K.2 Proton-halos, the Oxygen Anomaly, and the Steep Increase Around $N = 32$

The aluminum isotopic chain provides an opportunity to study the structure of proton-halo nuclei [165, 166, 167], where the isotopes ^{22,23}Al are proton-halo candidates. Proton-halo nuclei exist in close proximity to proton dripline and as a result their binding energy is relatively weak, leading to a large radial proton distribution. Laser spectroscopy is able to probe that distribution to characterize this phenomenon. Apart from determining the charge distribution of the proton-halos, the nuclear charge radii can constrain components of the nuclear force [168, 169].

The oxygen isotopic chain contains strong indications for three additional shell closures ($N = 6, 14, 16$) [170, 171, 172, 173] apart from traditional $N = 8$. The heaviest oxygen isotope, ^{24}O, lies at the neutron dripline. This doubly magic nucleus is unexpectedly close to the valley of stability, where an addition of a proton ($Z = 8 \rightarrow Z = 9$) will bind six additional neutrons to make ^{31}F [174]. The unanticipated additional neutron-rich isotopes in fluorine is called the oxygen anomaly [175], and it challenges nuclear theory which initially predicted the location of the neutron dripline to be at the $N = 20$ shell closure of ^{28}O [176, 177]. In order to investigate the structure around ^{24}O, laser spectroscopy on neutron rich O and F isotopes can extract the magnetic dipole and spectroscopic quadrupole moments from hyperfine spectra. The magnetic moments are sensitive to the configuration mixing of nucleons in the nucleus, and these data can be used to improve upon nuclear theory, thus characterizing the oxygen anomaly.

The titanium isotopic chain can be used to investigate the steep increase around $N = 32$. Neutron-rich K and Ca isotopes show a dramatic increase in the charge radius around $N = 32$, which has been challenging to reproduce using nuclear theories [59, 53, 44, 178]. Measuring across $N = 32$ with neutron rich ^{53,54,55,56}Ti will help elucidate the magic character of $N = 32$ near $Z = 20$ and provide a standard for nuclear theory. This light to mid-mass region ($Z = 20$) near doubly magic ^{40}Ca and ^{48}Ca provides the unique opportunity to test nuclear theories that generally are used to describe global trends of nuclear properties.

K.3 Charge Radii from Ca to Ni: Updated Preliminary Sc Systematics

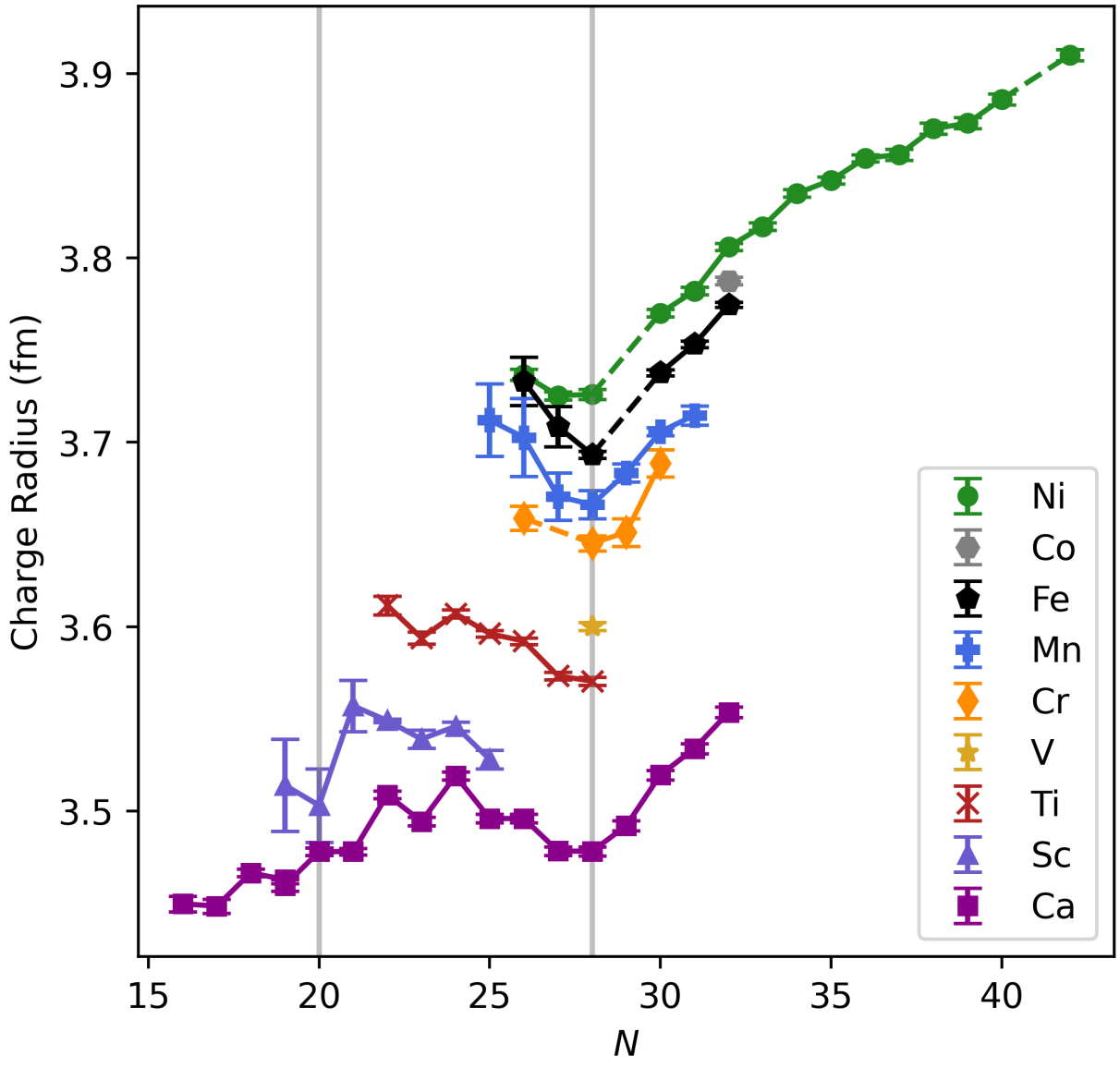

Figure 104: Charge radii from Refs. [55, 56, 57, 45, 179, 180, 58, 59, 44, 60, 51, 181] with updated Sc chain (preliminary values at $N = 19$ and $N = 20$). Notice that there is a pronounced kink structure at $N = 20$, contrary to the Ca chain.

K.4 Charge Radii Across the Nuclear Chart

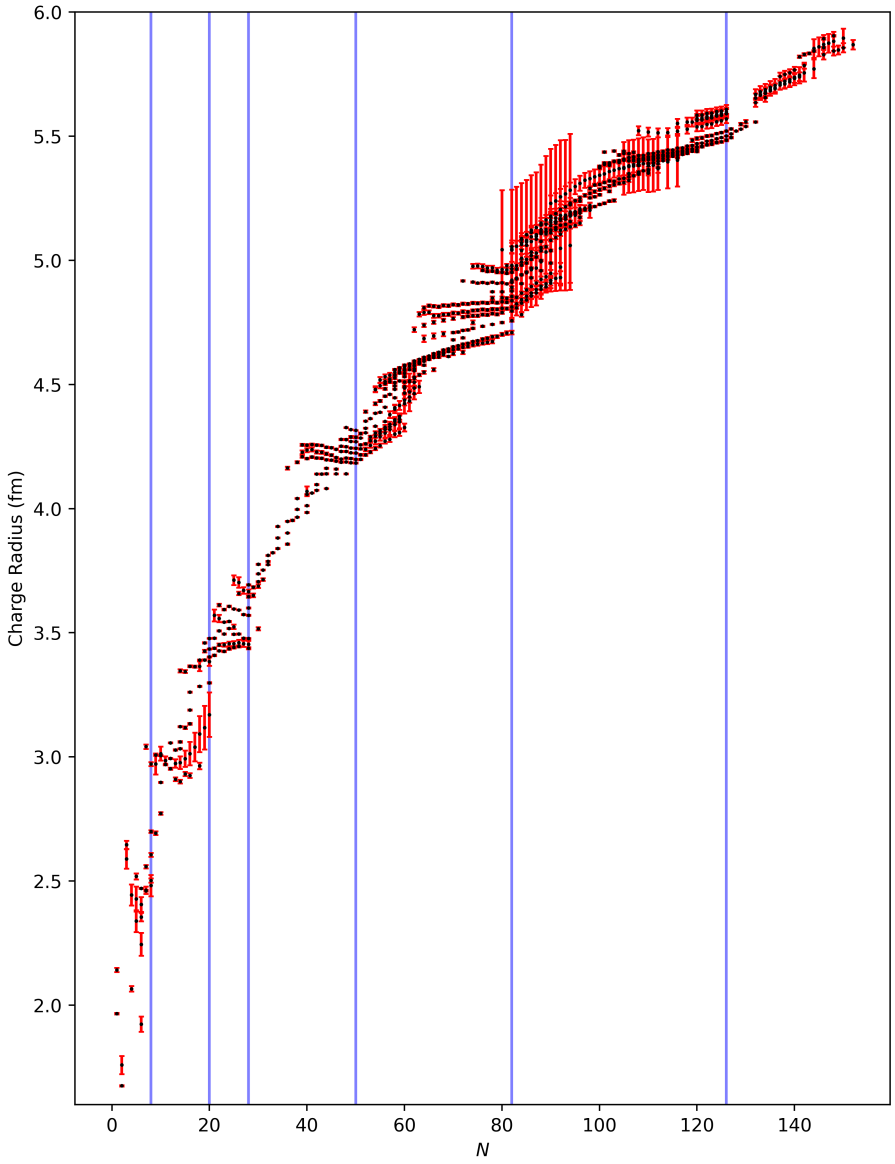

Figure 105: Experimental rms charge radii plotted as a function of neutron number from Ref. [45], with traditional magic numbers indicated by the blue vertical lines. Kink structures can be seen at each of the traditional magic numbers, as well as the potentially new magic number $N = 14$.

Appendix L BECOLA During the COVID-19 Pandemic

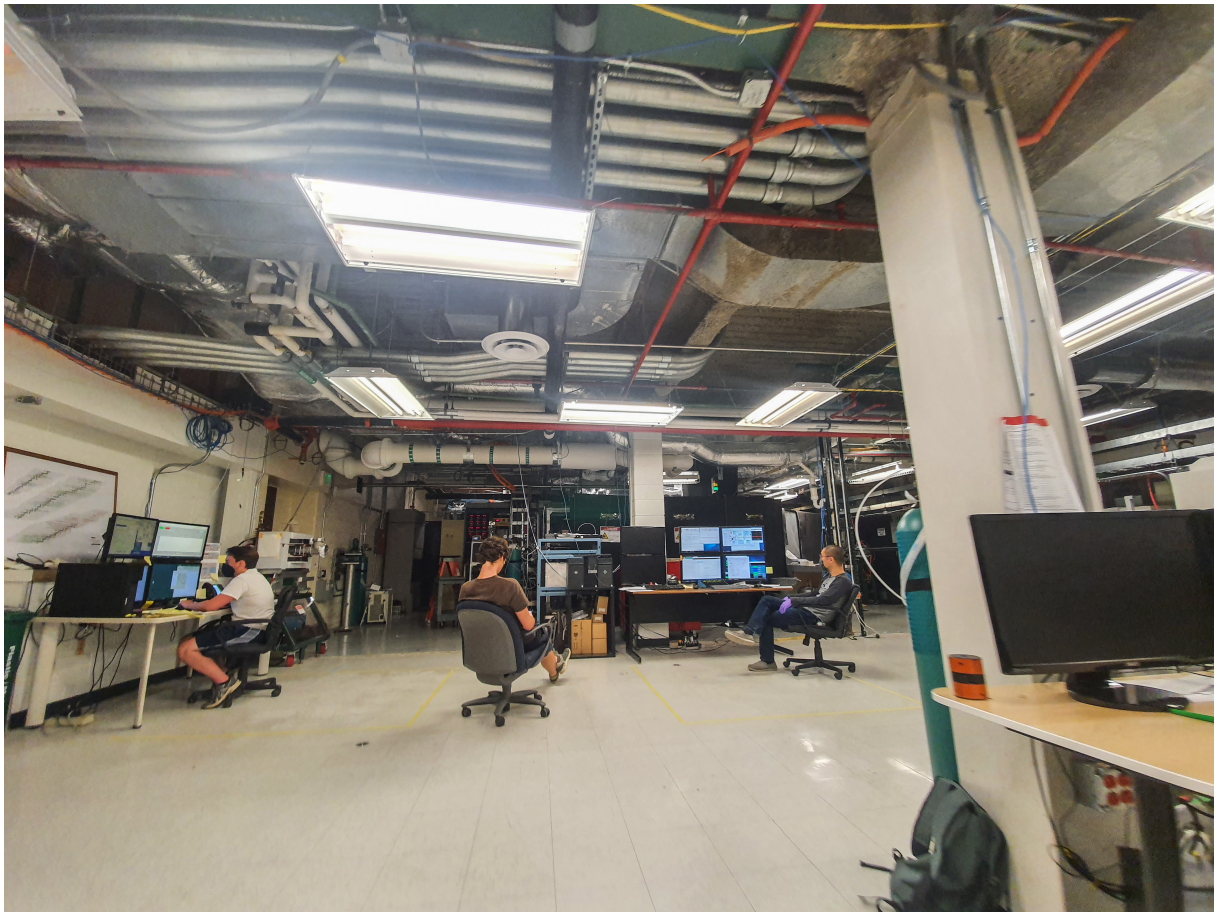

Figure 106: Picture of an online shift for ^{54}Ni during the pandemic. Yellow tape is on the floor to indicate six feet of distance, and all members are wearing masks.

The COVID-19 pandemic marked a considerable change in laboratory protocols and daily working conditions at BECOLA and, of course, around the world. The pandemic made laboratory work more tedious, time consuming, and unfortunately affected the learning experience. Online experiments were delayed and pushed back (e.g. ^{54}Ni,^{40}Sc,^{32}Si), with lots of uncertainty as to when the experiments would actually be conducted. I express gratitude to all of the people who made the BECOLA experiments and in general work in the laboratory possible amidst the state of emergency. After all, safety is the number one priority. I would like to detail some challenges and the overall experience working at NSCL/FRIB during those uncertain times.

In a typical day at the laboratory, one would walk through the doors and do a temperature and face scan to make sure they did not have a fever. Sanitizer by the scanner would allow you to sanitize your hands before proceeding to the nearest sink where your hands would be washed for a minimum of 20 seconds before starting to work. A cleaning checklist would need to be completed and emailed to management every four

hours, sanitizing computers, tools, and doorknobs with ethyl or isopropyl alcohol. Each tool, after being used, would need to be placed into a bin, and would need to be sanitized before another person could touch it. During online experiments, those on shift would take turns by performing office checks every six hours to make sure people in offices were wearing their masks. Masks were typically worn for eight hours a day, which sometimes would hurt to wear for such a long time.

Only one person was allowed in the 1440 laser room, and therefor it made learning (e.g. alignment techniques) challenging or just not possible. Each person needed to stay six feet apart at all times, which in turn made two-person jobs much more difficult and time consuming. There were a few months where we were unable to enter the laboratory due to various Executive Orders, which brought progress to a halt until special permission was granted to work at the laboratory. Early executive orders from Michigan *"prohibits all businesses and operations from requiring workers to leave their homes, unless those workers are necessary to sustain or protect life or to conduct minimum basic operations"*. For the BECOLA on-line experiments, collaborators could not join due to global lockdown, making shifts longer and more difficult due to short staff. On a psychological level, trying to do analysis while in months of isolation in my apartment and going through various family emergencies was quite difficult. There was a point in which I had not interacted with another human in person for several months, since I did not go outside for even groceries.

I would like to emphasize that I am not blaming anyone for the challenges everyone experienced during the pandemic. Some good things came out of the experience as well, for example, through Zoom the world learned that certain jobs and meetings did not require people to be on-site. Now hybrid meetings are common and more people are able to join such lectures and conferences virtually, where they otherwise would not have joined at all.

Due to government lockdown and stay-at-home orders, special permission was granted to continue working in the laboratory under stringent safety procedures.

For historical purposes, I include that the BECOLA experiment on Sc isotopes was the last experiment performed with the NSCL coupled cyclotrons before the laboratory officially transitioned to FRIB. I thank them for letting the other group members and I sign the key that turned on the entire cyclotron system Fig. 107.

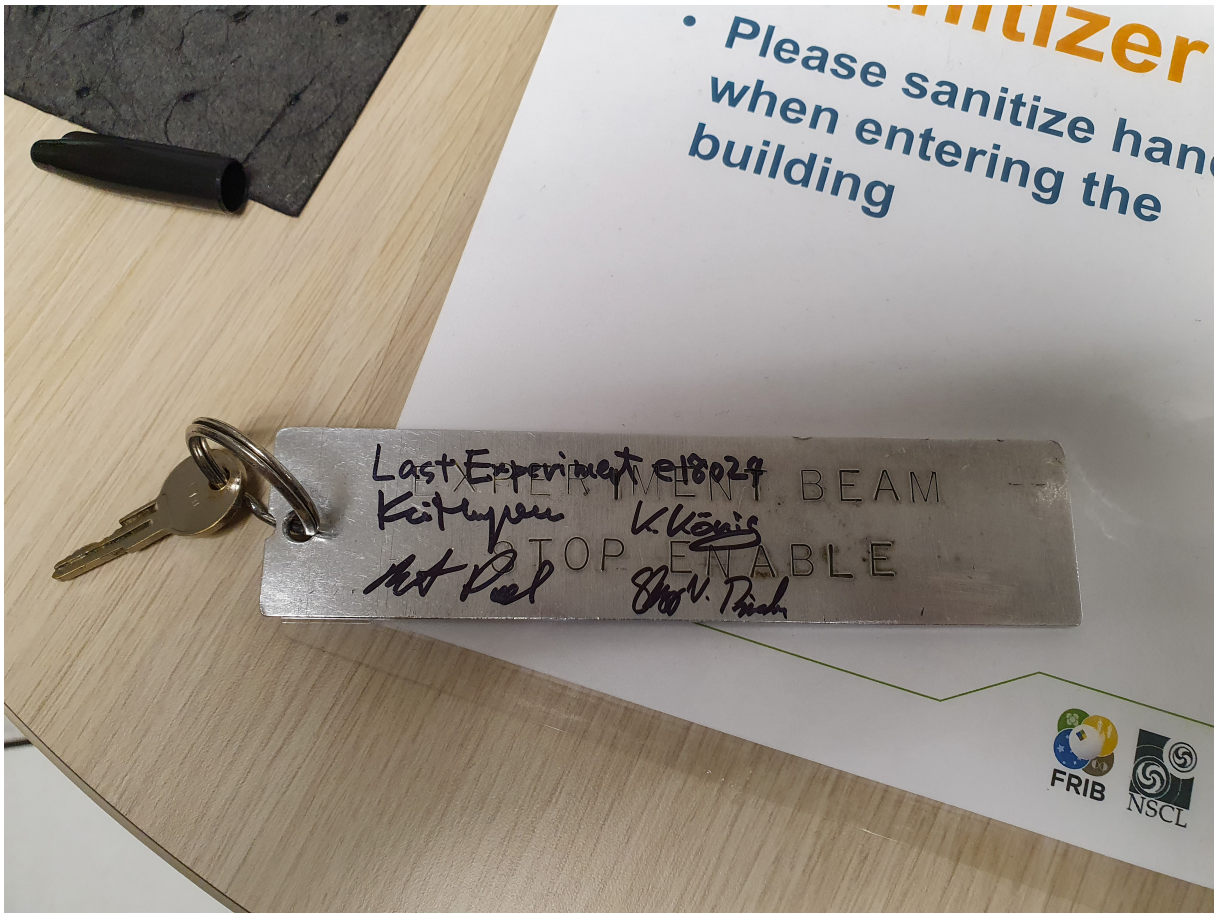

Figure 107: Key signed by BECOLA group members after the last experiment from NSCL was completed before transitioning to FRIB. This key is now in the FRIB operating room. The metal tag on the key reads EXPERIMENT BEAM STOP ENABLE. In marker: Last Experiment e18029. Signatures: Kei Minamisono (top left), K. König (top right), Robert Powel (bottom left), Skyy V. Pineda (bottom right).

Appendix M Personal Contributions

M.1 Publications

1. F. Sommer, K. König, D. M. Rossi, N. Everett, D. Garand, R. P. de Groote, J. D. Holt, P. Imgram, A. Incorvati, C. Kalman, A. Klose, J. Lantis, Y. Liu, A. J. Miller, K. Minamisono, T. Miyagi, W. Nazarewicz, W. Nörtershäuser, **S. V. Pineda**, R. Powel, P.-G. Reinhard, L. Renth, E. Romeo-Romero, R. Roth, A. Schwenk, C. Sumithrarachchi, and A. Teigelhöfer. "Charge radii of ^{55,56}Ni reveal a surprisingly similar behavior at $N = 28$ in Ca and Ni isotopes". *Physical Review Letters* **129**, 132501 (2022). DOI: 10.1103/PhysRevLett.129.132501

2. R. Powel, B. A. Brown, J. D. Holt, A. Klose, K. König, J. Lantis, K. Minamisono, T. Miyagi, **S. Pineda**. "Ground State Magnetic Dipole Moment of ^{40}Sc". *Physical Review C* **105**, 034310 (2022). DOI: 10.1103/PhysRevC.105.034310

3. **S. V. Pineda**, K. König, D. Rossi, B. A. Brown, A. Incorvati, J. Lantis, K. Minamisono, W. Nörtershäuser, J. Piekarewicz, R. Powel, F. Sommer. "Charge Radius of Neutron-deficient ^{54}Ni and Symmetry Energy Constraints Using the Difference In Mirror Pair Charge Radii". *Physical Review Letters* **127**, 182503 (2021). DOI: 10.1103/PhysRevLett.127.182503

4. R. Powel, M. Koble, J. Palmes, N. Everett, P. Imgram, K. König, J. Lantis, K. Minamisono, W. Nörtershäuser, R. Parker, **S. Pineda**, F. Sommer, and A. Klose. "Improved Wavelength Meter Calibration in Near Infrared Region via Doppler-Free Spectroscopy of Molecular Iodine". *Applied Physics B* **127**, 104 (2021). DOI: 10.1007/s00340-021-07650-5

5. K. König, F. Sommer, J. Lantis, K. Minamisono, W. Nörtershäuser, **S. Pineda**, and R. Powel. "Isotope-shift measurements and King-fit analysis in nickel isotopes". *Physical Review C* **103**, 054305 (2021). DOI: 10.1103/PhysRevC.103.054305

6. K. König, K. Minamisono, J. Lantis, **S. Pineda**, and R. Powel. "Energy determination via collinear laser spectroscopy". *Physical Review A* **103**, 032806 (2021). DOI: 10.1103/PhysRevA.103.032806

7. B. A. Brown, K. Minamisono, J. Piekarewicz, H. Hergert, D. Garand, A. Klose, K. König, J. D. Lantis, Y. Liu, B. Maaß, A. J. Miller, W. Nörtershäuser, **S. V. Pineda**, R. C. Powel, D. M. Rossi, F. Sommer, C. Sumithrarachchi, A. Teigelhöfer, J. Watkins, and R. Wirth. "Implications of the ^{36}Ca-^{36}S and ^{38}Ca-^{38}Ar difference in mirror charge radii on the neutron matter equation of state". *Physical Review*

Research **2** 022035(R) (2020).

DOI: 10.1103/PhysRevResearch.2.022035

8. A. Klose, K. Minamisono, A. J. Miller, B. A. Brown, D. Garand, J. D. Holt, J. D. Lantis, Y. Liu, B. Maaß, W. Nörtershäuser, **S. V. Pineda**, D. M. Rossi, A. Schwenk, F. Sommer, C. Sumithrarachchi, A. Teigelhöfer, and J. Watkins. "Ground-state electromagnetic moments of ^{37}Ca". *Physical Review C* **99**, 061301(R) (2019). DOI: 10.1103/PhysRevC.99.061301

9. E. L. Westerman, N. Antonson, S. Kreutzmann, A. Peterson, **S. Pineda**, M. R. Kronforst, and C. F. Olson-Manning. "Behaviour before beauty: Signal weighting during mate selection in the butterfly *Papilio polytes*". *Ethology* **125**, 565-574 (2019). DOI: 10.1111/eth.12884

10. A. J. Miller, K. Minamisono, A. Klose, D. Garand, C. Kujawa, J. D. Lantis, Y. Liu, B Maass, P. F. Mantica, W. Nazarewicz, W. Nörtershäuser, **S. V. Pineda**, P. -G. Reinhard, D.M. Rossi, F. Sommer, C. Sumithrarachchi, A. Teigelhöfer, and J. Watkins. "Proton superfluidity and charge radii in proton-rich calcium isotopes". *Nature Physics* **15**, 432-436 (2019).

DOI: 10.1038/s41567-019-0416-9

M.2 Presentations

Underline denotes presenter

M.2.1 Oral Presentations

1. "Symmetry Energy Constraints Using the Difference in Mirror Pair Charge Radii for the ^{54}Ni-^{54}Fe Pair", **Skyy V. Pineda**; *FRIB Research Discussion Seminar Series*, East Lansing, Michigan; 6 October, **2022**.

2. "Symmetry Energy Constraints Using the Difference in Mirror Pair Charge Radii for the ^{54}Ni-^{54}Fe Pair", **Skyy V. Pineda**, Kristian König, Dominic M. Rossi, B. Alex Brown, Anthony Incorvati, Jeremy D. Lantis, Kei Minamisono, Wilfried Nörtershäuser, Jorge Piekarewicz, Robert Powel, Felix Sommer; *International Nuclear Physics Conference (INPC)*, Cape Town, South Africa; 15 December, **2022**.

3. "Determination of the neutron-deficient ^{54}Ni charge radius and symmetry energy constraints using the difference in mirror pair charge radii", **Skyy V. Pineda**, Kristian König, Dominic M. Rossi, B. Alex Brown, Anthony Incorvati, Jeremy D. Lantis, Kei Minamisono, Wilfried Nörtershäuser, Jorge Piekarewicz, Robert Powel, Felix Sommer; *Nuclear Structure*, Berkeley, California; 15 June, **2022**.

4. "Charge Radius of Neutron Deficient ^{54}Ni and Symmetry Energy Constraints Using the Difference in Mirror Pair Charge Radii", **Skyy V. Pineda**, Kristian König, Dominic M. Rossi, B. Alex Brown, Anthony Incorvati, Jeremy D. Lantis, Kei Minamisono, Wilfried Nörtershäuser, Jorge Piekarewicz, Robert Powel, Felix Sommer; *FRIB Precision Measurements Group Meeting*, Virtual; 10 January, **2022**.

5. "Charge Radius of Neutron Deficient ^{54}Ni and Symmetry Energy Constraints Using the Difference in Mirror Pair Charge Radii", **S. V. Pineda**, K. König, D. M. Rossi, B. Alex Brown, A. Incorvati, J. D. Lantis, K. Minamisono, W. Nörtershäuser, J. Piekarewicz, R. Powel, F. Sommer; *Fall Meeting of the Division of Nuclear Physics (DNP)*, Virtual; 14 October, **2021**.

6. "Charge radius of neutron deficient ^{54}Ni and its mirror pair for constraints on slope parameter L in the neutron equation of state," **S. V. Pineda**, D. M. Rossi, K. König, B. A. Brown, J. D. Holt, A. Incorvati, J. Krämer, A. Klose, J. D. Lantis, Y. Liu, B. Maaß, A. Miller, K. Minamisono, W. Nörtershäuser, R. Powel, M. Pearson, A. Schwenk, F. Sommer, C. Sumithrarachchi; *Fall Meeting of the Division of Nuclear Physics (DNP)*, Virtual Meeting; 31 October, **2020**.

M.2.2 Poster Presentations

1. "Charge radii of Ni isotopes across the $N = Z = 28$ Shell Closure", F. Sommer, K. König, D. M. Rossi, N. Everett, D. Garand, R. P. de Groote, J. D. Holt, P. Imgram, A. Incorvati, C. Kalman, A. Klose, J. Lantis, Y. Liu, A. J. Miller, K. Minamisono, T. Miyagi, W. Nazarewicz, W. Nörtershäuser, **S. V. Pineda**, R. Powel, P-G Reinhard, L. Renth, E. Romero-Romero, R. Roth, A. Schwenk, C. Sumithrarachchi, and A. Teigelhöfer; *International Nuclear Physics Conference (INPC)*, Cape Town, South Africa; 12 September, **2022**.

2. "Charge Radius of Neutron-deficient ^{54}Ni and Symmetry Energy Constraints Using the Difference in Mirror Pair Charge Radii," **S. V. Pineda**, K. König, D. Rossi, B. A. Brown, A. Incorvati, A. Klose, J. Lantis, K. Minamisono, W. Nörtershäuser, J. Piekarewicz, R. Powel, F. Sommer; *Euroschool on Exotic Beams*, Virtual; 14 September, **2021**.

3. "Charge radius of ^{54}Ni and Slope Parameter in Nuclear Equation of State," **S. V. Pineda**, K. König, D. Rossi, B. A. Brown, A. Incorvati, A. Klose, J. Lantis, K. Minamisono, W. Nörtershäuser, J. Piekarewicz, R. Powel, F. Sommer; *International Conference on HYPERFINE Interactions and their Applications*, Brasov, Romania/Virtual; 7 September, **2021**.